Effects Of Microstructure And Processing On Fracture And Fatigue Crack Growth Of Ti-43.5al-4nb-1mo (Tnm) Third Generation Turbine Blade Material

by

MATTHEW SCOTT DAHAR

Submitted in partial fulfillment of requirements for the degree of
Doctor of Philosophy

Department of Materials Science and Engineering

CASE WESTERN RESERVE UNIVERSITY

January 2018

CASE WESTERN RESERVE UNIVERSITY

SCHOOL OF GRADUATE STUDIES

We hereby approve the dissertation of

Matthew Scott Dahar

candidate for the Doctor of Philosophy degree*.

(signed) Prof. John J. Lewandowski

(Chair of the Committee)

Prof. Jennifer L. W. Carter

Prof. Gerhard Welsch

Prof. Clare Rimnac

Dr. Sesh A. Tamirisakandala

(date) 11/13/2017

*We also certify that written approval has been obtained for any proprietary material contained therein.

Dedication

To my parents for 27+ years of dedication and support of my dreams.

Table of Contents

List of Figures

List of Tables

Effects of Microstructure and Processing on Fracture And Fatigue Crack Growth Of Ti-43.5Al-4Nb-1Mo (TNM) Third Generation Turbine Blade Material

Abstract

By

MATTHEW SCOTT DAHAR

The effects of thermal and thermomechanical processing, sample orientation, and load ratio on the room temperature fatigue crack growth and fracture behavior of a third-generation gamma titanium aluminide Ti-43.5Al-4Nb-1Mo-0.1B (TNM) were determined in this study. Bend bar specimens, excised from TNM in as-cast, cast + hot isostatic pressing, and forge + heat treat conditions in the longitudinal and transverse directions, were tested at room temperature in lab air. Load ratios in the range 0.1 – 0.9 were used in fatigue testing to determine their effects on the fatigue threshold, Paris law slope, and stress intensity at overload. Microscopy, fractography, and X-ray diffraction were used to understand the effects of process and testing variables on the fatigue crack path and morphology. The effects of microstructure length scales and microconstituents are discussed in relation to the properties measured.

Acknowledgements

This work was supported by the US Air Force Metals Affordability Initiative (Agreement Order No. FA8650-15-2-5201 AO#43). The supply of material has been from Arconic Titanium & Forged Products. MD acknowledges the co-op support at Arconic. Partial financial support provided by the CWRU Arthur P. Armington Professorship of Dr. John Lewandowski.

Additionally, I am grateful to Dr. John J. Lewandowski for his support, advising, and contributions to shaping this project and analyzing the results. He ensured that the work was set up for success every tsep of the way by imparting knowledge, providing guidance, and so much more.

The work wouldn't have been possible without the advice and guidance of my co-adviser Dr. Sesh Tamirisakandala of Arconic Titanium and Forged Products for his assistance, expertise, dedication and provision of excellent advice on the direction of the project and complemented the work

Additional acknowledgements go to Chris Tuma for his technical assistance in training on the various equipment to run experiments of this project. The machine shop crew, including Wayne Schmidt, John Weber, and Sam Salvatore provide excellent support.

Lastly, I would like to thank my family and friends for being there when I need them. Without their support and encouragement, this work would have been extremely difficult to complete.

1. Background and Introduction

1.1 General Introduction

Although superalloys are the current choice for high temperature (1073K-1273K) structural applications in aircraft engine technology, the need for more efficient engine performance has necessitated a search for materials exhibiting lower densities, higher moduli, and higher temperature capabilities. One such material system that has attracted significant attention in the last twenty years for their attractive properties conducive for high temperature automobile and aerospace applications are the titanium aluminides [[1]–[4]]. One of the foremost applications that titanium aluminides have been considered for are high performance gas turbine engines [5]. Replacement of Ni-based superalloys is expected to reduce the structural weight of gas engines by 20%-30% [6].

1.2 Importance of Titanium Aluminide

Advantages of titanium aluminides includes low density (3.9 – 4.2 g/cm^3), high specific yield strength, high specific stiffness, good oxidation resistance, and good creep properties up to high temperatures (800°C). The variations of specific yield strength with temperature of γ-TiAl based alloys is shown in comparison to Ni-base superalloys in Figure 1.1 [7]. Because of the long range order typically present in intermetallics, titanium aluminides generally lack room temperature ductility, may have poor fracture toughness and are difficult to process and machine at room temperature. Fatigue crack growth rates are also an area of concern [8]. However, advances in manufacturing technologies and micro-alloying led to the first commercial use of titanium aluminides in high performance turbochargers for Formula One and sports cars in 1999 [9]. Titanium aluminides have also been used in the General Electric GEnx gas turbine engine designed for the Boeing 787 Dreamliner [10], and are being used in low pressure turbine (LPT) blades.

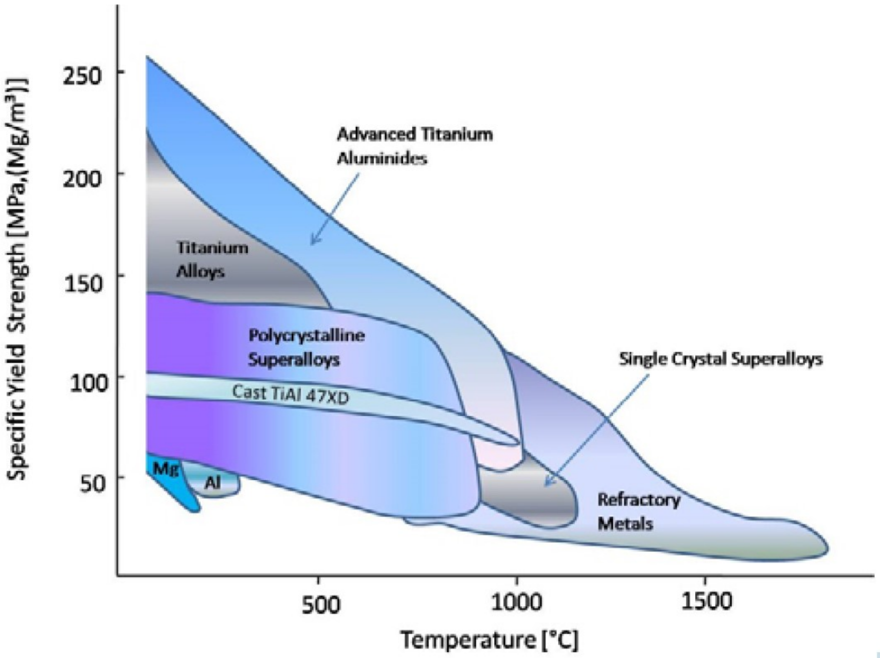

Figure 1.1: Variation of specific yield strength with temperature of selected structural materials in comparison with intermetallic γ-TiAl based alloys [7].

1.3 Microstructural Characteristics

The binary Ti-Al phase diagram is shown in Figure 1.2. Gamma-TiAl based alloy systems typically contain 42-56 atomic percent aluminum. Stoichiometric and aluminum rich alloys (Al >50%) are typically single-phase γ alloys. γ-TiAl is an ordered, intermetallic compound of Ti and Al with a $L1_0$ structure (face center tetragonal) as shown in Figure 1.3a. The unit cell of γ-TiAl is slightly distorted with a $c/a \approx 1.02$ and consists of alternating planes of Ti and Al atoms in the [001] direction [3]. Most alloys of engineering interest are aluminum-lean and are two-phase alloys, the second phase being

α_2-Ti_3Al which is an ordered hexagonal compound ($D0_{19}$) as shown in Figure 1.3b. The α_2-volume fraction is controlled by the amount of Al and alloying elements which are typically in the range of 5 to 20 percent. However, heat treatments and thermomechanical processing also have a strong influence on the γ/α_2 volume fraction in γ-TiAl based alloys. Al-lean alloys that contain additions of Cr, Nb, Mo, or W show a significant amount of β-TiAl phase, which is a disordered, body-centered cubic (BCC) structure and β_0-TiAl that exhibits the B2 structure (BCC) shown in Figure 1.4. Micro-alloying with C, B, and Si leads to the formation of carbides, borides and silicides because of the limited solubility of these elements in γ-TiAl and α_2-Ti_3Al phases [9].

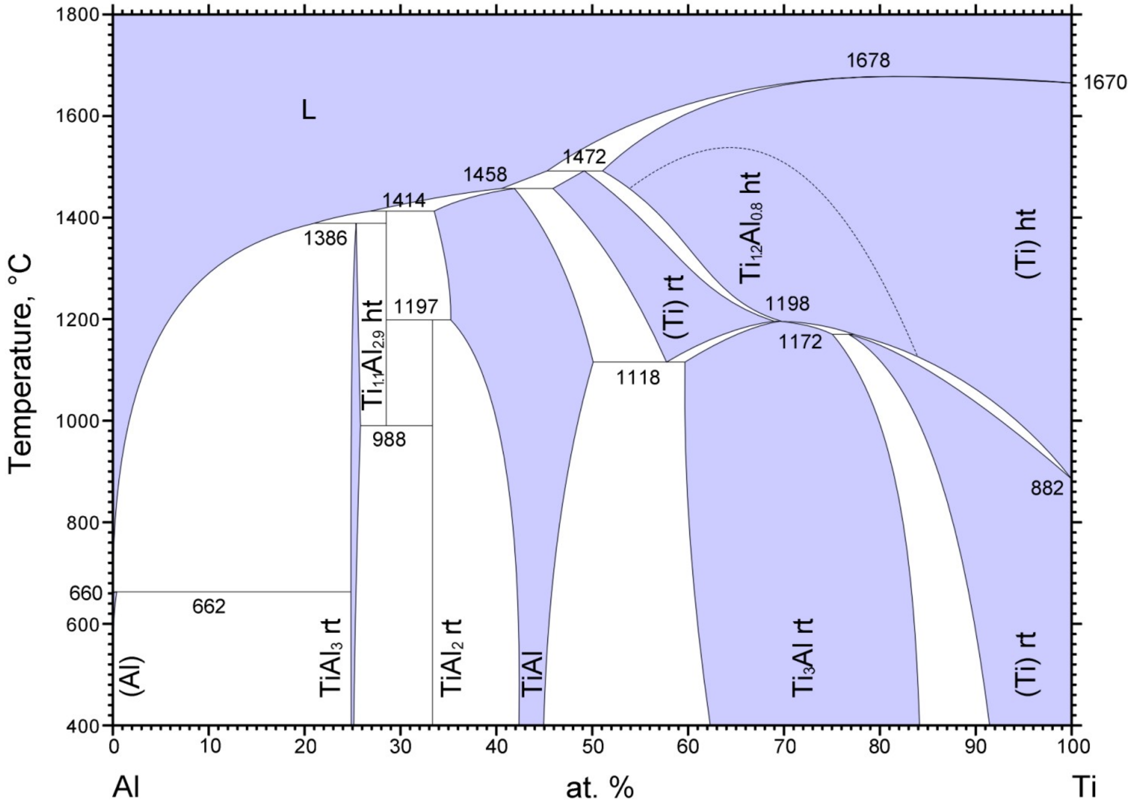

Figure 1.2: Ti-Al Phase Diagram [11].

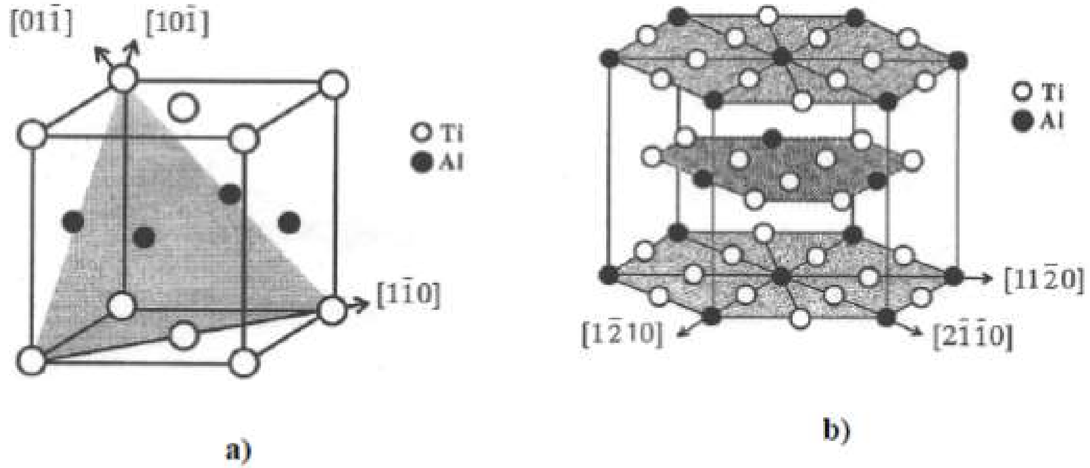

Figure 1.3: Crystal Structures for (a) γ-TiAl, and (b) α_2-Ti_3Al [12].

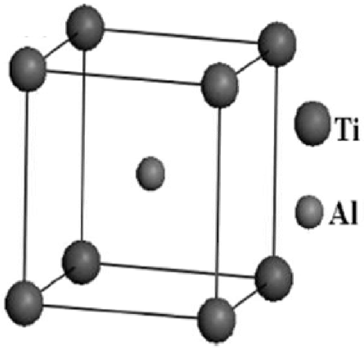

Figure 1.4: Crystal Structure for β_o-TiAl.

The strength and ductility of γ-TiAl based alloys are controlled by the chemical composition and microstructure. For fine-grained binary TiAl alloys, the room temperature elongation to fracture varies with the aluminum content, showing a maximum at the two-phase composition Ti-48Al [3]. The low temperature ductility is a major concern for structural applications, so the γ-TiAl alloys of importance are based on Ti-(42-48)Al [3], [13]. From the beginning of the alloy development, it was recognized that binary two-phase alloys cannot be used because of their inability to meet requirements such as creep strength and resistance to oxidation. This led to extensive research and development programs studying the effects of alloying elements on the mechanical properties of two phase γ-TiAl based alloys. These programs resulted in the creation of 1st and 2nd generation TiAl alloys summarized by Kim [3] [13]. Alloying additions such as Cr, Mn, and C with thermo-mechanical processing produced further improvements, with elongation at fracture up to 3% [13], [14].

1.4 2nd Generation Titanium Aluminide

The composition of 2nd generation γ-TiAl based alloys can be summarized as follows:

Ti-(45-48)Al-(1-3)X-(2-5)Y-(<1)Z

where X= Cr, Mn, V ; Y= Nb, Ta, W, Mo ; Z= Si, B, C. The alloying elements alter the position of the phase boundaries of the Ti-Al phase diagram. An engineered γ-TiAl based alloy of the 2nd generation contains at least one X element and one Y element to account for a good balance between ductility at room temperature and sufficient creep and oxidation resistance at elevated temperature. An example of a 2nd generation alloy, Ti-48Al-2Nb-2Cr, has been introduced as a turbine blade material in GEnx jet engines [3], [12]. Depending on the alloy chemistry and microstructure, these alloys exhibit good workability, medium to good tensile properties, and tensile fracture strain in the range of 1-3% at room temperature as well as fracture toughness values ranging from 10 to 25 MPa√m.

The mechanical properties of dual phase α_2+γ have been found to be very sensitive to its microstructure, grain size, and small volumes of micro-alloying constituents [15]. The dual phase alloys have also exhibited RT and high temperature strengths equivalent to that of superalloys [9], while the creep and oxidation resistance have been shown to be acceptable for temperatures up to 850ºC [16].

The phases present in dual-phase titanium aluminides can exhibit a wide range of microstructures depending on the processing techniques and/or heat treatment. The microstructures have been broadly classified into four categories: 1) Near-Gamma, 2) Duplex, 3) Nearly-Lamellar, and 4) Fully lamellar [15] as shown in Figure 1.5. Of these microstructures, the duplex and fully lamellar microstructures have exhibited mechanical properties conducive for a range of commerical applications [14].

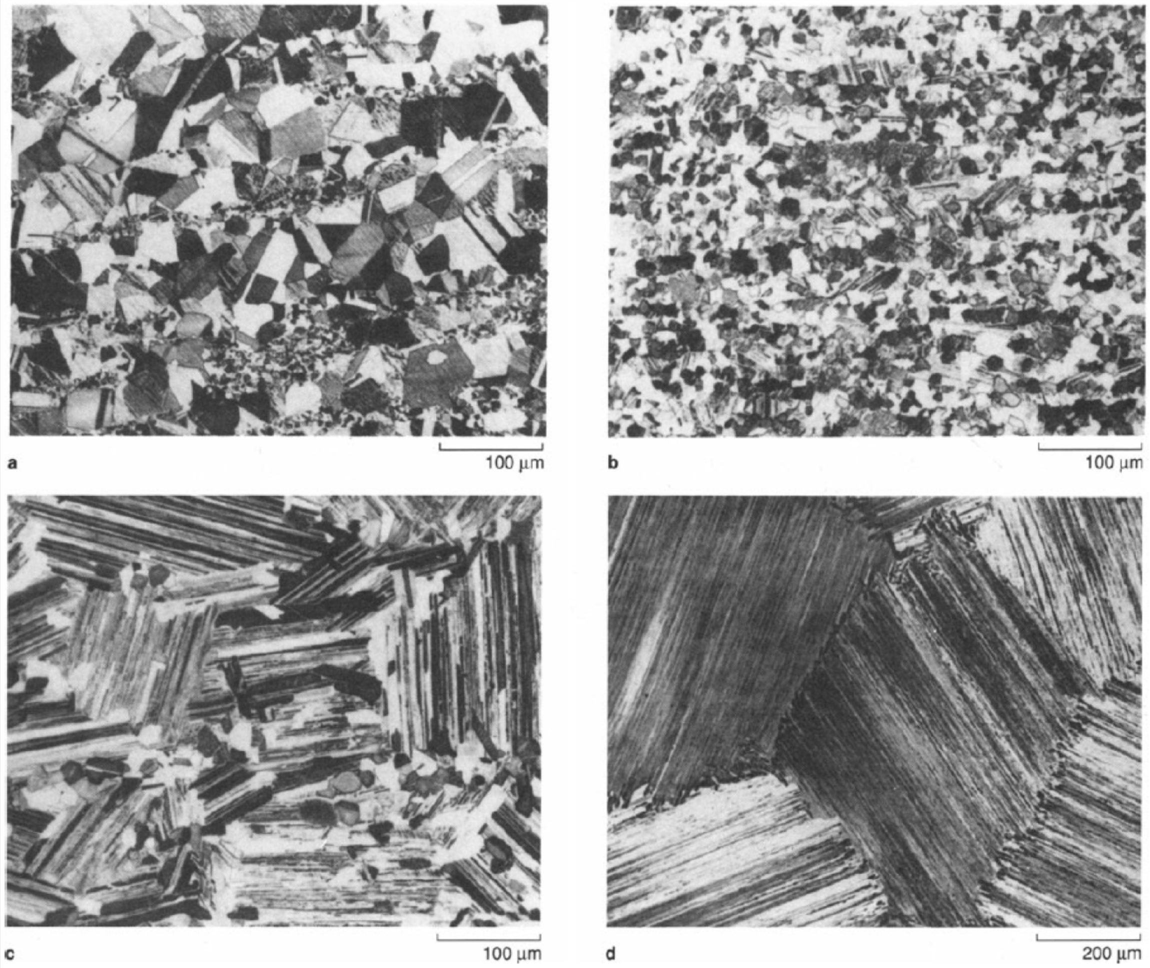

Figure 1.5: Microstructure types in dual-phase titanium aluminides (a) Near-gamma, (b) Duplex, (c) Nearly-Lamellar, and (d) Fully Lamellar [17].

The development of each of these microstructures is achieved via different heat treatments. The fully lamellar microstructures (Figure 1.5d) are achieved by solutionizing in the single phase α regime and subsequently fast cooling. The transformation of prior alpha into variants of γ and α_2 plates produces a lamellar microstructure. Since the solutionizing temperatures are quite high, the prior-α grains are large and the resultant lamellar colonies have large grain sizes. The typical grain (colony) size of a lamellar microstructure is 100-150 μm. Duplex structures (Figure 1.5b) are formed when the material is annealed below the α-solvus temperature in the (α+γ) phase region. The duplex microstructure consists of lamellar α_2/γ colonies and γ-TiAl grains. The lamellar thickness measures several hundred μm to a few μm. The percentage of lamellar grains increases with increasing temperature in the (α+γ) region.

Near gamma microstructures are formed after a heat treatment just above the eutectoid temperature (i.e, 1125°C) and produce a small amount of α_2 phase at the grain boundaries of the globular γ-TiAl grains. Coarse annealing twins are sometimes formed during grain growth of γ-TiAl phases.

The γ and α_2 lamellae in the fully lamellar (FL) microstructure are observed to have the "Blackburn" [18] orientation relationship:

$$\{111\}\gamma \parallel (0001)\alpha_2 \; and < 110 > \gamma \parallel < 11\bar{2}0 > \alpha_2$$

The interface plane is parallel to the close packed planes in each phase, namely the (0002) basal plane in α_2 and {111} in γ. There are six differently oriented γ variants in the lamellar structure as <110] and <101] directions in the $L1_0$ structure are not equivalent [18]. Each of these variants is related by rotation of 60°. Adjoning gamma variants meet to form three different types of γ-γ interfaces: Pseudo-twins (60 ° rotation), a 120° rotation-twin (variant interface) and a perfect twin (180° rotation), as shown in Figure 1.6 [19], [20]. These interfaces are mainly found along the close-packed habit planes. Even within a single γ lath, the different variants can meet, forming order domain boundaries. These are thought to be formed by the independent nucleation, lateral growth and impingement of two different γ variants. These order domain boundaries do no follow particular habit planes.

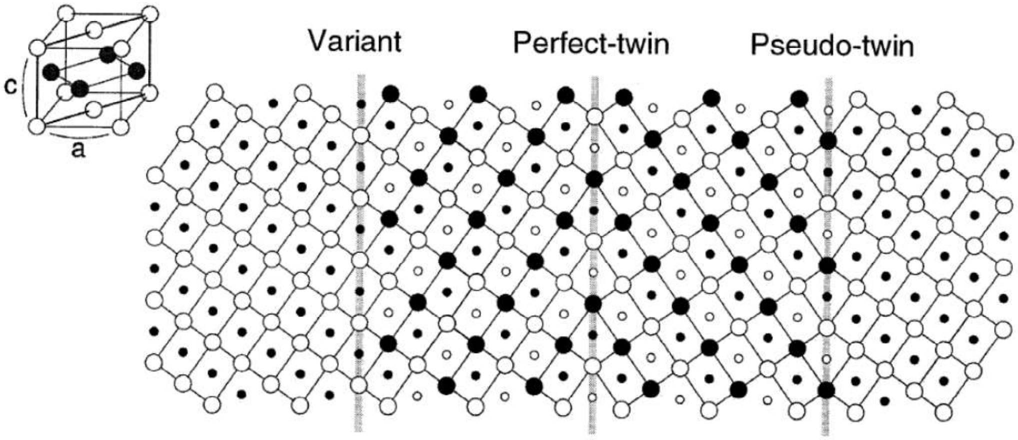

Figure 1.6: Atom configuration of {110} planes showing the three types of interfaces in $L1_0$ structure. (Small circle represent the atom positions on the plane one above or below the planes with the large circles. Solid and open symbols refer to Ti and Al atoms [20].

The transformation of α into α_2 and γ plates is the result of two factors a) the low misfit between the phases along the close packed planes b) the relative ease of transformation mechanisms that leads to this orientation relationship. It is generally accepted that the γ lamellae probably nucleates from stacking faults in the α matrix lying on the basal planes. The growth of γ from α phases is facilitated by subsequent passage of one of the Shockley partials bordering the stacking fault. Repeating this process at every other basal plane of the hexagonal matrix brings about the desired change in staking necessary to achieve the change in crystal structure [21]. It is often envisioned that the growth of gamma occurs by the movement of ledges (of the Schockley types) on the α_2/γ interface. Since only one habit plane (the basal plane in the prior α grain) is available, a single orientation of the lamellar plates is obtained in one colony. The residual α trapped between the growing γ lamellae then transforms into the ordered α_2 phase below the eutectoid temperature.

Segregation, compositional imhomogeneities and inconsistencies in temperature gradients during the actual processing and heat treatment can lead to microstructures other than that described above. Zhang et al. [22] shows that the γ laths can sometimes precipitate on some non-basal planes of the α matrix, even at very slow cooling rates. The formation of packet type lamellar microstructures dominated by APBs and true twin boundaries which are arranged in packets has been reported. This was observed when the cooling rate though the $\alpha + \gamma$ phase filed is large.

1.5 Effect of Chemistry

Varying the aluminum content can lead to single phase γ-alloys (Al content at or above stoichiometry), or two-phase $\alpha_2+\gamma$ alloys (below stoichiometry). The α_2 volume fraction increases with decreasing Al content. In the composition range from 43 to 53 at.% Al, the lowest strength occurs at compositions around 51 at.%. Room temperature ductility also varies with the aluminum content, exhibiting a maximum ductility around two-phase compositions of Ti-48Al [13].

There is overwhelming evidence that small quantities of V, Cr and Mn significantly enhances the ductility of two-phase gamma alloys [3], [13], [15]. This favorable effect on ductility has been reasoned to be either because of phase stabilization or due to the nature of site occupancy as Cr, Mn, and V have been shown to partition preferentially to α_2 [23]. It has been suggested that stabilization of α_2 is beneficial since α_2 acts as an ideal scavenger of interstitial impurities such as boron, oxygen and nitrogen, which would otherwise cause embrittlement of gamma phase [13]. It has also been suggested that Mn and Cr decrease the covalent nature of bonding in γ-TiAl [24], [25]. This is reported to reduce the tetragonality of the $L1_0$ structure and cause an increase in the number of deformation modes [26].

The addition of several alloying elements including Nb, Zr, Mo, V, W, Hf, Sn and Ta has been shown to increase the creep resistance [13]. It has been proposed that the addition of W and Ta significantly reduces diffusion in the gamma phase [20]. These slow diffusing species also tend to stabilize the fully lamellar microstructures by reducing lamellar coarsening processes. It has also been proposed that W lowers the stacking fault energy and this makes dislocation recovery mechanisms more difficult [23], [27].

Si is shown to enhance the high temperature oxidation resistance [28]. In small quantities, it is also an excellent solid solution strengthener. Higher levels of Si have been shown to cause precipitation of silicides, producing significant strengthening [29]. Si has also been credited for the retardation of dynamic recrystallization and microstructure refinement [28], [29]. In lamellar microstructures, the addition of Si has been reported to change the misfit between α_2 and γ and leads to the formation of interfacial misfit screw dislocation networks [30]. The addition of silicon has also been reported to be severely detrimental to the fracture toughness.

Cr, V, Nb and Mo have been shown to stabilize a third phase, the B2 phase. B2 is an ordered body centered cubic phase with CsCl structure. The B2 phase has a Ti/Al ratio close to that of α_2 but contains 10-15% BCC stabilizing elements. B2 is also observed to have precipitated at the colony boundaries in FL alloys and at grain boundaries in equiaxed alloys, after annealing [31]. The presence of the B2 phase has often been suggested to improve room temperature ductility, but adversely affects creep properties [32].

Interstitial elements such as C, B, O and N have been shown to affect the mechanical properties significantly [23]. Carbon and Nitrogen containing alloys have been shown to cause extensive precipitation hardening and show typical age hardening behavior. Both Carbon and Boron additions have been credited with grain size refinement [26]. Plate-like borides that form from the melt and during aging have been suggested as a reason for microstructural refinement [33]. Boron additions are also seen to promote the formation of duplex and equiaxed microstructures, and cause a discontinuous α_2 and packet structure of fine α_2 lamellae in fully lamellar microstructures.

Manipulation of the microstructure and alloy design has lead to the general improvement of both room temperature and high temperature properties.

1.6 3rd Generation Titanium Aluminide

In order to increase the economic feasibility of γ-TiAl, wrought processing methods are needed which can use conventional equipment with minor or inexpensive modifications. The following demands are placed on the alloy: (a) after casting and solification, the alloy should possess a refined equiaxed microstructure with no texture; (b) the composition of the alloy must be defined to ensure a solidification path according to $L \rightarrow L+\beta \rightarrow \beta \rightarrow ...$ instead of crossing a peritectic which is prone to segregation; (c) during ingot breakdown as well as secondary hot-forming operation, a large volume fraction of disordered BCC β-phase is needed to improve the deformability at elevated temperature and suppresses grain growth. At service temperatures, the volume fraction of the β_0-phase which is an ordered B2, should be small in order not to deteriorate creep properties; (d) in order to avoid grain growth, the existence of a single phase region needs to be avoided; and (e) the alloys should provide a well-balanced phase ratio of γ-TiAl and α_2-Ti_3Al (and β/B2) which can be converted by means of simple and reproducible heat-treatments [32].

In order to increase the high temperature capabilities of γ-TiAl base alloys and meet the demands above, current alloy development efforts are focused on high Nb and Mo containing alloys along with precipitation hardening alloys [34], [35]. For a large number of 3rd generation alloys, the formulation can be written as:

Ti – (42 -48) Al – (0 – 10)X – (0 – 3) Y – (0 -1)Z – (0-0.5 RE)

Where X = Cr, Mn, Nn ,Ta; Y = Mo, W, Hf, Zr; Z = C , B, Si, and RE denotes rare earth elements. γ-TiAl based alloys with Nb content in the range of 5 to 10 at.% and small amounts of B and C are classified as TNB alloys [36], while another class called TNM alloys contain Nb and Mo β stabilizers. At elevated temperatures, TNM contains a large amount of disordered bcc β-phase which improves the hot workability. It has been shown that TNM alloys, in contrast to TNB alloys, can be forged using conventional forging techniques [35], [37] which allows for cheaper and larger scale production of parts. Both TNM and TNB alloys exhibit improved strength properties and oxidation resistance when compared to the 2nd generation TiAl alloys. Room temperature tensile strength is in the range of 800-1100 MPa with a plastic tensile strain >2% [32]. The β stabilizers impede the diffusion process, thus decreasing the climb rate of dislocations. This behavior is an advantage with regards to creep and thermal stability, however the kinetics of phase transformation, and recrystallization are reduced. This means that the parameters for heat treatment and hot working needs to be carefully considered.

To select an alloy which fulfills the demands as defined above, thermodynamic calculations based on the CALPHAD method were conducted for the prediction of the constituent phase and transition temperatures by Clemens [35]. Two different software packages (Thermocalc and MatCal) were used with the same commercial TiAl database [38]. It has been found that the thermodynamic database used poorly describes the transition temperatures and phase proportions in high Nb γ-TiAl based alloys as shown in the literature [39], [40]. It should be noted that the calculations were done to find alloying trends rather than to give absolute values of phase fraction and transition temperatures. Three alloys were modeled with constant Al (43 at.%) but varying content of β-stabilizing alloys Nb (4-5 at.%) and Mo (1-1.5 at.%). The Nb decreases the stacking fault energy in the β-TiAl, slows down diffusion in both the γ and α_2, and improves oxidation behavior. Mo is also a β-stabilizing element in the Ti-Al system and raises the activation energy of diffusion in both γ and α_2, but has a much larger partition coefficient than Nb. A boron content of 0.1% was selected to ensure a grain refining effect during solidification. Boron also forms borides which are beneficial in the case of heat treatments at high temperatures by pinning the grain boundaries.

Figure 1.7 shows the calculated phase fraction diagram as a function of temperature for TNM using Ti-43Al-4Nb-1Mo-0.1B (4341) composition [34]. The figure predicts an ordering reaction $\beta \rightarrow \beta_o$ at about 1410°C to 1420°C depending on the alloy composition. All three of the compositions modeled show a minimum of the β-phase fraction at around 1275°C and above this temperature the fraction of β strongly increases. At this temperature (1275°C), Ti-4341 shows the smallest fraction of β-phase, and only this alloy showed a pronounced "C-shaped" curve for the β-phase in the model. Increasing the amount of Nb or Mb considerably increased the minimum amount of β. Below the eutectoid temperature (T_{eu} = 1115°C) the ordered β/β_o phase fraction decreases with decreasing temperature and seems to vanish at about 600°C in the case of Ti-4341 and Ti-4351. All three of the modeled alloys show an adjustable volume fraction of β in the temperature range where hot working is preformed. However, only Ti-4341 shows the potential of β-phase being avoided by heat-treatments, as the phase fraction of β is small at 1275°C and can be dissolved with short annealing time. It must be noted that Figure 1.8 predicts phase conditions under thermodynamic equilibrium. However, γ-TiAl based alloys processed under technically relevant conditions always show a distinct deviation from phase equilibrium [35].

In order to better understand the phase evolution and phase transformation, in-situ neutron diffraction was conducted in the temperature range from 900 to 1450°C. It was found that the ordering of the β-phase occurs around 1210°C [41]. Schmoelzer et al. [42] conducted DSC experiments at 10, 20, and 30 K/min and found that Teu is 1174°C, Tα is 1247 ± 5, and the β_0 to β transition was found to be 1224°C. The current phase diagram for TNM alloys is given by Fig 1.7 [43] and is based on DSC and high energy XRD. During solidification, the TNM alloy undergoes a transformation pathway which is expressed as L→L+β→β→β+α→α+β+γ→α+β+βo→α+βo+γ→α+α2+βo+γ→α2+βo+γ.

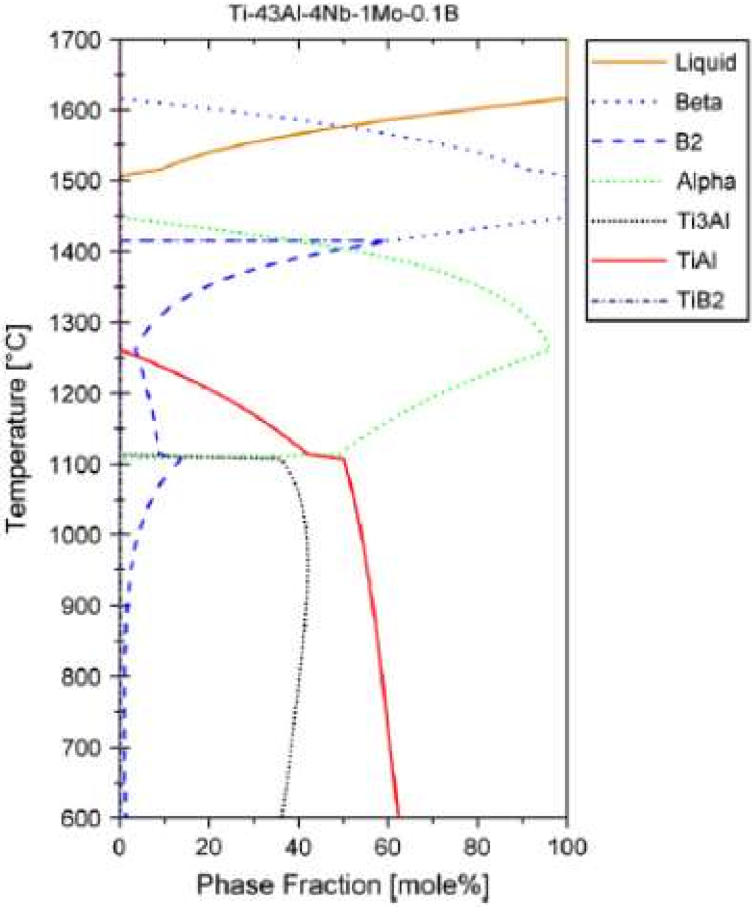

Figure 1.7: Calculated phase fractions as a function of temperature for the investigated alloy [34].

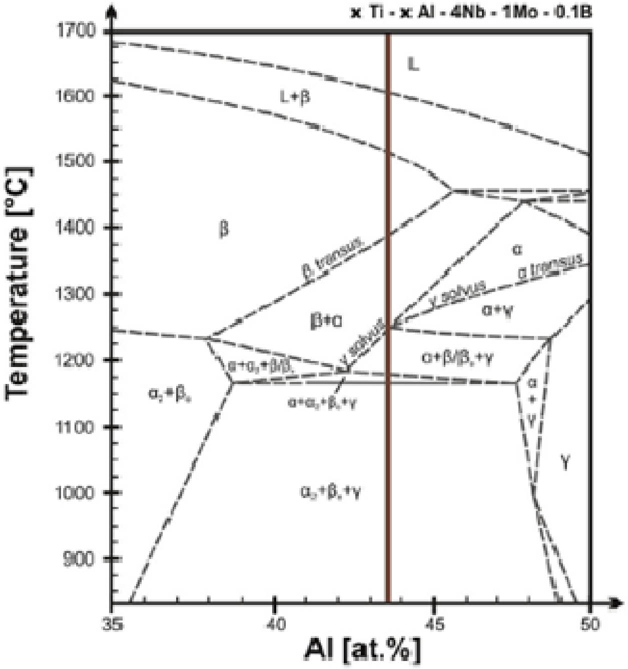

Figure 1.8: Experimental quasi-binary section thought TNM alloying systems. The line represents an alloy with 43.5 atomic percent of aluminum. Reprinted from Reference [43].

.

For TNM alloys, the optimum balance between fracture toughness and creep resistance on one hand, and room temperature tensile ductility and strength on the other hand, is expected for a microstructure composed of relatively small lamellar colonies (50 to 100 μm) in diameter and narrow lamellar spacing with a small volume fraction of globular γ and β_0 [32]. The amount of β_o phase needs to be controlled since the large number of slip present in β_o promotes creep at service temperatures. A schematic of a TNM alloy microstructure is given in Figure 1.9 which shows microstructure components and their effects on various mechanical properties.

Figure 1.10 shows SEM images of the microstructure of TNM alloy Ti-43.5Al-4Nb-1Mo-0.1B with different production processes and chemistries. Figure 1.9a is from the as-cast condition and the microstructure can be explained by the complete solidification via the β-phase as predicted by modeling shown in Figure 1.6. The microstructure contains lamellar $(\gamma+\alpha_2)$ colonies with colony diameters less than 100 μm. The high cooling rate leads to a lamellar spacing that is too small and cannot be resolved at the magnification used. The ordered β-phase is located along the colony boundary and only a small volume fraction is present within the colonies. The as-cast material shows residual porosity and phases that are not in thermodynamic equilibrium.

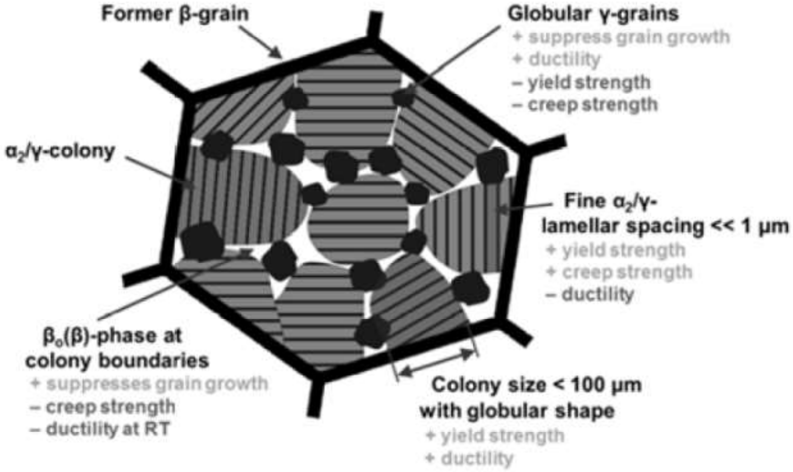

Figure 1.9: Schematic drawing of a designed microstructure which can be adjusted in the forging and heat treatment of TNM alloy. The microstructural constituents' influences on mechanical properties are shown. [32], [37], [44]

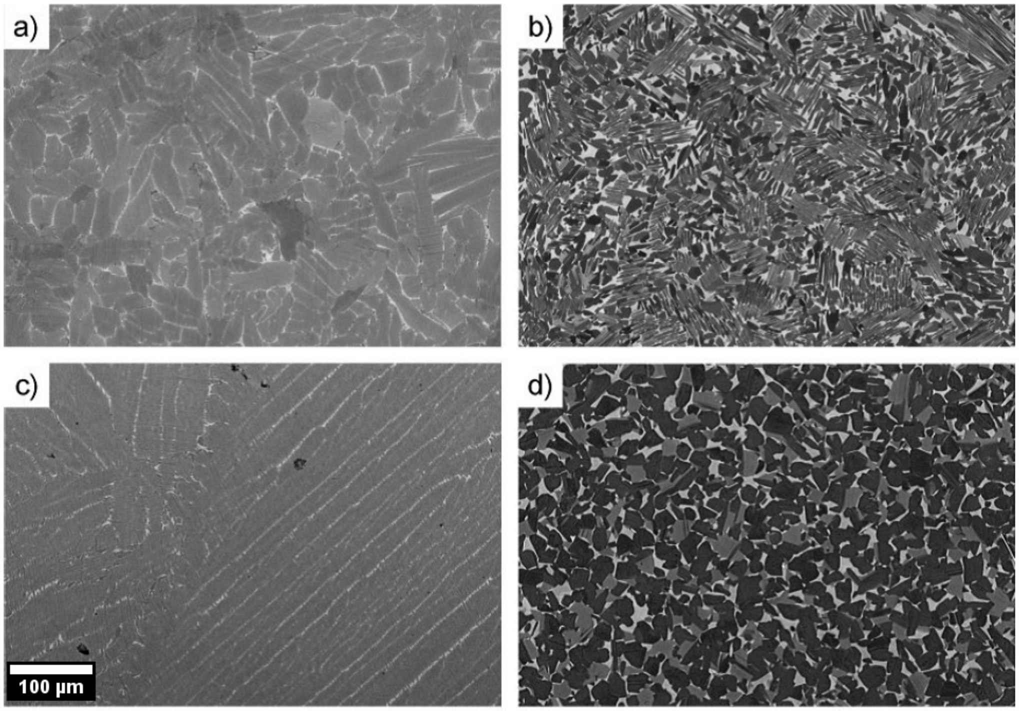

Figure 1.10: Microstructure of TNM alloys with different processing procedures. (a) Ti-43.5Al-4Nb-1Mo-0.1B in the as-cast condition; (b) cast material after HIPing for 4 h at 1200°C and 200 MPa, followed by slow cooling ; (c) cast and HIPed without B; (d) HIPed Ti-43.5Al-4Nb-1Mo-0.1B gas-atomized powder. SEM images are taken in BSE, γ-TiAl appears gray to dark, α_2 –Ti_3Al light gray, and β_o-TiAl exhibits the brightest contrast [32].

To close porosity and improve chemical homogeneity the material is subject to hot isostatic pressing (HIPing) which is conducted at 1200°C for 4 hr. at 200MPa followed by slow cooling. Figures 1.10b and 1.11 show representative as-HIPed microstructures. The phase fractions are now more in line with what the phase diagram predicts in Figure 5. A large fraction of γ-TiAl grains and lamellar γ/α_2-colonies are produced from the phase transformations during HIPing. The beneficial role of B in the as-cast TNM alloy can be seen by comparing Figure 1.10b to Figure 1.10c which exhibits the microstructure of an alloy which was produced without adding the grain refining agent B. After casting and HIPing, the microstructure still needs to undergo forging and a dual heat treatment to produce acceptable properties.

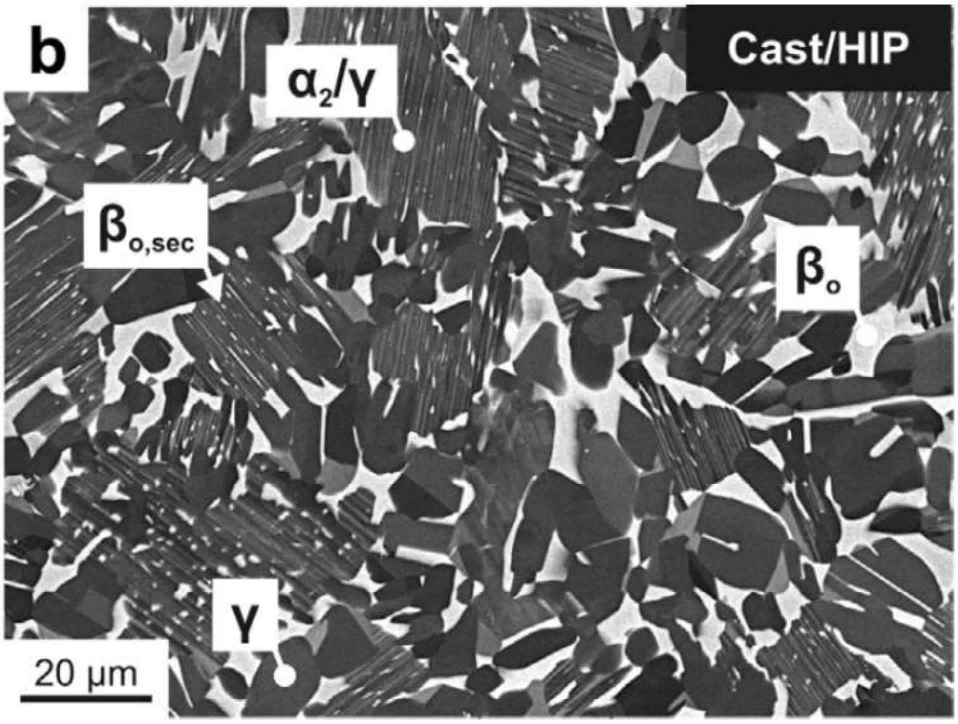

Figure 1.11: Reference microstructure of as-cast + HIPed determined by SEM in BSE with phases identified [43].

In order to obtain a microstructure which provides balanced mechanical properties, a two-step heat treatment has been developed for TNM alloys [37]. The first heat treatment is in the temperature range of the (α+β) or $(\alpha+\beta_0+\gamma)$ phase field region with rapid cooling, resulting in a microstructure consisting of a small volume fraction of β or β_o and γ-grains as well as larger supersaturated α_2 grains. The second step heat treatment in the $(\alpha_2+\beta_0+\gamma)$ phase field region allows the lamellar α_2/γ-colonies to form in the supersaturated grains. As the temperature of the second heat treatment is increased from 800°C to 900°C, the microstructure shows a higher fraction of colonies transformed by a cellular reaction[45]. The second step is very important as the lamellar spacing is primarily connected to the strength and hardness of the material [35], [37].

1.7 Deformation in Gamma TiAl

Many properties of γ-TiAl have been attributed to the nature of bonding. The Ti-Al bonds are strong and covalent and consequences of this are that γ remains ordered to the melting point (~1440°C) and retains high stiffness. The strong bonding also leads to a high barrier to diffusion and a large anti-phase domain boundary (APB). The high elastic modulus and high diffusion barrier produce brittle behavior. The low ductility that is produced also results in low fracture toughness and poor fatigue properties. Stress concentrations, unpredictable loading conditions and impact loading can lead to catastrophic failure.

1.7.1 Common Deformation Modes in γ-TiAl

As in closed packed cubic structures, slip occurs on the {111} planes in closed packed directions. The 1/2[110] dislocations are ordinary perfect dislocations and are referred to as easy slip dislocations in Figure 1.12. The [101] and [011] dislocations, which are equivalent, are the higher energy superdislocations. The 1/2 [112] dislocations are also superdislocations on the close packed planes. Slip systems on planes that are not closed packed, such as <100>{110} are active only at very high temperatures.

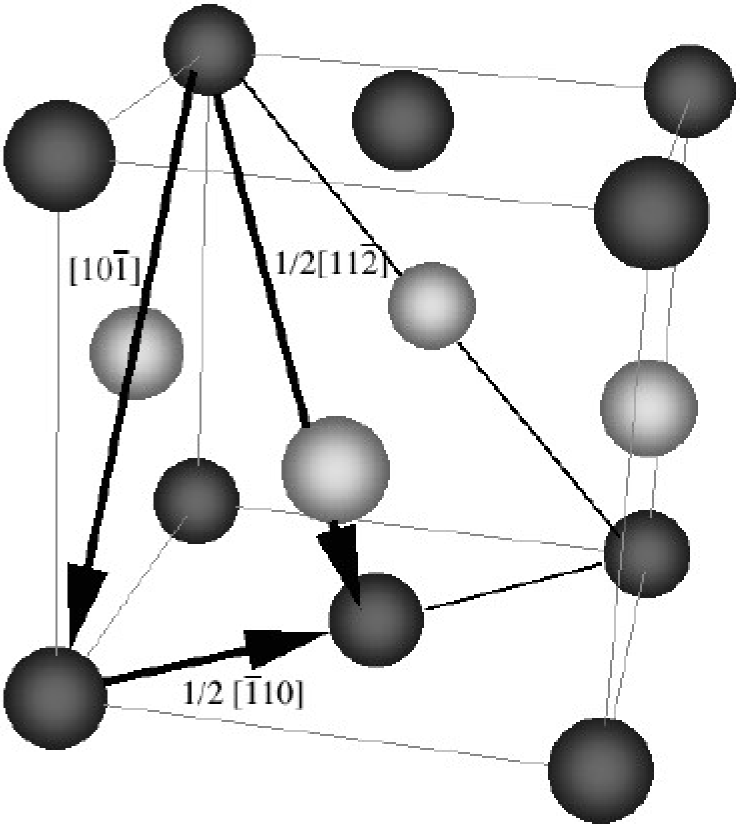

Figure 1.12: The ordinary and superdislocations are indicated for a $L1_0$ structure

Various dislocation dissociation reactions can take place on ordinary and super dislocations and these create partial dislocations. Ordinary dislocations can dissociate into two Shockley partials. Due to the nature of $L1_0$, the Shockley partials are separated by a complex stacking faults (CSF) instead of an intrinsic stacking fault.

$$1/2[\bar{1}10] \rightarrow 1/6[\bar{2}11] + CSF + 1/6[\bar{1}2\bar{1}]$$

The [011] superdislocation can dissociate into two 1/2[011] partials that are separated by an antiphase boundary (APB).

$$[011] \rightarrow 1/2[011] + APB + 1/2[011]$$

The 1/2[011] can further dissociate into Shockley partials. Again, owing to the nature of $L1_0$ ordering the fourfold dissociation gives rise to bordering stacking faults of different nature. the total reaction is

$$[001] \rightarrow 1/6[\bar{1}21] + CSF + 1/6[112] + APB + 1/6[\bar{1}21] + SISF + 1/6[112]$$

SISF is a superlattice intrinsic stacking fault. The SISF energy is much smaller than that of the CSF, so the dissociation is often threefold. The 1/2[112] superdislocation can undergo two dissociation reactions:

$$1/2[112] \rightarrow 1/6[112] + SISF + 1/6[112] + SESF + 1/6[112]$$

$$1/2[112] \rightarrow 1/2[101] + 1/2[011]$$

These 1/2[101] and 1/2[011] dislocations further dissociate in reactions similar to those described earlier.

Besides slip, twinning is the other major deformation mode. Twinning in γ-TiAl occurs through a 1/6$[\bar{1}1\bar{2}]$ type shear vector on the $(\bar{1}11)$ twin plane. This shear vector creates a true twin. This type of twinning can be achieved by successive cross-slip of the twinning dislocations 1/6$[\bar{1}1\bar{2}]$ on the $(\bar{1}11)$ plane that leave 1/6[011] stair-rod dislocations on the (100) plane. Twins are typically seen to nucleate from grain boundaries [46]. Twins can also nucleate within the grain interior by a pole mechanism involving a Frank partial dislocation turning around a perfect dislocation [47], [48].

γ-TiAl exhibits a strong flow stress anomaly. Yield stress is seen to be constant up to 600°C above which it increases with increasing temperatures and peaks at around 800°C [49], [50]. Veyserre et al. have suggested that the anomaly is the result of the formation of Kear-Wilsdorf (KW) locks. These locks are fomed by the dissociation of the <011] superdislocations on the {111} planes. The energy of the APB formed is minimized along the {001} plane. This leads to a non-planar or dissociation configuration that is essentially sessile. It has been suggested that the increasing number of pinning points (jogs) on ordinary screw (due to frequent cross-slip processes) dislocations is the source of this yield strength anomaly. High CSF energies have been calculated in γ-TiAl which leads to the compact nature of the screw dislocation that is prone to frequent cross-slip.

1.7.2 Deformation in lamellar two-phase alloys

Two-phase alloys have been shown to exhibit a higher ductility than single-phase alloys. Deformation in TiAl seems to be highly sensitive to the oxygen content. It has been suggested that reducing the oxygen content enchances ductility via the enhanced activity of 1/2[110] dislocations. The brittleness of γ-TiAl with oxygen has been related to the enhancement of bond directionality due to oxygen [51].

The deformation response of individual colonies depends on the lamellar orientation with respect to the stress axis. Colonies with lamellae that are parallel or perpendicular to the stress axis are referred to as being in the "hard orientation" and the deformation mode is referred to as "hard-mode". The hard mode deformation involves shear that is translamellar and takes place by slip or twinning. The lamellar interfaces act as barriers to twin and slip transmission and consequently, this orientation is stronger and less ductile [27]. The yield strength has been reported to be related to the lamellar spacing through a Hall-Petch type relation.

Grains with lamellae oriented between 30-70° to the stress axis are in the "soft" or "easy" orientation. The soft-oriented grains are dominated by the so-called 'Soft-mode" deformation that takes place by shear parallel to the lamellar interfaces involving twinning and slip.The mean free path for dislocation movement is related to the domain size or colony size, which is two to three orders of magnitude larger than the lamellar spacing, making this orientation ductile and weak.

Colony boundaries can be completely eliminiated in single colony and these are referred to as Poly-Synthetically Twinned (PST) crystals. The orientation of the PST crystal is characterized by the angle ϕ. Samples with $\phi \sim 35\text{-}55°$ are referred to as B oriented and these are soft oriented. Mechanical properties of PST are extremely anisotrpic.

The α_2 - phase with $D0_{19}$ structure is deformed primarily by the slip dislocations $2/3<11\bar{2}0>$ on the basal $<11\bar{2}0>(0001)$, prismatic $<11\bar{2}>$ $(1\bar{1}00)$ and pyramidal $<\bar{1}\bar{1}26>(11\bar{2}1)$ slip systems, as shown in Figure 1.13 [52]. A large amount of tensile elongation can be produced by prismatic slip but limited amount of ductility is present in basal plane slip. Stress relaxation due to twinning is absent in the α_2 phase which causes strain incompatibilities at the α_2/γ interfaces, and generates stress concentrations at these sites, which initiate interfacial cracking [53]. The lack of slip systems in the α_2 phase, especially when the c-axis is parallel to the tensile load is thought to be a contributing factor for poor ductility of two phase TiAl Alloys. Above the brittle to ductile temperature of around 700 °C, pyramidal slip is the major cause of the deformation [53].

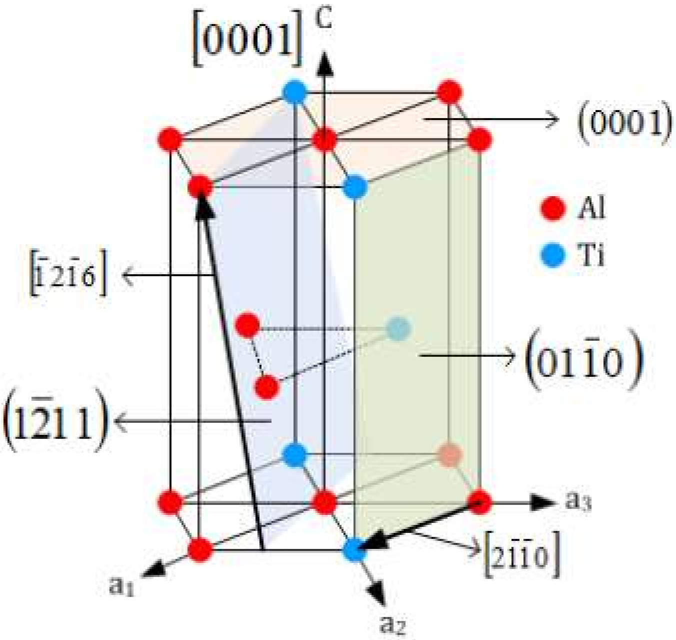

Figure 1.13: Preferential glide directions (shaded) in $D0_{19}$ crystal structure. The slip dislocations $2/3<11\bar{2}0>$ on the basal $<11\bar{2}0>$ (0001), prismatic $<11\bar{2}0>$ $(1\bar{1}00)$ and pyramidal $<\bar{2}\bar{2}26>(11\bar{2}1)$ slip systems are shown [52].

1.8 Mechanical Properties

1.8.1 Linear Elastic Fracture Mechanics

Fracture is the fragmentation, or separation, of a solid body into two or more parts under the application of stress. The fracture process can be considered to be made up of two components, crack initiation and crack propagation. Fracture can be classified as ductile or brittle. A ductile fracture is characterized by distinguishable plastic deformation prior to and during crack propagation, while brittle fracture is characterized by a rapid rate of crack propagation, with no gross deformation.

The laws that govern the crack propagation in materials are of interest. The major concepts are known as linear elastic fracture mechanics with small scale yielding (LEFM) and elastic-plastic fracture mechanics (EPFM). The concept of (LEFM) is based on elastic deformation of a cracked body. This concept can be further extended by including a small plastic zone ahead of the crack tip (small scale yielding). If the size of the plastic zone is too big LEFM is violated and elastic-plastic fracture mechanics (EPFM) is used.

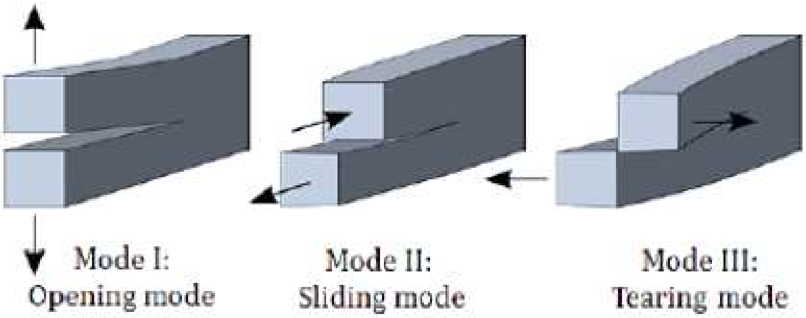

Figure 1.14: Three modes of crack surface displacement [54]

Fracture occurs in different modes due to various loading types. These modes are shown in Figure 1.14. In mode I, the crack surfaces move directly apart under the action of tensile stress perpendicular to the surfaces. In mode II called sliding mode, the shear acts parallel to the crack plane and the crack surfaces move normal to the crack front. This mode resembles an edge dislocation. Mode III, called tearing mode, the shear stress which acts parallell to the crack plane as well as the crack front. This resembles the motion of a screw dislocations [54].

1.8.2 Stress intensity factor

It is known that the theoretical cohesive stress is much higher than that of observed fracture stress of metals. This led to the idea of intrinsic cracks or defects, which locally raise the stress to a value of the theoretical cohesive stress. In some cases, LEFM solutions can be found to describe the stress field around the crack tip.

Stress intensity factor (SIF) is used in fracture mechanics to more accurately predict the stress around a crack tip caused by the loading. It has the symbol $K_{n(n=I,II,III)}$. SIF can be calculated with analytical or numerical methods and is given by Eq. 1.1 , where σ_n^a is the fracture stress from the applied load, a is the crack length and F is the geometry factor which depends on the crack and sample geometry.

$$K_n = F * \sigma_n^a \sqrt{\pi a} \tag{1.1}$$

1.8.3 Fracture Toughness

In LEFM unstable crack propagation will occur when the SIF reaches a critical value known as the critical stress intensity factor K_{Ic}, which is an inherent property of a material. For a specimen thinner than a critical thickness B, a plane-stress state dominates and produces a higher value of toughness known as plane-stress fracture toughness K_n.

Above this critical thickness a plane-strain state of stress exists, which results in maxium constraint and produces a constant value known as the plane-strain fracture toughness as shown in Figure 1.15.

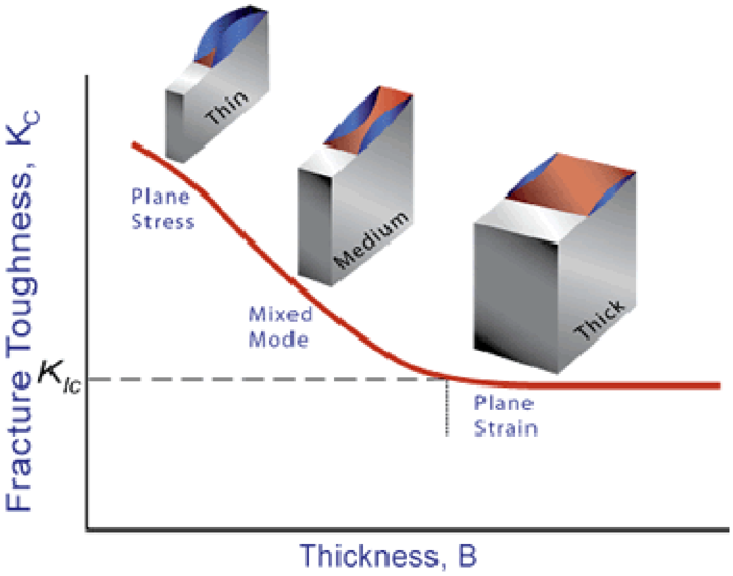

Figure 1.15: Effects of the specimen thickness on the fracture toughness (Kc) [55]

A properly measured value of K_{1c} represents the fracture toughness of the material independent of the crack length, geometry and loading system.

For measuring plane-strain fracture toughness with different testing methods, the ASTM 399 standard has been widely accepted [56]. In the case of three-point bend tests, the fracture toughness is caluclated according to the following formula in Eq 1.2

$$K = \frac{P_q S}{BW^{3/2}} \tag{1.2a}$$

$$f\left(\frac{a}{W}\right) = 3 * \sqrt{a/W} * \frac{1.99-\left(\frac{a}{W}\right)\left(1-\frac{a}{W}\right)[2.15-3.93\left(\frac{a}{W}\right)+2.7(\frac{a}{W})^2}{2(1+2(\frac{a}{W})(1-\frac{a}{W})^{3/2}} \tag{1.2}$$

where P is the force, S is bending span, B is thickness of the specimen, W is width of specimen, a is crack length, and f(a/W) is geometry factor.

1.8.4 Limit of Linear Elastic Fracture Mechanics

Eq 1.2a is only applicable when the size of the plastic zone ahead of the crack tip is condiderably smaller than the specimen dimensions. Therefore, as advised in ASTM 399 [56], the specimen dimensions should fulfill the following critera in eq 1.3. σ_y is the yield stress and K is the fracture toughness of the tested material.

`

$$B > 2.5(\frac{K}{\sigma_y})^2 \tag{1.3}$$

1.8.5 Fatigue Crack Growth Theory

Fatigue has been defined as "the microstructural damage and failure of materials under cyclically varying loads" [57]. Propagation-controlled fatigue crack growth testing is characterized by three regimes: threshold, Paris slope and overload as shown in Figure 1.16. The threshold regime is characterized by decreasing fatigue crack growth rates (da/dN) and a fatigue threshold, ΔK_{th}, below which the crack growth rate is below 10^{-8} mm/cycle. In the overload regime, the maximum stress intensity during fatigue nears the fracture toughness (i.e. K_C) of the material and the crack growth rate increases drastically. The overload regime has a large influence from microstructure, mean stress, and thickness. In the intermediate crack growth regime the crack growth can be described by the Paris law (Eqn. 1.4): d*a*/d*N* is the fatigue crack grow rate while ΔK is the stress intensity range (MPa√m) [58], m is the Paris exponent as shown by the slope of the line in regime B in Figure 1.16. The Paris exponent is a measurement of resistance to crack growth and appears in the exponent in Eqn. 1.4, so a small change in *m* will have a large effect on d*a*/d*N*.

$$\frac{da}{dN} = C\Delta K^m \quad (1.4)$$

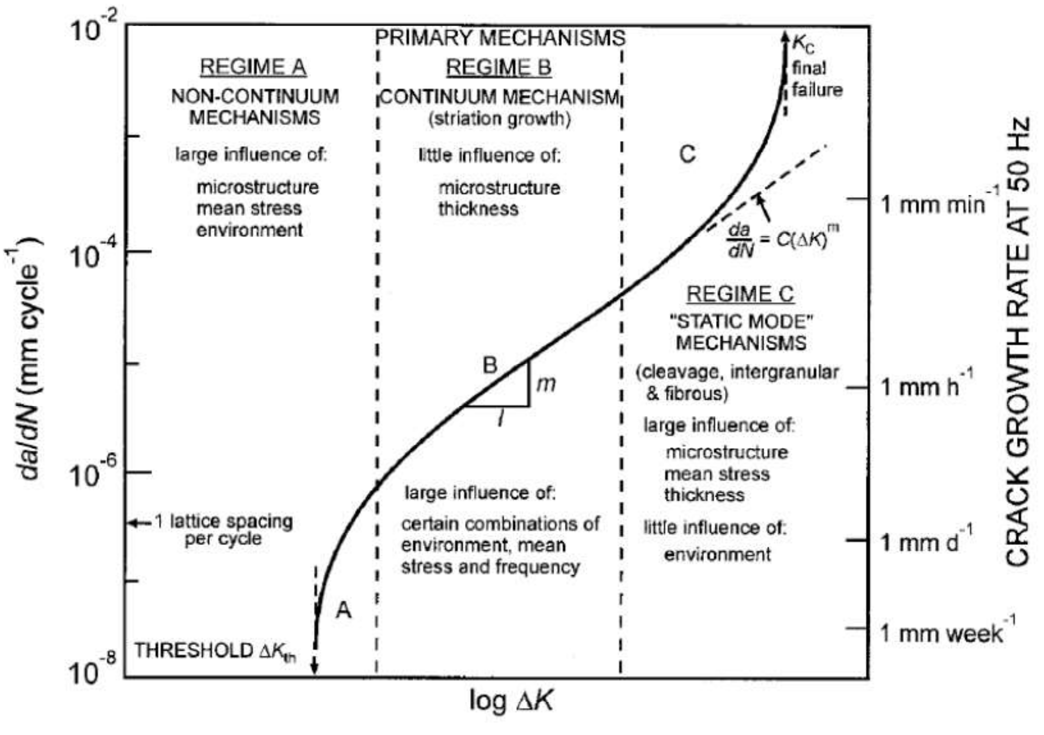

Figure 1.16: Schematic illustration of the typical variation in fatigue-crack growth d*a*/d*N*, as a function of the applied stress-intensity range ΔK in metallic materials, showing the regimes of primary growth-rate mechanisms and effects of several major variables in crack-growth behavior [59].

The extension of the fatigue crack occurs from the competition between two classes of mechanisms, intrinsic and extrinsic. According to Ritchie [57], crack growth is promoted ahead of the crack tip by intrinsic damage mechanisms in the microstructure, and is impeded by extrinsic mechanisms acting primarily behind the crack tip, which serves to shield the crack tip from far-field driving forces [60]. Intrinsic damage mechanisms typically involve processes which create microcracks or voids by dislocation pile-ups or interface decohesion in the highly stressed region ahead of the tip. Intrinsic mechanisms are considered an inherent property of the material and thus are irrespective of the length of the crack or the geometry of the test specimen [57].

Extrinsic mechanisms act primarily behind the crack tip. Extrinsic shielding mechanisms result from the creation of an inelastic zone surrounding the crack wake or physical contact between the crack surfaces via wedging, bridging, sliding or a combination [60]. Extrinsic mechanisms act in the crack wake and thus are dependent on crack size geometry. Zone shielding is produced by both transformation and microcrack toughening in ceramics where the phase transformation or microcracking ahead of the crack tip can lead to inelastic zones in the crack wake that impart closing tractions on the crack surface.

Intrinsic toughening mechanisms have been largely unsuccessful in ceramics and intermetallics. Rather, these systems are most effectively toughened using various extrinsic shielding mechanisms. Unlike conventional metal fatigue that exhibits fatigue striations in the Paris regime, the morphology of a fatigue fracture surface in intermetallics is almost identical to that exhibited under monotonic loading. However, the microstructure typically has a significant effect on fatigue crack growth rates in intermetallics, unlike that exhibited by conventional metals in the Paris regime. As a result of this, the sensitivity of fatigue crack growth rate to cyclic stress intensity is extremely high in intermetallics. The exponent *m* in the simple Paris Equation 1.4 can take values as high as ~15-50 and above. Such high exponents result from a marked sensitivity of growth rates to K_{max} rather than ΔK [61]. The Paris slope in metals is typically in the range 3-5, with no change with respect to the R-ratio.

1.8.1.1 Intrinsic and Extrinsic Mechanisms

The extension of the crack is from the competition of two classes of mechanisms shown in Figure 1.17. According to Ritchie [57], crack growth is promoted ahead of the crack tip by intrinsic damage mechanisms in the microstructure, and is impeded by extrinsic mechanisms acting primarily behind the crack tip, which serves to shield the crack tip from far-field driving forces [60]. Intrinsic damage mechanisms typically involve processes which create microcracks or voids by dislocation pile-ups or interface decohesion in the highly stressed region ahead of the tip. Intrinsic mechanisms are considered an inherent property of the material and thus are irrespective of the length of the crack or the geometry of the test specimen [57].

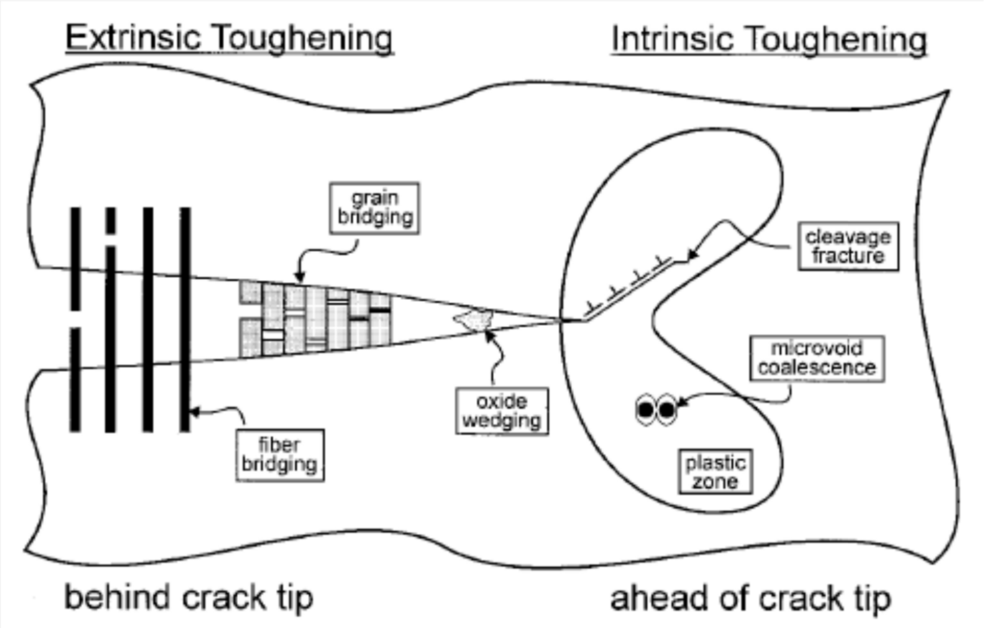

Figure 1.17: Schematic illustration of mutual competition between intrinsic mechanisms of damage/crack advance and extrinsic mechanisms of crack-tip shielding involved in crack growth [57].

Extrinsic mechanisms act primarily behind the crack tip and the different extrinsic toughing mechanisms are shown in Figure 1.17. Extrinsic shielding mechanisms result from the creation of an inelastic zone surrounding the crack wake or physical contact between the crack surfaces via wedging, bridging, sliding or a combination [60]. Extrinsic mechanisms act in the crack wake and thus are dependent on crack size geometry. Zone shielding is produced by both transformation and microcrack toughening in ceramics where the phase transformation or microcracking ahead of the crack tip can lead to inelastic zones in the crack wake that impart closing tractions on the crack surface.

Contact shielding is from bridging tractions imposed across a crack by unbroken fibers, laminated layers, or a particulate phase in composite materials, or the wedging or corrosion debris or fracture surface roughness. A general source of contact shielding during cyclic crack growth arises from the wedging action of fracture surface roughness where crack tip opening displacements (CTOD) are small and where significant crack-tip shear occurs[60]. Roughness-induced fatigue crack closure is most effective at low stress intensities, particularly where the crack path morphology can be made torturous. The extent of wedge shielding depends on the degree of fracture surface roughness and the extent of mode II crack tip displacements. The closure can be modeled by equation 1.4.

$$K_{cl} = K_{max}\left(\frac{2\gamma X}{1 + 2\gamma X}\right)^{.5} \tag{1.4}$$

where γ is a measure of surface roughness taken as the ratio of height h to width w of asperities and X is the ratio of mode II to mode I crack tip displacements. The roughness-induced crack closure has been found to play a significant role in influencing fatigue crack growth in a wide range of materials including coarse grain size ferritic steels and titanium alloys [60].

1.9 Focus of Thesis

Information on the TNM mechanical properties and fatigue properties in various microstructures are not available. Thus the focus of this work is to determine the mechanisms affecting the fatigue crack growth properties in different orientations with respect to the casting direction and after post-processing. In particular, the effects of the load ratio, R, on the fatigue crack growth properties have been determined as this provides a convenient way to assess the importance of K_{max} and ΔK controlled mechanisms. After failure, SEM, metallography, and XRD are used to document the changes in the fracture surface present in different regimes of fatigue crack growth (i.e, threshold, Paris regime, overload). These were used to determine the micromechanisms controlling fatigue crack growth in both as-cast and forged TNM.

Fatigue testing in this thesis is performed at room temperature although low pressure turbine blades typically operate at high (i.e., 700 °C) temperature, it is first essential to develope the baseline at room temperature since the engines intially are operated at room temperature. Fatigue crack growth information is needed at different R to insure that damage to the leading edge of the blades during service does not cause a catastrophic failure.

2.0 Experimental Methods

2.1 Materials

The material used in this study, Ti-43.5Al-4Nb-1Mo-0.1B (at.%) (TNM), was initially produced by double plasma arc melting with positive pressure provided by helium at Arconic, Niles, OH. The material was first cast into approximately 10 foot long billets with a nominal diameter of 2 inches. The cast material was then cut into roughly 12” pieces as shown in Figure 2.1 for subsequent testing. The chemistry was determined in numerous locations along the casting direction using Spark-OES (Optical Emission Spectrometry) at Arconic in Niles, OH, in order to determine uniformity of chemistry and adherence of the material to the specifications shown in Table 2.1. Hot isostatic pressing (HIPing) was then performed on 2" ⌀ and 12" inch billets at 2165°F (1185°C) (cf. Figure 2.2) at 25 ksi (172 MPa) for 4 hr at Pressure Technology, Inc. (PTI) prior to grinding the 12 inch long billets to approximately 1.77 inches in diameter (cf. Figure 2.1).

Table 2.1: Chemistry goal and actual chemistry used in the current study (at.%)

Material	**Ti**	**Al**	**Nb**	**Mo**	**B**	**C**	**O (ppm)**
Goal	Bal.	43.5	4	1	0.1	<.01	<800
Actual	Bal.	43.56	4.05	0.97	0.1	0.008	558

Figure 2.1: As-cast (left) billet was approximately 2 inches in diameter x 1 feet long while HIPed (right) and machined billet was approximately 1.77 inches diameter x 1 feet long. The as-cast sub-scale billet was removed from the original 10 feet x 2 inch diameter cast billet.

After HIPing, seven (7) upset isothermal forgings were performed at a strain rate of $0.001s^{-1}$ at a temperature of 2150°F (1176.6 °C) (cf. Figure 2.2) on billets that were 2.655” (67.3 mm) tall with a diameter of 1.77” (45 mm). The material was forged to a final height of approximately 0.75” (19 mm) which represents a 72% height reduction and true compressive strain of 1.26 in/in. Three (3) sidepress-forgings were performed under the same conditions used for the upset forgings. In these cases, the starting billet had 3.2” length x 1.77” diameter and was forged to a final shape of approximately 0.75” x 4.3” x 2.5”. This represents a 57% reduction and equates to a compressive strain of 0.85 in/in. The forging input stock and the final products are shown in Figure 2.3.

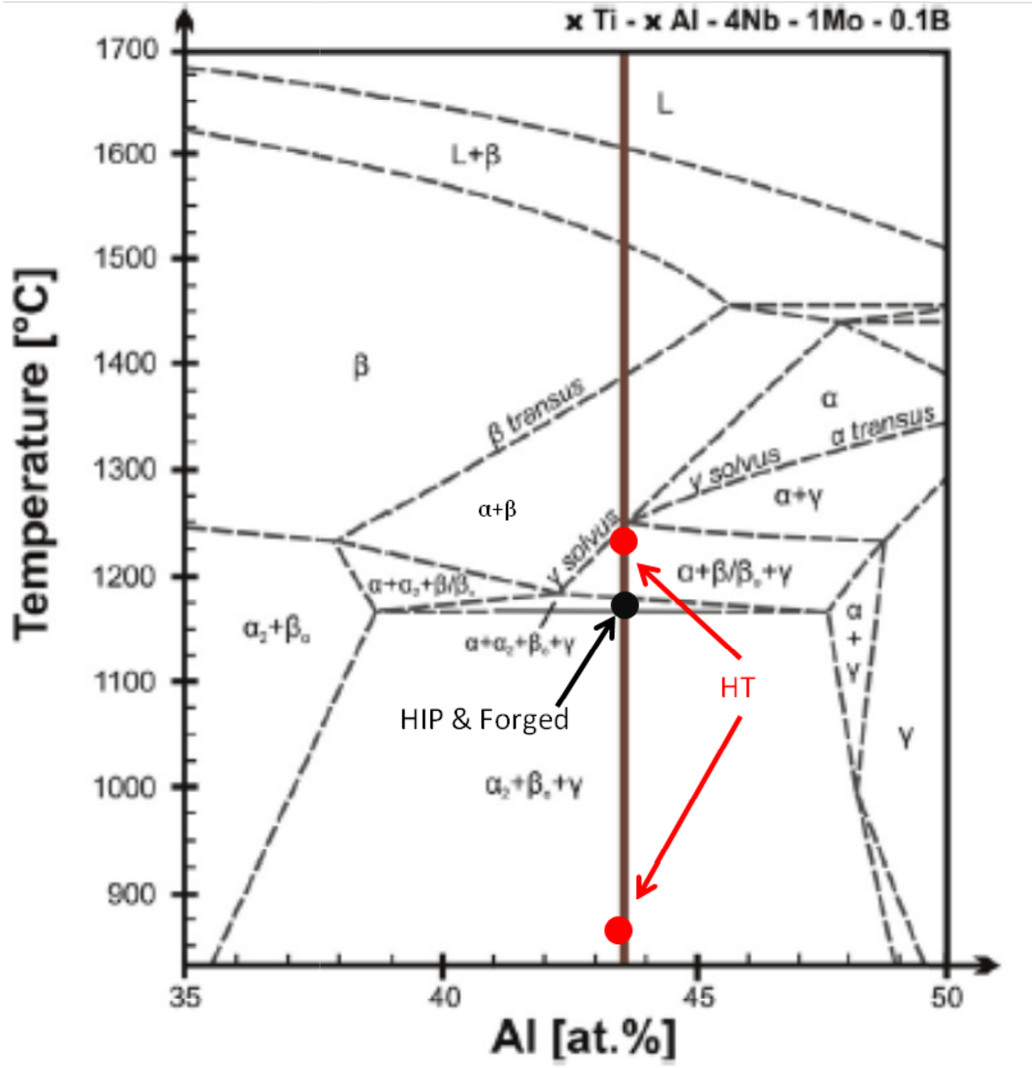

Figure 2.2: Phase diagram for TNM with HIP, forging, and heat treatment temperatures noted.

After forging, the materials were heat treated at 2225°F(1218°C)/2hr/AC + 1562°F (850°C)/6hr/FC (cf.Figure 2.2) in a furnace in air at Arconic in Niles, OH, with +/- 10°F temperature uniformity. For future reference, material was forged in either the upset or sidepress direction and then dual heat treated and will be referred to as upset-forged or sidepress-forged, respectively.

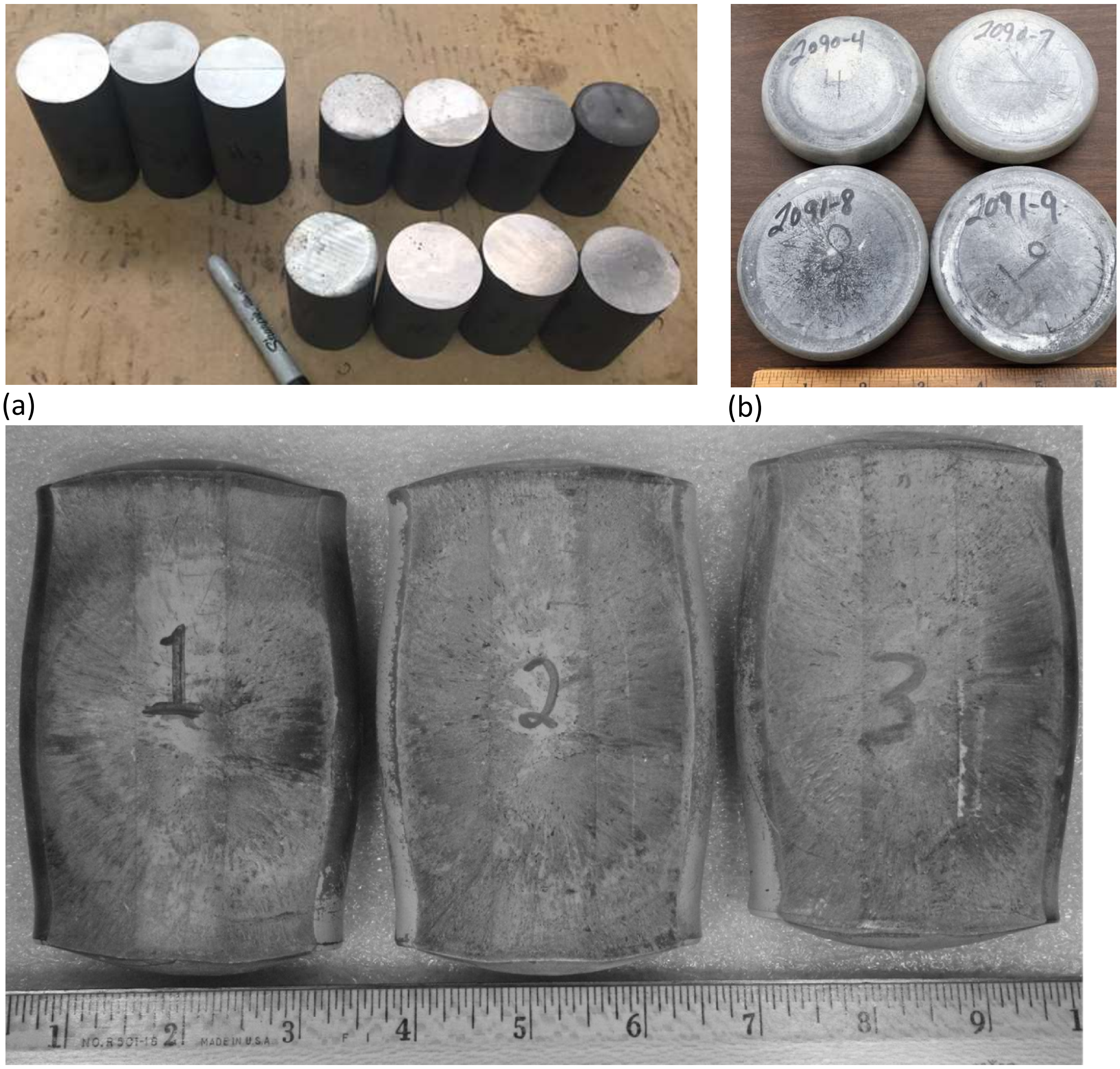

(a) (b)

(c)

Figure 2.3: (a) Sub-scale forging billets showing both upset and side press forging inputs (b) Upset-forging to a final height of ~ 0.75” and ~ 3” diameter (c) Sidepress-forging to final dimensions of 2.5” x 4.3”x 0.75”.

2.2 Microstructure

2.2.1 Scanning Electron Microscopy

Metallographic specimens were prepared from as-cast and as-cast + HIPed material in both the cast and radial directions. Small regions of the material were sectioned, mounted in conductive mount, and then sequentially polished with water lubrication to a 0.05 μm finish using a series of silicon carbide coated papers of decreasing grit size. Final polishing used colloidal silica on a Buehler VibroMet 2 vibratory polisher. Samples were subsequently washed for five minutes in an ultrasonic bath of deionized water to remove any residual colloidal silica.

Scanning electron microscopy (SEM) was preformed using backscatter scanning electron (BSE) imaging mode using a Zeiss Evo Ma 25 at a working distance of about 6 to 8 mm, accelerating voltage of 20 KeV and a current of 2.5A. The material was imaged via SEM-BSE at 500X, 1000X, and 2000X and the resulting SEM-BSE images were stitched together to create a three dimensional (3D) microstructure representation of the as-cast microstructure (Figure 2.4a). The microstructure of the as-cast material contains fine lamellar colonies, approximately 30 μm in length, consisting of alternating γ and α_2 with a spacing of approximately 500 ± 30 nm. The colony size was measured using MIPAR software and lamellar spacings were measured using SEM-BSE images at 40,000X (Figure 2.4b). Quantification of the microstructure was performed by taking 3 BSE images at each magnification (i.e., 500x, 1000x, 2000x). Each image was then segmented by color to determine the area fraction for each phase. The phase fraction in each image were than averaged and the number reported.

The microstructure of HIPed material was examined in the same manner as above and the 3D microstructure is shown in Figure 2.4c. The HIPed microstructure contains globular β_o (white), globular γ (dark) and α_2/γ (grey). Thresholding was used to determine the following phase fractions: 15% β_o, 48% γ, and 37% α_2. X-ray diffraction was also used to determine rough phase fractions as summarized later.

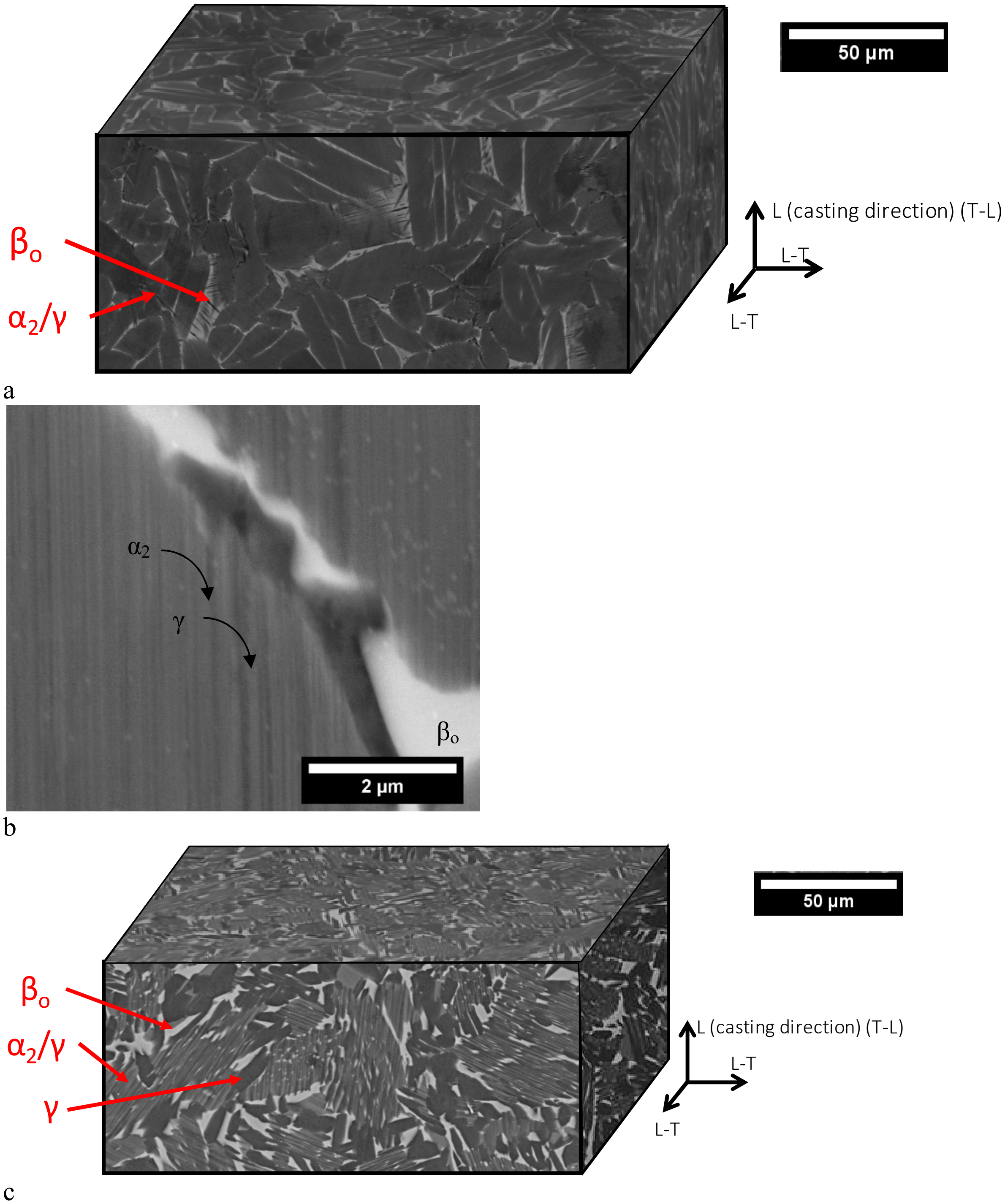

Figure 2.4: (a) 3D microstructures of the as-cast material taken with SEM-BSE at 1000X.(b) High magnifcation image of the lamellar microstructure viewed in BSE (c) 3D microstructure of the HIPed material taken with SEM-BSE at 1000X.

The forgings were imaged using the same procedure conducted on the as-cast material above. SEM-BSE images of the upset- and sidepress-forged material were taken at 1000X and the 3-D microstructures are shown in Figure 2.5(a,b). All three phases are evident. Thresholding was again performed on images taken from both forgings. The upset-forging contained 57% α_2, 17% β_o, and 26% γ while the sidepress-forgings had 50% α_2, 9.6% β_o, and 37%γ.

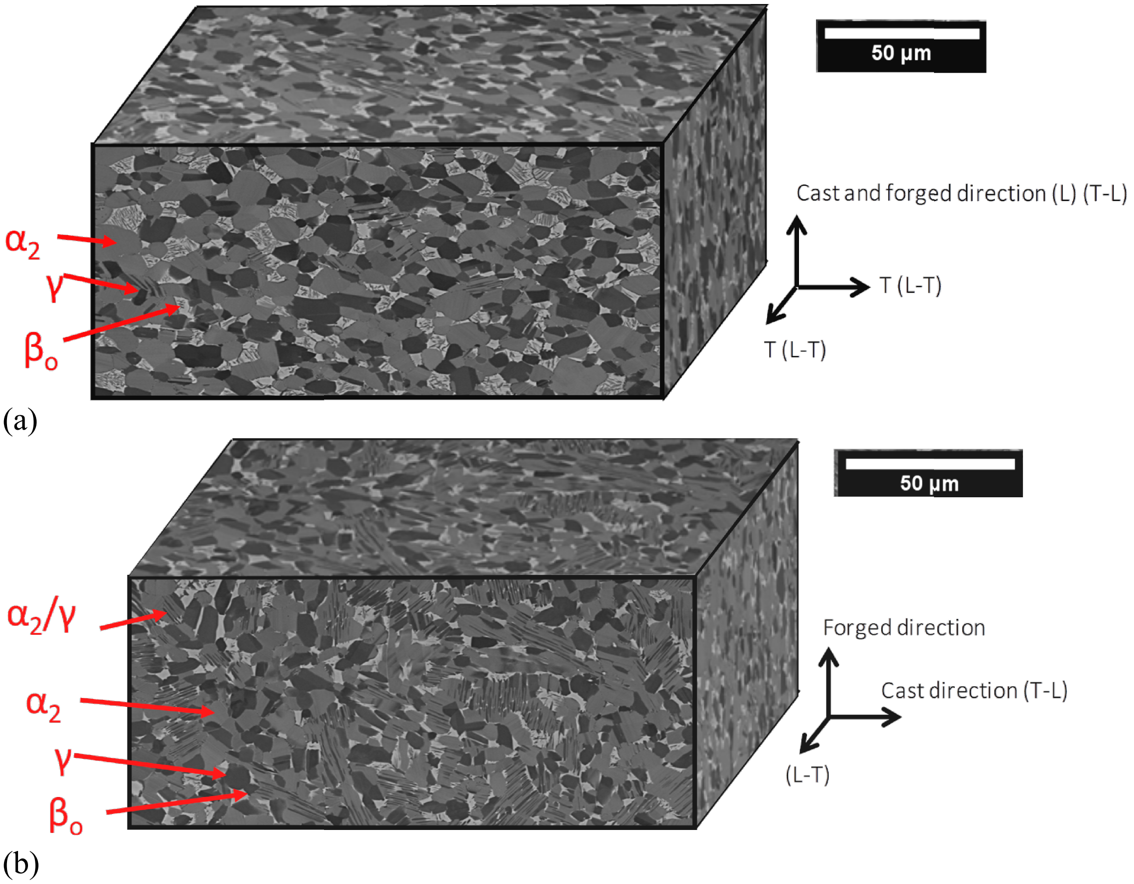

Figure 2.5: 3D microstructures taken with SEM-BSE at 1000X (a) upset-forged (b) sidepress-forged.

2.3 Specimen Geometry

Bend bar samples for toughness and fatigue crack growth experiments were machined from the as-cast and as-cast + HIPed billets, Figure 2.6a, in accordance with ASTM E399. The span to width ratio, S/W, was maintained at 4:1 when possible.

However, stock material size constraints limited many samples to S/W = 2. The bend bar samples were removed in two different orientations. Samples with the first orientation had their long axis aligned with the casting direction, while samples with the second orientation had their long axis aligned with the longitudinal direction, Figure 2.6a. In Figure 2.6a, these orientations are denoted as T-L for transverse direction and L-T for longitudinal direction. The number of bend bar samples removed from the billets varied with stock size and experimental requirements. Typical L-T samples were 52 mm x 12 mm x 18 mm while T-L samples were 33 mm x 12 mm x 20 mm. For the upset- and sidepress-forged material, the bend bar samples were excised with dimensions similar to the T-L specimens (Figure 2.6 b,c) with dimensions 33 mm x 12 mm x 20 mm. Tensile specimens were excised in the same orientations as the fatigue specimens, starting with blanks of 12.5 mm x 12.5 mm x 50 mm.

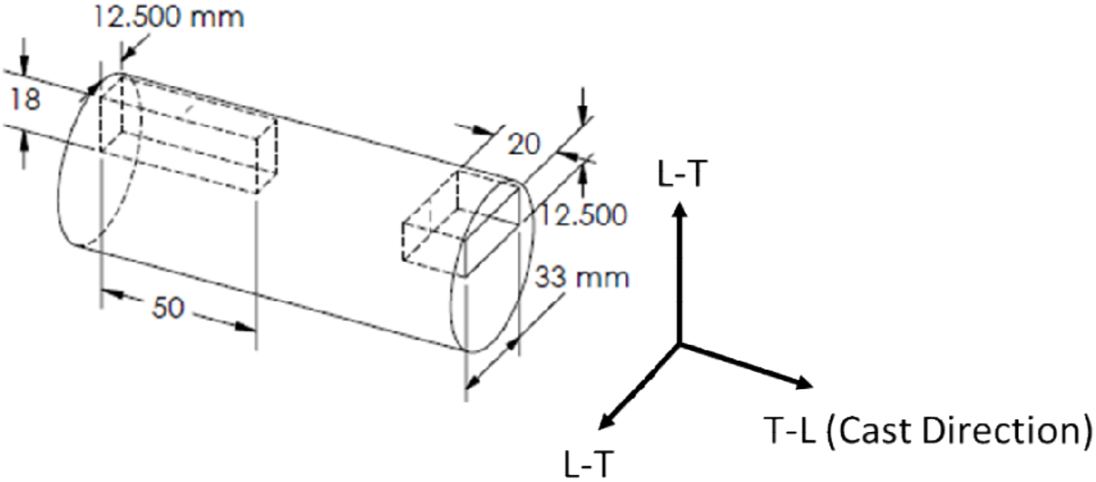

(a)

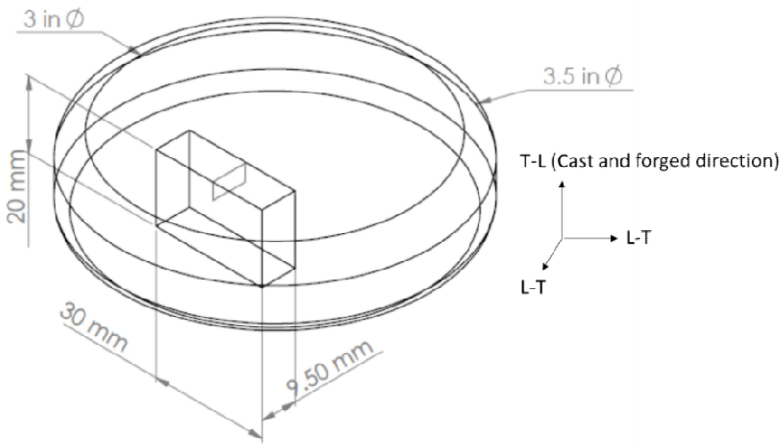

(b)

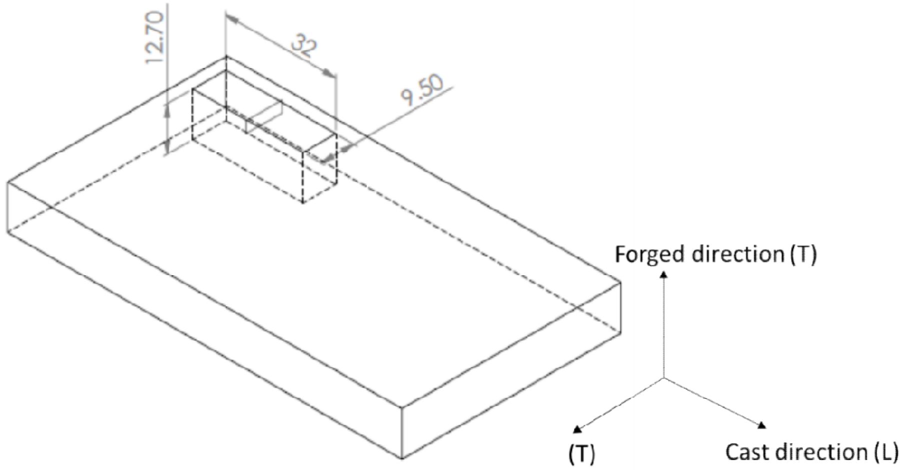

(c)

Figure 2.6: Schematic drawings revealing orientation of bend bar samples removed from (a) as-cast and as-cast+HIPed (b) upset-forged (c) sidepress-forged materials.

2.4 Mechanical Testing

In order to determine the effects of sample orientation on the mechanical properties of Ti-43Al-4Nb-1Mo-0.1B (at.%), two separate types of mechanical tests, tension and fatigue crack growth, were conducted on the as-cast, as-cast + HIPed, and forged samples. All fatigue crack growth testing was carried out in the Advanced Manufacturing and Mechanical Reliability Center (AMMRC) located at Case Western Reserve University [62]. For tensile testing, small-scale samples (5 mm diameter, 22 mm gage length) were tested in the AMMRC while larger scale tensile samples (6 mm diameter, 24 mm gage length) were tested at Westmoreland Mechanical Testing & Research Inc. in Youngstown, PA.

2.4.1 Fatigue Crack Growth

Room temperature fatigue crack growth (FCG) testing was performed on the TNM alloy three point bend bar samples using a 20 kip MTS 810 closed loop servo-hydraulic mechanical testing machine in accordance with ASTM E 647-15 [63]. A notch with 200 μm radius was placed in each bar to a length of a/W = 0.2-0.3 using a diamond blade, followed with notch extension via a diamond impregnated wire saw. The notch was placed in either the longitudinal or transverse direction. Testing was controlled using Fracture Technology Associates (FTA) fatigue crack growth software, while the interface between the MTS and Software was controlled using an Adwin-Gold Digital signal processor. The load ratios, R, used for fatigue testing, defined as:

$$R = \frac{\sigma_{min}}{\sigma_{max}} = \frac{K_{min}}{K_{max}} = \frac{P_{min}}{P_{max}} \tag{2.1}$$

were 0.1, 0.3, 0.7 and 0.9 for the L-T and T-L specimens in all conditions. R = 0.9 was not used for most materials as it was difficult to maintain stable crack growth at that high R. A sinusoidal load time curve was chosen for testing, with a frequency of 18 Hz in order to minimize the duration of testing. All tests were conducted in accordance with ASTM E 399 [56] and ASTM E 647 [63]. Crack lengths on fractured samples were initially determined using Mitutoyo digital calipers and then confirmed using 200x images taken on a Keyence optical microscope. As is the standard for fatigue crack growth testing, data is presented as the differential crack growth per cycle ($\frac{da}{dN}$) versus ΔK, on a log-log scale where ΔK is defined as:

$$\Delta K = K_{max} - K_{min} \tag{2.2}$$

During the start of testing, FTA software was run at low alternating stress intensities between 1-3 MPa√m in order to equilibrate the components and to ensure the sample was correctly positioned. Fatigue crack growth testing was begun by carefully increasing the alternating stress intensity every 6 hours until detectable crack growth was recorded with the use of direct current potential drop (dcPD). The progress of each sample was checked periodically using remote viewing software in order to insure crack growth had commenced or was continuing. In cases where the crack had stalled, or threshold was eventually reached, the alternating stress was increased to enable completion of the test.

The crack was grown to threshold using accepted load shedding schemes, followed by testing to failure with constant load cycling that produced rising ΔK conditions. This approach to fatigue crack growth testing is shown schematically in Figure 2.7. The red regime indicates testing under falling ΔK conditions to produce the fatigue threshold, ΔK_{th}, defined as when da/dN < 10^{-7} mm/cycle. The test was then stopped and restarted at an intermediate ΔK (blue regime) and continued under constant load cycling to produce rising ΔK and eventual failure.

Figure 2.7: Schematic diagram of fatigue crack growth testing showing threshold testing (1, red) followed by rising ΔK test (2, blue). Fatigue threshold (ΔKth), Paris Law slope (m), and overload toughness (K_c) were obtained from testing in this manner.

2.4.1.1 Compression-Compression Pre-cracking of Fatigue Crack Growth Specimens

Many samples were very resistant to initiate fatigue precracks in bending fatigue and simply failed catastrophically once a fatigue crack was initiated. Cyclic compression loading was successfully used to induce stable fatigue precracks at the start of testing, as documented for a range of materials [64]–[67]. This was used successfully for both as-cast + HIPed and forged specimens in both directions (Figure 2.8). All compression fatigue pre-cracking was conducted at room temperature in lab air at a temperature of 22°C. The fatigue pre-cracks were introduced in uniaxial compression at a frequency of 10 Hz with a sinusoidal wave form and a load ratio, R = 10. The load ratio is defined as the ratio of the minimum load to the maximum load of the fatigue cycle, Eqn. 2.1. All testing was performed on a 50 kip MTS 810 closed loop servo-hydraulic mechanical testing machine using a peak load of 80 kN and 10 Hz frequency. The cyclic compression pre-cracking produced a stable fatigue pre-crack between 0.5 to 2 mm long. The compression precracking produces a cyclic plastic zone of ~ 1 mm

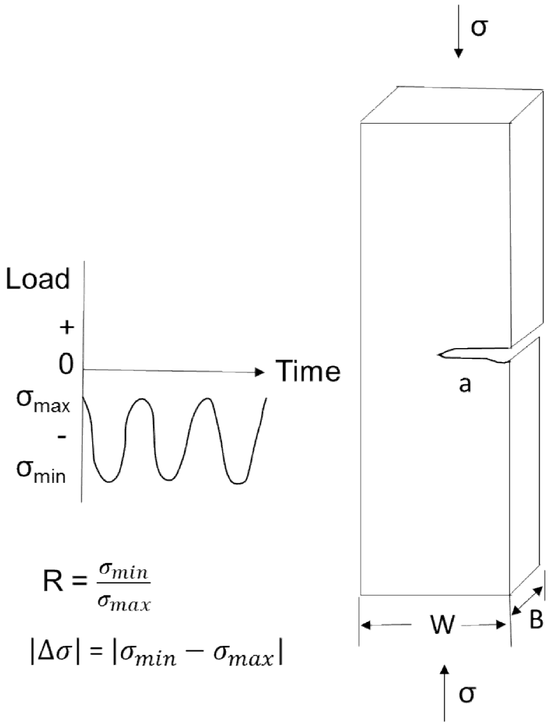

Figure 2.8: Schematic representation of the procedure for pre-cracking in uniaxial cyclic compression.

2.4.1.2 Direct Current Potential Drop Control

Fatigue crack growth measurements were accomplished using direct current potential drop (dcPD). Small holes were drilled on the surface of the three point bend bar specimens to allow for voltage and current leads to be attached to the specimen by peening. Voltage and current leads were attached by peening with a spring loaded punch because spot welding was found to be an ineffective method for joining the wire leads to TiAl specimens. The wires were made of constantan, a copper nickel alloy insulated with fiberglass sleeving designed to prevent the wires touching and shorting. The insulated wires were first taped to the test fixture to prevent contact and also to remove any stress from the peening site in order to reduce the possibility of the wires coming loose. A schematic diagram of the holes and leads is shown in Figure 2.8. The voltage leads, 0.508 mm (0.020 in.) in diameter were placed 5 mm apart and across the notch, Figure 2.9. The current leads, 0.813 mm (0.032 in.) in diameter were attached to the center of the face of both ends of the samples. A current of 2 Amps was used to insure sufficient signal return current to measure crack extension, as described below.

A DC power source and a 1000X Ectron amplifier were used in conjunction with the Adwin Gold DSP and FTA DC switch. This allowed for crack growth to be measured in-situ using the reverse direct current potential drop method (dcPD). The FTA, Inc., FCGR (Fatigue Crack Growth Rate) software was used for machine control, data collection, and data analysis. The software adjusted the data collection rate depending on the crack growth rate that was observed from the dcPD measurements and smoothed the resulting data using a modified secant of 7-point polynomial method.

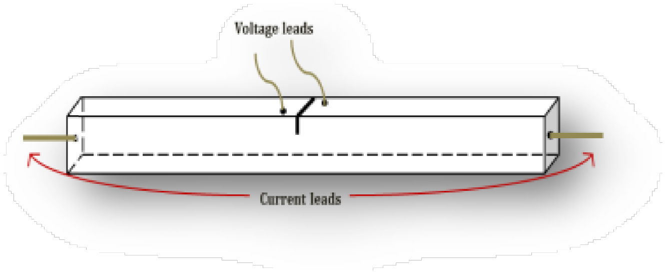

Figure 2.9: Three point bending configuration used for fatigue crack growth testing. Schematic shows location of dcPD leads.

2.4.1.3 ΔK Threshold

Fatigue crack growth tests were designed to shed load from an intermediate ΔK until reaching the fatigue threshold using K-control, Figure 2.7. When in K-control the machine operates with the following equation:

$$K = K_i * e^{C(a-a_i)} \quad (2.3)$$

Where: K is ΔK, K_i is the initial Δ K, C is the K- gradient, and a and a_i are the current and initial crack length. The load-shedding was performed by the FTA software on the basis of a 20% percent load reduction per mm of crack growth using a K-gradient of -.200 (1/mm) for the majority of the samples. Some samples required the load to be shed and then raised and shed for a second time in order to reach threshold. The K_{min} / K_{max} graph for constant R with load shedding in given in Figure 2.10. Threshold testing was continued until a sizeable amount of data existed below threshold which ASTM E647 defined as 10^{-7} mm/cycle. The fatigue crack threshold in the present work was considered as 10^{-7} or 10^{-8} mm per cycle. Once threshold was firmly established, the test was stopped, subsequent testing was conducted using rising ΔK conditions to failure. Each threshold test took approximately three days to reach the ASTM-defined value for threshold.

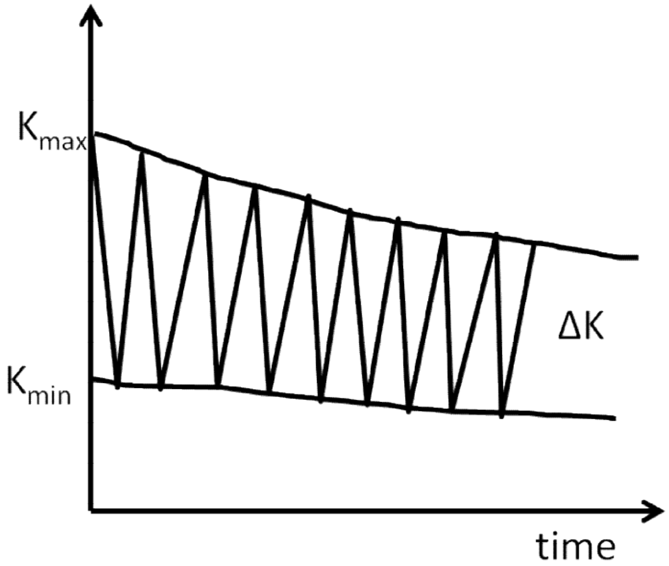

Figure 2.10: K_{min} /K_{max} graph for load shedding with falling ΔK and constant R

2.4.1.4 Paris Law Relationship

Voltage and current leads were left attached to the sample after threshold determination, so it was possible to then capture fatigue crack growth information during the rising ΔK conditions to failure. As shown in Figure 2.6, the slope of the log d*a*/d*N* vs. log ΔK plot is the Paris law relationship, m. The Paris slope is found with equation 2.5 where m is the exponent.

$$\frac{da}{dN} = C\Delta K^{m} \tag{2.5}$$

The Paris law relationship was calculated using FTA software which plotted a point every time the crack extended 50 μm and included the rate of crack growth and ΔK. The slope of the line was determined using Excel after catastrophic failure had occurred.

2.4.1.5 Overload Stress Intensity (Toughness) at Failure

The overload stress intensity during fatigue failure (i.e. overload fracture toughness) was also recorded during the fatigue crack growth experiments. It was possible to capture the crack length and final load during catastrophic crack growth using dcPD, enabling conversion of the final ΔK_c to the peak K at failure (i.e., K_c). While this is not identical to the plane strain fracture toughness (i.e., K_{Ic}), it is representative of the maxium stress intensity at failure.

In this regime, specimens were subjected to rising ΔK with fatigue crack growth tests as in Section 2.4.1 and Figure 2.7 with constant load at a constand R and a K_{min}/K_{max} trace is given in Figure 2.11. At catastrophic failure the final crack length and K_{max} were recorded from the FTA software. The samples were also examined under the SEM where the final crack length was also measured to allow for calculation of K_c per ASTM E399 and ASTM 1820 [56], [68]. The SEM measurements of crack length and dcPD measurements of crack length were compared to calculate the overload K_c.

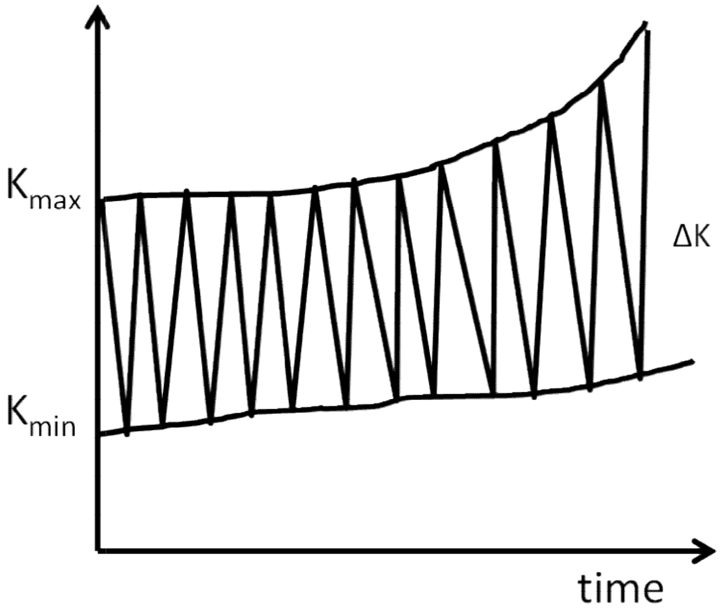

Figure 2.11: Kmin/Kmax graph for constant load in rinsing ΔK with constant R

2.4.2 Tensile Testing

Tensile blanks for the as-cast and as-cast + HIPed material were excised from the sub-scale billets and taken parallel to the casting direction in four quarters, Figure 2.12. The samples were excised in this manner to avoid testing along the centerline of the original casting and thereby avoiding any regions of macrosegregation/porosity. The tensile blanks were machined with dimensions of 0.6" x 0.6" x 2" and sent to Westmoreland Mechanical Testing and Research in Youngstown, PA, to be machined down into a double button head design (Figure 2.13) for subsequent tensile testing. Prior to the mechanical testing, the specimens were polished through 1200 grit using SiC sandpaper with the help of a drill press operated at a low RPM. The specimens were then tested with a high alignment fixture in the AMMRC at CWRU on an Instron 1125 machine with a strain rate of $0.001s^{-1}$. Elongation of the specimen was measured with a UVID, Inc., Arion 1D non-contact video extensometer by video recording the instantaneous position of fiducial marks placed on the gage length of the sample. In this case, three (3) orange dots were placed on the specimen with a paint pen to enable the video recording the sequential movement of the dots to calculate the strain on the sample. Figure 2.14 shows the general test arrangement and includes the high alignment fixture and video extensometer.

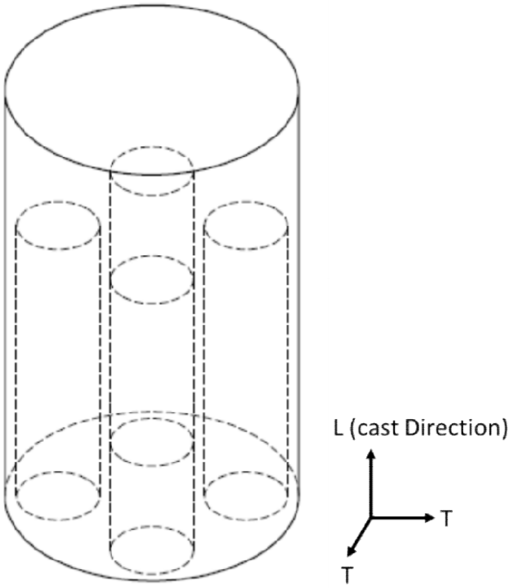

(a)

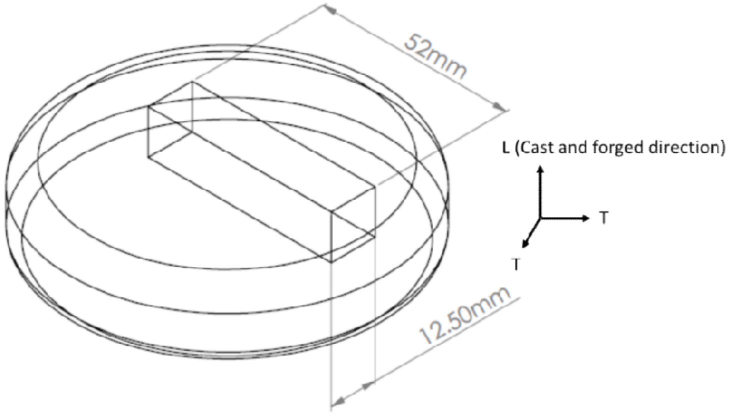

(b)

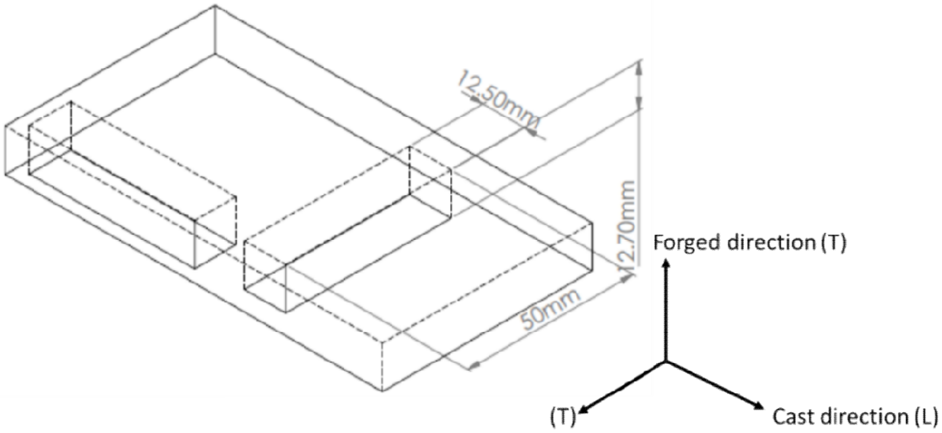

(c)
Figure 2.12: Schematic showing tensile blanks excised from (a) as-cast and as-cast + HIPed (b) upset-forged (c) sidepress-forged materials.

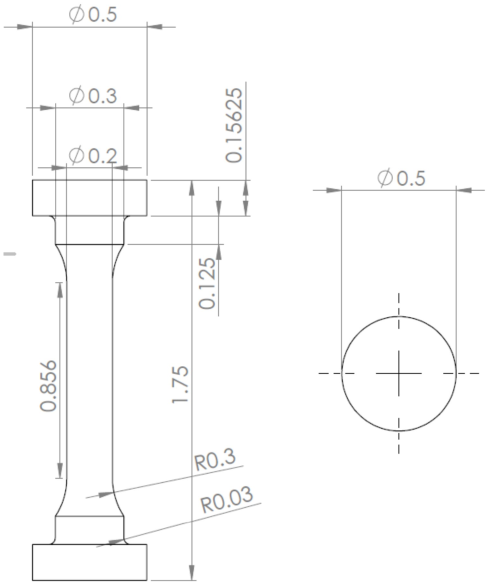

Figure 2.13: Schematic of double button head design for as-cast and as-cast + HIPed materials.

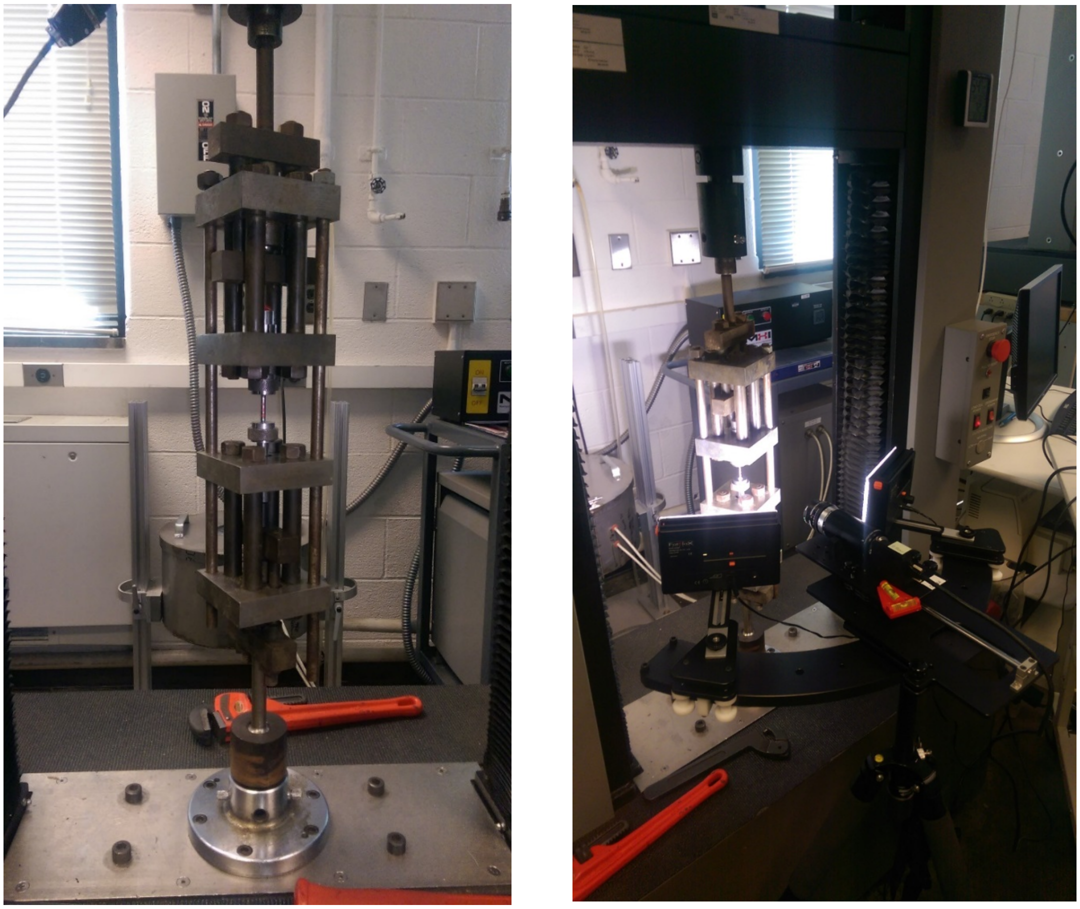

Figure 2.14: Image of tensile testing step up with double button head specimens and high alignment fixture (left) UVID, LLC non-contact video extensometer arrangement enable in-situ strain measurement (right).

Additional tensile samples were machined and tested at Westmoreland Mechanical Testing Lab (Youngstown, Pa) with the same starting size blanks as above. These tensile tests were conducted at a strain rate of $0.001s^{-1}$ and room temperature on round ASTM E8 [55] small-size specimens shown in Figure 2.15. Specimens tested at Westmoreland in this manner included: as-cast, as-cast + HIPed, upset-forged, and sidepress-forged specimens. The as-cast and as-cast + HIPed samples were excised from the same direction as the specimens above and tested at room temperature. The upset-forged specimens were excised from the transverse direction and tested at room temperature, 300°C (572°F), 700°C (1292°F), 750°C (1382°F), and 800°C (1472°F). In addition, sidepress-forged samples were excised from both the transverse and longitudinal directions and tested at 300°C (572°F), 700°C (1292°F), 750°C (1382°F), and 800°C (1472°F)

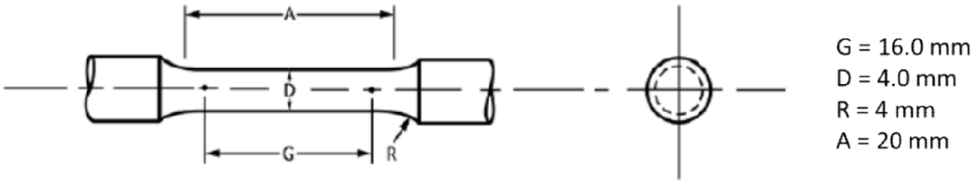

Figure 2.15: Tensile Specimen Geometry for samples tested at Westmoreland Mechanical Testing and Research, Inc.

Based upon the load and displacement measurements as recorded by testing software, the stress and strain were calculated. From the individual stress-strain curves for each specimen, 0.2% Offset Yield Strength, and Ultimate Tensile Stress were determined. This determination was done using Excel 2010. The 0.2% Offset Yield strength was determined by manually identifying the intercept between the stress-strain curve for each tension test and the 0.2% offset line generated in Excel. The Ultimate Tensile Strength (UTS) for each of the tension tests was determined using Excel by searching for the maximum stress in each data file. The percent elongation and percent reduction in area were calculated based on the final diameter and length of each sample. In order to calculate the percent reduction in area at the neck, the minimum diameter at the neck must be known. Knowing the final diameter, d_f, and the initial diameter, d_o, the percent reduction in area, %RA can be calculated from the initial area, A_o, and the final area A_f, as:

$$\%RA = \frac{A_o - A_f}{A_o} x\ 100 = \frac{d_o^2 - d_f^2}{d_o^2} \qquad (2.6)$$

Final diameter measurements were taken using a caliper by finding the region of greatest diameter reduction in each tension specimen. For confirmation, several specimen diameters were measured via Scanning Electron Microscopy.

2.5 Fracture Surface Analysis

2.5.1 Scanning Electron Microscopy (SEM)

In order to link the mechanical property changes with microstructural changes, scanning electron microscopy (SEM) of the fracture surfaces was employed. Most of the SEM work was conducted on a Zeiss EVO MA 25 (Niles, OH) at Arconic Titanium and Engineered Products located in Niles, OH. The secondary electron images (SEI) were taken with a tungsten filament emission tip at 20-25 KV with a working distance of 8 mm. Limited high-resolution SEM imaging was completed on a Nova NanoLab 200 FEG-SEM with a field emission tip located in the Swagelok Center for the Surface Analysis of Materials (SCSAM) on the campus of CWRU.

2.5.2 Scanning Electron Microscopy (SEM) of Tensile Fracture Surfaces

After completion of the tension tests the fractured specimens were imaged on a Zeiss EVO MA 25 (Niles, OH) as described above. In order to examine the nature of sub-surface damage/fracture in the tensile specimens, the fractured specimens were metallographically polished along their longitudinal axis to their midline.

2.5.3 Scanning Electron Microscopy (SEM) of Fatigue Crack Growth Fracture Surfaces

SEM analyses of the fracture surfaces were performed at different distances from the notch corresponding to different regions of the fatigue crack growth curves (e.g., threshold, Paris law regime, overload (i.e, catastrophic fracture). Images of the fractures surface were taken in five different regions: Threshold, Low ΔK, Medium ΔK, High ΔK and catastrophic overload.

2.5.4 Metallographic Cross-Sections of the Fracture Surfaces

Two fatigue specimens from each processing condition at $R = 0.3$ and 0.7 were metallographically sectioned perpendicular to and along the crack growth direction in order to directly examine the details of the crack path with respect to the microstructure. The fracture surfaces were sectioned a few mm below the surface and then mounted in copper-impregnated conductive powder in order to improve imaging. The mounted samples were polished to 0.03 μm using SiC paper and Al_2O_3 suspension polishing, followed by imaging in BSE mode on Ziess MAI 25 (Niles, OH) at Arconic, Niles, OH.

2.5.5 X-ray Diffraction of Metallographic X-Sections and Fracture Surfaces

In addition to the metallographic cross sections, X-ray diffraction characterization was also carried out on various sections of the fracture surfaces (i.e., threshold, Paris Law, overload) using a Bruker Discover D8 with a Våntec-500 solid state detector with Co K_α radiation, λ=1.79 Å, an applied voltage of 45 keV and a current of 400 mA. The scanned 2θ range was 35-65° with a 30° detector for 10 minutes. The beam had a spot size of 500 μm with a penetration depth of 10 μm. The fracture surfaces were oscillated 2 mm in the x direction to insure a large area of the surface was sampled and to avoid a single phase area and a area with poor reflection due to the fracture surface. Before each fracture surface scan session an alumina reference specimen was run to ensure the machine was calibrated properly.

X-Ray diffraction (XRD) was conducted on the fracture surfaces of the tensile specimens to determine the phases present and to assess if a preferential crack path exists. Both sides of the fracture surfaces were scanned to determine the phase % present.

XRD was conducted in the threshold, Paris law, and overload regimes on the fatigue crack growth surfaces in order to determine the phases present along the crack path. XRD was again conducted on both sides of the fatigue fracture surface, in addition XRD was conducted along a polished sample taken from along the cast direction. This was conducted in order to determine if the crack path was preferentially sample specific microstructural features.

Diffraction patterns were analyzed after collection using Diffrac.EVA for phase identification with ICDD database. Peaks for the three phases (γ, β_o, α_2) were identified and phase fractions were calculated using the integrated intensity and the area under the curve method [70] using Origin 9.4 from OriginLab. These calculations for phase fractions were then compared to the metallographic techniques described earlier (i.e., Section 2.2.1) where thresholding and quantitative metallography techniques were used. Phase fractions were determined by separation of phases by backscatter contrast in FIJI.

3 Experimental Results

3.1 Microstructure

The resulting SEM-BSE microscopy images, taken in three different orientations with respect to the casting/forging directions, were combined to create three dimensional (3D) representations for the as-cast, as-cast + HIPed, upset forged, and sidepress-forged materials. These are provided in Figures 3.1-3.4 where the casting and/or forging directions are noted.

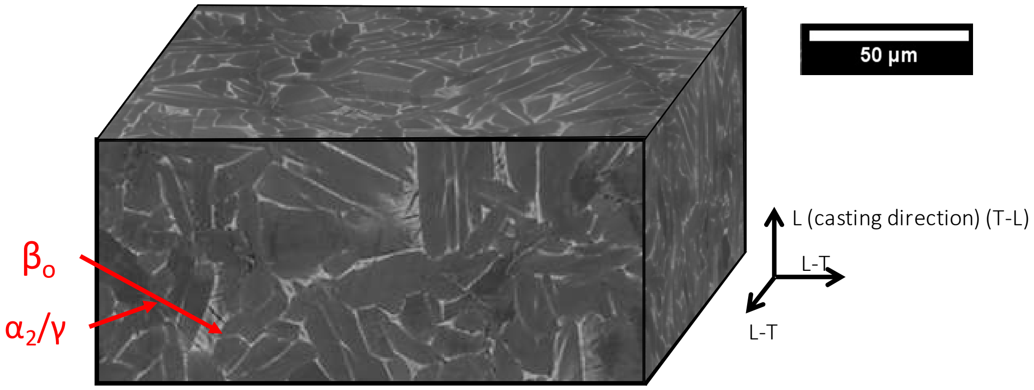

Figure 3.1: SEM/BSE images showing 3D microstructure and phases for the as-cast material.

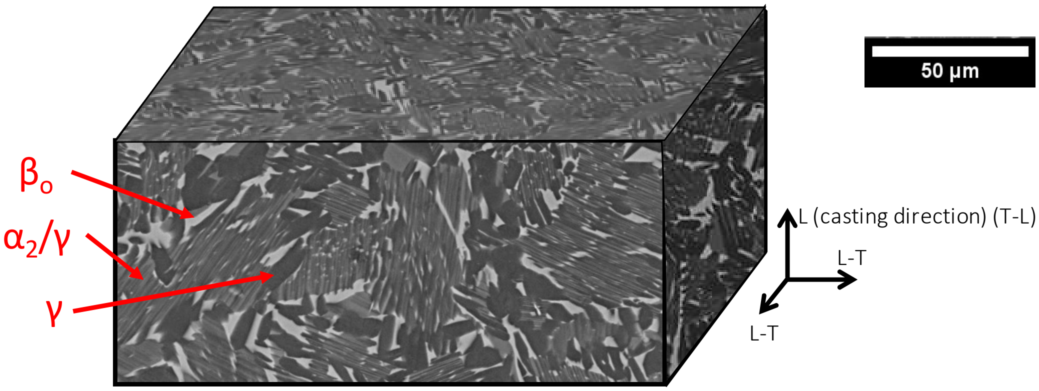

Figure 3.2: SEM/BSE images showing 3D microstructure and phases for the as-cast + HIP material.

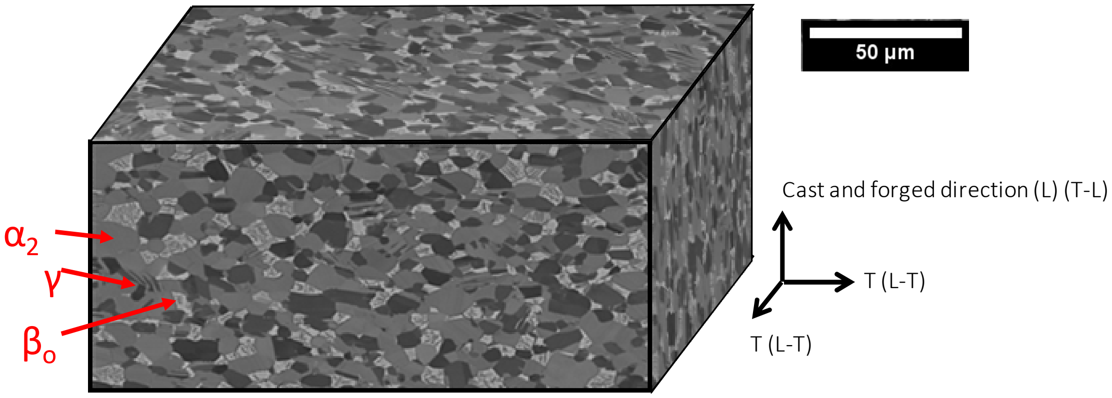

Figure 3.3 SEM/BSE images showing 3D microstructure and phases for the cast + upset-forged material.

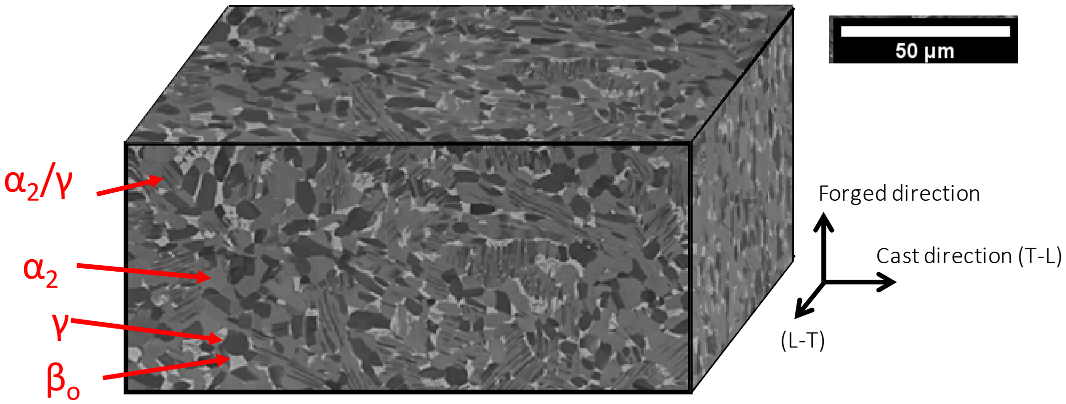

Figure 3.4: SEM/BSE images showing 3D microstructure and phases for the cast + sidepress-forged material.

3.2 Tension Tests from Longitudinal and Transverse Directions

Tension testing in the longitudinal and transverse direction was completed as described in Section 2.4.2. One or two tensile tests in each condition were performed as the focus of the present work was concentrated on the fatigue crack growth behavior of the alloy.

The results of all Yield strength, UTS, elongation, and percent reduction area from each tension test are provided in Table 3.1 for all of the samples. A few samples failed in the grip portion and are denoted with *. The strain was $0.001s^{-1}$ for all tests and test orientation (i.e., L, T) is listed in the table.

Table 3.1: Effects of processing, sample orientation, and test temperature on tensile results.
* indicates failure in the grips

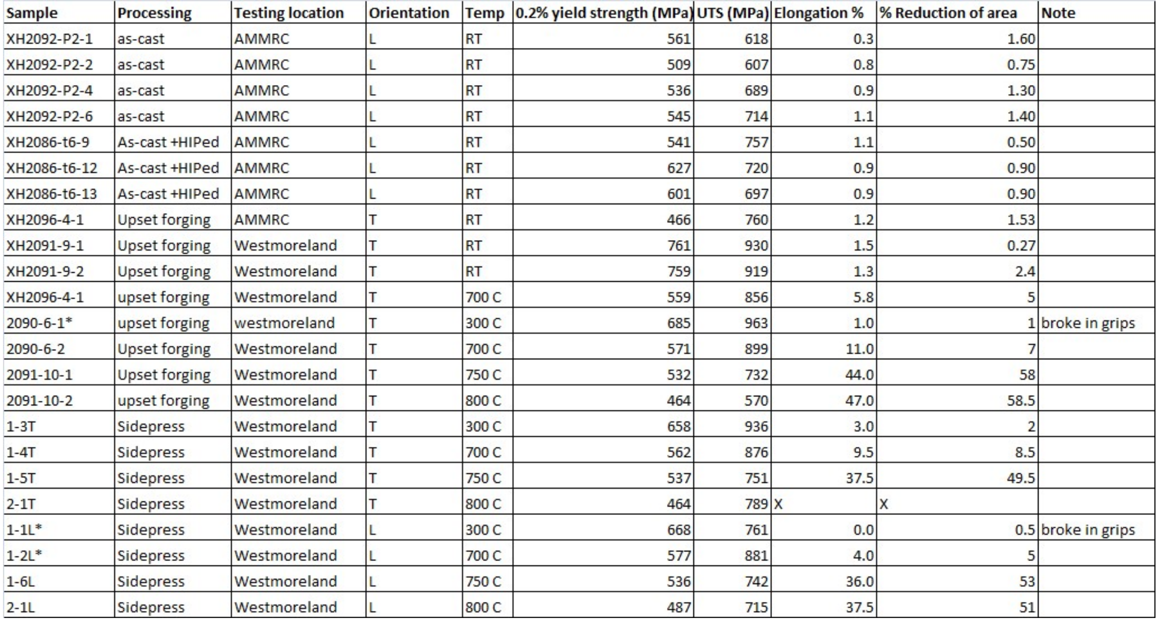

Sample	Processing	Testing location	Orientation	Temp	0.2% yield strength (MPa)	UTS (MPa)	Elongation %	% Reduction of area	Note
XH2092-P2-1	as-cast	AMMRC	L	RT	561	618	0.3	1.60	
XH2092-P2-2	as-cast	AMMRC	L	RT	509	607	0.8	0.75	
XH2092-P2-4	as-cast	AMMRC	L	RT	536	689	0.9	1.30	
XH2092-P2-6	as-cast	AMMRC	L	RT	545	714	1.1	1.40	
XH2086-t6-9	As-cast +HIPed	AMMRC	L	RT	541	757	1.1	0.50	
XH2086-t6-12	As-cast +HIPed	AMMRC	L	RT	627	720	0.9	0.90	
XH2086-t6-13	As-cast +HIPed	AMMRC	L	RT	601	697	0.9	0.90	
XH2096-4-1	Upset forging	AMMRC	T	RT	466	760	1.2	1.53	
XH2091-9-1	Upset forging	Westmoreland	T	RT	761	930	1.5	0.27	
XH2091-9-2	Upset forging	Westmoreland	T	RT	759	919	1.3	2.4	
XH2096-4-1	upset forging	Westmoreland	T	700 C	559	856	5.8	5	
2090-6-1*	upset forging	westmoreland	T	300 C	685	963	1.0	1	broke in grips
2090-6-2	Upset forging	Westmoreland	T	700 C	571	899	11.0	7	
2091-10-1	Upset forging	Westmoreland	T	750 C	532	732	44.0	58	
2091-10-2	upset forging	Westmoreland	T	800 C	464	570	47.0	58.5	
1-3T	Sidepress	Westmoreland	T	300 C	658	936	3.0	2	
1-4T	Sidepress	Westmoreland	T	700 C	562	876	9.5	8.5	
1-5T	Sidepress	Westmoreland	T	750 C	537	751	37.5	49.5	
2-1T	Sidepress	Westmoreland	T	800 C	464	789	X	X	
1-1L*	Sidepress	Westmoreland	L	300 C	668	761	0.0	0.5	broke in grips
1-2L*	Sidepress	Westmoreland	L	700 C	577	881	4.0	5	
1-6L	Sidepress	Westmoreland	L	750 C	536	742	36.0	53	
2-1L	Sidepress	Westmoreland	L	800 C	487	715	37.5	51	

Engineering stress-strain curves were determined for each condition tested and are provided in Figures 3.5 to Figure 3.8. The Young's Modulus for the room temperature tensile tests were calculated: As-cast = 82 GPa, HIP = 98 GPa and Upset Forged = 151 GPa. The beneficial effects of deformation processing on the behavior is shown by comparison of as-cast, HIPed, upset forged and sidepress-forged specimens. The effect of changes in test temperature and sample orientation are also shown as well. In order to aid comparison between the different processing conditions, Figures 3.9 to 3.12 plot the Yield Strength, UTS elongation, elongation and percent reduction in area as a function of temperature.

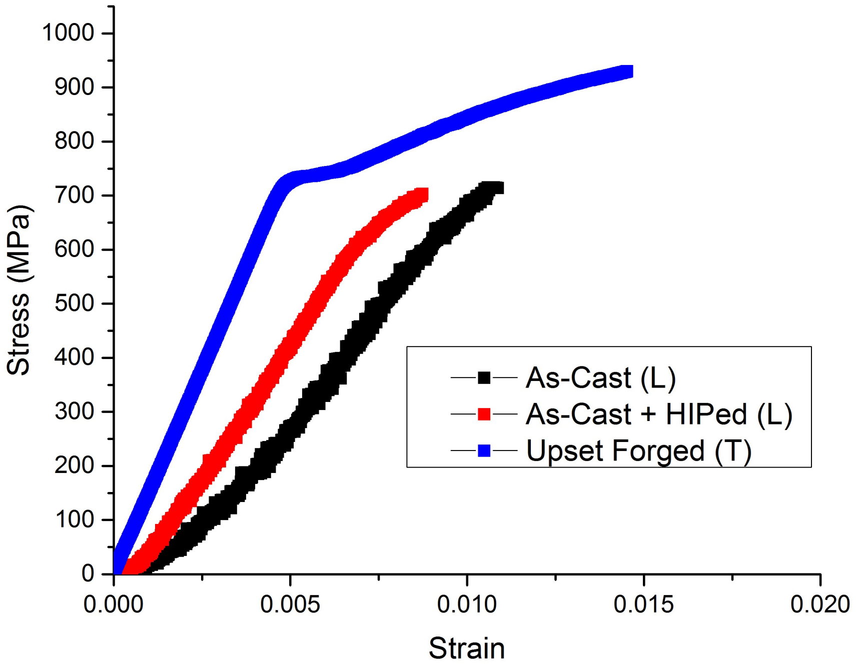

Figure 3.5: Representative engineering stress-strain curves comparing TNM in three conditions. Tension testing conducted at room temperature in lab air at 0.001s^{-1}.

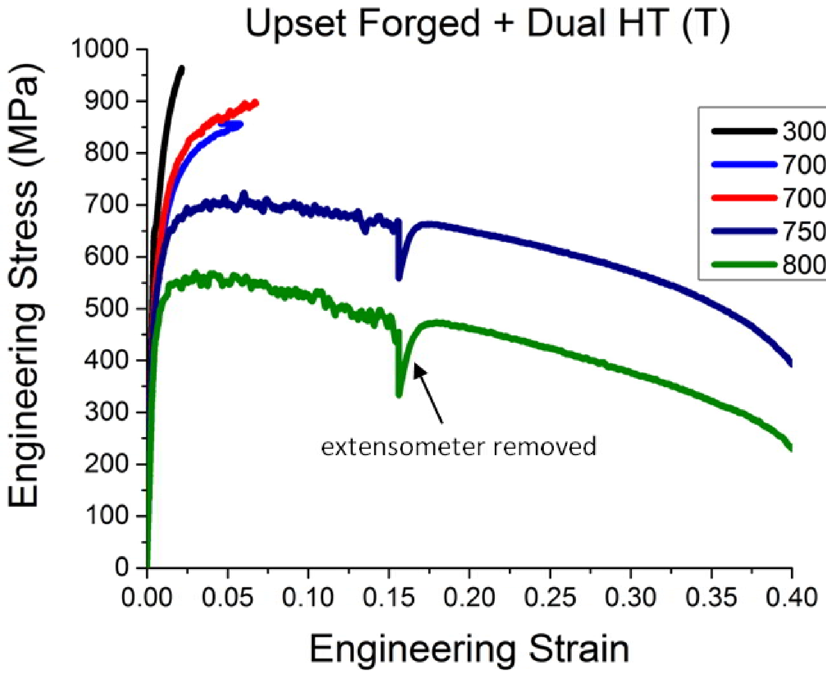

Figure 3.6: Engineering stress-strain curves on upset-forged material tested in the transverse direction at temperatures noted. Tensions tests conducted at 0.001s^{-1}.

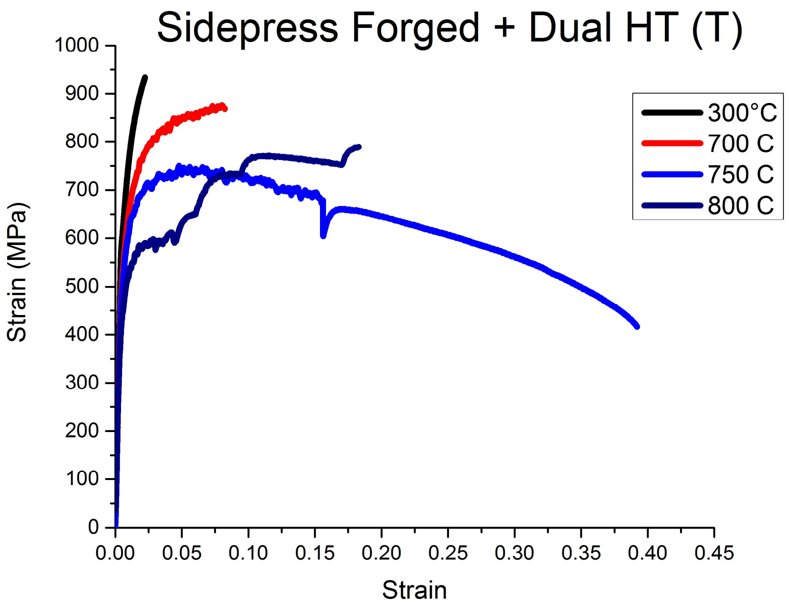

Figure 3.7: Engineering stress-strain curves on sidepress-forged material tested in the transverse at various temperatures as noted. Tension tests conducted at $0.001s^{-1}$.

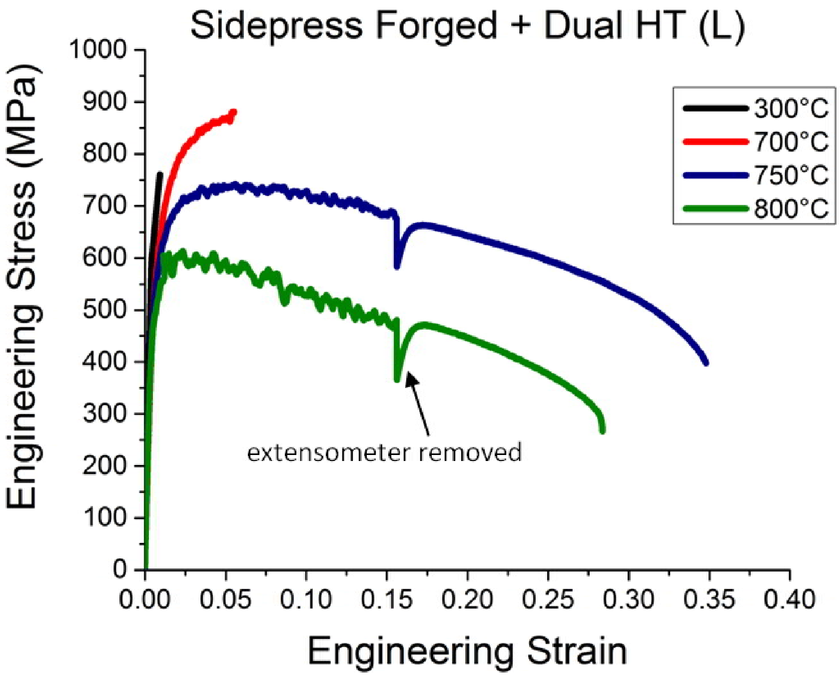

Figure 3.8: Engineering stress-strain curves on sidepress-forged material tested in the longitudinal direction at various temperatures as noted. Tension tests conducted at $0.001s^{-1}$.

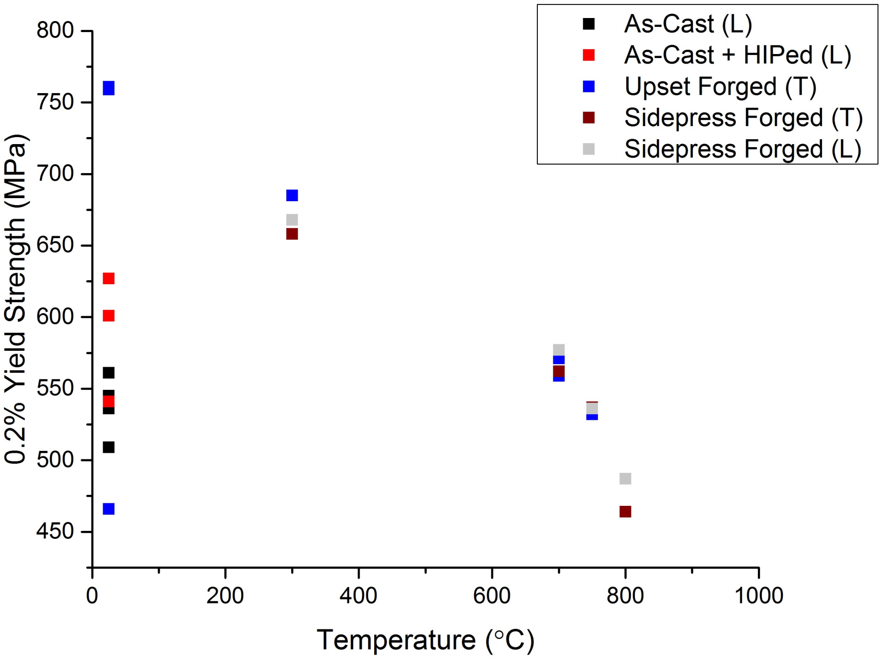

Figure 3.9: Effect of processing condition, sample orientation, and test temperature on 0.2% Offset Yield Strength at $0.001 s^{-1}$.

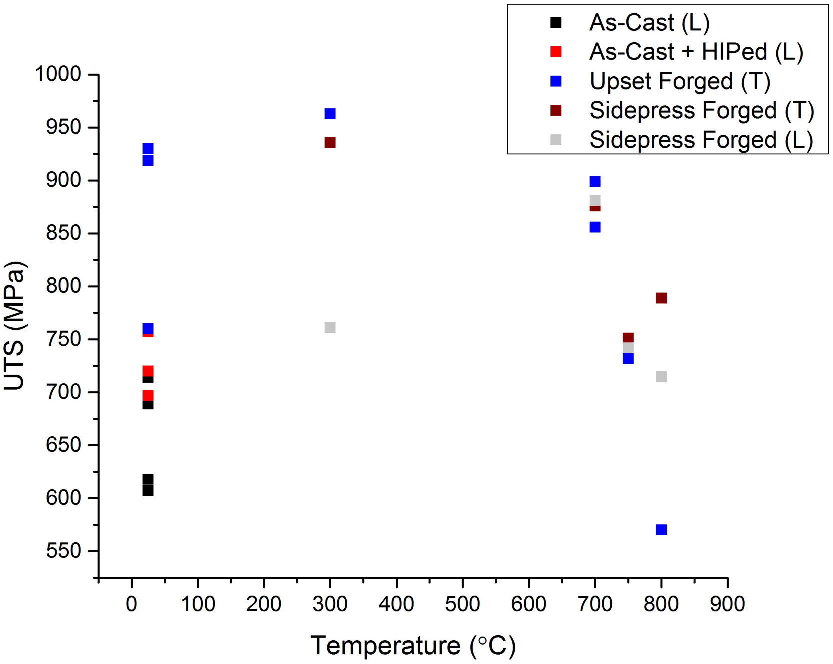

Figure 3.10: Effect of processing condition, sample orientation, and test temperature on Ultimate Tensile Strength at $0.001 s^{-1}$.

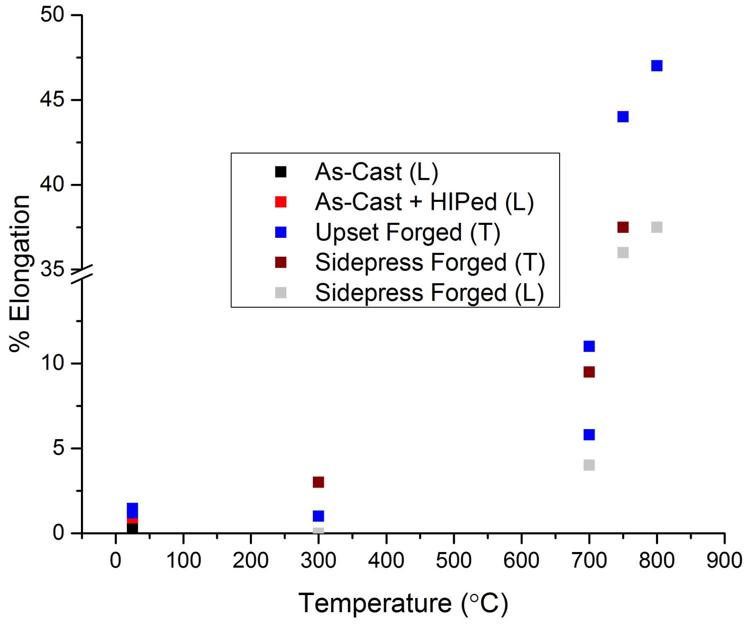

Figure 3.11: Effect of processing condition, sample orientation, and test temperature on Percent Elongation at $0.001s^{-1}$.

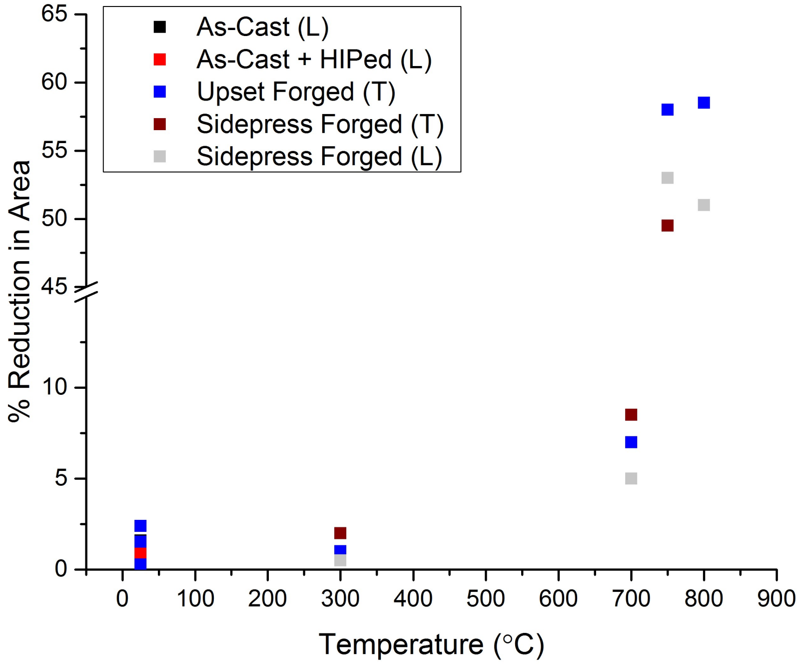

Figure 3.12: Effect of processing condition, sample orientation, and test temperature on Percent Reduction in Area at $0.001s^{-1}$.

3.3 Fatigue Crack Growth

3.3.1 Fatigue Crack Growth Curves

Fatigue crack growth data are plotted in terms of (d*a*/d*N*) versus ΔK in accordance with the ASTM E 647 standard [63]. Results are summarized for As-cast L-T and T-L in Figures 3.13, 3.14; As-Cast + HIPed L-T and T-L are provided in Figures 3.15, 3.16: Upset- and Sidepress-forged data are provided in Figures 3.17, 3.18.

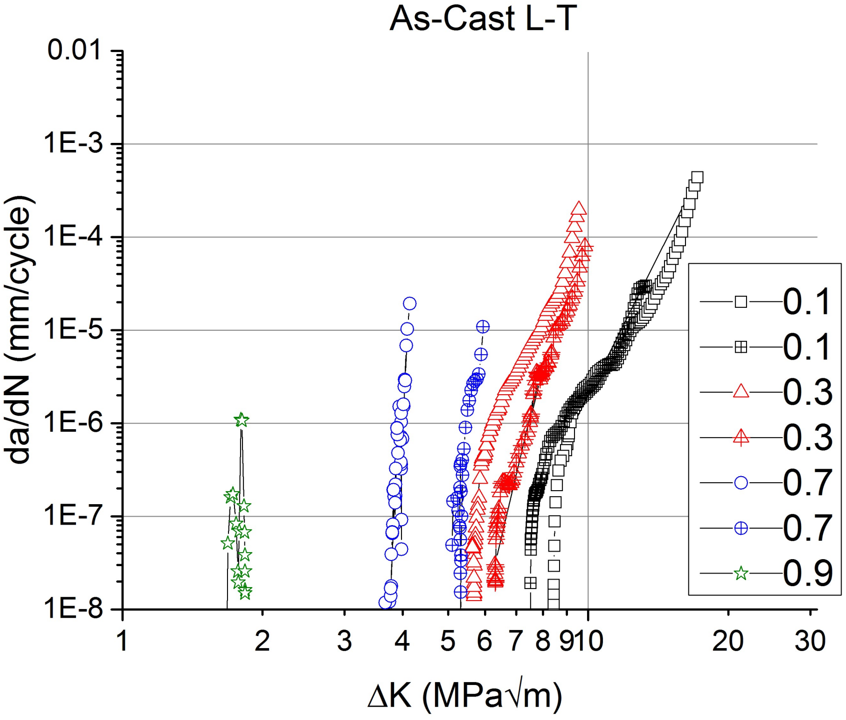

.

Figure 3.13: Fatigue crack growth curves for all as-cast L-T tests. Legend shows load ratio, R.

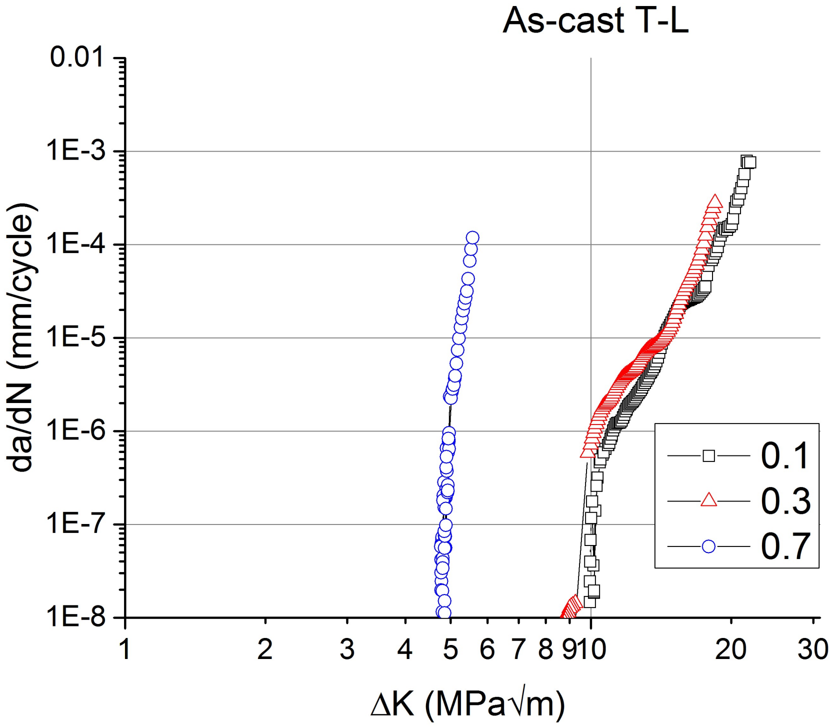

Figure 3.14: Fatigue crack growth curves for all as-cast T-L tests. Legend shows load ratio, R.

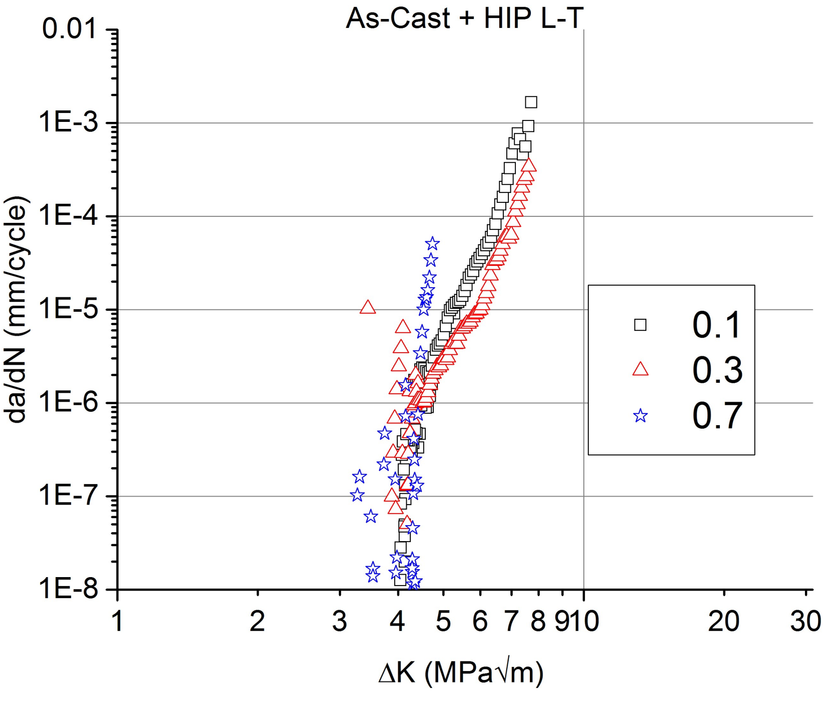

Figure 3.15: Fatigue crack growth curves for all as-cast + HIPed L-T tests. Legend shows load ratio, R.

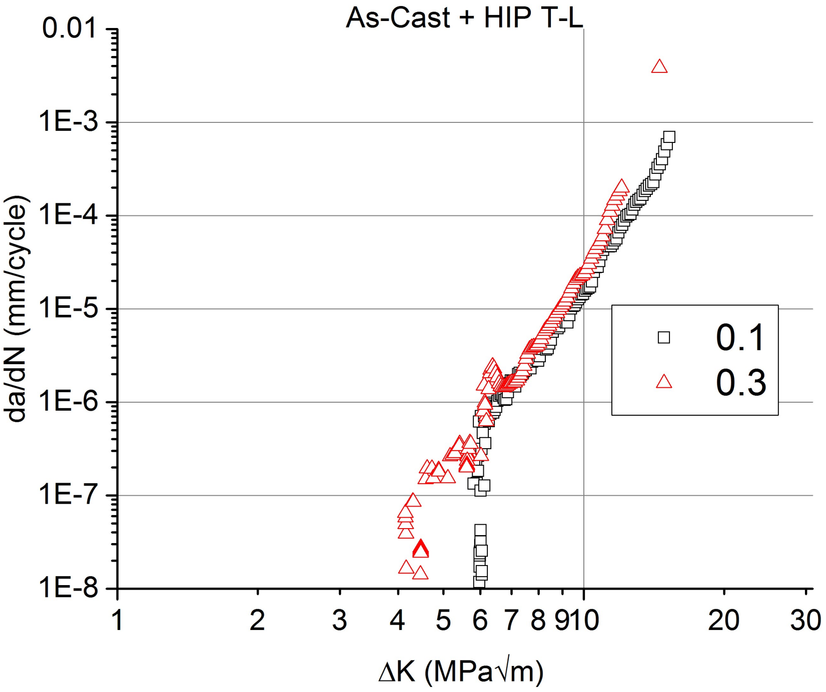

Figure 3.16: Fatigue crack growth curves for all as-cast + HIPed T-L tests. Legend shows load ratio, R.

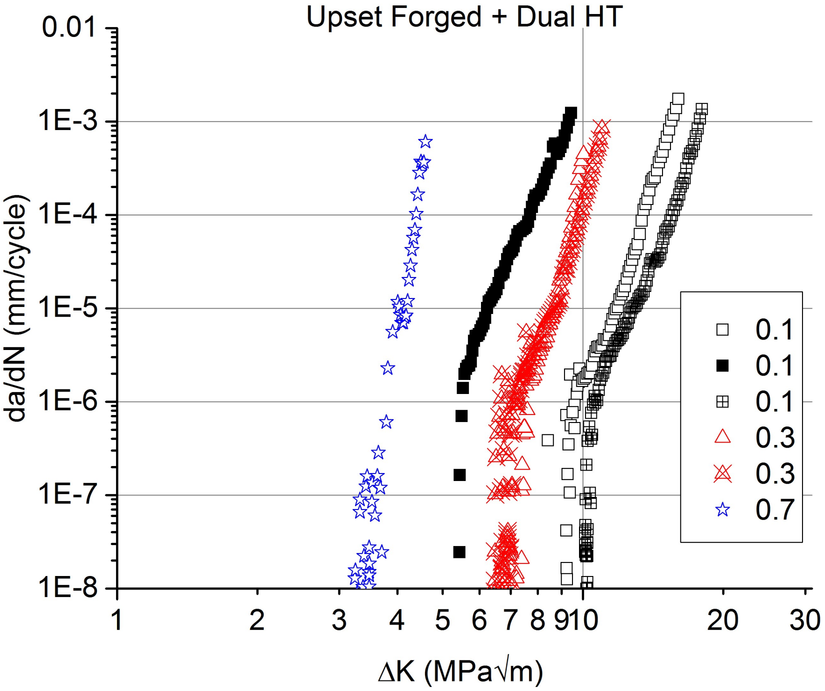

Figure 3.17: Fatigue crack growth curves for upset-forged samples in the T-L direction. Legend shows load ratio, R.

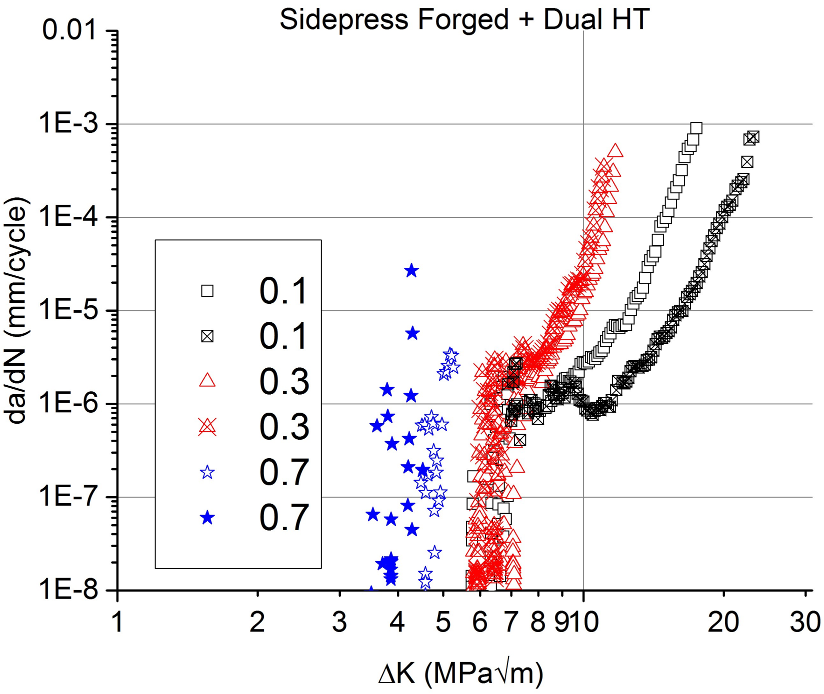

Figure 3.18: Fatigue crack growth curves for all sidepress-forged samples. Legend provides load ratio, R.

3.4.2 Fatigue Threshold

The fatigue threshold, ΔK_{th} was measured as described in Section 2.4.1.3 and shown in Figure 2.4. ΔK_{th} was determined in this manner for all the fatigue tests shown in Figures 3.13-3.18 and are summarized in Tables 3.2-3.5. The TNM material, in all conditions and orientations, exhibits a decreasing ΔK_{th} with increasing load ratio, R. The influence of sample orientation on ΔK_{th} was more pronounced in the as-cast material than the HIPed material as shown by the more rapid drop in ΔK_{th} with increasing load ratio, R.

3.4.3 Paris Law Slope

The Paris law relationship which is reported as m, are presented in Tables 3.2-3.5 for all of the different specimens and processing conditions tested presently. The Paris relationship, m, for all processing conditions increases with increasing load ratio, R.

3.4.4 Critical K at Overload (K_c)

Tests conducted under rising ΔK conditions will eventually produce catastrophic failure as shown in Figure 2.6. As a result, each specimen exhibited a critical ΔK at which catastrophic overload occurred, termed ΔK_c. Although not identical to the plane strain fracture toughness, K_{IC}, determined from a fracture toughness test, ΔK_c can be converted to a maximum K_C at a failure when the load ratio, R, is known. Therefore, considering K_{max} at overload in the rising ΔK portion of the (da/dN) and based on Equation 2.1, K_{max} at overload is given as:

$$K_{max} = \frac{\Delta K_c}{1 - R}$$

In all Tables, the K_{max} at catastrophic fatigue overload is reported as K_c. Tables 3.2 to 3.5 summarize ΔK_{th}, C, m, and ΔK_c. Some samples were only run to failure so no threshold data was determined. The K_c at failure in fatigue was not significantly affected by load ratio, R or sample orientation.

Table 3.2: Effect of sample orientation and load ratio, R, on fatigue crack growth of As-cast TNM

Orientation	**R**	**Test Type**	**ΔK_{th} (MPa√m)**	**Paris Slope, m**	**Overload K_c (MPa√m)**
L-T	0.1	Threshold, Rising ΔK	8.4	9.1	19.1
L-T	0.1	Threshold, Rising ΔK	7.5	9.2	14.7
L-T	0.3	Threshold, Rising ΔK	6.3	9.3	14
L-T	0.3	Threshold, Rising ΔK	5.6	9.3	13.6
L-T	0.7	Threshold, Rising ΔK	3.8	35.6	13.8
L-T	0.7	Threshold, Rising ΔK	5.4	37	19.8
L-T	0.9	Threshold, Rising ΔK	1.7	93.8	18.3
T-L	0.1	Threshold, Rising ΔK	9.9	9	24.4
T-L	0.3	Threshold, Rising ΔK	8.5	9.3	26
T-L	0.7	Threshold, Rising ΔK	4.8	50	18.7

Table 3.3: Effect of sample orientation and load ratio, R, on fatigue crack growth of As-cast + HIPed TNM

Orientation	**R**	**Test Type**	**ΔK_{th} (MPa√m)**	**Paris Slope, m**	**Overload K_c (MPa√m)**
L-T	0.1	Threshold, Rising ΔK	4.13	6	8.58
L-T	0.3	Threshold, Rising ΔK	3.86	6.3	11.1
L-T	0.7	Threshold, Rising ΔK	4.3	51	15.8
T-L	0.1	Threshold, Rising ΔK	5.87	7.27	16.9
T-L	0.3	Threshold, Rising ΔK	4.1	7.76	17.23

Table 3.4: Effect of sample orientation and load ratio, R, on fatigue crack growth of Upset-forged material

Orientation	**R**	**Test Type**	**ΔK_{th} (MPa√m)**	**Paris Slope, m**	**Overload K_c (MPa√m)**
T-L	0.1	Threshold, Rising ΔK	9.3	13.1	17.8
T-L	0.1	Threshold, Rising ΔK	5.4	16.5	10.7
T-L	0.1	Threshold, Rising ΔK	10.1	12.5	20
T-L	0.3	Threshold, Rising ΔK	7.2	18	14.3
T-L	0.3	Threshold, Rising ΔK	6.8	17	15.7
T-L	0.7	Threshold, Rising ΔK	3.5	35	15.3

Table 3.5: Effect of sample orientation and load ratio, R, on fatigue crack growth of sidepress-forged material

Orientation	**R**	**Test Type**	**ΔK_{th} (MPa√m)**	**Paris Slope, m**	**Overload K_c (MPa√m)**
L-T	0.1	Threshold, Rising ΔK	6.6	13.1	19.3
L-T	0.1	Rising ΔK	X	8.5	25
L-T	0.3	Threshold, Rising ΔK	6.4	16.5	16.8
L-T	0.3	Threshold, Rising ΔK	6.3	12.5	15.8
L-T	0.7	Threshold, Rising ΔK	4.5	18	14.3
L-T	0.7	Threshold, Rising ΔK	3.6	17	17.3

3.5 Fracture Surface Analyses

After completion of the tension tests and fatigue crack growth tests, selected fracture surfaces were analyzed using Scanning Electron Microcopy (SEM) and X-ray Diffraction (XRD). The orientation of the sample while imaging was maintained, so as to provide a comparison between fracture surfaces from different processing and testing conditions.

3.5.1 Tensile Specimen Fracture Surface Features

In order to provide a representative sampling of fracture surface features, SEM images from as-cast, as-cast + HIPed and forged specimens were compared from different orientations and test temperatures in Figures 3.19-3.28.

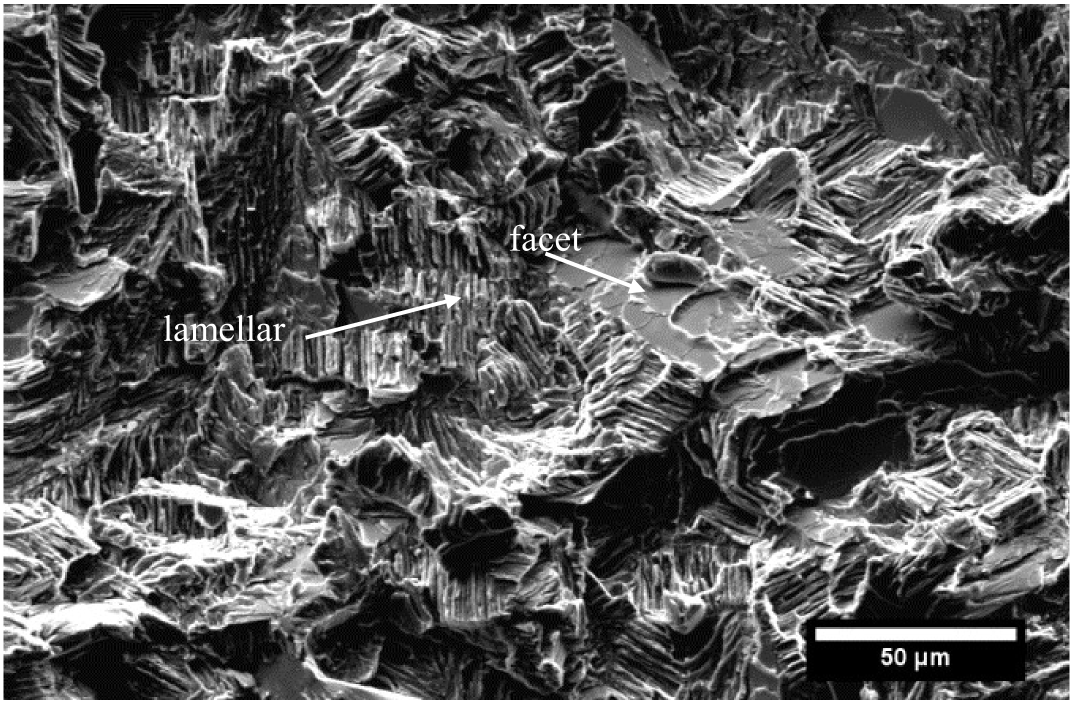

Figure 3.19: SEM-SE image of the tensile room temperature fracture surfaces taken of the as-cast tested at a strain rate of $0.001s^{-1}$ with elongation less than 1%. The fracture surfaces show flat facets indicative of brittle fracture as well as lamellar structure.

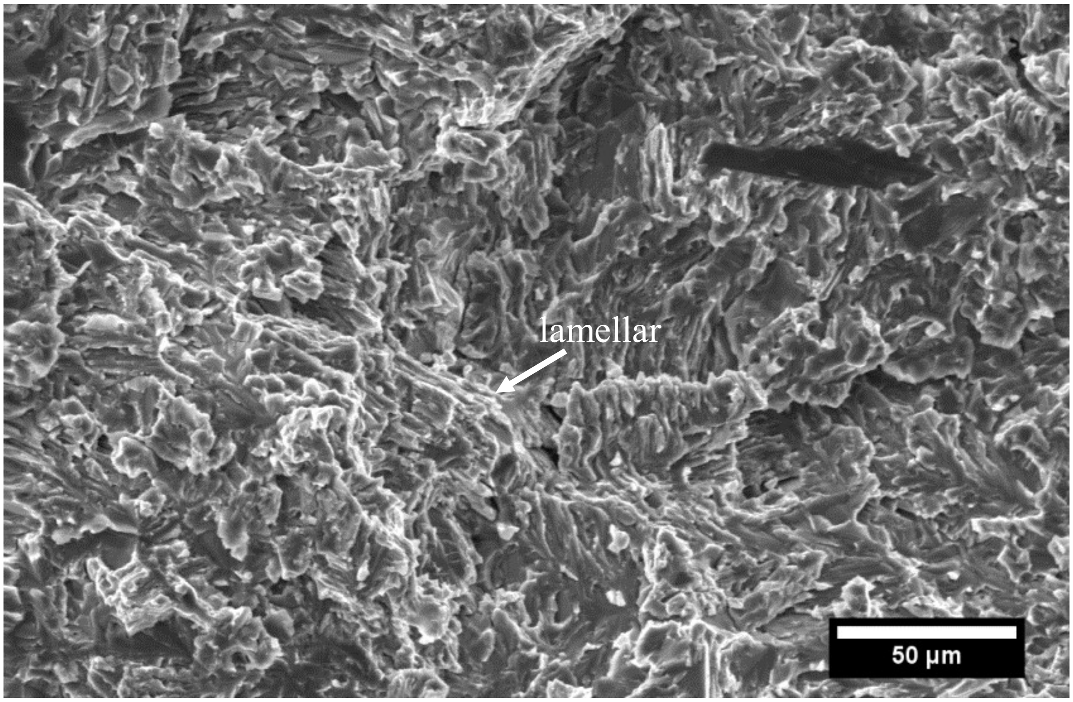

Figure 3.20: SEM-SE image of the tensile room temperature fracture surfaces taken of the as-cast + HIPed tested at a strain rate of 0.001s^{-1} with elongation less than 1%.

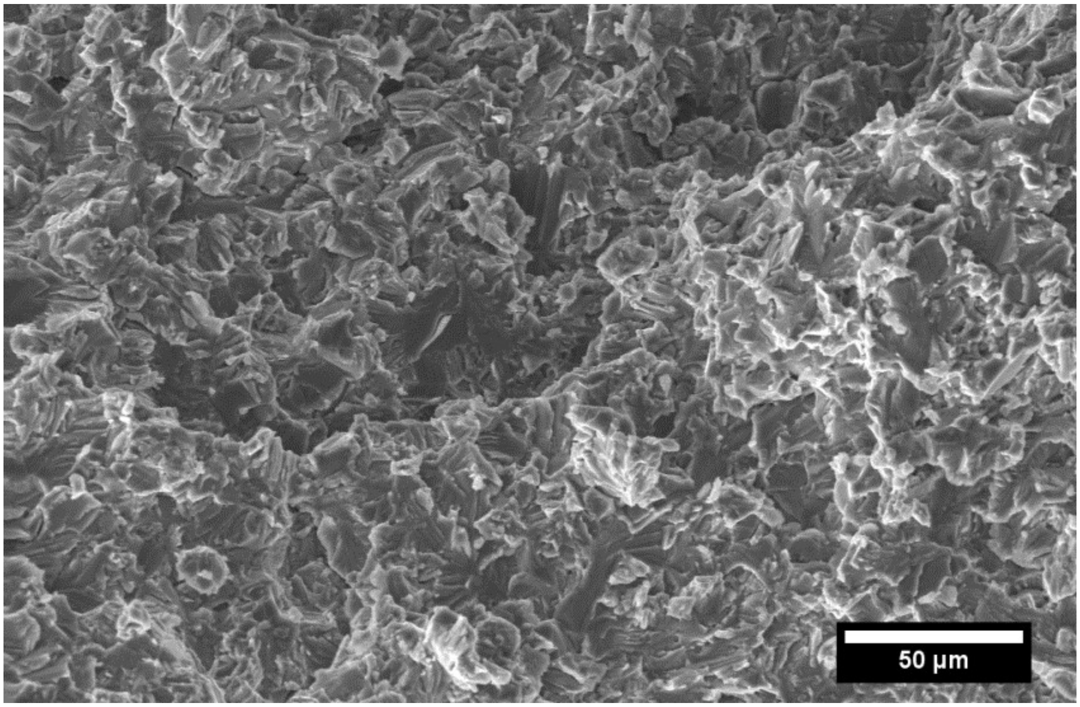

Figure 3.21: SEM-SE image of room temperature tensile fracture surfaces taken of the upset-forged tested at a strain rate of 0.001s^{-1} with elongation of 1.5%. Fracture surfaces show small facets from cracking between phases

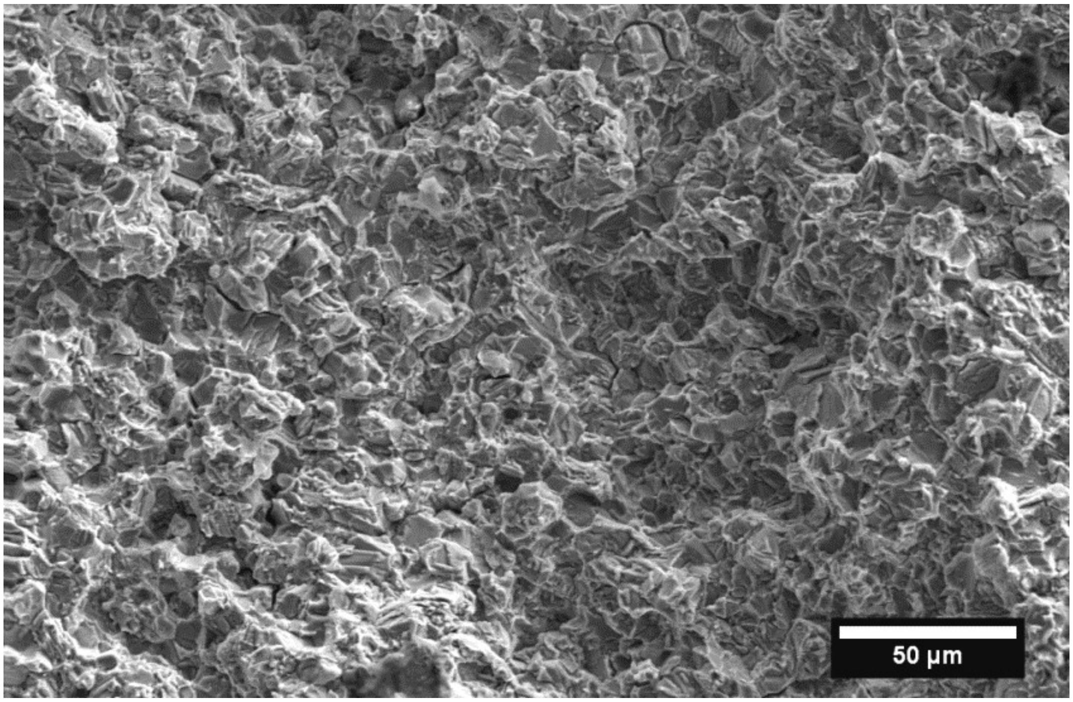

Figure 3.22: SEM-SE image of tensile fracture surface taken of upset-forged specimen tested at 700°C at a strain rate of $0.001s^{-1}$ with elongation of 3%. Facture surface shows small facets from cracking between phases.

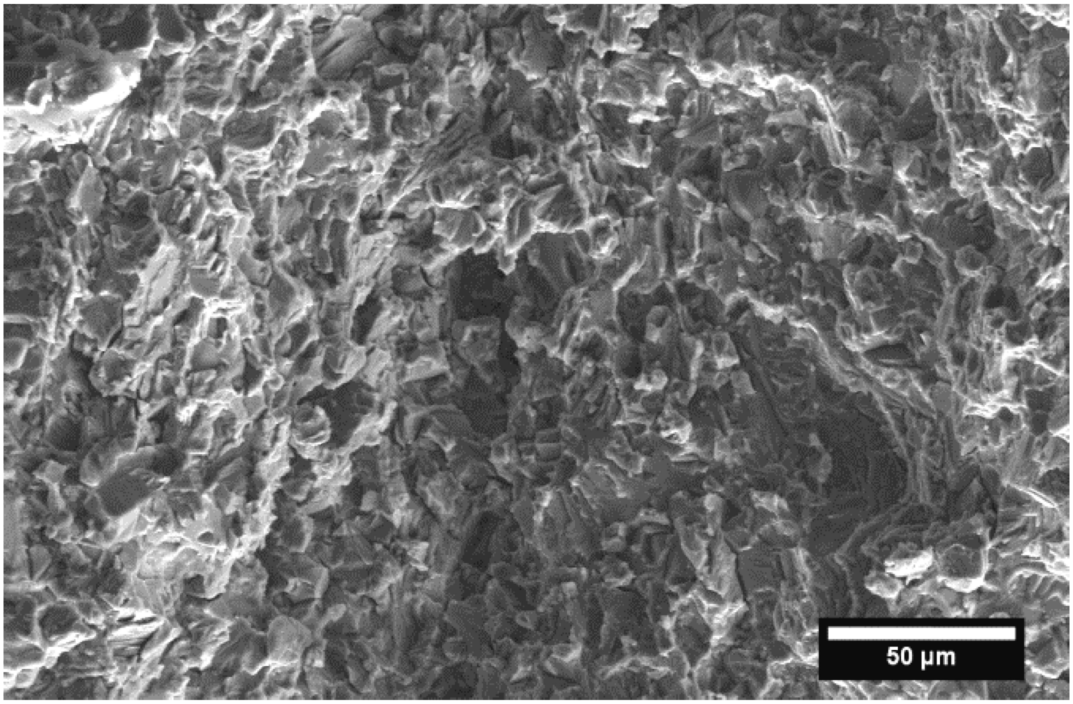

Figure 3.23: SEM-SE image of the tensile fracture surface taken of the sidepress-forged specimens tested in air in the transverse direction at $0.001s^{-1}$ at 300°C.

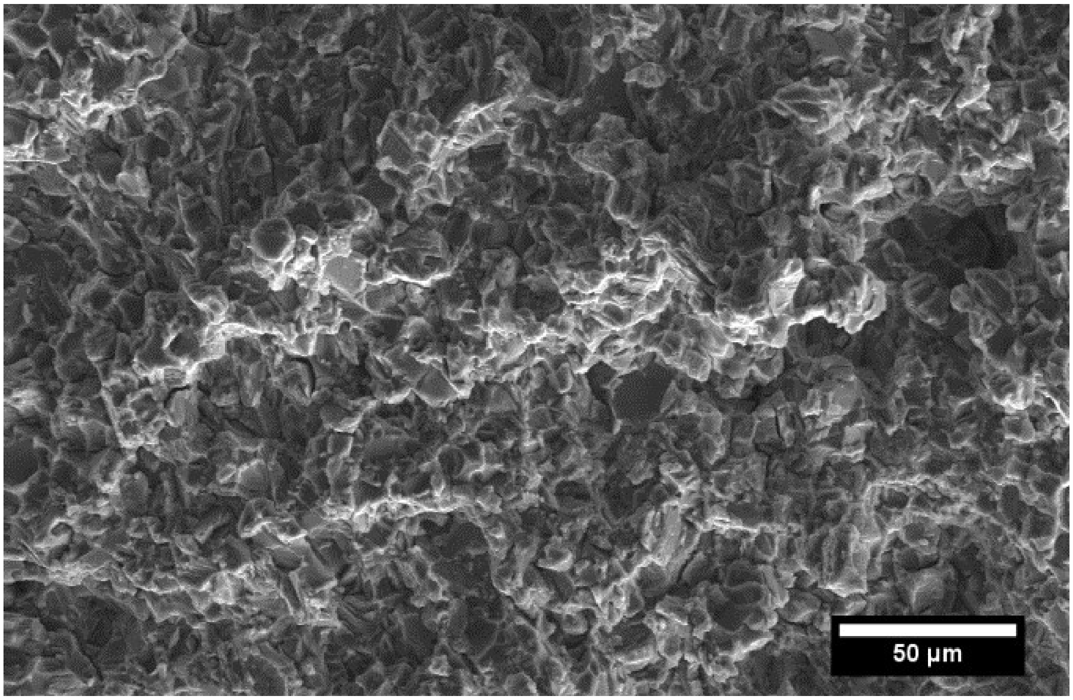

Figure 3.24: SEM-SE image of the tensile fracture surface taken of the sidepress-forged specimens tested in air in the transverse direction at $0.001s^{-1}$ at 700°C. Fracture surfaces shows facets from cracking between phases.

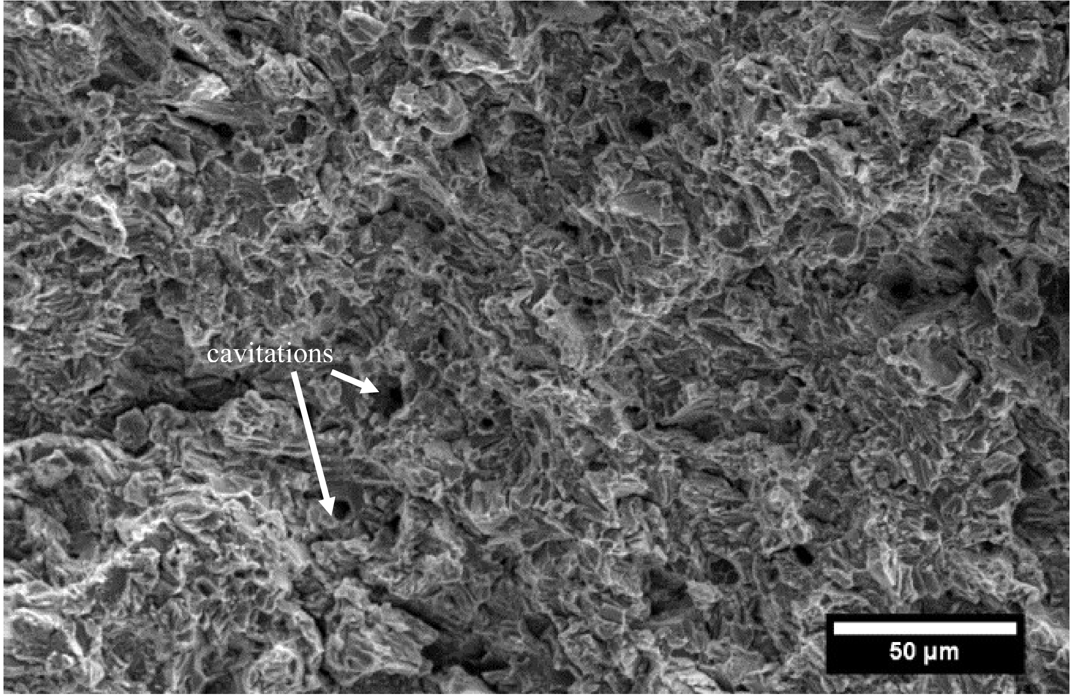

Figure 3.25: SEM-SE image of the tensile fracture surface taken of the sidepress-forged specimens tested in air in the transverse direction at $0.001s^{-1}$ at 750°C with elongation of 30%. The fracture surfaces shows cavitation from the β_0 phase.

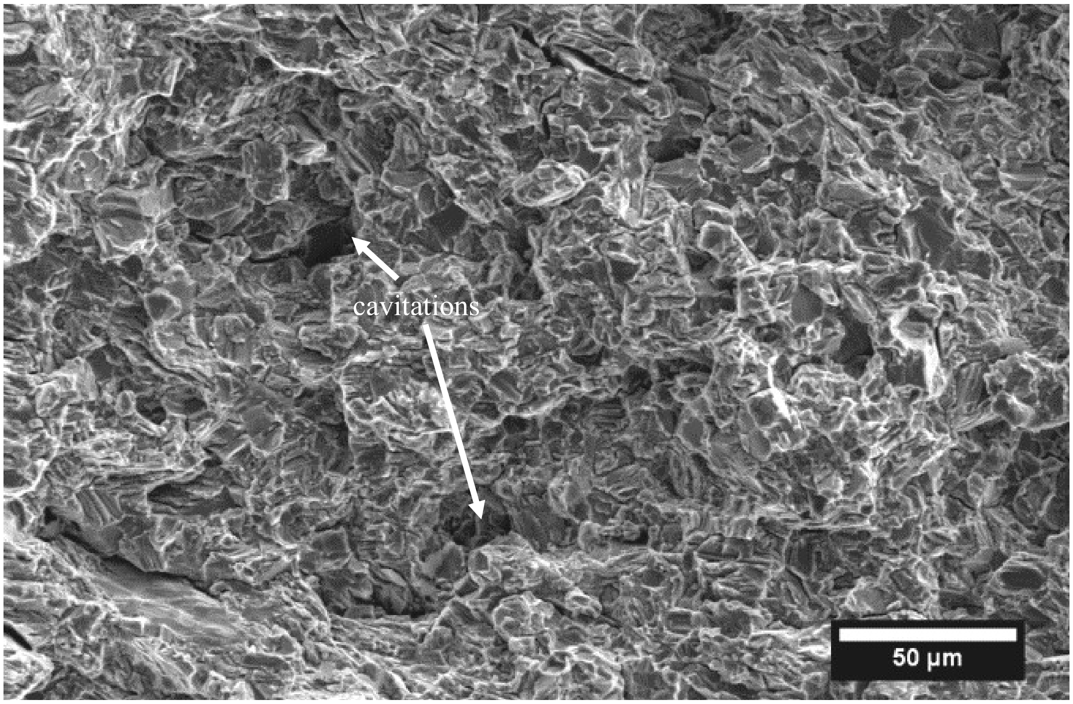

Figure 3.26: SEM-SE image of the tensile fracture surface taken of the sidepress-forged specimens tested in air in the transverse direction at $0.001s^{-1}$ at 800°C with over 40% elongation. The fracture surface shows cavitation from the β_o phase.

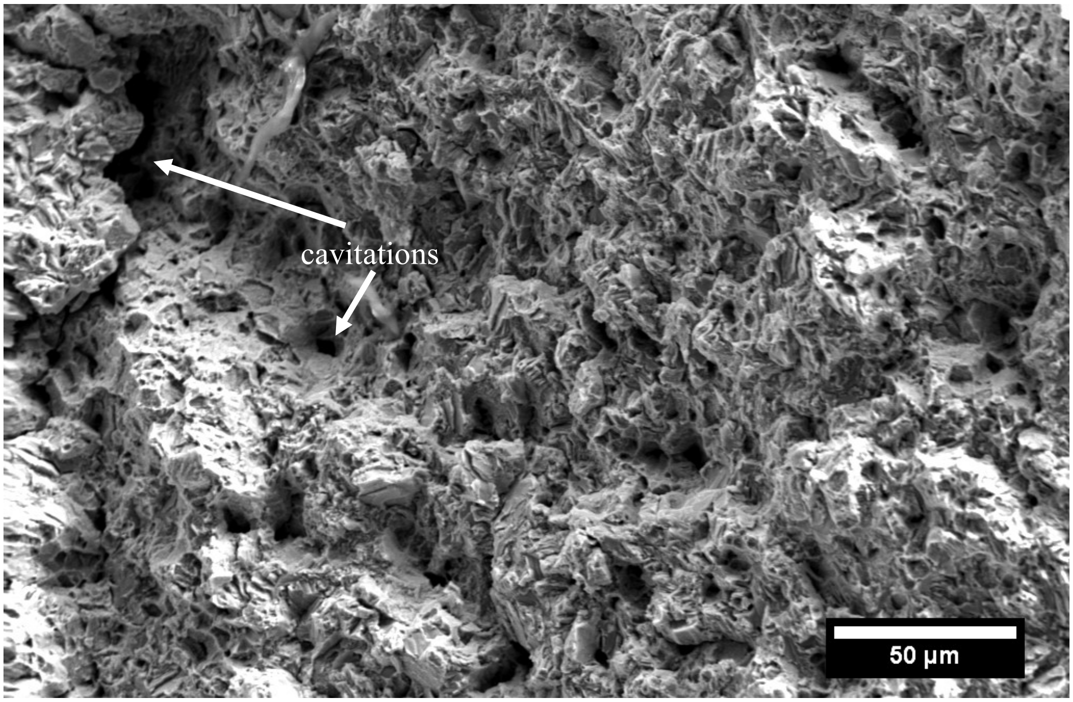

Figure 3.27: SEM-SE image of the tensile fracture surface taken of the sidepress-forged specimens tested in air in the longitudinal direction at $0.001s^{-1}$ at 750°C with elongation of 30%. The fracture surface shows massive cavitation and flat facets.

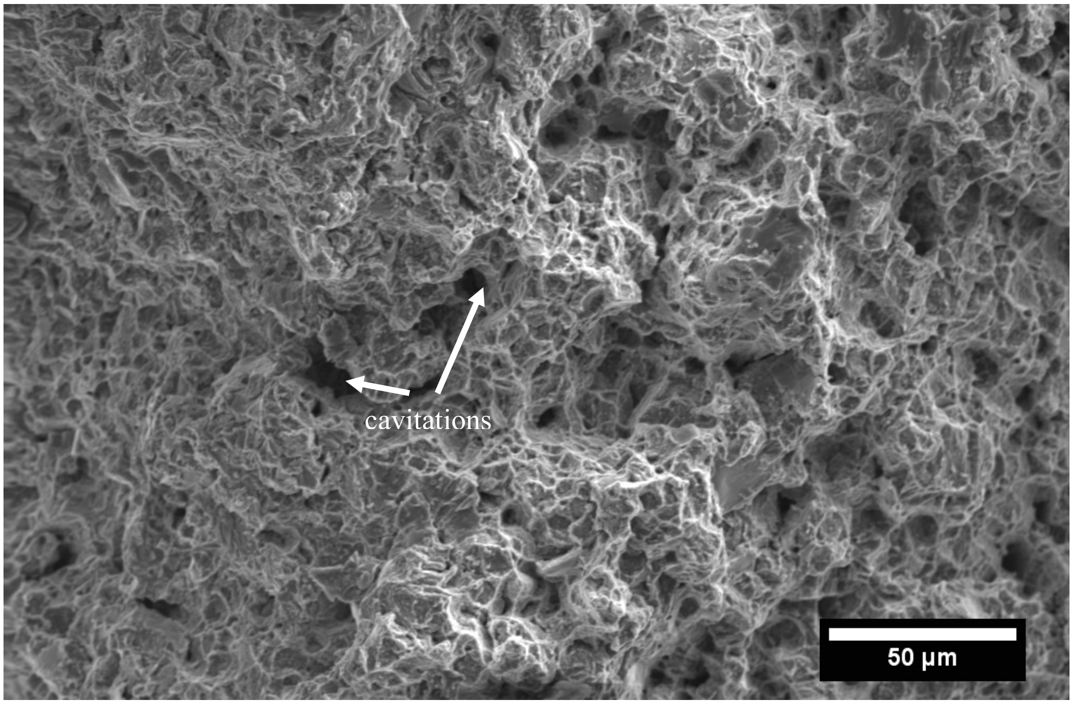

Figure 3.28: SEM-SE image of the tensile fracture surface taken of the sidepress-forged specimens tested in air in the longitudinal direction at $0.001 s^{-1}$ at 800°C with elongation of over 40%. The fracture surface shows cavitation.

SEM images were taken near the fracture surface of each sample and the images are shown in Figures 3.29 through 3.38. While all samples exhibited subsurface cracking, the extent and location of cracking was affected by the different processing conditions as this affected the phases present and their morphology in the microstructure. The extent of sub-cracking and damage increased with the increased ductility that accompanied testing at the higher temperatures, with the most extensive sub-surface cracking in samples tested at 750 °C and 800 °C.

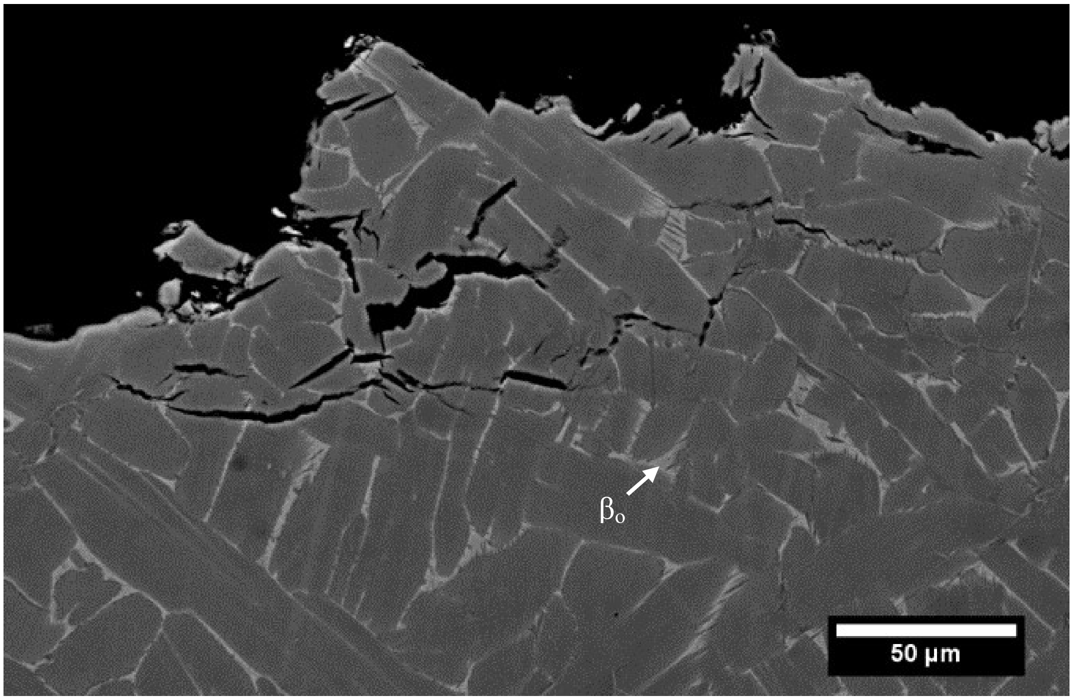

Figure 3.29: SEM-BSE image of the polished midplane of as-cast tensile specimen tested room at room temperature at a strain rate of $0.001s^{-1}$ with less than 0.5% elongation. Subsurface damage is evident and the crack appears to follow β_0.

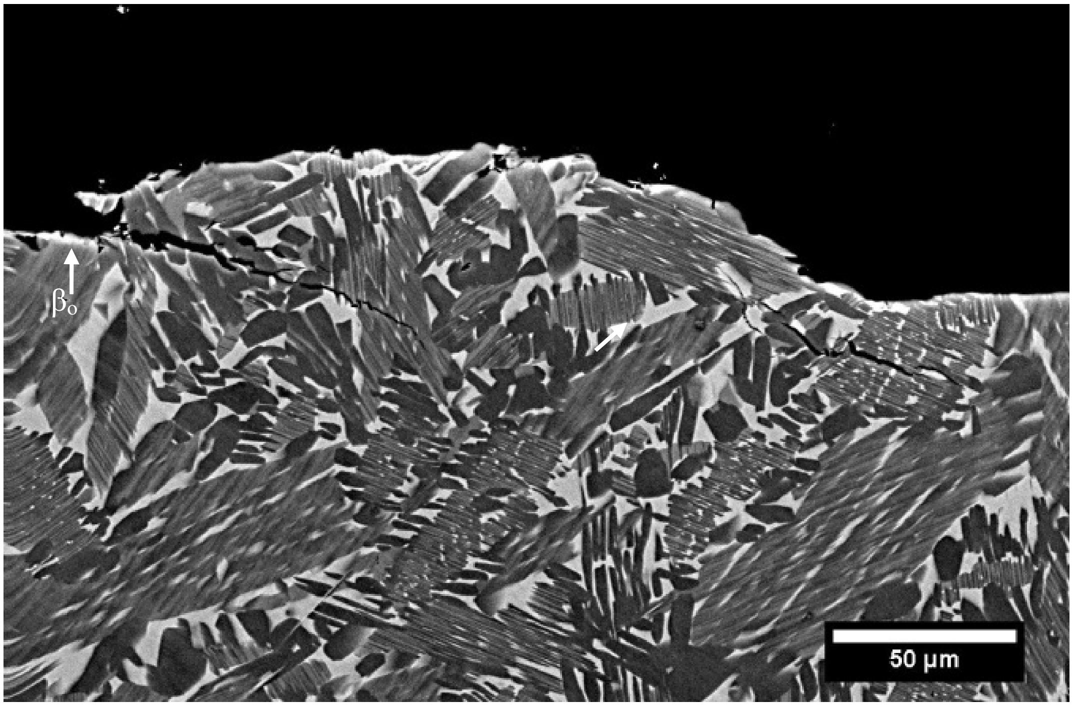

Figure 3.30: SEM-BSE image of the polished midplane of As-cast + HIP tensile specimen tested room at room temperature at a strain rate of $0.001s^{-1}$ and less than 0.5 elongation. Subsurface damage is evident and crack tries to follow β_0.

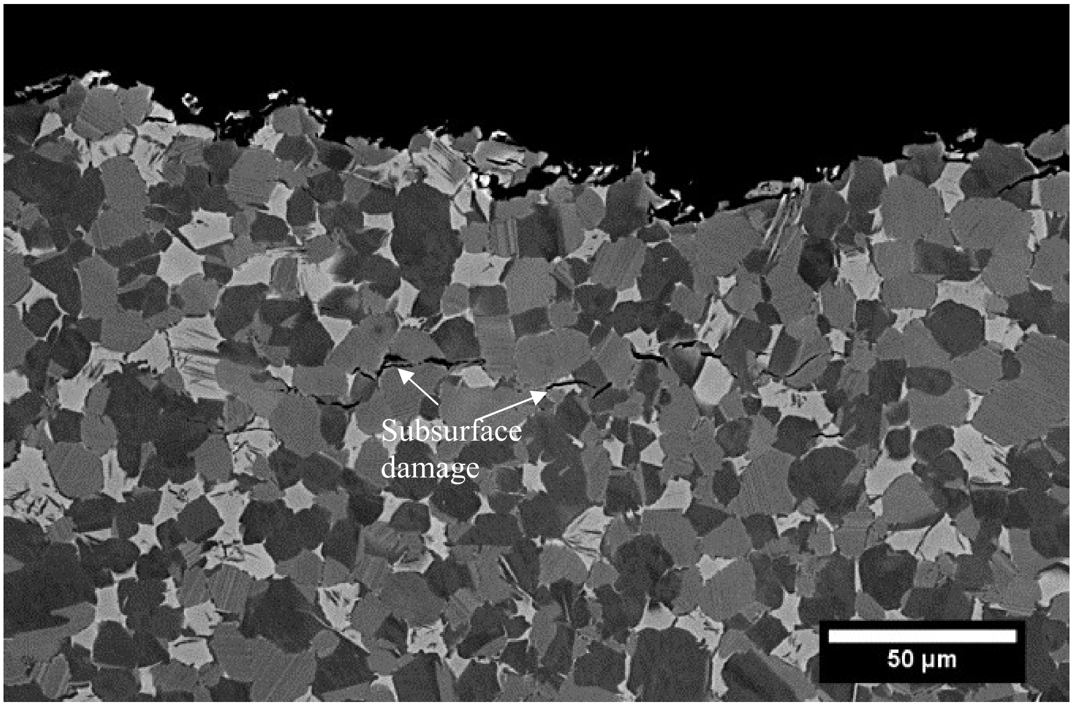

Figure 3.31: SEM-BSE image of the polished midplane of Upset-forged tensile specimen tested room at room temperature at a strain rate of 0.001s^{-1} with elongation of 1.5%. Subsurface damage is evident but the cracks do preferential crack in a phase.

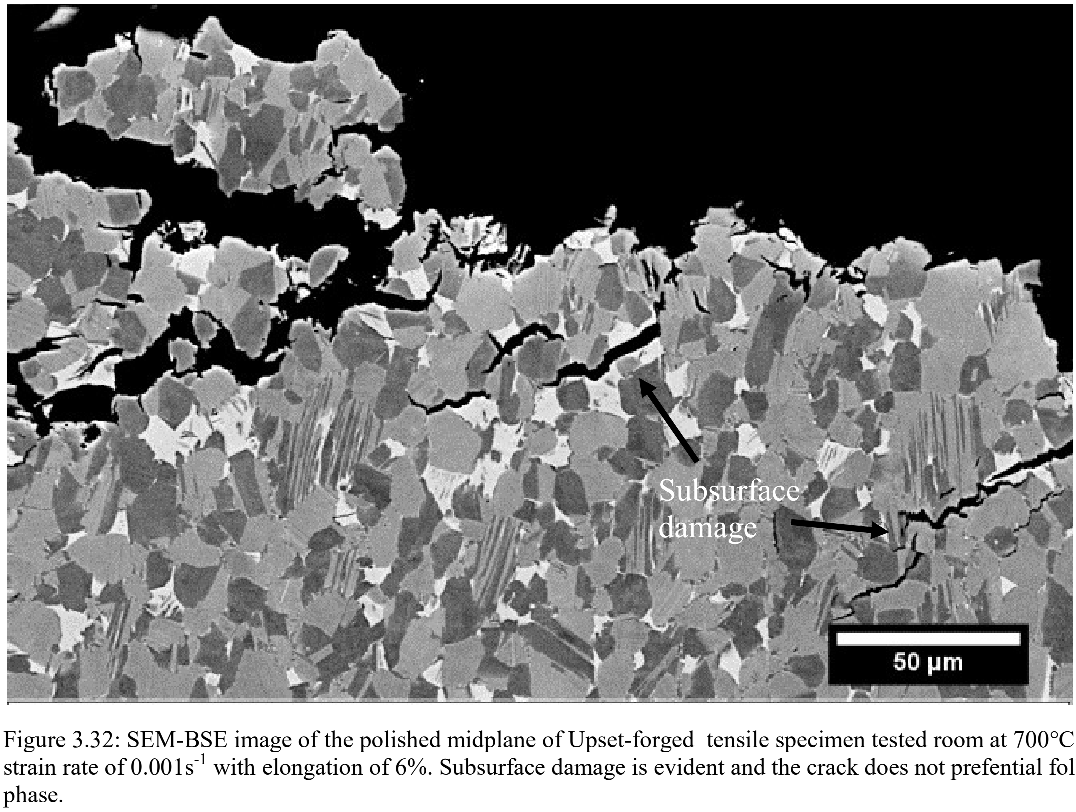

Figure 3.32: SEM-BSE image of the polished midplane of Upset-forged tensile specimen tested room at 700°C at a strain rate of 0.001s^{-1} with elongation of 6%. Subsurface damage is evident and the crack does not prefential follow a phase.

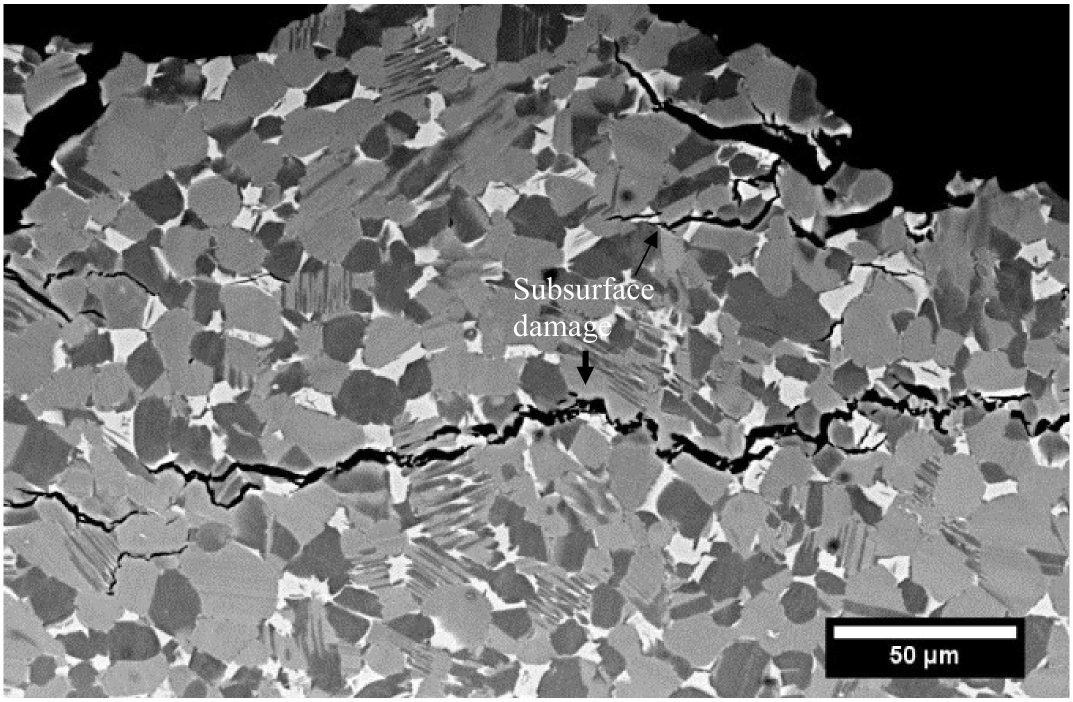

Figure 3.33: SEM-BSE image of the polished midplane of sidepress- forged tensile specimens tested in the transverse direction at 300°C at a strain rate of $0.001 s^{-1}$ with 3% elongation. Sub-surface damage was evident, but the crack does not preferential follow a phase.

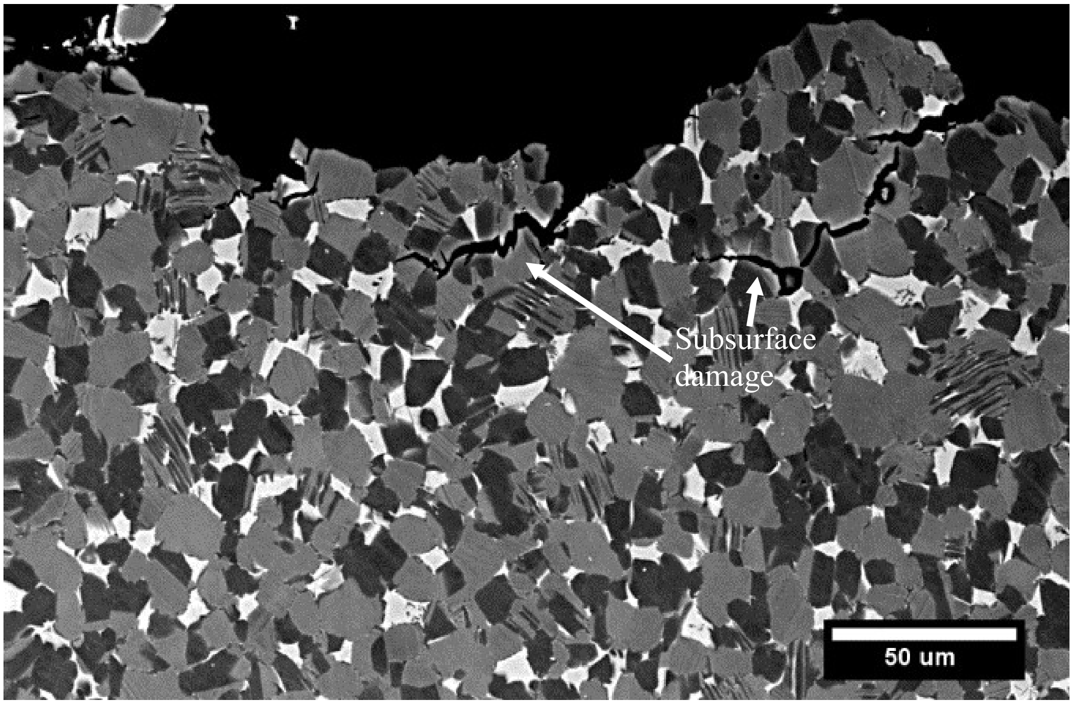

Figure 3.34: SEM-BSE image of the polished midplane of sidepress-forged tensile specimens tested in the transverse direction at 700°C at a strain rate of $0.001 s^{-1}$ with elongation of 6%. Sub-surface damage was evident. No preferential cracking is seen

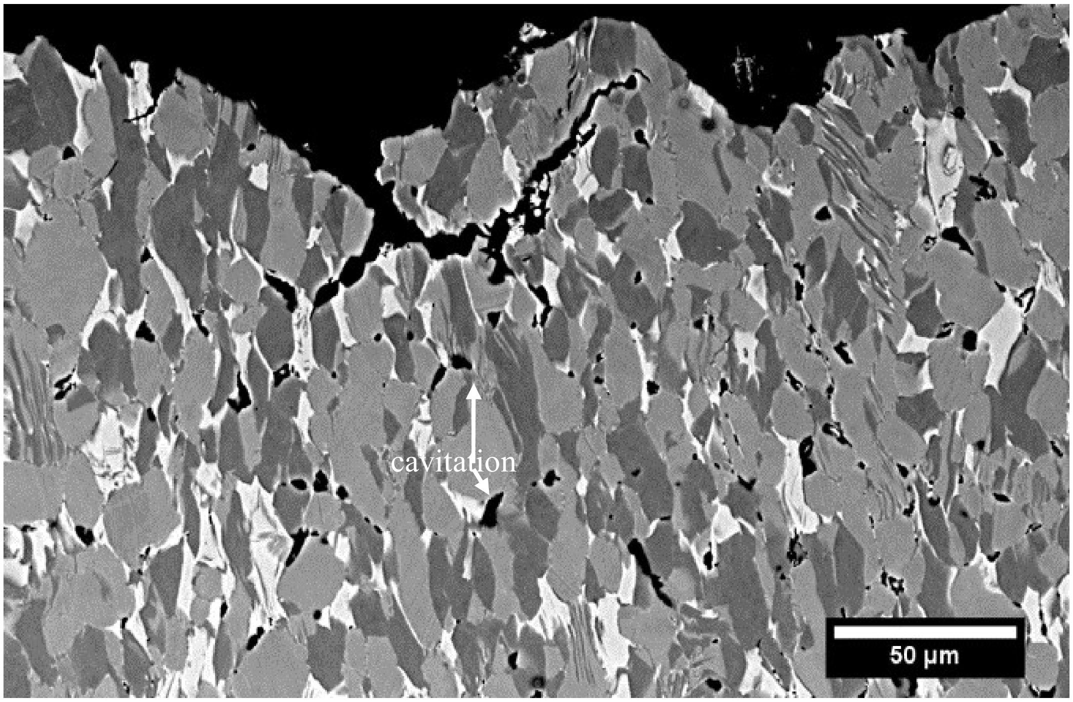

Figure 3.35: SEM-BSE image of the polished midplane of sidepress-forged tensile specimens tested in the transverse direction. Specimens were tested at 750°C at a strain rate of $0.001s^{-1}$ Sub-surface damage was evident with cavitation.

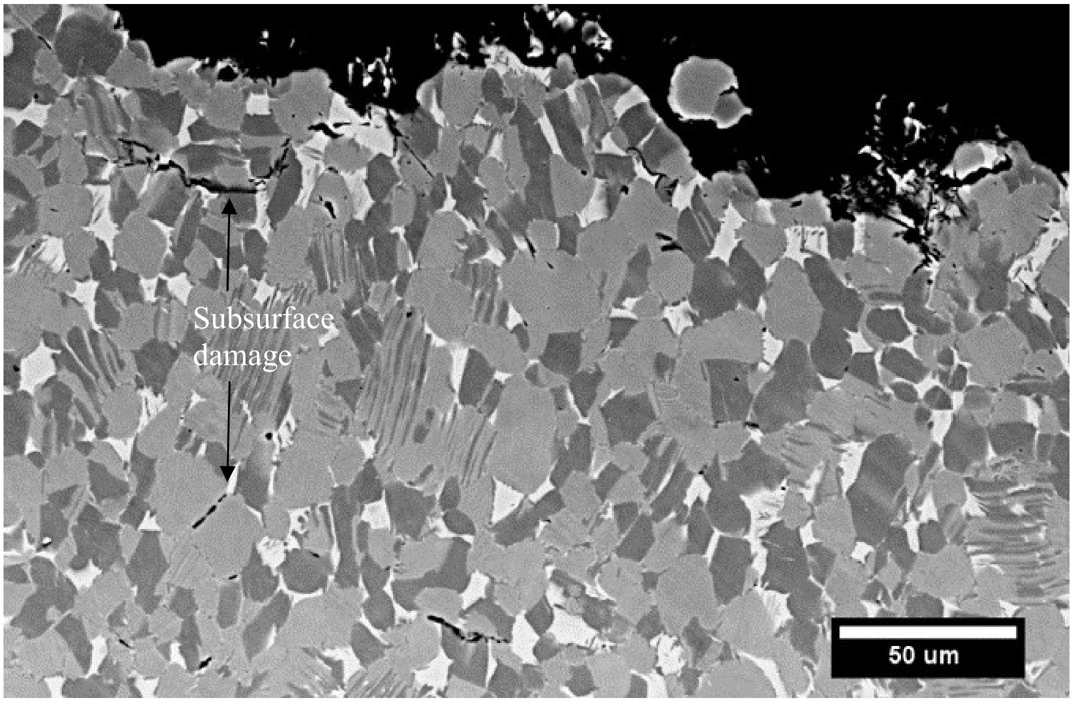

Figure 3.36: SEM-BSE image of the polished midplane of sidepress-forged tensile specimens tested in the transverse direction. Specimens were tested at 800°C at a strain rate of $0.001s^{-1}$. Sub-surface damage was evident.

.

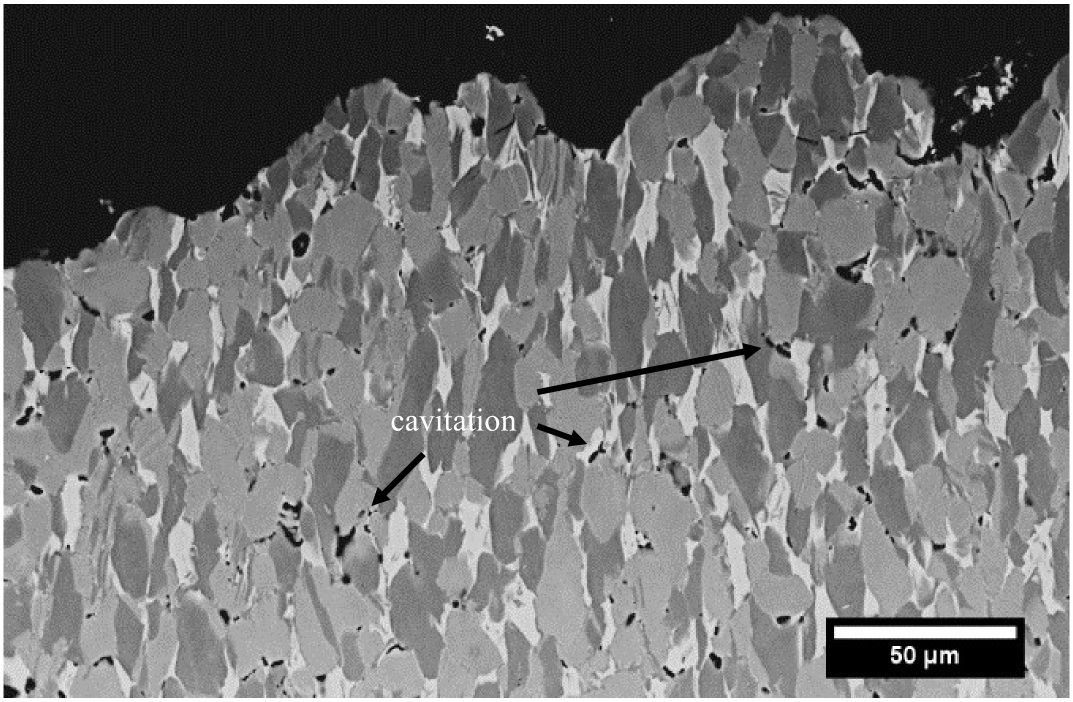

Figure 3.37: SEM-BSE image of the polished midplane of sidepress-forged tensile specimens tested in the longitudinal direction. Specimens were tested at 750°C at a strain rate of $0.001s^{-1}$ Sub-surface damage was evident.

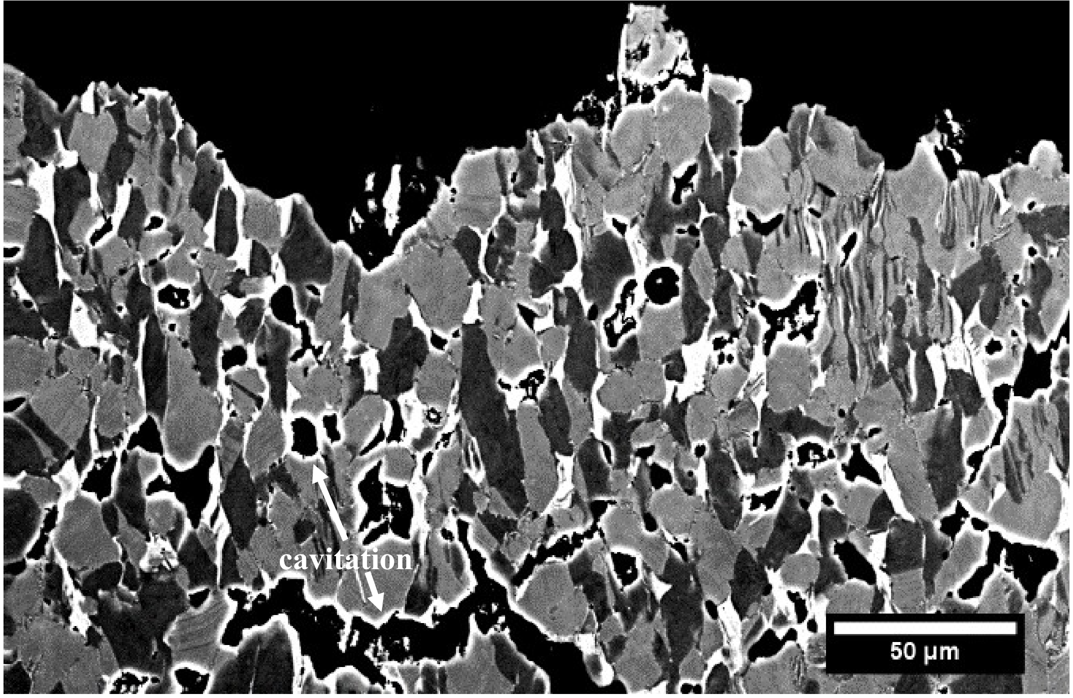

Figure 3.38: SEM-BSE image of the polished midplane of sidepress-forged tensile specimens tested in the longitudinal direction. Specimens were tested at 800°C at a strain rate of $0.001s^{-1}$. Sub-surface damage was evident as well as extensive cavitation.

3.5.2 X-Ray Diffraction of Tensile Specimen Fracture Surfaces

X-Ray diffraction (XRD) results for the as-cast fractured sample are shown in Figure 3.39. The phases that correspond with each peak are noted on the image while Table 3.6 shows the phase fractions calculated from the integrated areas for each peak.

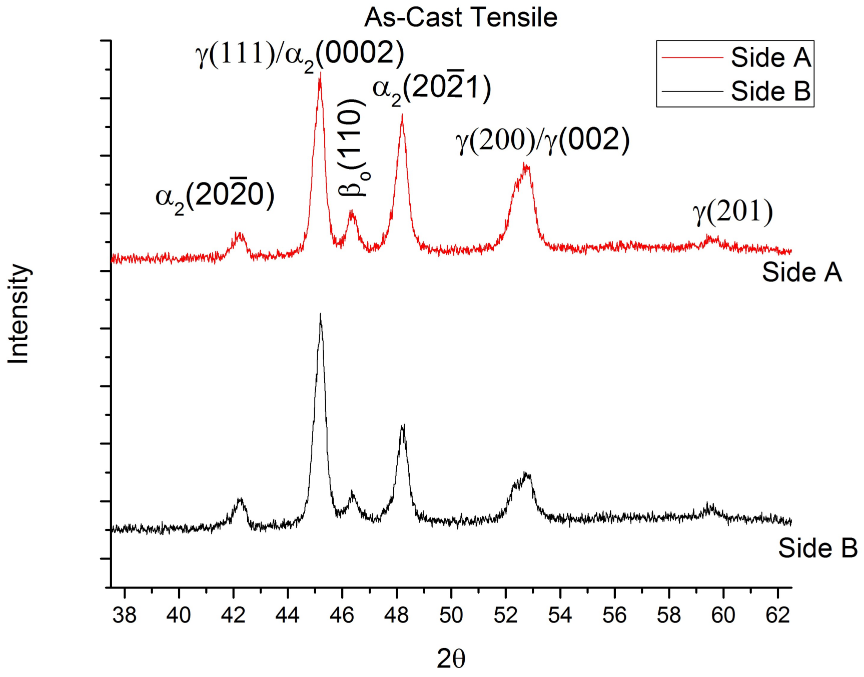

(a)

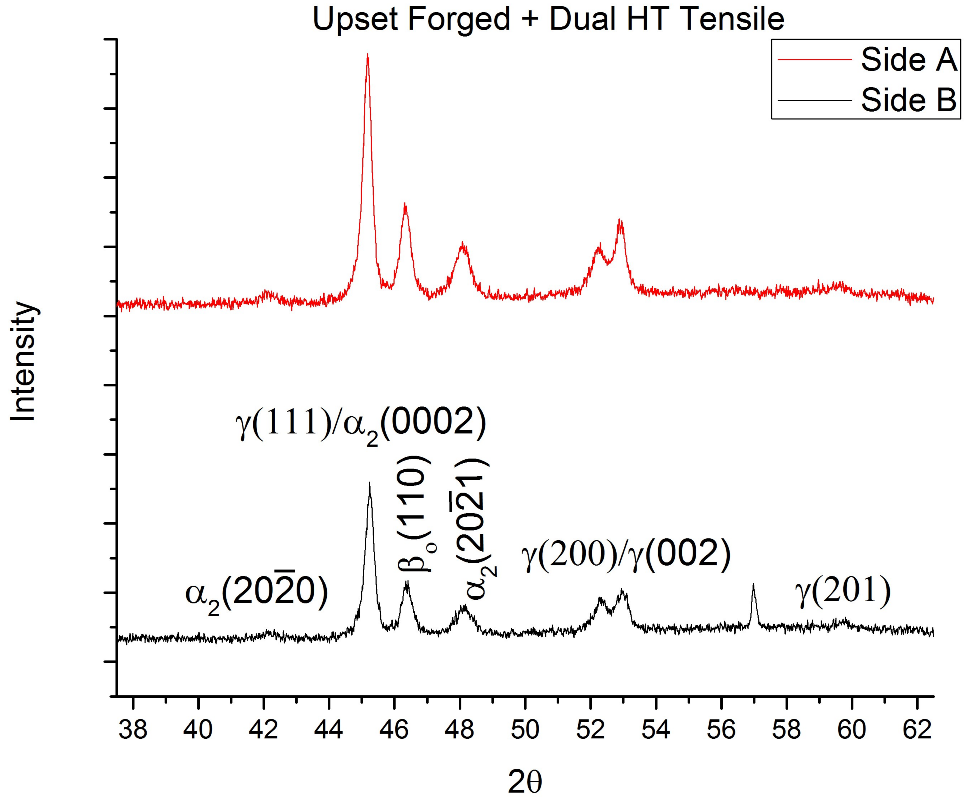

(b)

Figure 3.39: X-Ray diffraction spectrum of fracture surface of (a) as-cast tensile specimens (b) Upset-forged + Dual HT

Table 3.6: Phase fractions present on the fracture surface of tensile specimen determined using the integrated intensity of peaks.

As-Cast	**Phase fraction (volume %)**
α_2	54,51
β_o	7,5
γ	38,43
HIPed	
α_2	32,41
β_o	12,9
γ	55,49
Upset Forged	
α_2	33,36
β_0	17,17
γ	49,46

3.5.3 SEM of Fatigue Crack Growth Fracture Surfaces

SEM analyses of the fracture surfaces were performed and fatigue striations were not evident. In order to systematically study the fractographic observations, specific regions of the fracture surface were examined. Using the dcPD fatigue data, each image was linked to a specific K_{max} value in order to enable comparison of different samples at similar levels of stress intensity. All SEM images that follow are oriented such that crack growth occurs from the top to the bottom of the image. Figures 3.40 to 3.59 show representative images of the L-T and T-L samples from as-cast and as-cast + HIPed, in addition to images from T-L upset-forged and sidepress-forged samples. The fracture surfaces exhibit brittle faceted features resembling cleavage fracture in addition to lamellar regions. In general, the fracture surface features in all orientations and processing conditions show predominantly brittle failure with only small amounts of local plastic deformation.

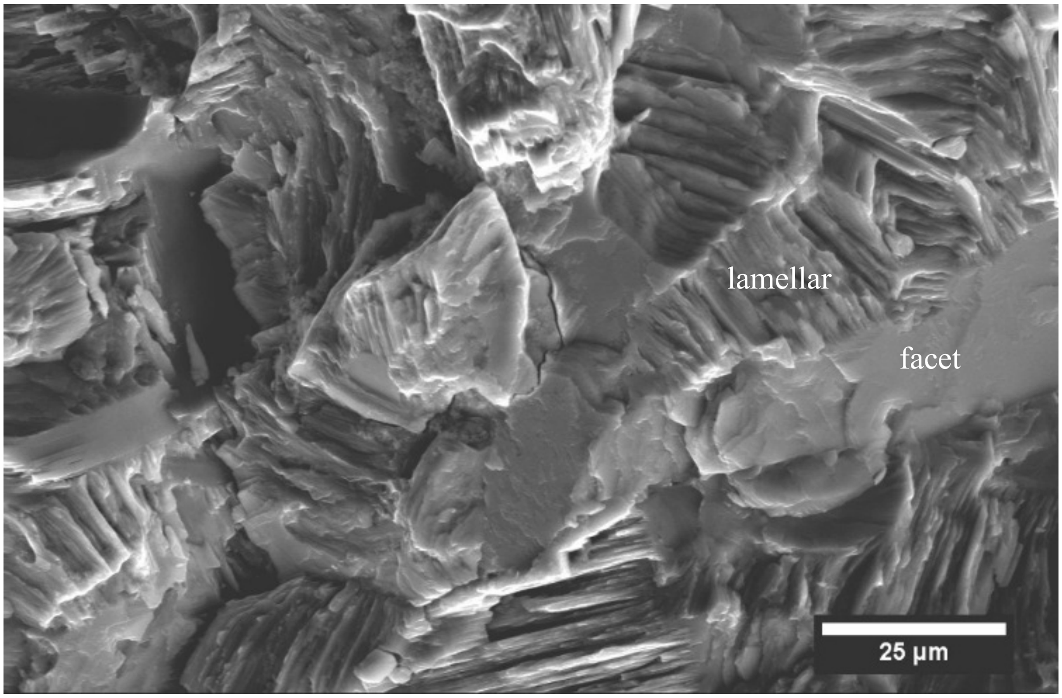

Figure 3.40: SEM-SE fractography of As-cast (L-T) fatigue fracture features in the low ΔK regime at $R = 0.3$. Crack direction is from top to bottom. The fracture surface show facets and lamellar microstructure.

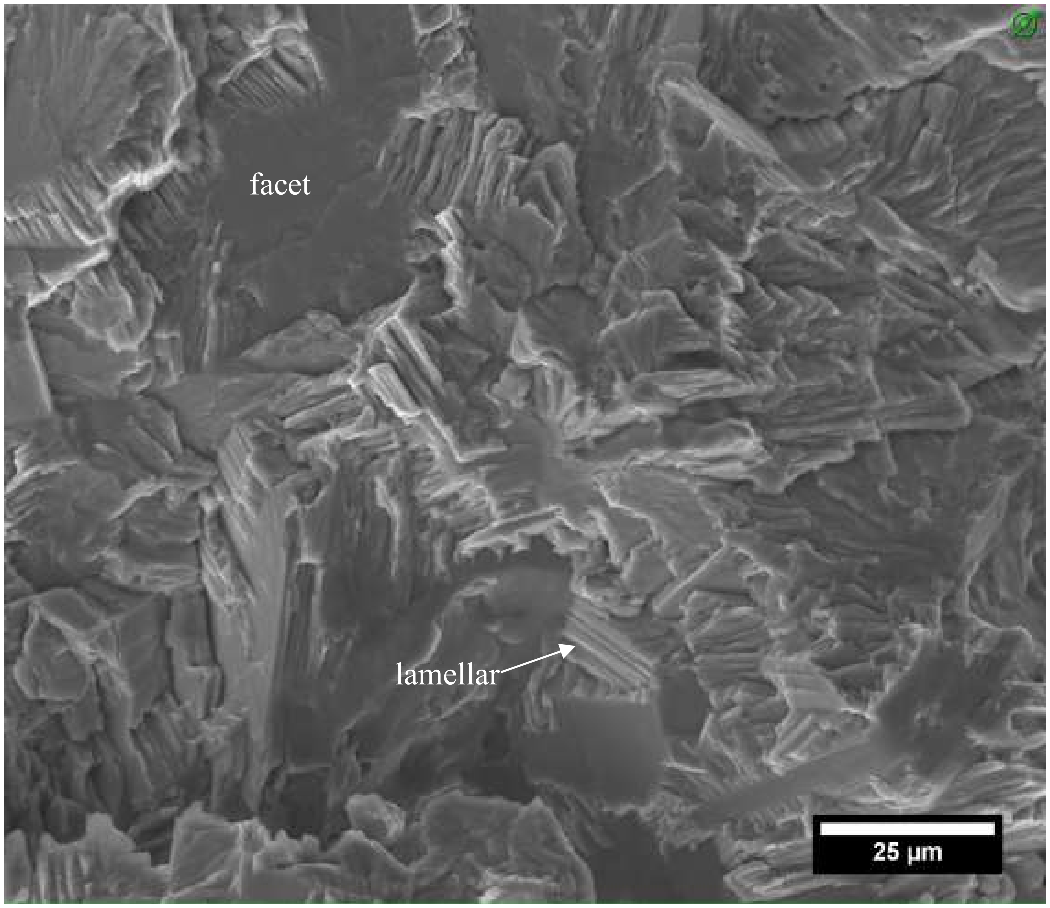

Figure 3.41: SEM-SE fractography of As-cast (T-L) fatigue fracture features in the low ΔK regime at R = 0.3. Crack direction is from top to bottom. The fracture surface shows facets and lamellar features.

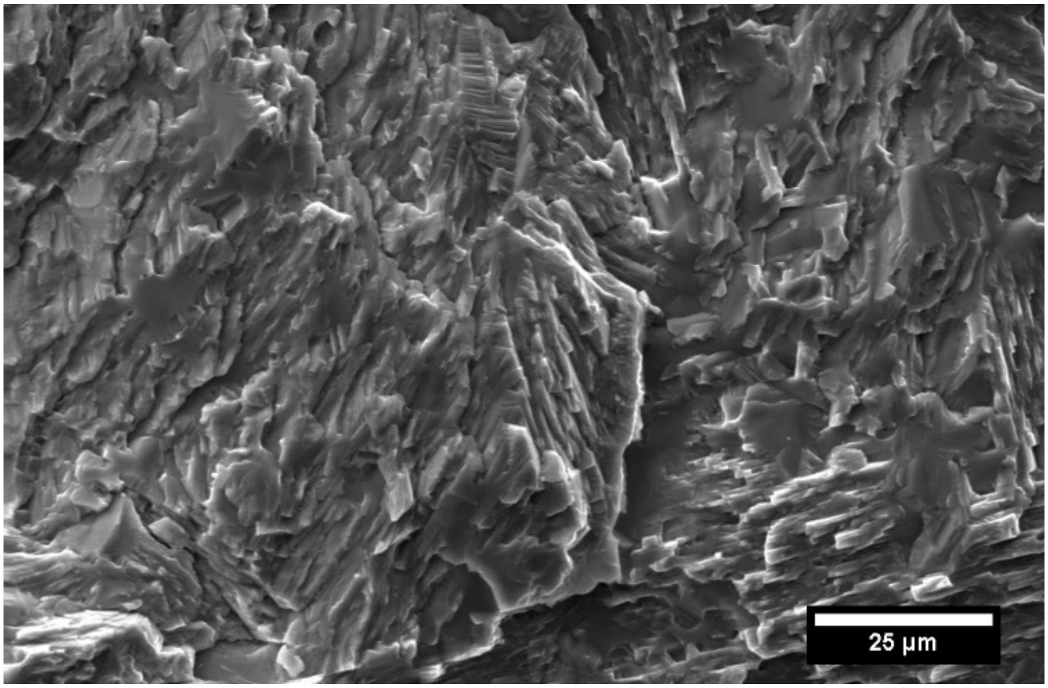

Figure 3.42: SEM-SE fractography of As-cast + HIP (L-T) fatigue fracture features in the low ΔK regime at R = 0.3. Crack direction is from top to bottom.

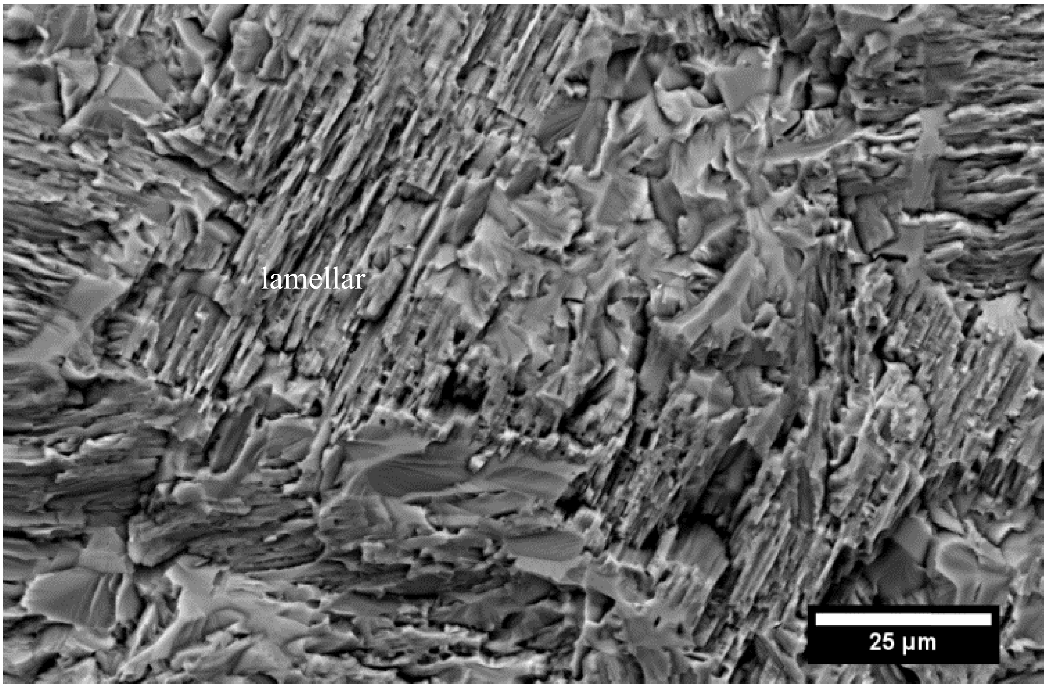

Figure 3.43: SEM-SE fractography of As-cast + HIP (T-L) fatigue fracture features in the low ΔK regime at R = 0.3. Crack direction is from top to bottom. The fracture surface show lamellar microstructure features.

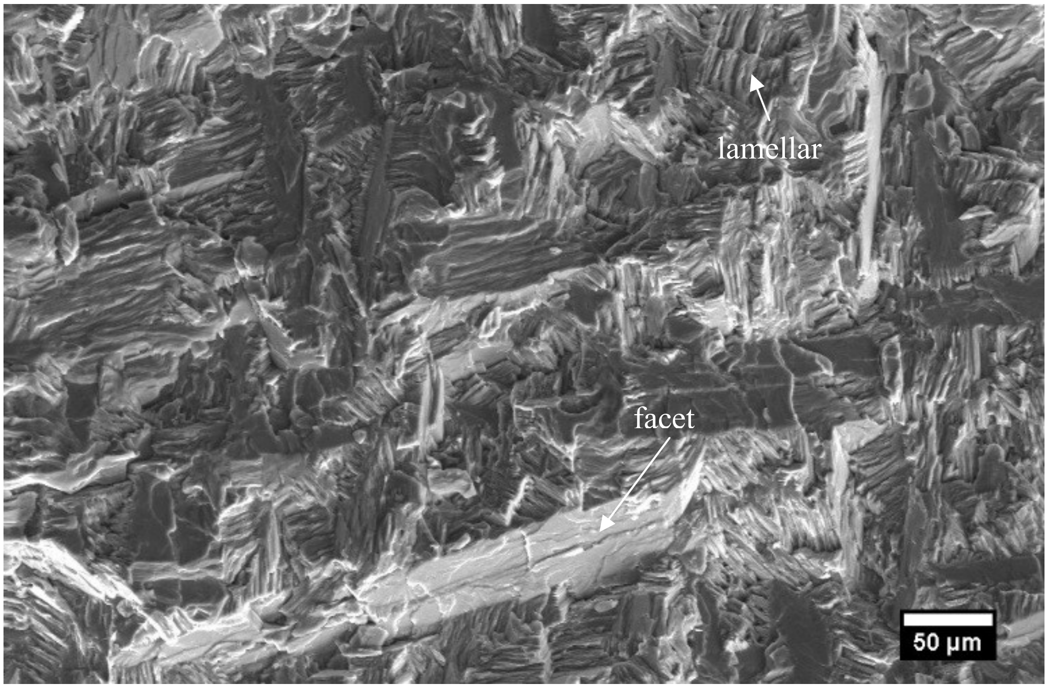

Figure 3.44: SEM-SE fractography of As-cast (L-T) fatigue fracture features in the high ΔK regime at R = 0.3. Crack direction is from top to bottom.

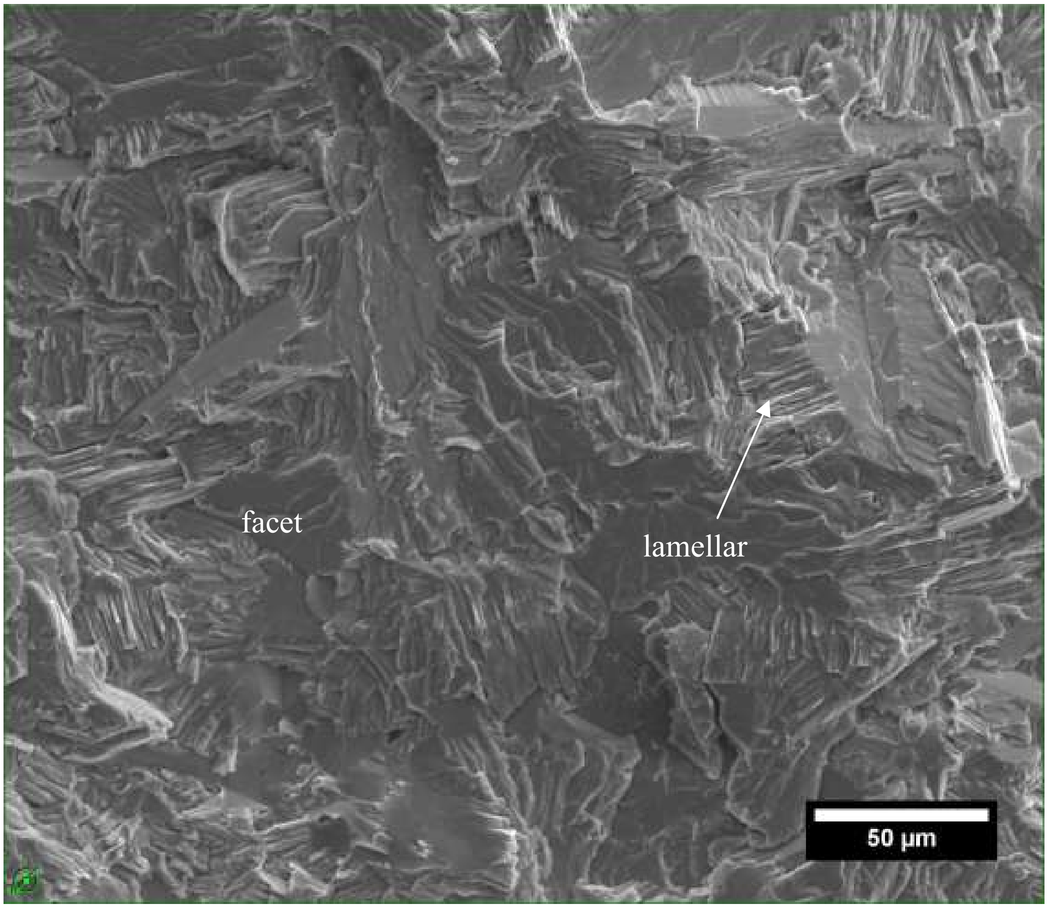

Figure 3.45: SEM-SE fractography of As-cast (T-L) fatigue fracture features in the high ΔK regime at R = 0.3. Crack direction is from top to bottom.

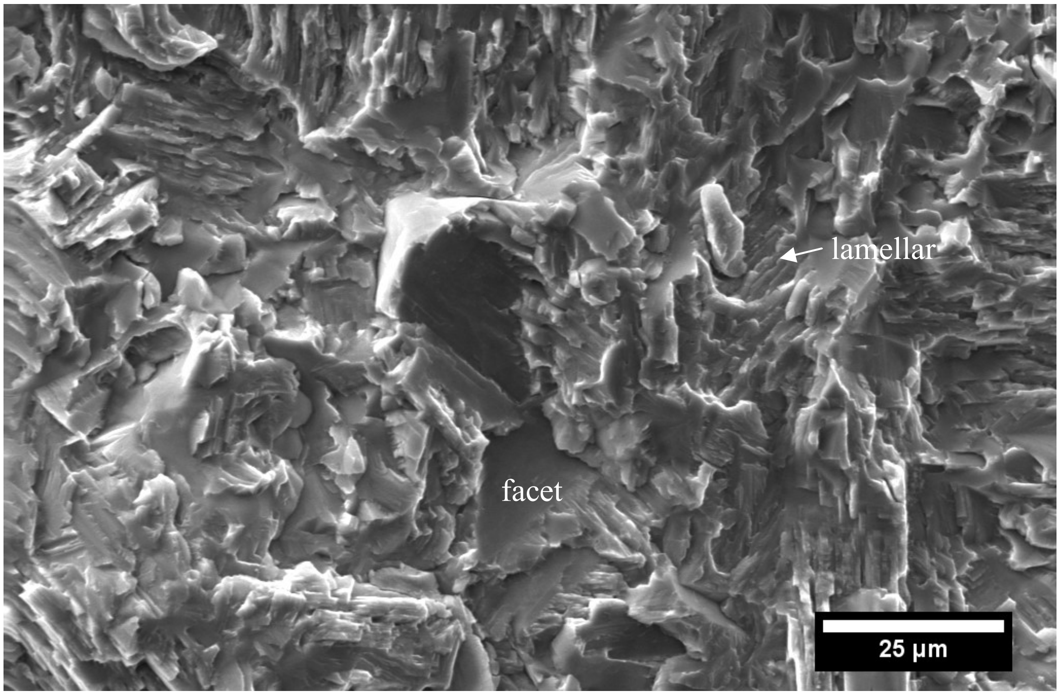

Figure 3.46: SEM-SE fractography of As-cast + HIP (L-T) fatigue fracture features in the high ΔK regime at R = 0.3. Crack direction is from top to bottom.

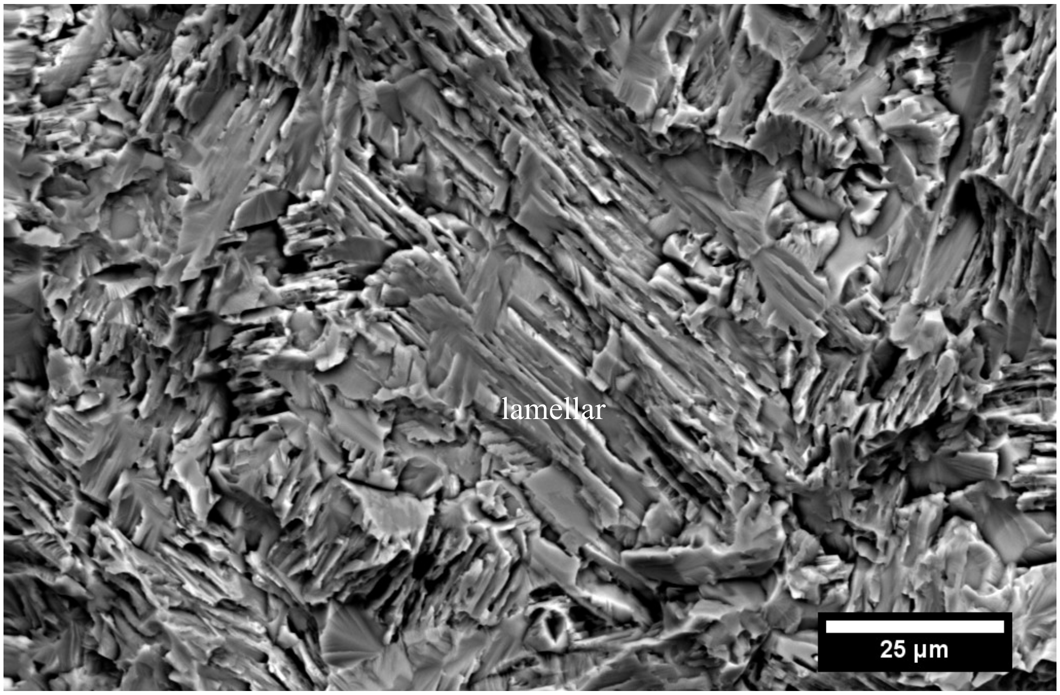

Figure 3.47: SEM-SE fractography of As-cast + HIP (T-L) fatigue fracture features in the high ΔK regime at R = 0.3. Crack direction is from top to bottom.

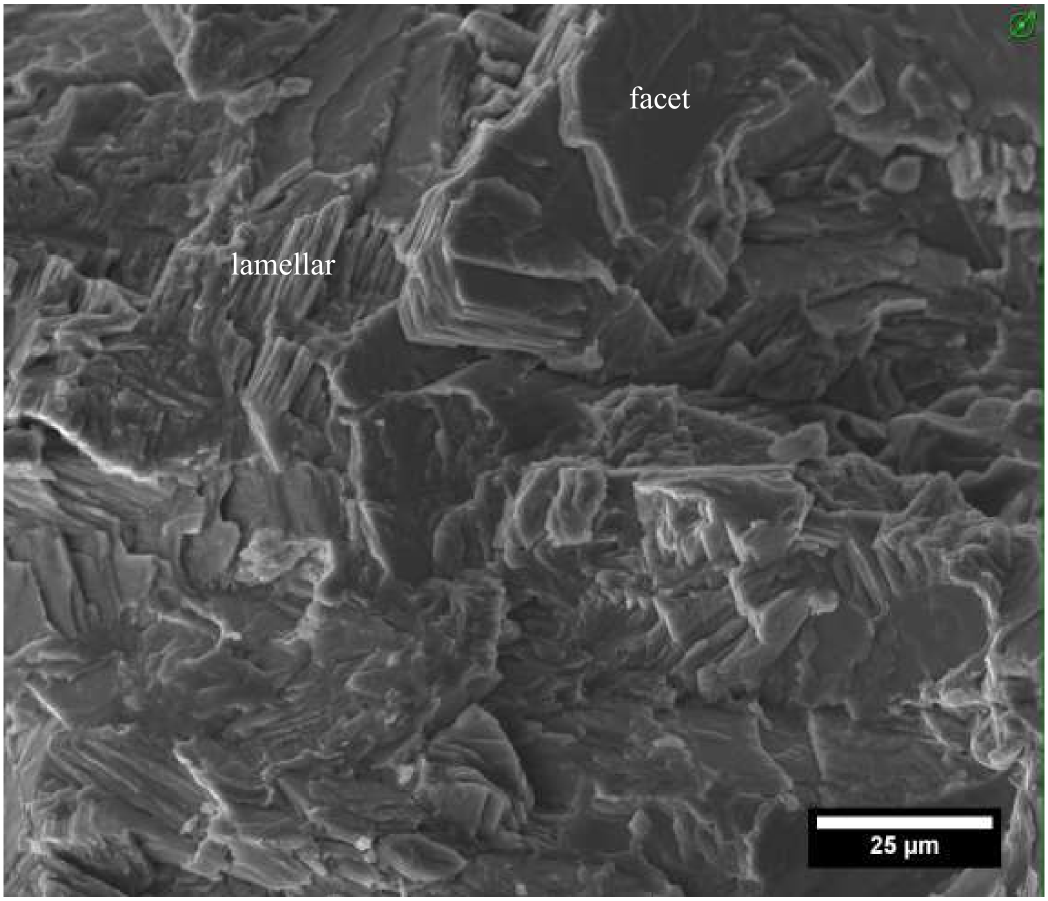

Figure 3.48: SEM-SE fractography of As-cast (L-T) fatigue fracture features in the overload regime at R = 0.1. Crack direction is from top to bottom. The fracture surface shows large facets and lamellar microstructure.

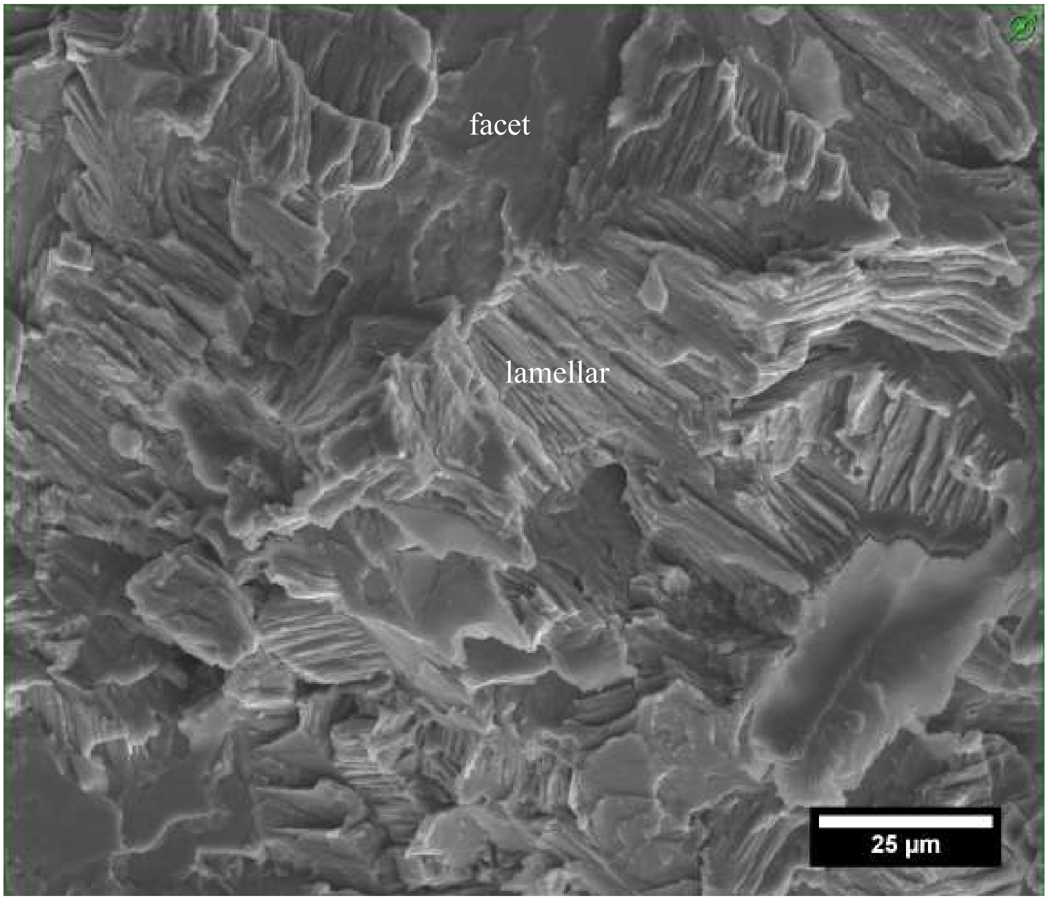

Figure 3.49: SEM-SE fractography of As-Cast (T-L) fatigue fracture features in the overload regime at R = 0.1. Crack direction is from top to bottom. The fracture surfaces shows factes and lamellar microstructure.

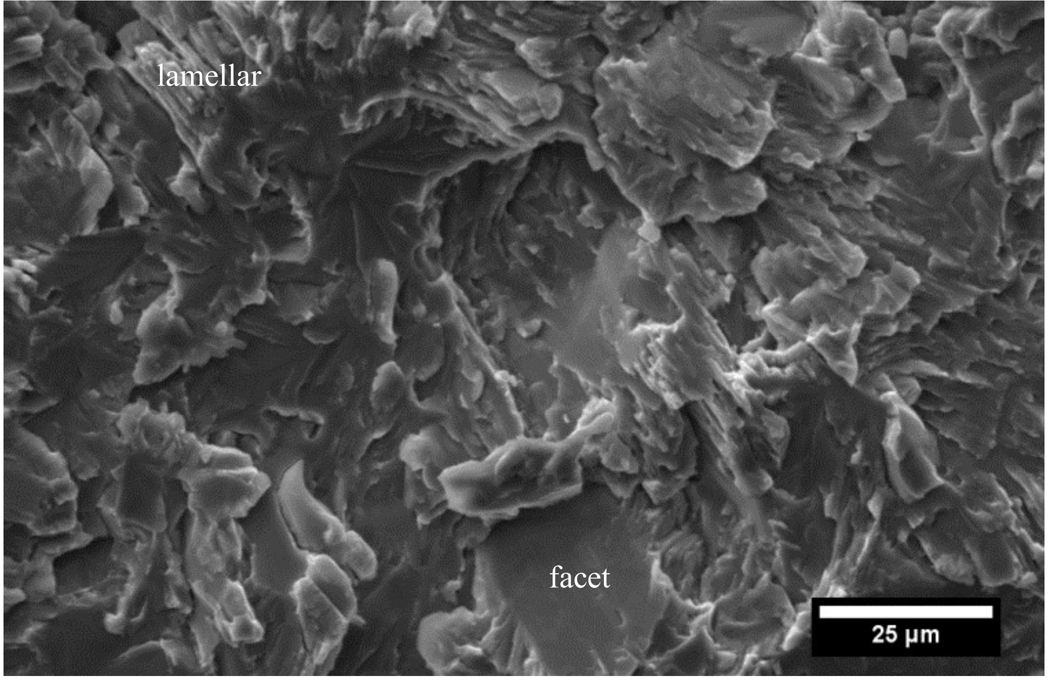

Figure 3.50: SEM-SE fractography of As-cast + HIPed (L-T) fatigue fracture features in the overload regime at R = 0.1. Crack direction is from top to bottom.

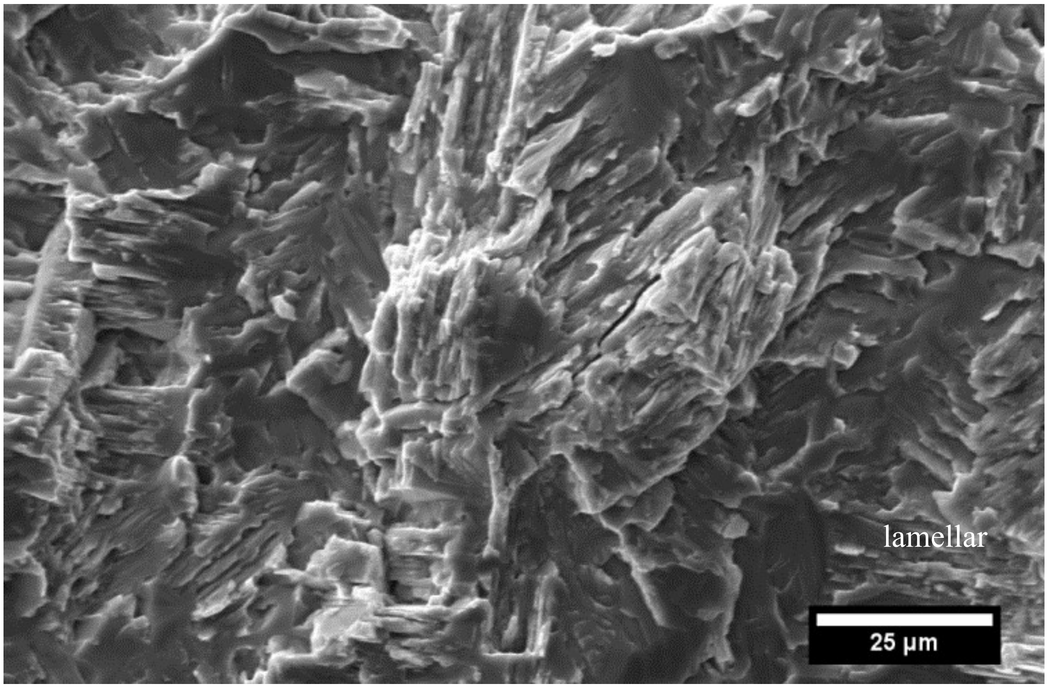

Figure 3.51: SEM-SE fractography of As-cast + HIPed (T-L) fatigue fracture features in the overload regime at R = 0.1. Crack direction is from top to bottom.

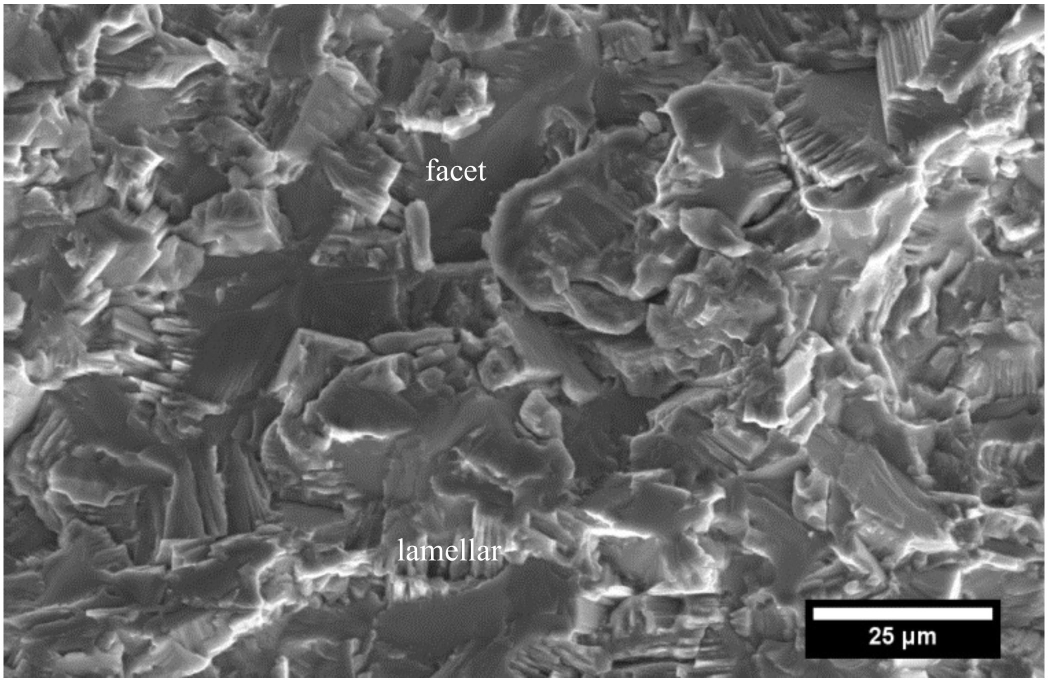

Figure 3.52: SEM-SE fractography of Upset-forged fatigue fracture features in the low ΔK regime at R = 0.1. Crack direction is from top to bottom.

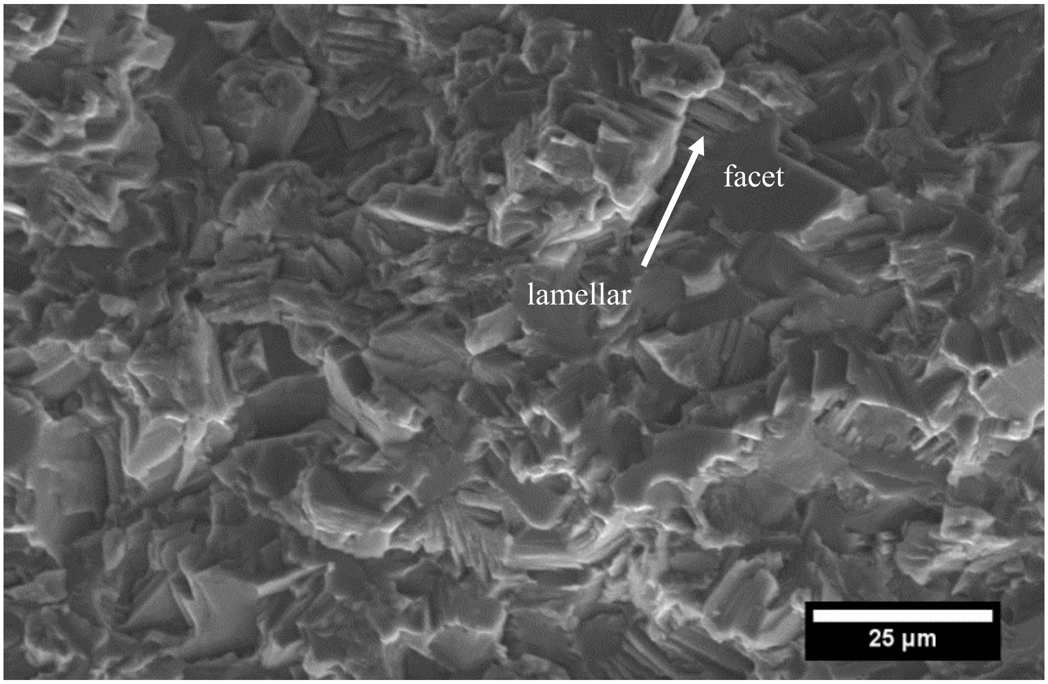

Figure 3.53: SEM-SE fractography of Upset-forged fatigue fracture features in the high ΔK regime at R = 0.1. Crack direction is from top to bottom.

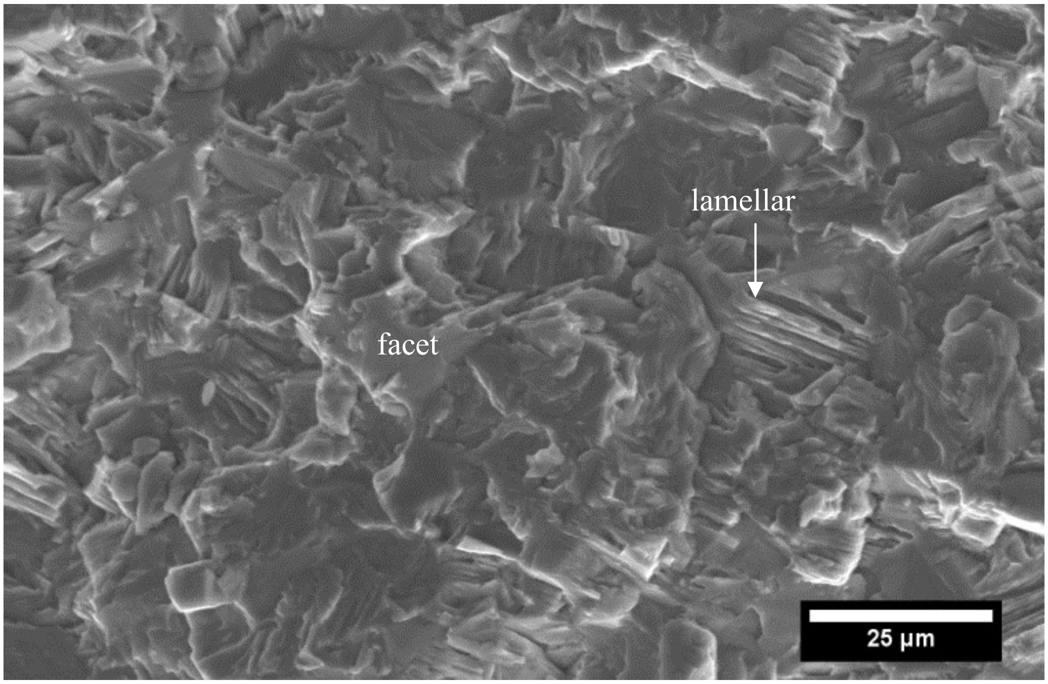

Figure 3.54: SEM-SE fractography of Sidepress-forged fatigue fracture features in the low ΔK regime at R = 0.1. Crack direction is from top to bottom.

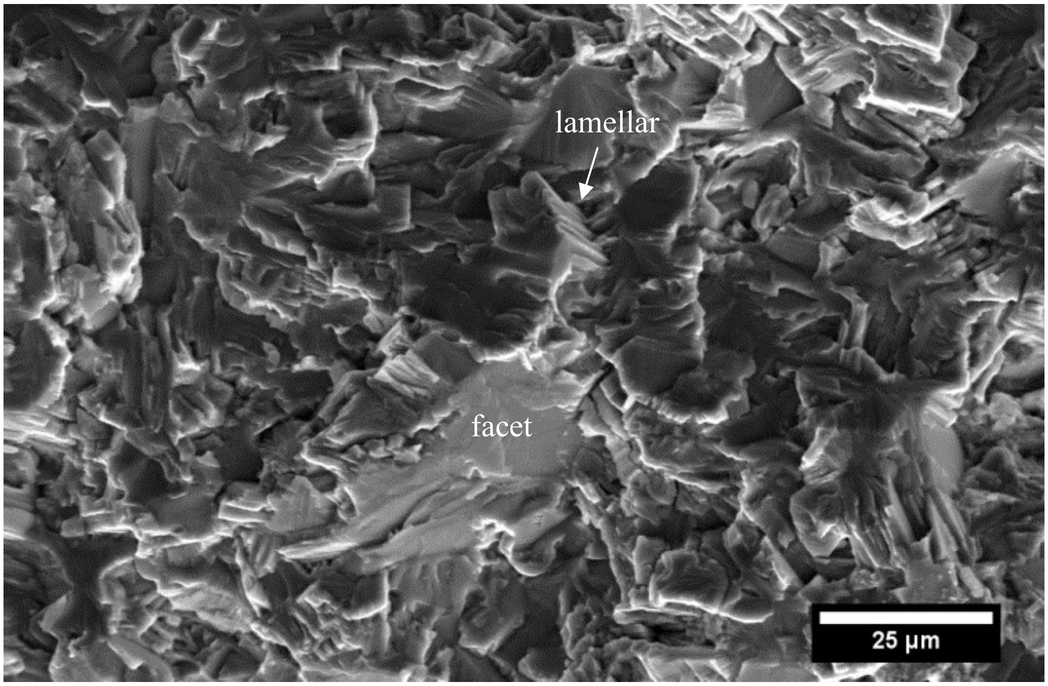

Figure 3.55: SEM-SE fractography of Sidepress-forged fatigue fracture features in the high ΔK regime at R = 0.1. Crack direction is from top to bottom.

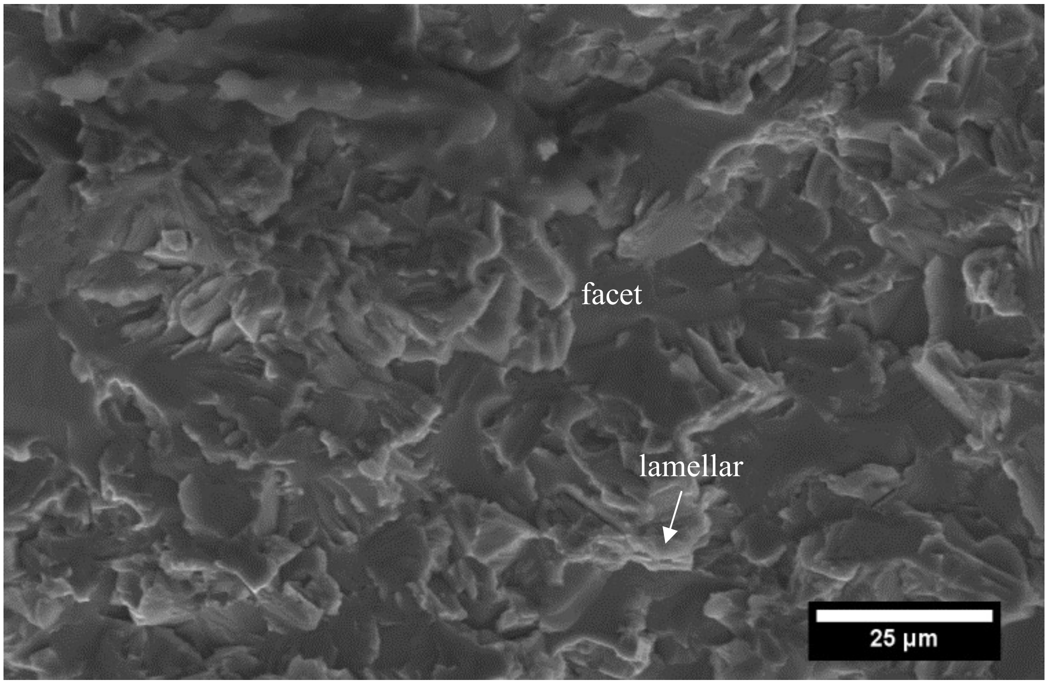

Figure 3.56: SEM-SE fractography of Upsest-forged fatigue fracture features in the low ΔK regime at R = 0.7. Crack direction is from top to bottom.

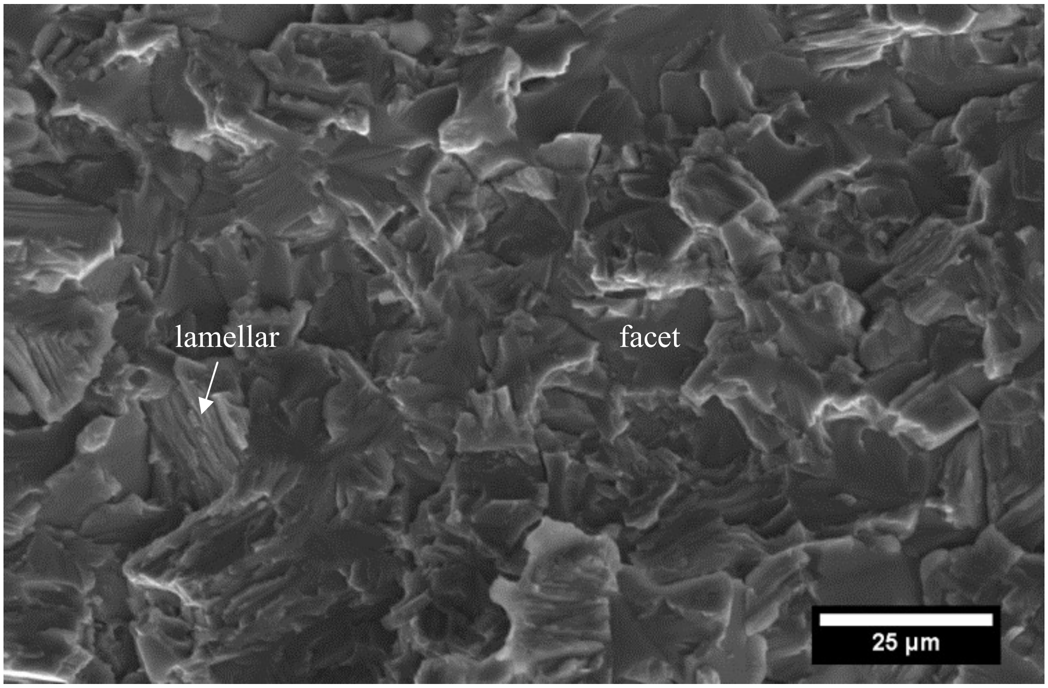

Figure 3.57: SEM-SE fractography of Upsest-forged fatigue fracture features in the high ΔK regime at R = 0.7. Crack direction is from top to bottom.

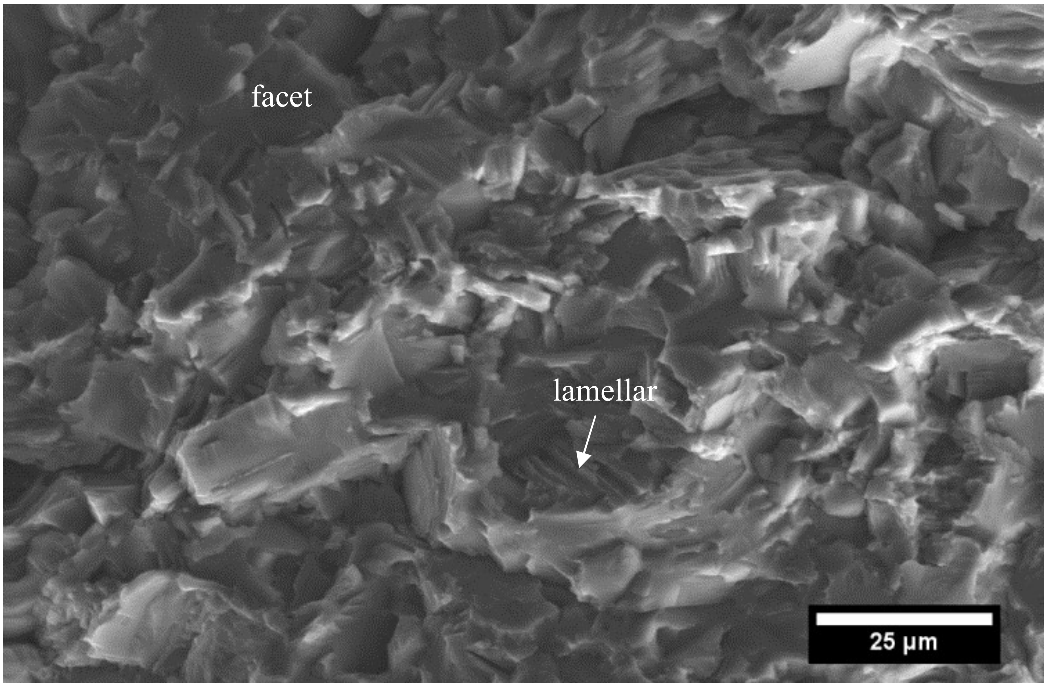

Figure 3.58: SEM-SE fractography of Sidepress-forged fatigue fracture features in the low ΔK regime at R = 0.7. Crack direction is from top to bottom.

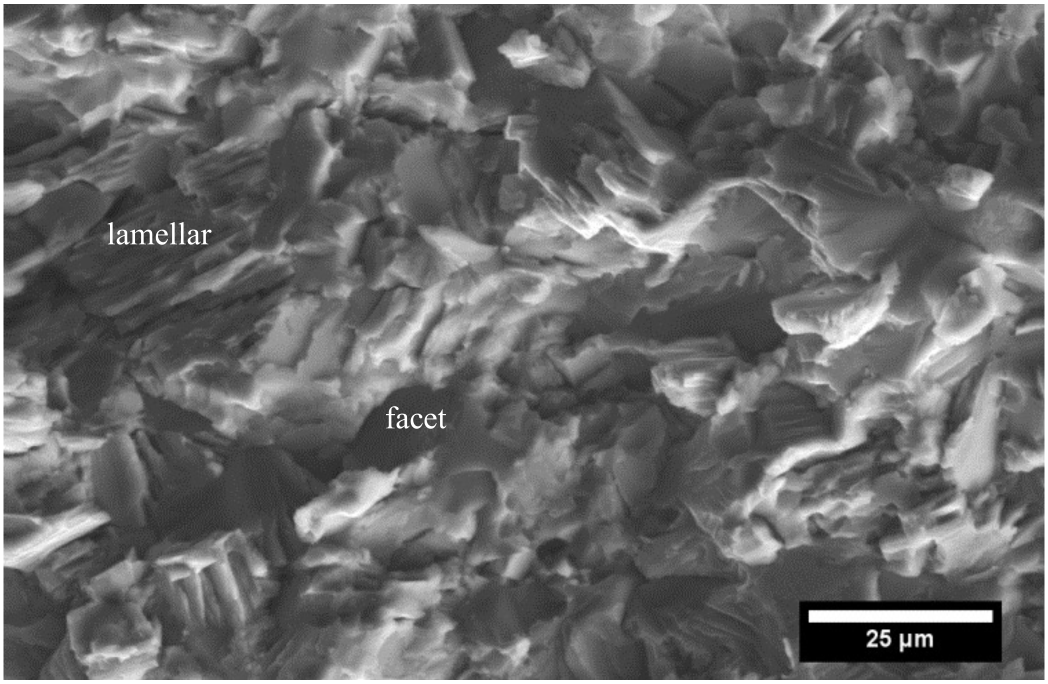

Figure 3.59: SEM-SE fractography of Sidepress-forged fatigue fracture features in the high ΔK regime at R = 0.7. Crack direction is from top to bottom.

3.5.4 X-Ray Diffraction of Fatigue Crack Growth Fracture Surfaces

X-Ray diffraction (XRD) conducted on both sides of the fatigue fracture surfaces, in addition to conducting XRD along polished samples taken from along the casting direction. The resulting fracture surface XRD scans for as-cast, upset-forged, and sidepress-forged samples are shown in Figures 3.60 to 3.65. The phases that correspond with each peak are noted on each of the images, while the phase fractions present were determined using the integrated intensity of each peak, summarized in Table 3.7.

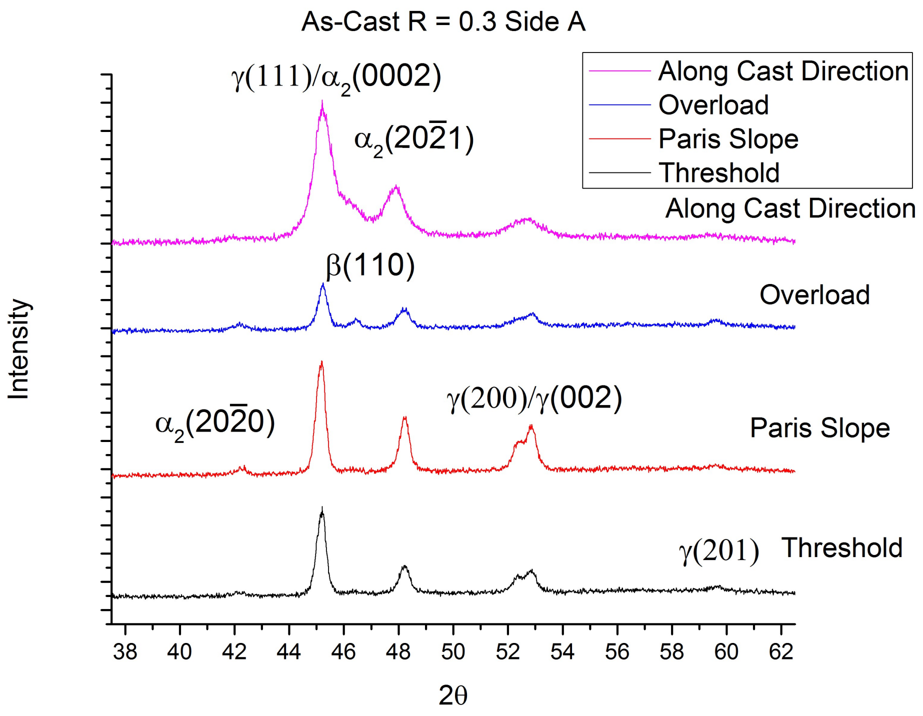

Figure 3.60: X-Ray diffraction results from Side A at different regions of the fatigue fracture surface of an as-cast L-T specimen fatigued at R = 0 .3.

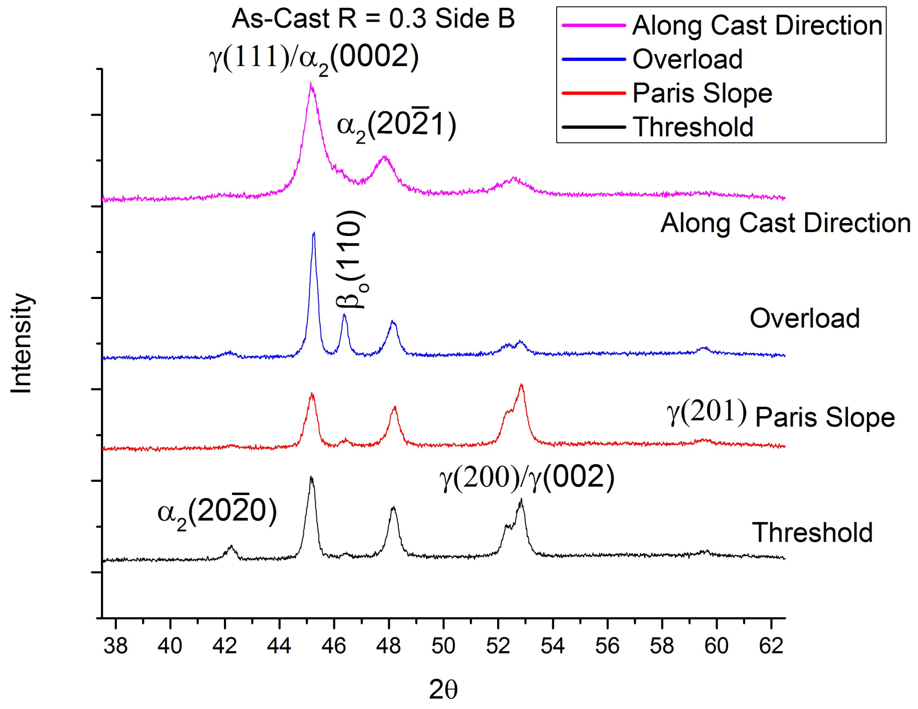

Figure 3.61: X-Ray diffraction results from Side B at different regions of the fatigue fracture surface of an as-cast L-T specimen fatigued at R = 0 .3.

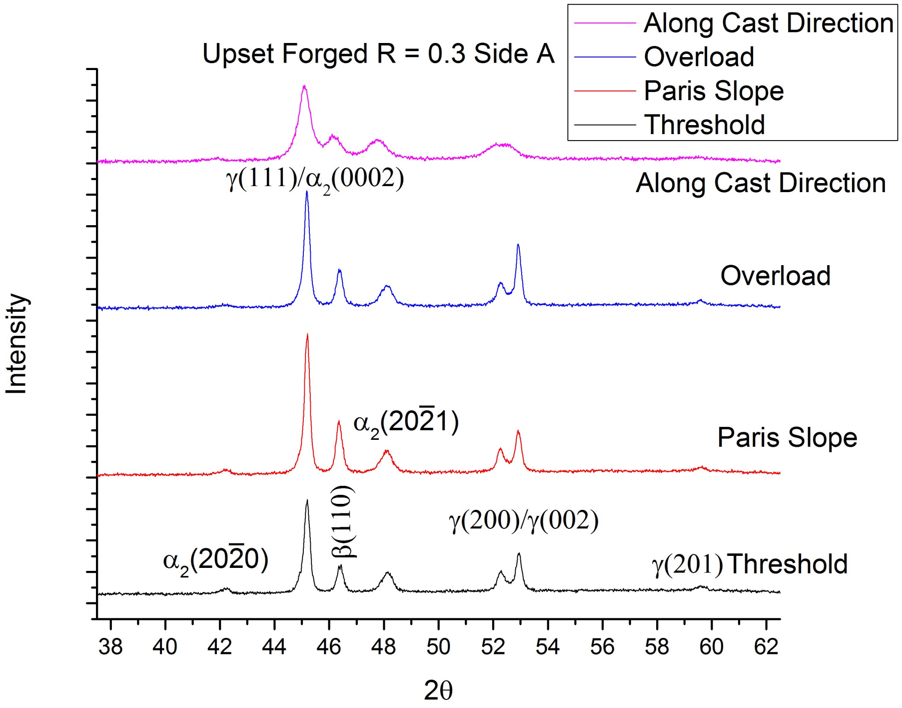

Figure 3.62: X-Ray diffraction results from Side A at different regions of the fatigue fracture surface of an upset-forged sample fatigued at R = 0 .3.

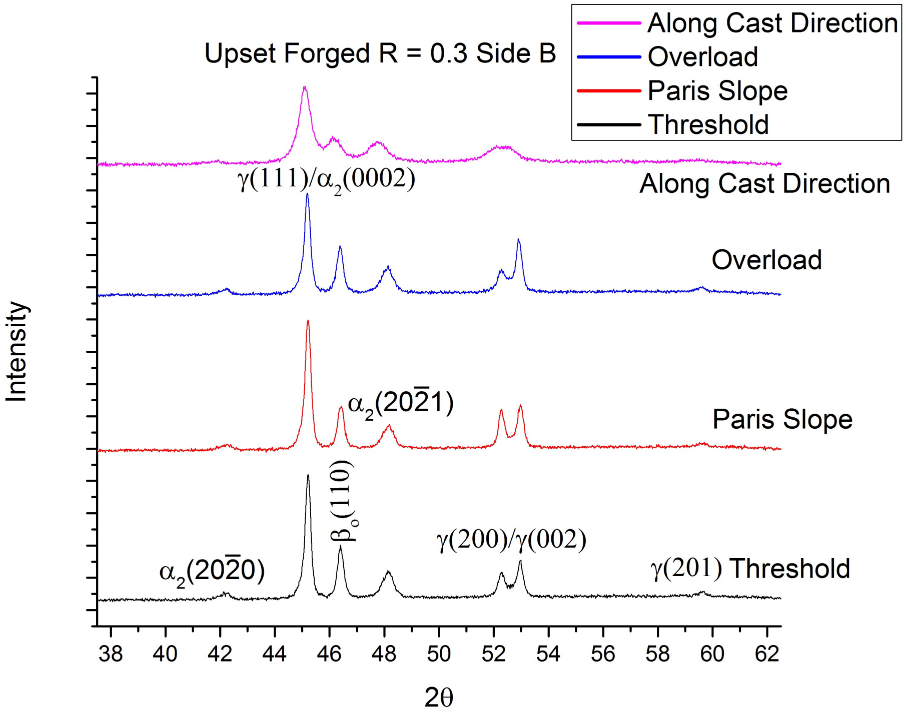

Figure 3.63: X-Ray diffraction results from Side B at different regions of the fatigue fracture surface of an upset-forged sample fatigued at R = 0 .3.

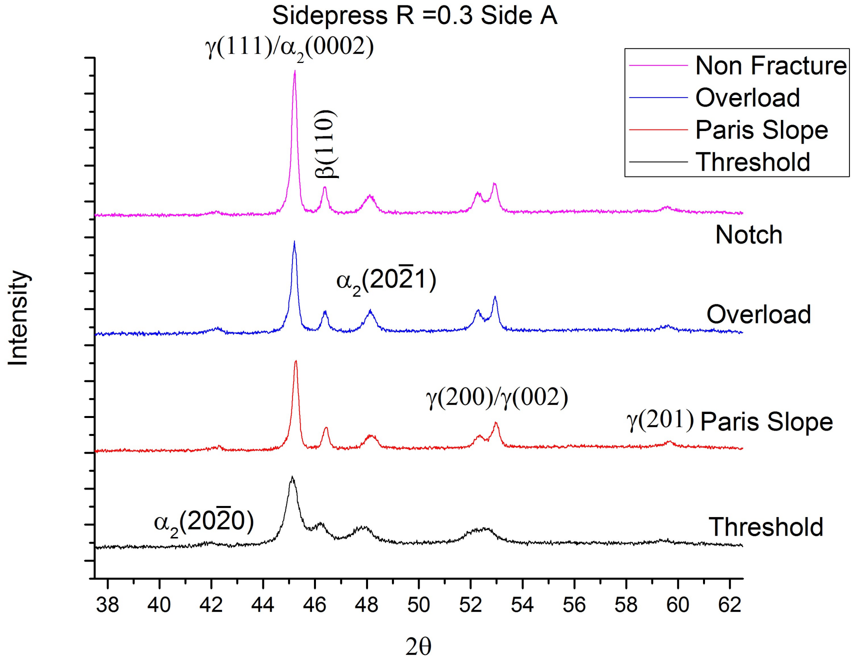

Figure 3.64: X-Ray diffraction results from Side A of sidepressed-forged at different regions of the fatigue fracture fatigued at R = 0 .3.

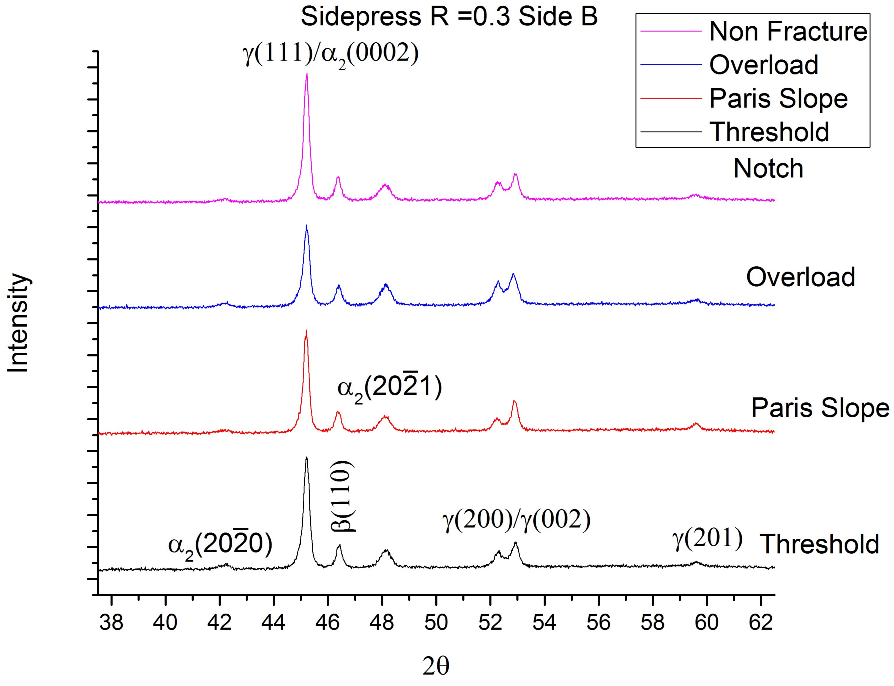

Figure 3.65: X-Ray diffraction results from Side B of sidepressed-forged at different regions of the fatigue fracture surface at R = 0 .3

Table 3.7: Phase fractions of as-cast and upset-forged material from XRD scans using the area under the curve method

Conditions	**Threshold**	**Paris Slope**	**Overload**	**X-Section**
As-Cast	**(Average Vol. %)**	**(Average Vol.%)**	**(Average Vol.%)**	**(Average Vol.%)**
α_2	46	44	49	57
β_o	**0.3**	**2**	**10**	**0**
γ	54	54	40	43
Upset Forged + Dual HT				
α_2	38	38	36	45
β_o	14	15	15	15
γ	48	47	50	40
Sidepress Forged + Dual HT				
α_2	46	42	30	41
β_o	13	9	8	8
γ	41	50	52	51

4. Discussion

The work conducted has examined TNM in the as-cast, cast + HIP, and forged + heat treated conditions. In order to discuss the behavior in a systematic manner and put the work into the proper perspective, the discussion will be presented in two sections.

The first Sections (i.e., 4.1 and 4.2) will discuss the behavior of the as-cast TNM in comparison to second generation as-cast Ti-48Al-2Cr-2Nb. The as-cast Ti48Al-2Cr-2Nb material served as the focus for my master thesis and provides an excellent material for comparison to the as-cast TNM. This approach will also demonstrate the evolution of this class of as-cast materials prior to discussion of the effects of post-processing on TNM. This work has already been published and a reprint of the published paper is provided in the appendix to this PhD thesis.

The second sections (i.e., 4.3 and 4.4) will discuss the behavior of the TNM in all of the conditions examined (i.e., as-cast, as-cast + HIP, upset-forged, sidepress-forged). These are discussed and compared in the second section of the discussion in order to demonstrate the significant effects of post-processing on both microstructure and resulting mechanical behavior. These results have been submitted for publication.

4.1 Comparisons of As-Cast TNM vs. Ti-48Al-2Nb-2Cr

Fatigue crack growth rate curves (da/dN vs ΔK) of as-cast both alloys in both *L-T* and *T-L* directions at $R = 0.1$, 0.3, 0.7, and 0.9 are presented in Figure 4.1. Fatigue threshold ΔK_{th}, Paris slope m, and $K_c = K_{max}$ at overload at various R as well as static notch fracture toughness for both alloys in both orientations are summarized in Figure

4.2. Both alloys exhibited decreasing ΔK_{th} with increasing R, Figure 4.2 and Table 4.1. The influence of orientation on ΔK_{th} was more pronounced in TNM (compared to 4822), as evidenced by the rapid drop in ΔK_{th} with increasing R, and the absolute ΔK_{th} values at equivalent R were lower (Figure 4.2 and Table 4.1). The ΔK_{th} at $R = 0.9$ for 4822 is significantly lower than that obtained at lower R, while increasing R shifted all of the da/dN-ΔK curves to the left. Paris slopes for both alloys in both orientations increased dramatically, from 9 at $R = 0.1$ to nearly 100 at $R = 0.9$. The K_c at failure in fatigue was not significantly affected by R, as seen in Figure 4.2c.

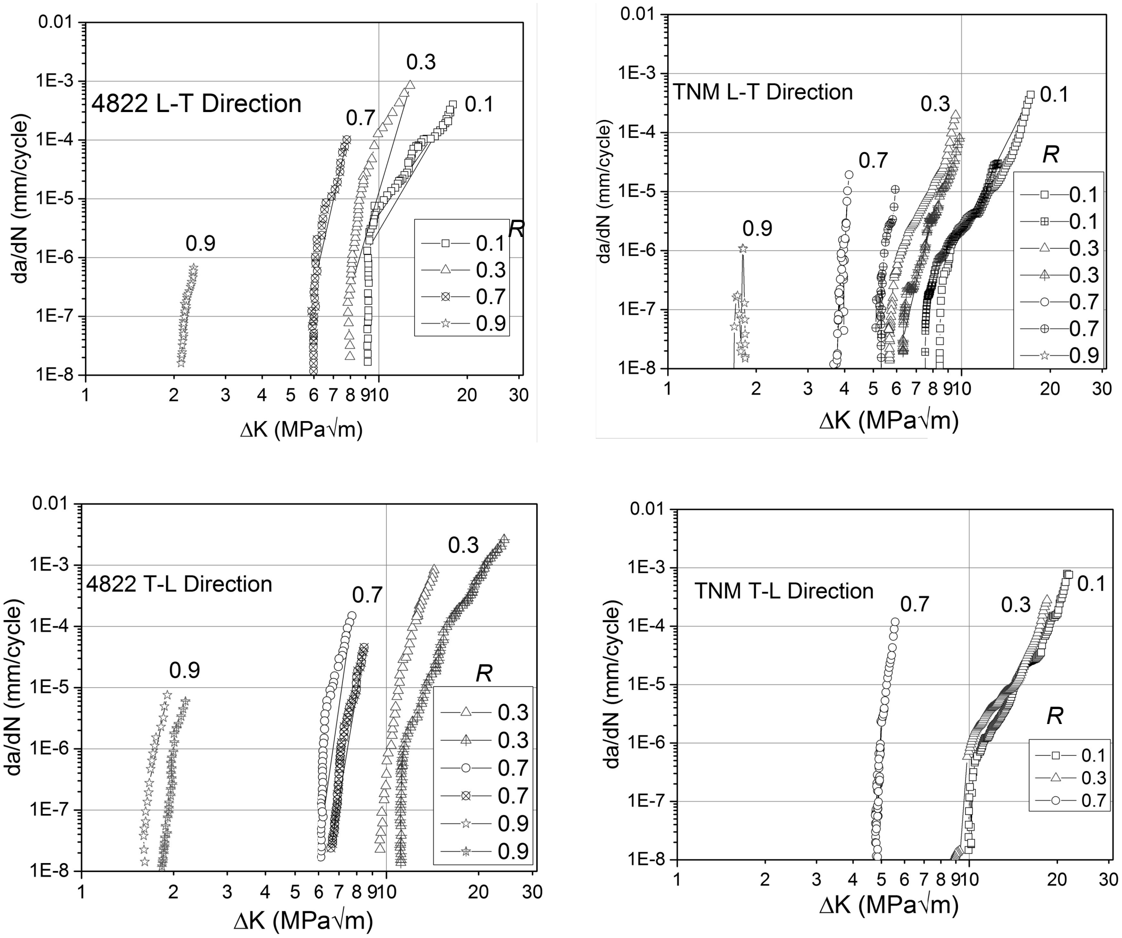

Figure 4.1: Effect of load ratio *R* on fatigue crack growth rate curves of specimens tested in *L-T* direction (top) and *T-L* direction (bottom) of as-cast 4822 (left) and TNM (right).

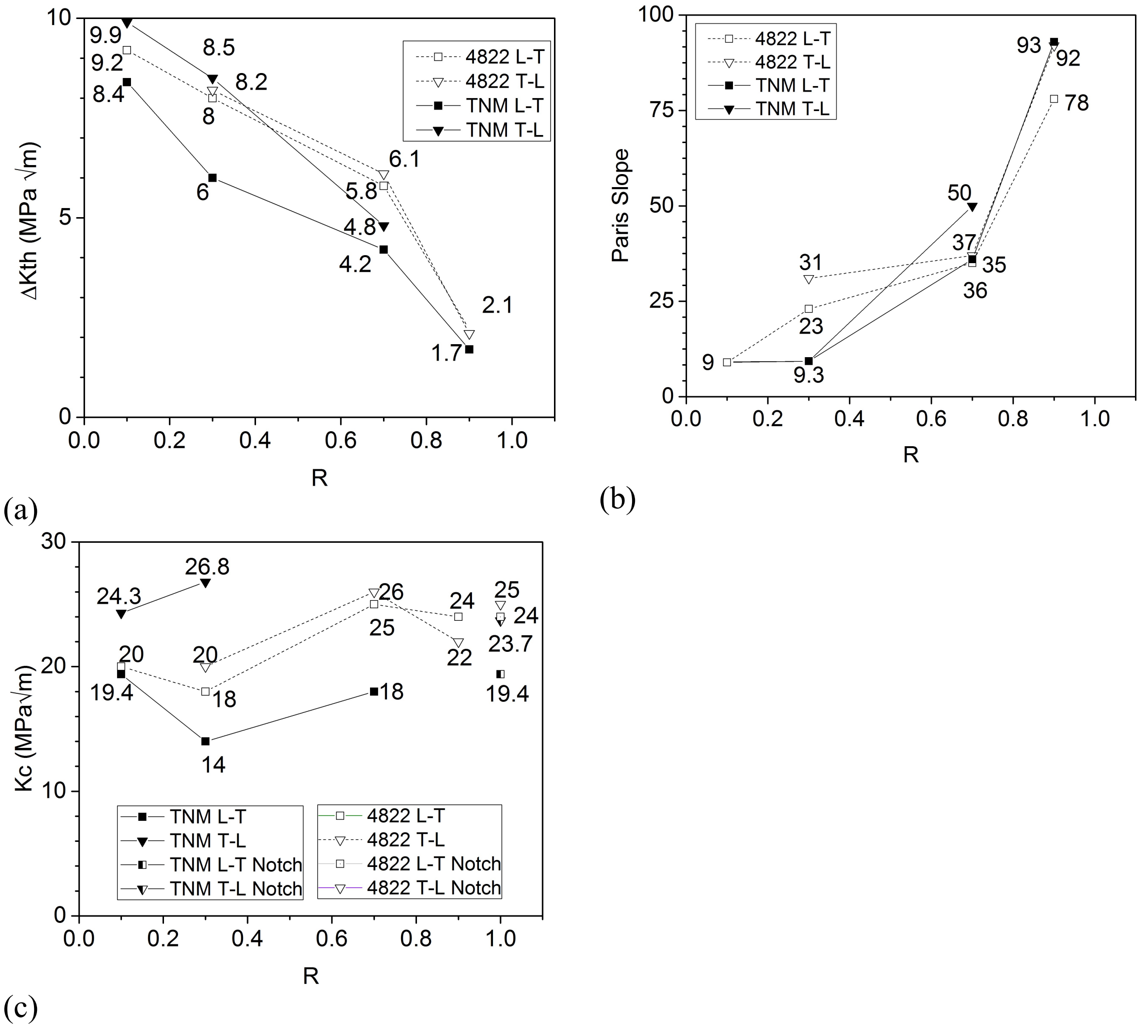

Figure 4.2: Effect of load ratio R on (a) fatigue threshold ΔKth, (b) Paris slope m, and (c) K at overload failure K_c and notch toughness for 4822 and TNM in both *L-T* and *T-L* orientations.

The fatigue crack growth data (Figure 4.1 and Table 4.1) reveals a large effect of R on the magnitude of the ΔK_{th} for 4822, decreasing from over 9 MPa√m for $R = 0.1$ to less than 2 MPa√m at $R = 0.9$. At a given R, the TNM shows a lower ΔK_{th} in both orientations compared to 4822. Crack closure can significantly impact the fatigue threshold and one key difference between the 4822 and TNM relates to the large differences in fracture surface roughness.

Table 4.1: Cyclic plastic zone size of 4822 and TNM at threshold calculated with ΔK_{th} and K_{max}.

Orientation	***R***	**ΔKth (MPa√m)**		**Kmax at ΔKth (MPa√m)**		**Radius of Cyclic Plastic Zone (µm) at Threshold using ΔK**		**Radius of Monitonic Plastic Zone (µm) at Threshold using Kmax**	
		4822	**TNM**	**4822**	**TNM**	**4822**	**TNM**	**4822**	**TNM**
L-T	0.1	9.2	8.4, 7.5	10.2	9.3, 8.3	10.6	1.9,19.5	52	9, 7
	0.3	8.0	6.3, 5.6	11.4	9, 8	8	1.1,0.8	65	9, 7
	0.7	5.8	3.8, 5.4	19.5	12.6, 17.7	4.3	0.4,0.8	174	17, 34
	0.9	2.2	1.7	21.5	17.8	0.6	0.1	212	34
T-L	0.1		9.9		11.1		2.7		13
	0.3	9.4	8.5	15.8	12.2	6.3	2	125	16
	0.7	6.0, 6.2	4.8	19, 20.9	16	4.5,4.8	0.6	182, 216	28
	0.9	1.6,1.8		16.1,18.4		0.3,0.4		131,171	
Orientation	***R***	**ΔK at overload (MPa√m)**		**Kmax at overload (MPa√m)**		**Radius of Cyclic Plastic Zone (µm) at Overload using ΔK**		**Radius of Monotonic Plastic Zone (µm) at Overload using Kmax**	
		4822	**TNM**	**4822**	**TNM**	**4822**	**TNM**	**4822**	**TNM**
L-T	0.1	17.5	17.2,13.2	19.4	19.1,14.7	38.6	7.8,4.7	190	39,23
	0.3	8.9	9.8,9.5	12.6	14,13.6	9.9	2.6,2.4	80	21,20
	0.7	6.1	4.1,5.9	20.2	13.8,19.8	4.7	0.5,1	208	21,43
	0.9	2.2	1.8	22.4	18.3	0.6	0.1	253	36
T-L	0.1		21.9		24.4		13		64
	0.3	16.6	18.4	18.8	25	240	9.2	286	73
	0.7	6.2,6.9	5.6	20.5,23	18.7	213,270	10.8	213,270	37
	0.9	1.7,2.2		16.8,21.8		0.4,0.6		143,242	

Typical fatigue fractographs taken at different magnifications for 4822 and TNM tested in the L-T and T-L orientation are compared in Figures 4.3-4.10. Overview images are given in Figures 4.3-4.8 while Figures 4.9-4.10 show the overload region. Both alloys exhibited brittle faceted features while the 4822 exhibited larger-scale features compared to the TNM. Closer examination of the flat facets on the fracture surface in the Paris law regime revealed an absence of fatigue striations (Figures 4.11-4.16). High magnification fractographs of the fatigue tests at various *R* for threshold are shown in Figures 4.11-4.12 while rising ΔK images are shown in Figures 4.13-4.16 . Fracture surface features in both alloys were predominantly brittle with small amounts of local plastic deformation. The influence of Δ*K* or *R* on fractographic features is not apparent.

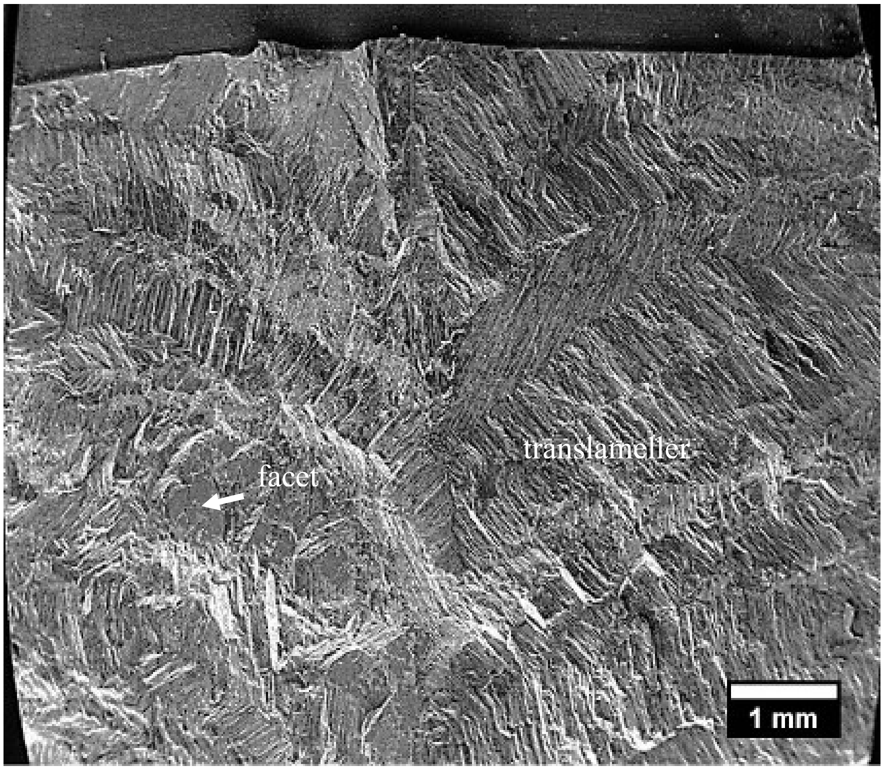

Figure 4.3: SEM overview of 4822 of fatigue specimen surface tested at R = 0.1 in the L-T direction. Crack growth direction is top to bottom.

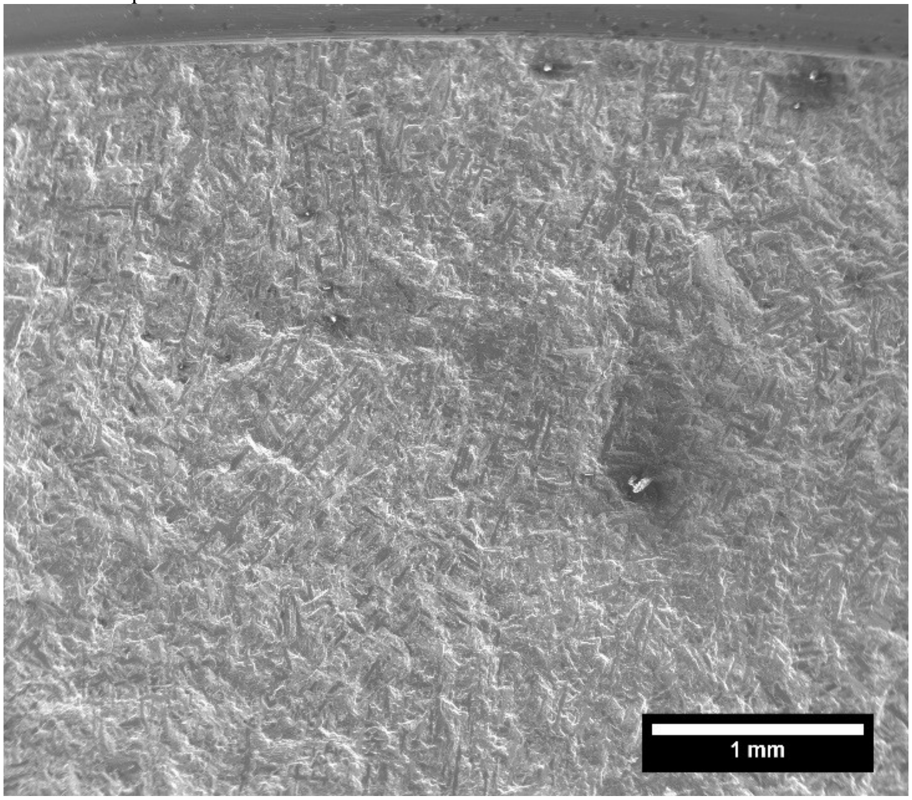

Figure 4.4: SEM overview of TNM of fatigue specimen surface tested at R = 0.1 in the L-T direction. Crack growth direction is top to bottom.

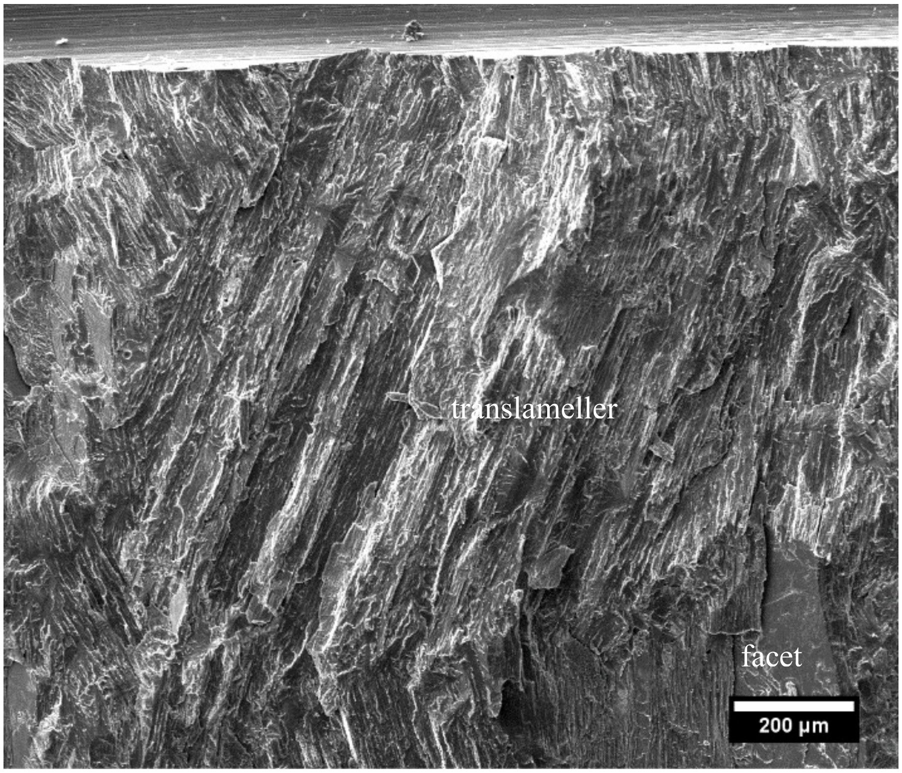

Figure 4.5: SEM overview of 4822 of fatigue specimen surface tested at R = 0.3 in the L-T direction. Crack growth direction is top to bottom.

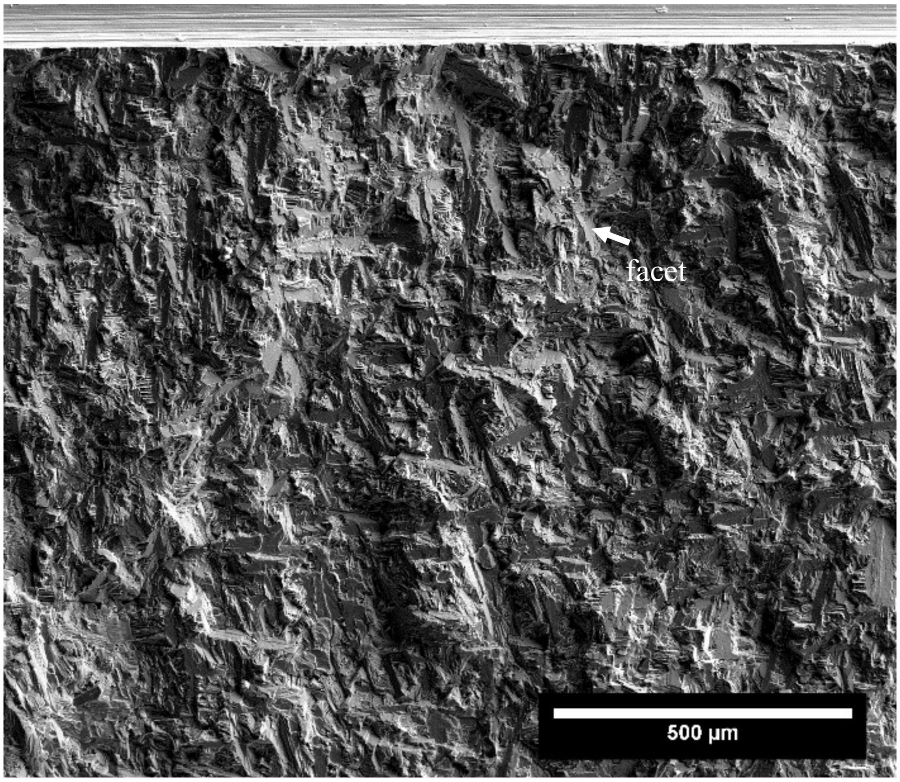

Figure 4.6: SEM overview of TNM fractograph of fatigue specimen surface tested at R = 0.3 in the L-T direction. Crack growth direction is top to bottom.

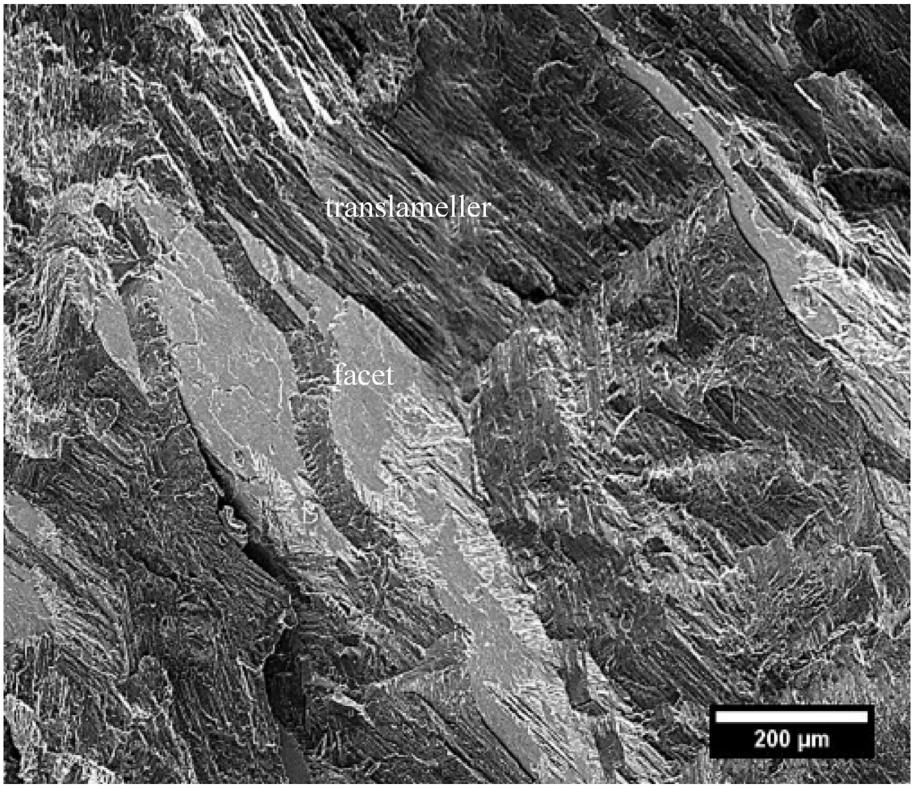

Figure 4.7: SEM of 4822 of fatigue specimen surface in overload regime tested at R = 0.1 in the L-T direction. Crack growth direction is top to bottom.

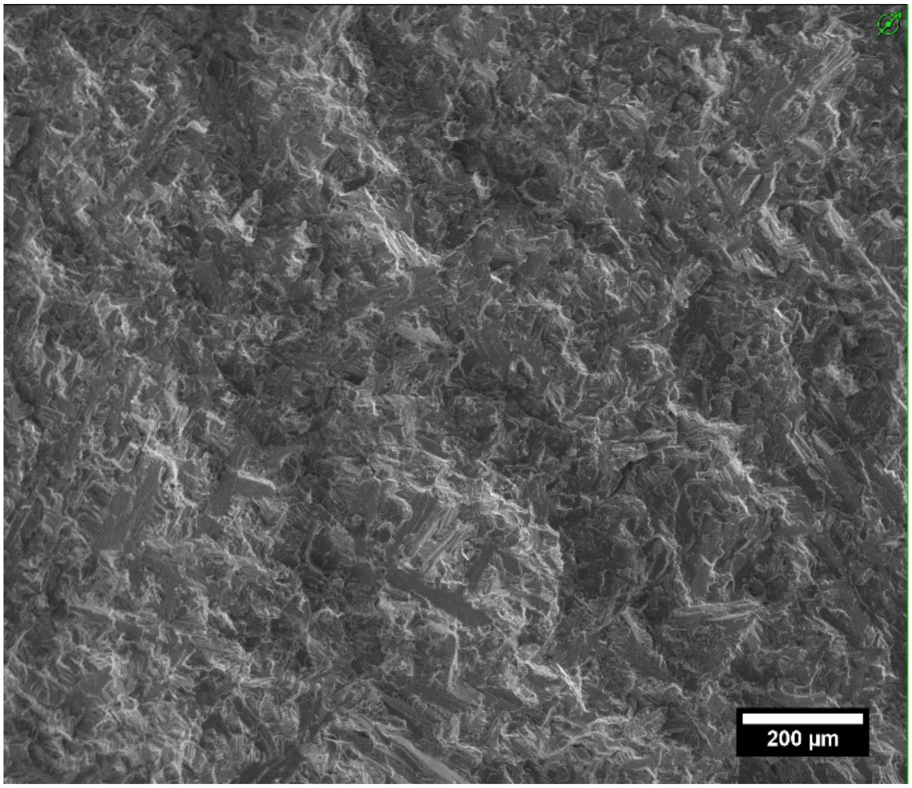

Figure 4.8: SEM of TNM of fatigue specimen surface in overload regime tested at R = 0.1 in the L-T direction. Crack growth direction is top to bottom.

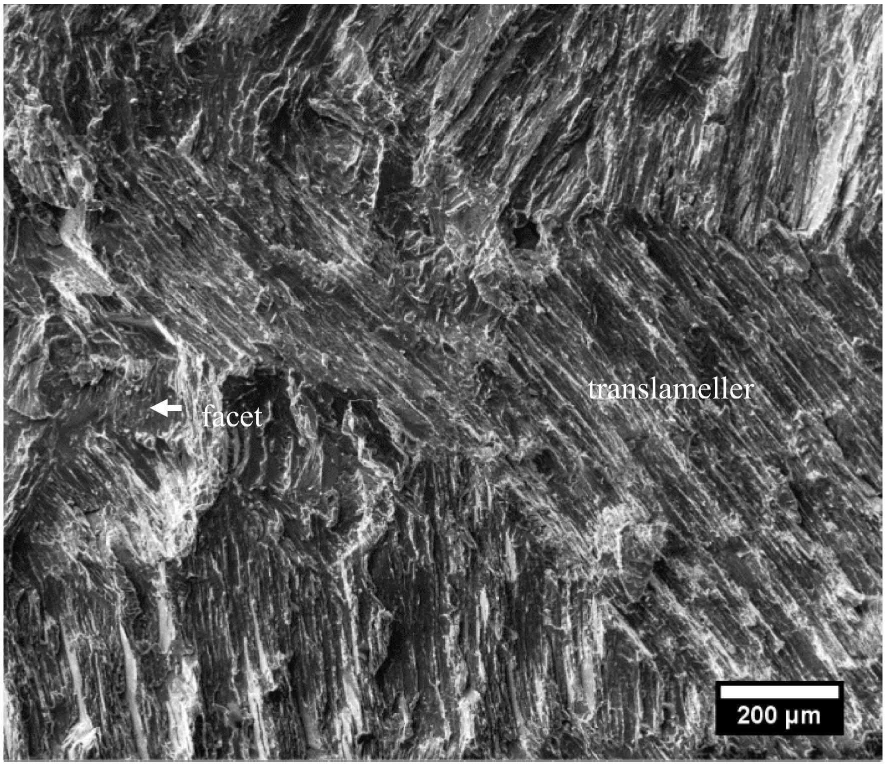

Figure 4.9: SEM of 4822 fractograph of fatigue specimen surface in the overload regime tested at R = 0.3 in the L-T direction. Crack growth direction is top to bottom.

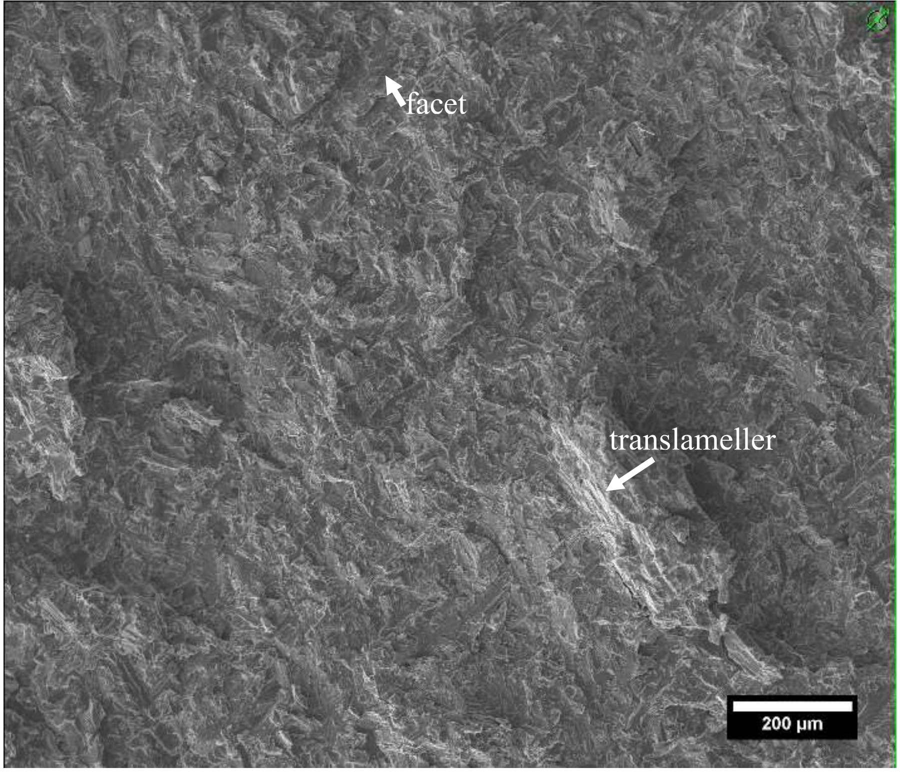

Figure 4.10: SEM of TNM fractograph of fatigue specimen surface in the overload regime tested at R = 0.3 in the L-T direction. Crack growth direction is top to bottom.

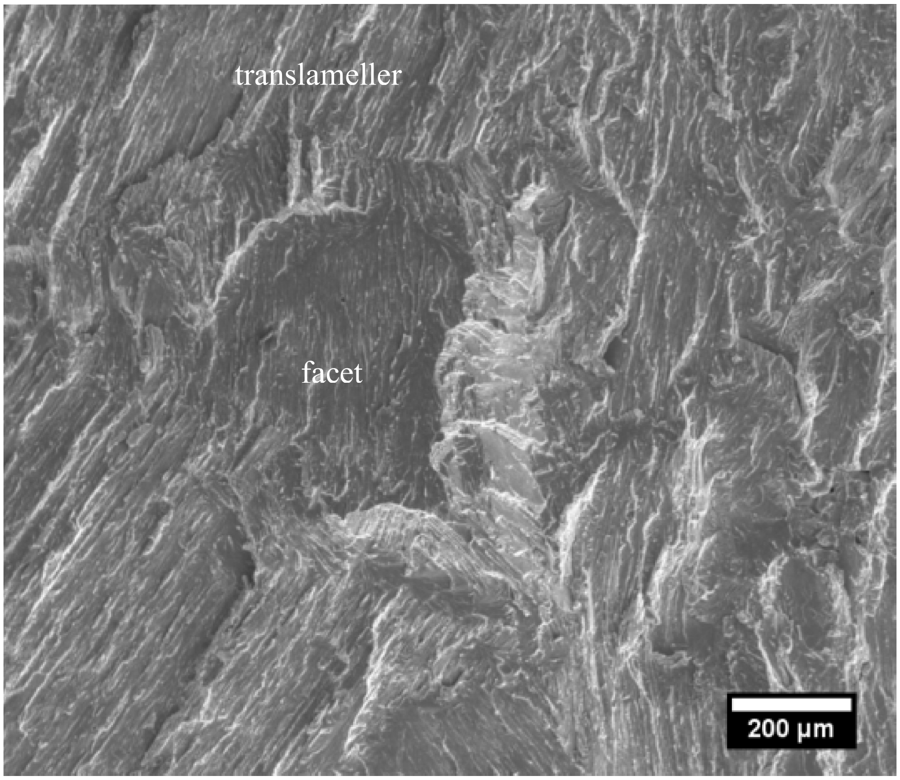

Figure 4.11: SEM fractograph of 4822 specimen surface at threshold tested at R = 0.7 in the T-L direction. Crack growth direction from top to bottom.

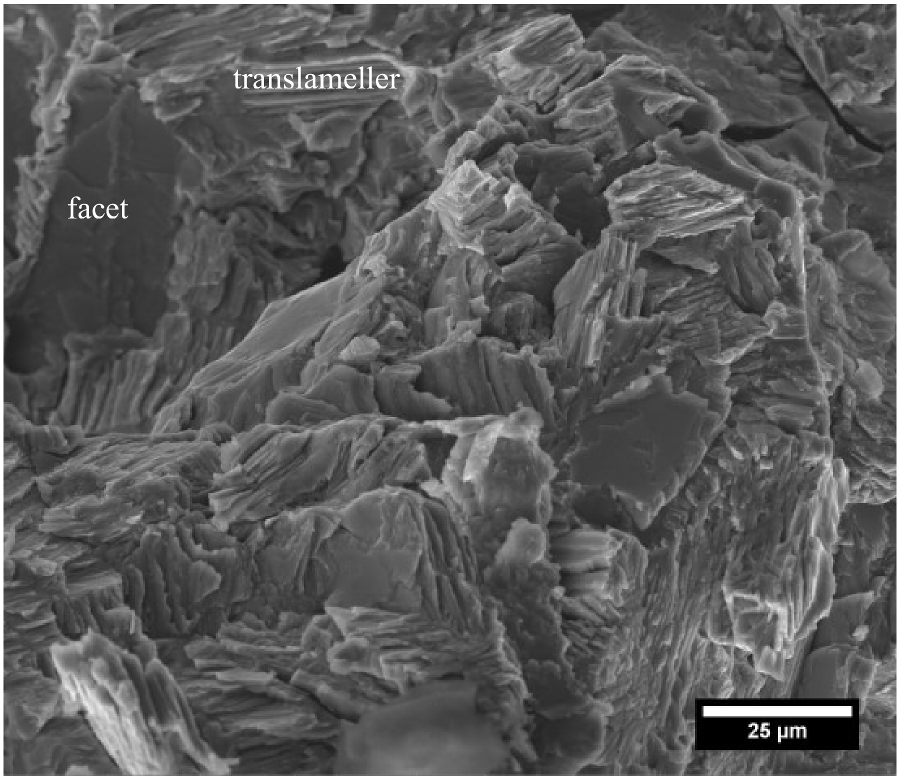

Figure 4.12: SEM fractograph of TNM specimen surface at threshold tested at R = 0.7 in the T-L direction. Crack growth direction from top to bottom.

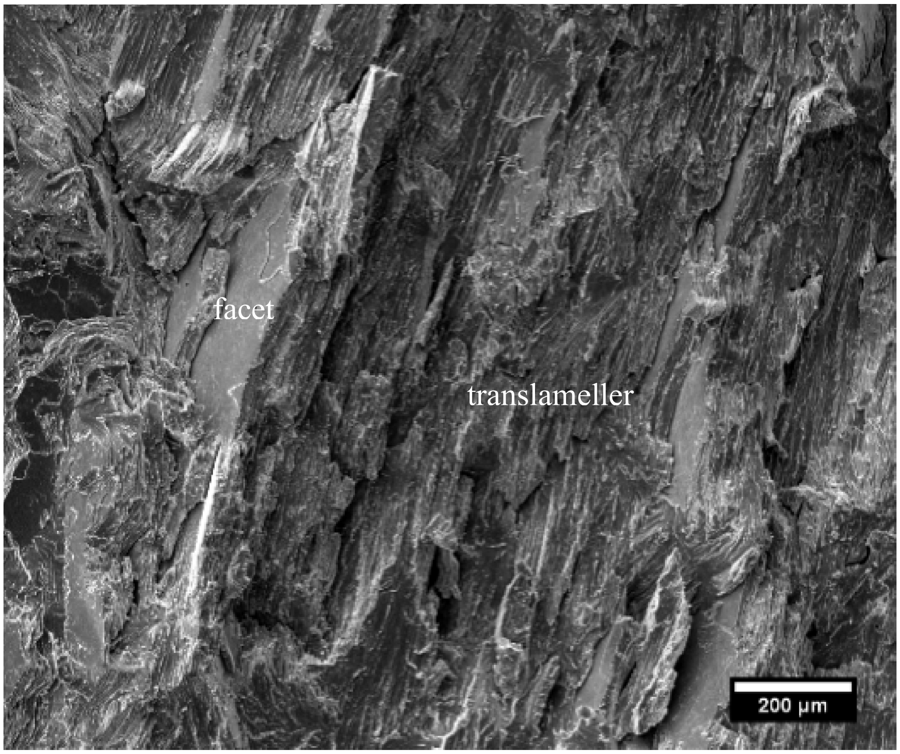

Figure 4.13: SEM fractograph of 4822 specimen surface in the rising ΔK regime at R = 0.3 in the T-L direction. Crack growth direction from top to bottom.

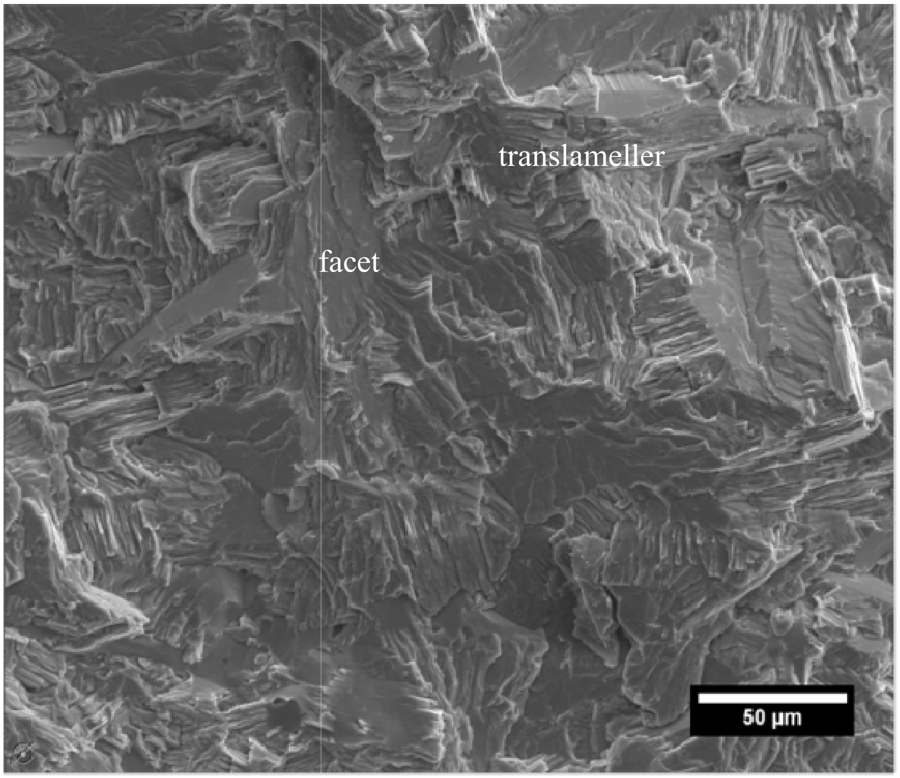

Figure 4.14: SEM fractograph of TNM specimen surface in the rising ΔK regime at R = 0.3 in the T-L direction. Crack growth direction from top to bottom.

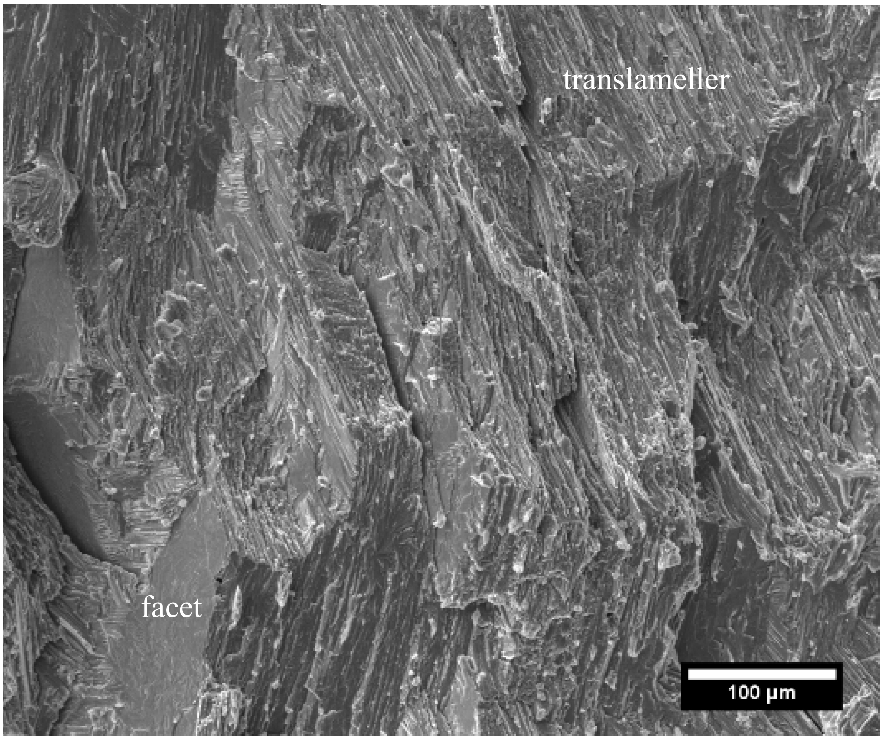

Figure 4.15: SEM fractograph of 4822 specimen surface in the rising ΔK regime at R = 0.9 in the L-T direction. Crack growth direction from top to bottom.

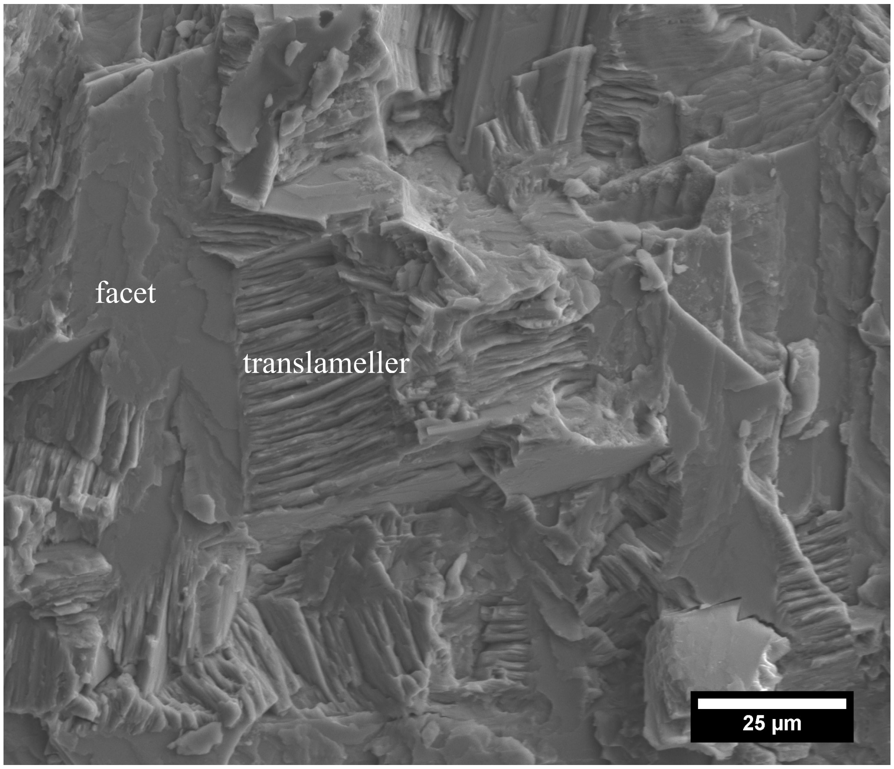

Figure 4.16: SEM fractograph of TNM specimen surface in the rising ΔK regime at R = 0.9 in the L-T direction. Crack growth direction from top to bottom.

As discussed elsewhere [71], the roughness-induced crack closure arises due to the linkage of mismatched planes of deflected microcracks via a process involving shear deformation and the fracture of thin ligaments. This has been postulated as the origin of roughness-induced closure observed in other Ti alloys and reported for TiAl alloys with large colony size similar to the 4822 in this study [72]. The higher fracture resistance exhibited by the lamellar microstructure is attributed to the deflected crack path which results in shear ligaments of large length and larger plastic dissipation contributed by the fracturing of the lamellar ligaments [71], [73]–[75].

The irregular or rough fracture surfaces can induce high closure loads at low R when in-plane shear wedges open the crack at contact points along the crack face. The reduction in the effectiveness of this closure mechanism increases as the crack tip open displacement (CTOD) increases [76] and the crack faces are held apart.

The effect of changes in ΔK and K_{max} in the fatigue cycle on the surface roughness can be estimated by determining the plastic zone size and examining how this compares to the microstructural features sampled. The monotonic plastic zone radius in plane-strain is given by

$$r_{os} = \frac{1}{6\pi}\left[\frac{K}{\sigma_o}\right]^2 \tag{4.1}$$

where σ_o is the yield strength of the material (342 MPa for 4822 and 680 MPa for TNM) [54]. The plastic zone size under cyclic loading will be smaller than that in static loading and is affected by reverse plasticity [54]. As the crack tip cycles during fatigue, the plastic zone leaves a wake of plasticity behind the crack tip. This induces residual stress in the crack tip region and may also play a role in crack closure. The cyclic plastic zone radius is given by

$$r_{oc} = \frac{1}{6\pi}\left[\frac{\Delta K}{2\sigma_o}\right]^2 \tag{4.2}$$

The calculated size of the monotonic and cyclic plastic zone at ΔK_{th} and overload for both 4822 and TNM ΔK and K_{max} are given in Table 4.1, assuming plain-strain conditions. The plastic zone size using K_{max} at threshold for the *T-L* test direction at $R = 0.3$ is 125 μm for 4822 which is considerably smaller than the colony size (~1000 μm). For TNM tested at R = 0.3, the plastic zone size at threshold using K_{max} is 16 μm, which is comparable to the colony size (~20–40 μm). Similar sizes are computed for other *R* values and orientations tested when using K_{max}. However, the cyclic plastic zone is considerably smaller than the colony size at the fatigue threshold for all of the *R* values and orientations tested, indicating that only a single colony is sampled in the plane of view, out of ~ 13 colonies of 4822 and 500 colonies of TNM sampled through the thickness. Thus, the orientation of only a few colonies dominates fatigue crack growth.

The cyclic plastic zone size at ΔK_{th} for 4822 is only on the order of the interlamellar spacing for all R values while the maximum plastic zone size is still only 1/5 to 1/10 of the colony size. The maximum plastic zone size still does not sample a full colony, suggesting that the drop in threshold with increasing *R* is from roughness-induced crack closure, consistent with the high surface roughness shown in Figure 4.17. At overload, the plastic zone sizes at K_{max} are still at most only 1/5 of the colony size at all *R* values, thus sampling only a few colonies throughout the sample and producing similar values for K_{max} at failure.

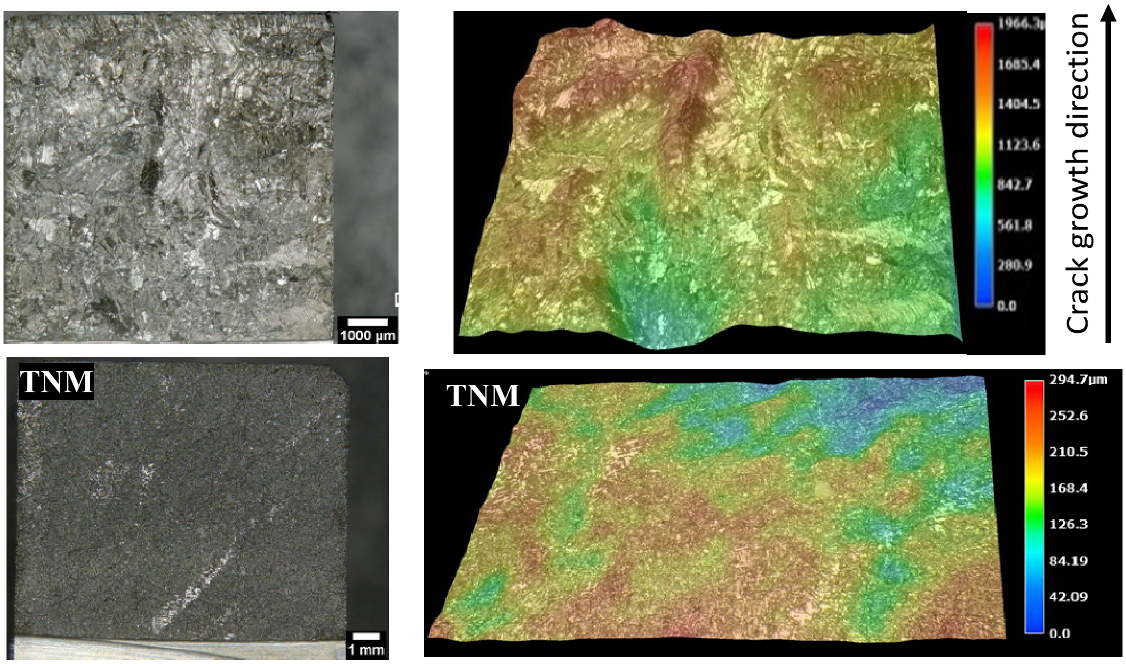

Figure 4.17: 3D surface roughness plot of 4822 (top) and TNM (bottom) 7 mm x 7 mm area taken at intermediate ΔK, both specimens fatigue tested in the *T-L* direction at $R = 0.3$. For 4822, a peak of 1750 µm exists at the top left corner with troughs of 800 µm. The peak represents large roughness resulting from fatigue crack growth across a grain oriented in a different direction to adjacent grains. TNM sample exhibits a peak height of approximately 280 µm and troughs of 50 µm.

For TNM, the cyclic plastic zone at threshold is on the order of the interlamellar spacing, while the maximum plastic zone size approaches the colony size. Thus, at high *R* values, the maximum plastic zone size will sample a full colony in the field of view and many through the sample thickness. However, this will enable the crack to follow the brittle β_o phase present on the colony boundaries and likely give rise to the large effects of R on the threshold. Since the surface roughness of the TNM samples, as seen in Figure 4.17, is low, this limits any contribution from roughness-induced closure. At overload, the plastic zone sizes at K_{max} are of the order of the colony size at all *R* values, easily sampling the brittle β_o regions on the colony boundaries throughout the sample thickness and producing similar values for K_{max} at failure for all R values.

Crack path analysis was performed on polished and etched cross-sections of failed fatigue specimens. An example for a 4822 *T-L* sample fatigue tested to threshold at R = 0.7 is presented in Figures 4.18a,b and 4.19. The crack path shows interlamellar and translamellar cracking that results from the propagation of the crack seeking the path of least resistance. The crack follows the colony boundaries and lamellae, causing the interlamellar and translamellar cracking along with some secondary cracking. Crack path for a TNM *L-T* sample tested to threshold at R = 0.1 presented in Figures 4.20a,b and 4.21 shows microcrack propagation along β_o at colony boundaries, both along the crack path and subsurface. Cross-sections of the failed fatigue specimens in the L-T direction at R = 0.7 were mounted and polished to show the crack path on one side of the specimens as shown in Figure 4.22.

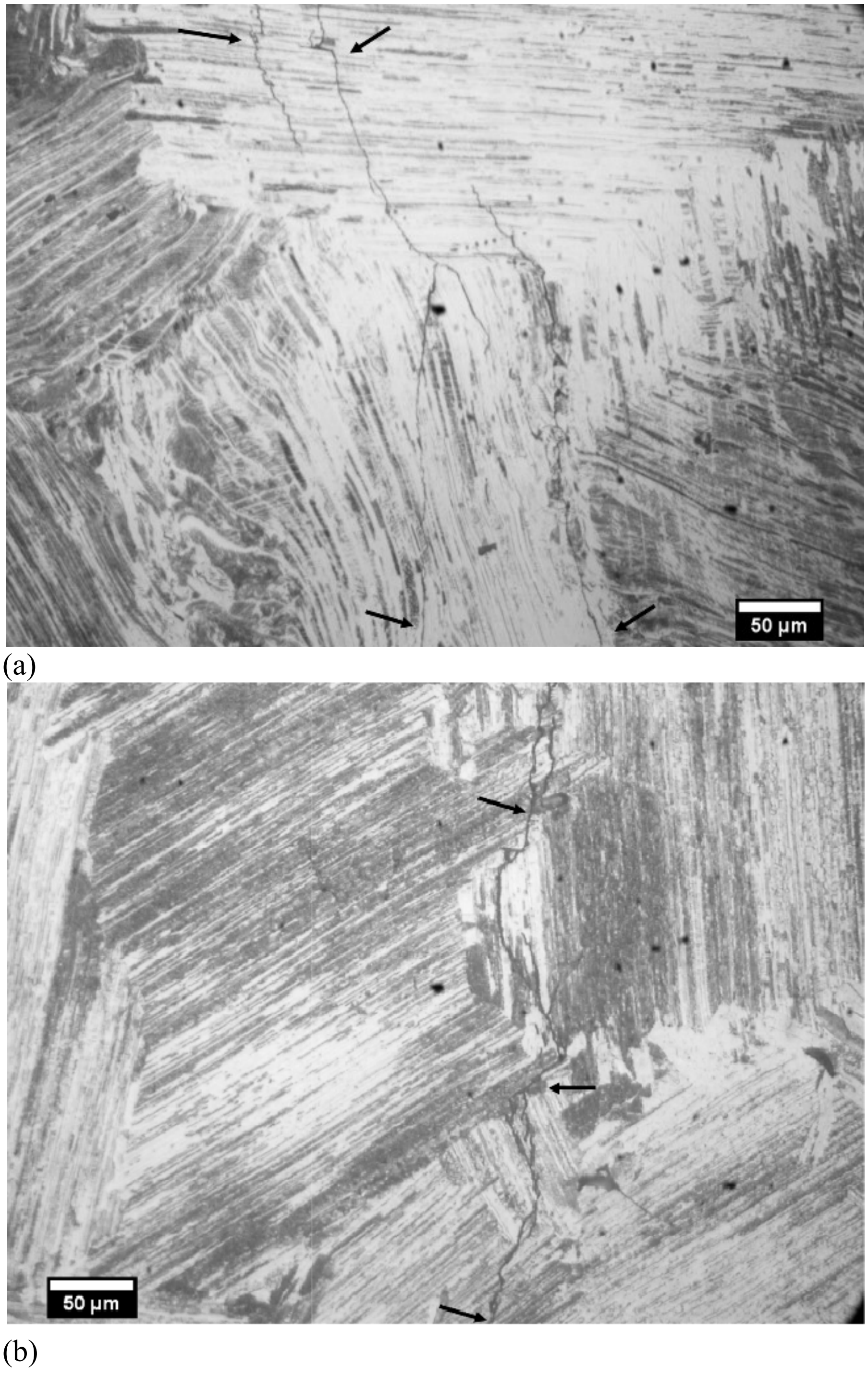

Figure 4.18: Crack path in 4822 specimen fatigue tested in the *T-L* direction to threshold at $R = 0.7$. Crack growth direction is from bottom to top with arrows in a,b pointing to the crack path. Optical micrograph (etched with Krolls reagent) showing (a) translamellar and interlamellar cracks as well as secondary cracking, (b) crack following a colony boundary.

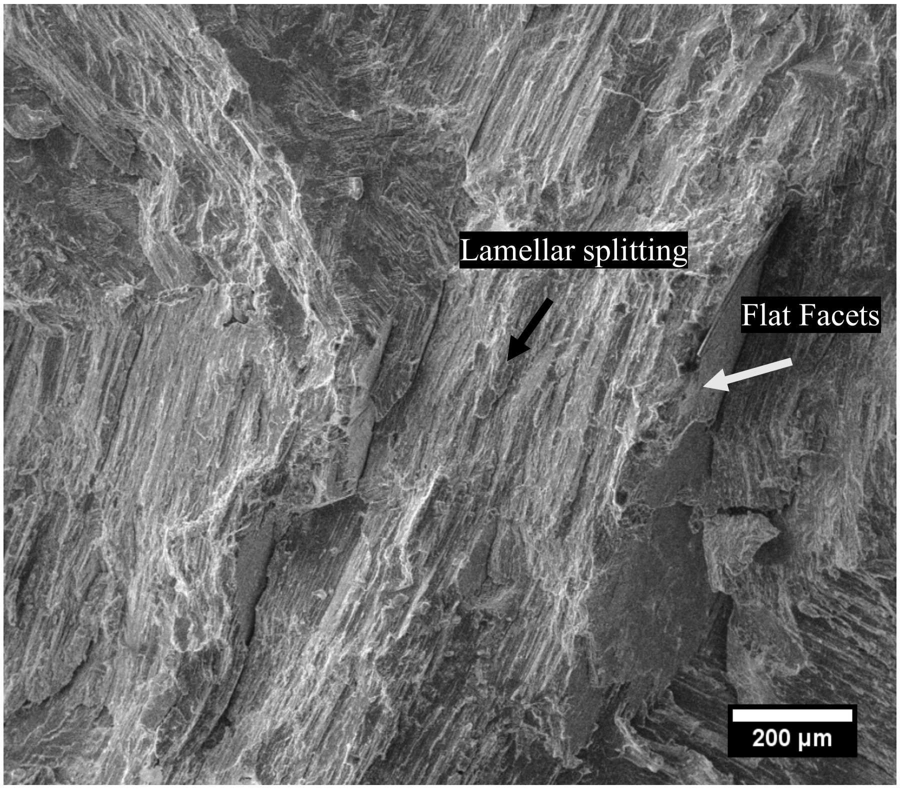

Figure 4.19: Crack path in 4822 specimen fatigue tested in the *T-L* direction to threshold at $R = 0.7$. Crack growth direction is from bottom to top with arrows in a,b pointing to the crack path. Optical SEM fractograph in the overload region showing lamellar splitting (black arrow) and flat brittle facets (white arrow)

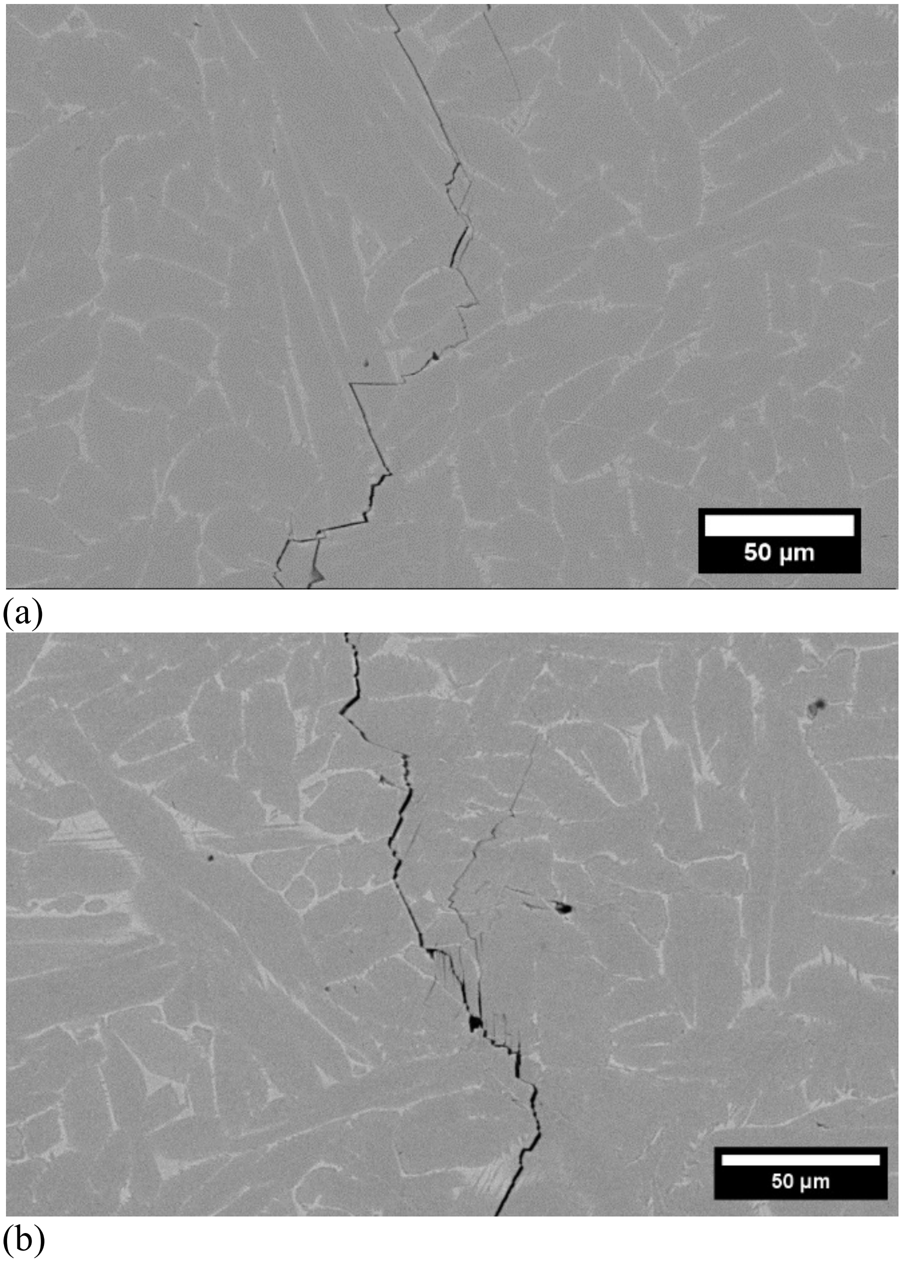

Figure 4.20: Crack path of TNM specimen fatigue tested in the *L*-*T* direction to threshold at $R = 0.1$. Crack growth direction is from bottom to top. Backscattered electron images showing (a) translamellar and interlamellar cracking with the crack following β_o at colony boundaries, (b) secondary cracking and microcracking away from the crack path

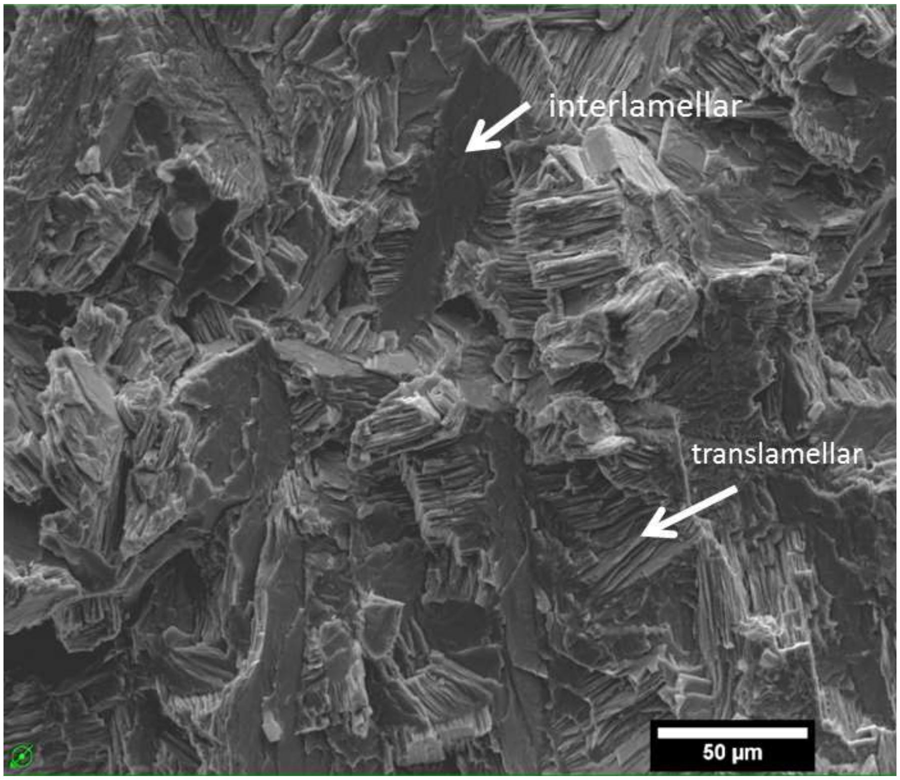

Figure 4.21: Crack path of TNM specimen fatigue tested in the *L*-*T* direction to threshold at $R = 0.1$. Crack growth direction is from bottom to top. SEM fractograph in the medium ΔK region showing translamellar cracking with lamellar splitting and interlamellar fracture.

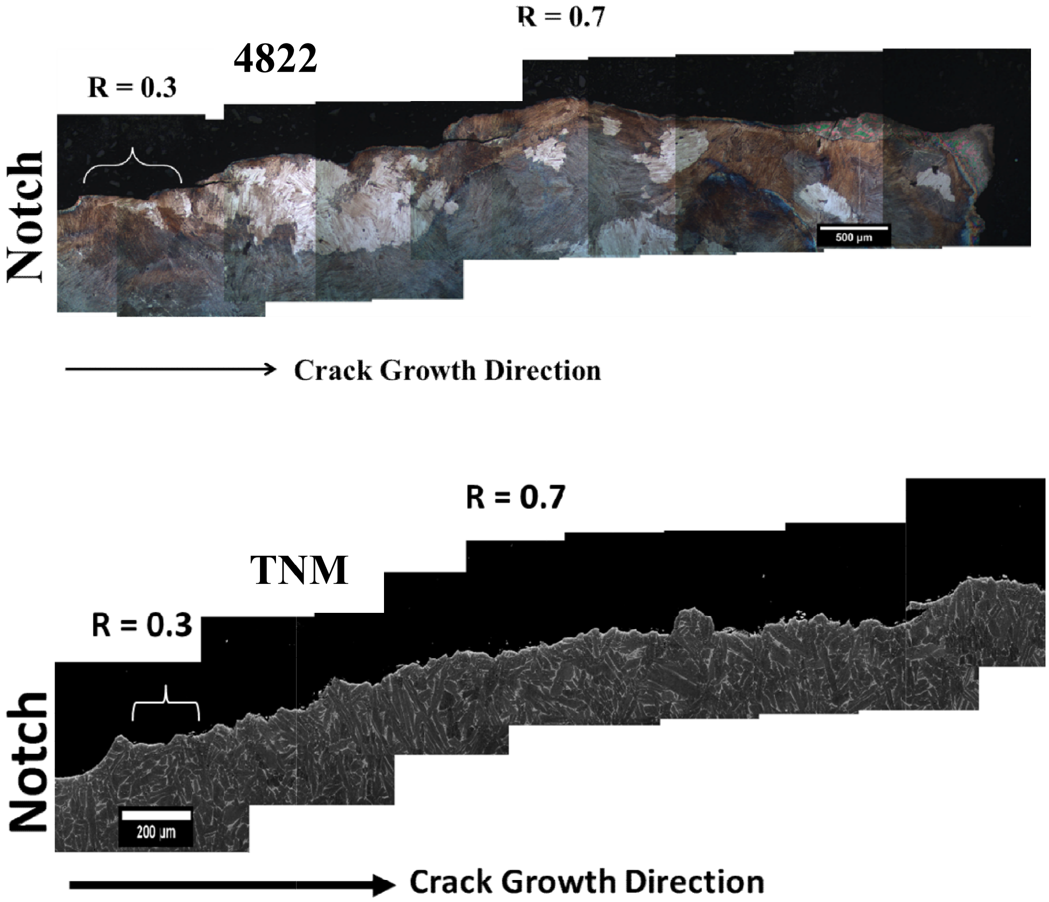

Figure 4.22: (Top) Crack path of (optical) 4822 L-T broken sample fatigued at R = 0.3 and then R = 0.7. Secondary cracking is seen and the crack path follows the microstructure and produces significant roughness. (Bottom) Crack path of TNM (BSE) L-T broken sample fatigued at R = 0.3 and then R = 0.7.

In order to begin to address the effects of microstructural features on the crack path as well as the R dependence of both ΔK_{th} and m, the fatigue crack growth data was first plotted as da/dN vs. K_{max} as shown in Figure 4.23. The data for both 4822 and TNM do not completely collapse onto a single curve, suggesting an important, but not completely dominating effect of K_{max} on the fatigue crack growth rate. This behavior is further discussed in the next section on TNM alone. In addition, m is ~ 9 at low R and approaches 100 at high R, again suggesting an important effect of K_{max} on the crack growth rate. Furthermore, brittle modes of failure and absence of striations on the fatigue fracture surfaces support an important role of K_{max} on the fatigue crack growth rate. For example, brittle fracture surface facets roughly 100 μm in size were exhibited by 4822. While these features are less than the colony size, they are in the range of the calculated plastic zone sizes and d*a*/d*N* in certain regions, consistent with incremental crack growth of that size in certain regions of the fracture surface.

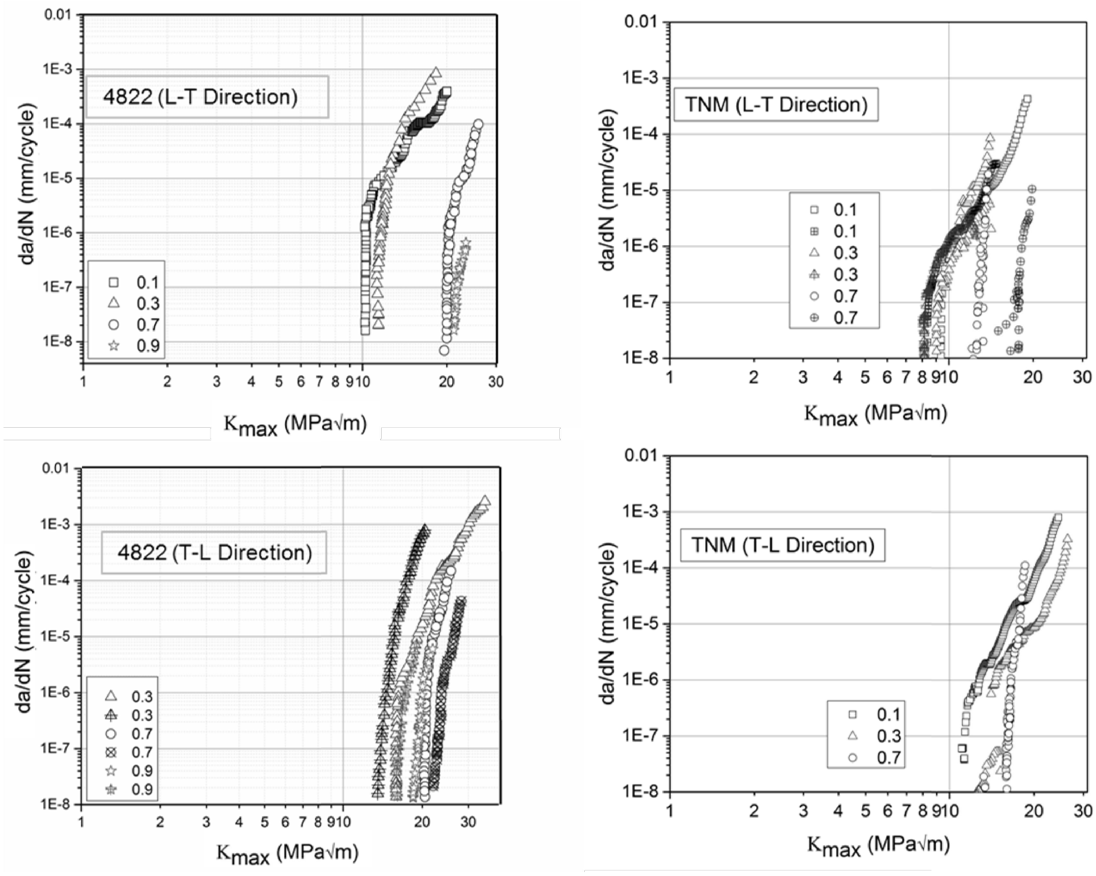

Figure 4.23: K_{max} vs. d*a*/d*N* curves of 4822 (left) and TNM (right) tested in *L-T* (top) and *T-L* (bottom) directions at various *R* values.

The data obtained on the 4822 and TNM exhibit characteristics that are similar to those exhibited by some metallic alloys [60], [77], [78] and intermetallics [79], with metallic-like Paris slopes in the range 3-5 at low *R* significantly increasing to >10 with an increase in *R*. In these systems, it has been shown that the increase in *m* with increasing *R* corresponds with an increase in static modes of brittle fracture that produce elevated crack growth rates that continue to increase with increasing *R*. In previous works [13,23-

25], such static modes of fracture included intergranular and cleavage failure. In the present work, the brittle fracture features in 4822 are likely to contribute to large increments in crack growth at a given ΔK, and are likely driven by K_{max} as no fatigue striations were evident. In TNM, the crack path appears to be dominated by brittle β_o along colony boundaries, also providing a brittle crack path that should be dominated by K_{max} and not ΔK. The continuous brittle β_o present around the lamellar colonies allow the crack, once initiated, to propagate unhindered. Once the crack reaches an end of a lamellar colony, the crack seeks a more favorable path, producing interlamellar and translamellar cracking. These fatigue crack growth mechanisms are similar to those reported by Leitner in TNM [80].

It must be noted that the present work was conducted on as-cast TNM material. Deformation processing is known to produce significant effects on the mechanical behavior of intermetallics due to various beneficial microstructure modification [81]. The work summarized in this section of the discussion was conducted in order to provide a baseline understanding of the features affecting fatigue crack growth in the starting as-cast material. The influence of deformation processing on fatigue and fracture behavior of TNM will be presented in the second section of the discussion.

4.2 TNM vs Ti-4822 Conclusions

The fatigue crack growth behavior of Ti-48Al-2Cr-2Nb (4822) and Ti-43.5Al-4Nb-1Mo-0.1B (TNM) in the as-cast condition were determined by testing over a range of *R* and stress intensity levels, in the *L-T* and *T-L* directions. Based on the observations of this investigation, the following conclusions were drawn:

i) The as-cast 4822 had a large ($\gamma+\alpha_2$) colony size (~1000 μm) and lath width of ~ 1.77 μm while the TNM had small colonies (20-40 μm) and fine lamellar spacing of ~ 0.2 μm.

ii) The fatigue fracture surfaces in both alloys in both orientations showed translamellar, interlamellar, and brittle fracture features. No fatigue striations were observed on the specimens tested in either orientation.

iii) The fatigue crack threshold was very dependent on load ratio. In particular, increasing the load ratio had a larger effect on reducing the fatigue threshold than reported for other TiAl materials.

iv) The fracture surface roughness quantified using confocal microscopy was large in 4822 (e.g., on the order of the colony size ~ 1000 μm). In contrast, the surface roughness of TNM was considerably less but similarly on the order of the colony size (20–40 μm). The roughness of the surface in 4822 is produced by the cracks traversing the lamellar colonies causing interlamellar and translamellar cracking. These crack patterns were also found in previous studies on TiAl containing a lamellar structure, but the scale of roughness on the fracture was much greater in the 4822 than in other versions including TNM.

v) The Paris slope m for as-cast 4822 and TNM shows a large dependence on R, increasing from around 9 at $R = 0.1$ to over 90 at $R = 0.9$. Microstructural effects on the crack path were used to rationalize this observation.

vi) The fatigue threshold, Paris slope, fracture toughness, and notch toughness are not measurably affected by sample orientation and are similar for 4822 and TNM.

4.3 Comparison of TNM Behavior After Various Processing Steps

The phase fractions present in the microstructures of the four materials shown in Figures 4.24a,b & 4.25a,b are provided in Table 3, obtained from SEM-BSE analyses and XRD. The SEM-BSE and XRD results produced differences in phase fractions due to the difficulty in detecting the fine-scale lamellar structure with XRD. The as-cast TNM (Figure 4.23a) exhibits a microstructure containing lamellar colonies surrounded by the β_o-phase, with only a small volume fraction of β_o present within colonies. HIPing of the as-cast material coarsens the lamellar structure in addition to producing globular γ along with globular β_o that is contiguous throughout the microstructure. Forging and heat treatment produces more significant changes to the microstructure. The initial lamellar structure is destroyed by upset-forging and heat treatment, producing globular γ, a globular α_2/γ lamellar structure, and globular β_o with precipitated γ, Figure 4.25a. All three phases are present at a size scale of 20 μm and are randomly distributed. The sidepress-forged plus heat treated material exhibits a similar structure to that seen in the upset-forged material. However, the sidepress-forged material did not experience as large a strain and thus retained some of the original lamellar structure, while the microstructure exhibits some directionality, Figure 4.25b. The sidepress-forged material similarly exhibits all three phases present at a size of 20 μm that are randomly distributed.

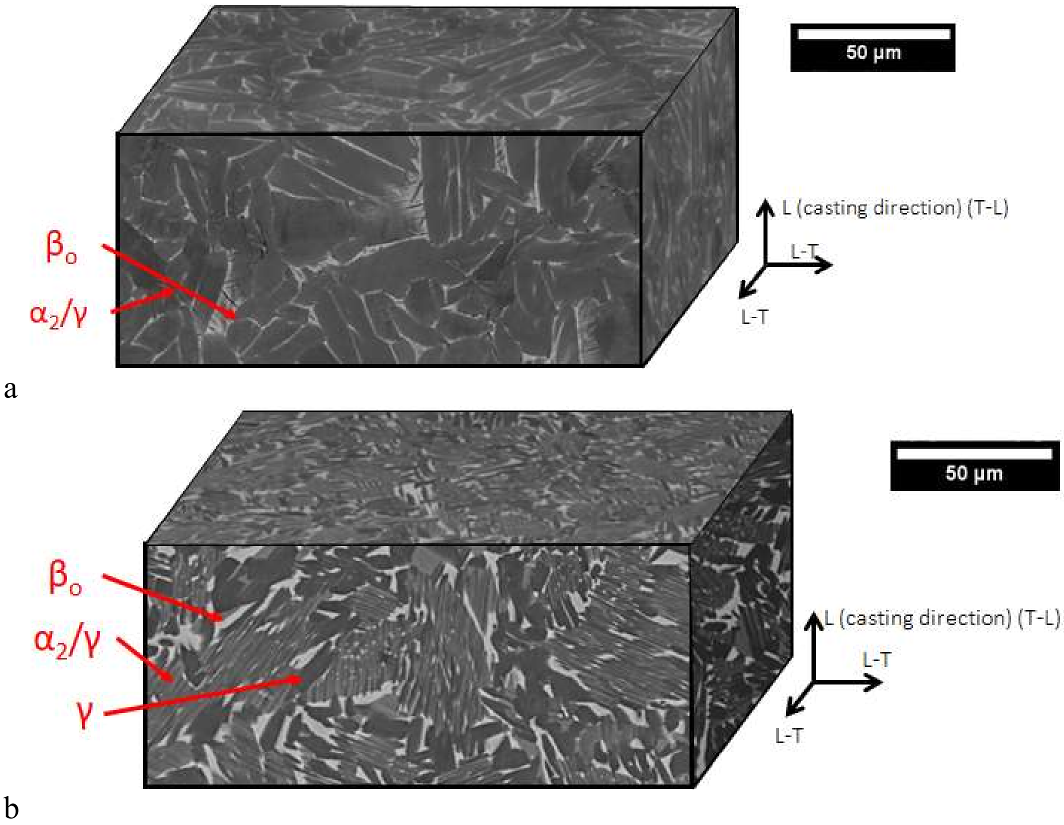

Figure 4.24: 3-D Microstructure taken with SEM-BSE (a) as-cast (b) as-cast + HIPed

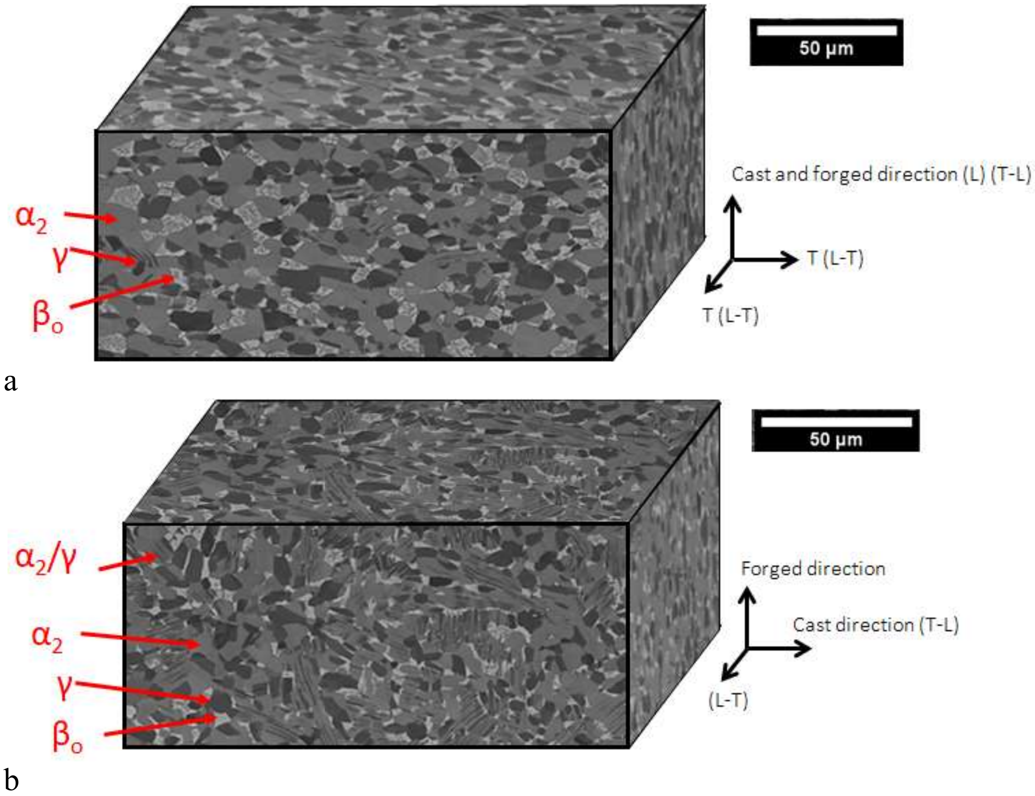

Figure 4.25: 3-D Microstructure taken with SEM-BSE (a) upset-forged (b) sidepress-forged

Table 4.2: Phase fractions calculated from XRD and MIPAR image analysis

	Volume % for XRD area under the curve	**MIPAR image analysis on SEM-BSE**
As-Cast		
α_2	53	91
γ	47	
β_o	0	9
HIPed		
α_2	53	37
γ	39	48
β_o	9	15
Upset-Forged		
α_2	43	57
γ	52	26
β	6	17
Sidepress-Forged		
α_2	41	50
γ	51	37
β_o	8	9.6

The tensile data shown in Figures 4.26-4.28 reveals an increase of 100 MPa after upset-forging and heat treatment when compared to as-cast and as-cast + HIPed material tested at room temperature. This increase in strength can be attributed to the destruction of the lamellar colonies and surrounding β_o in the as-cast and large globular β_o in the as-cast + HIPed material. The forging process and subsequent heat treatment eliminates the contiguity of β_o in the microstructure while creating a more random distribution of phases. The present yield strength for the upset forged material is slightly lower (e.g., 150 MPa) than that reported in other work [10], but exhibits higher ductility. This likely results from heat treatment at a higher temperature that decreases the β_o phase fraction and size.

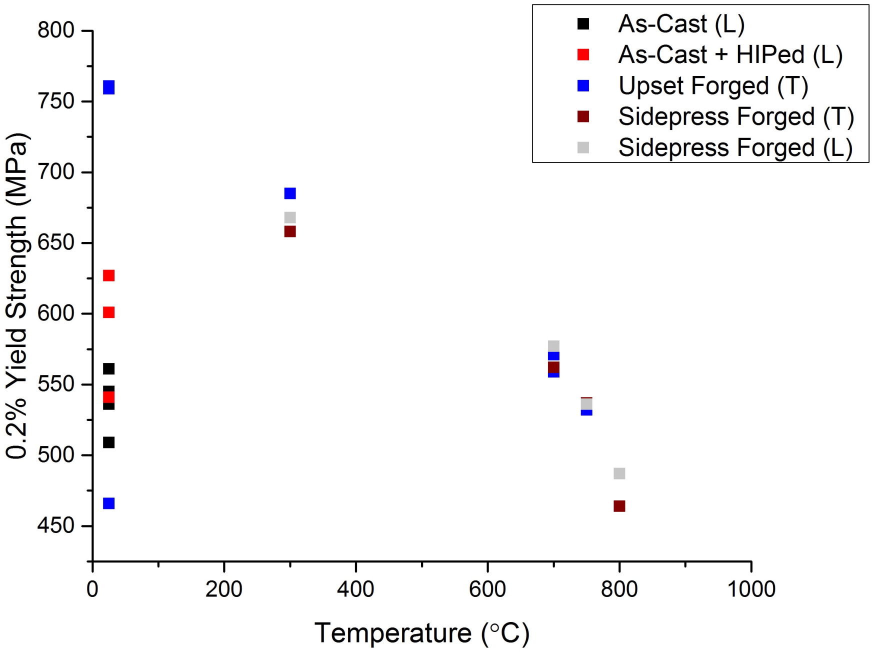

Figure 4.26: Effects of processing conditions, sample orientation, and test temperature on 0.2% yield strength.

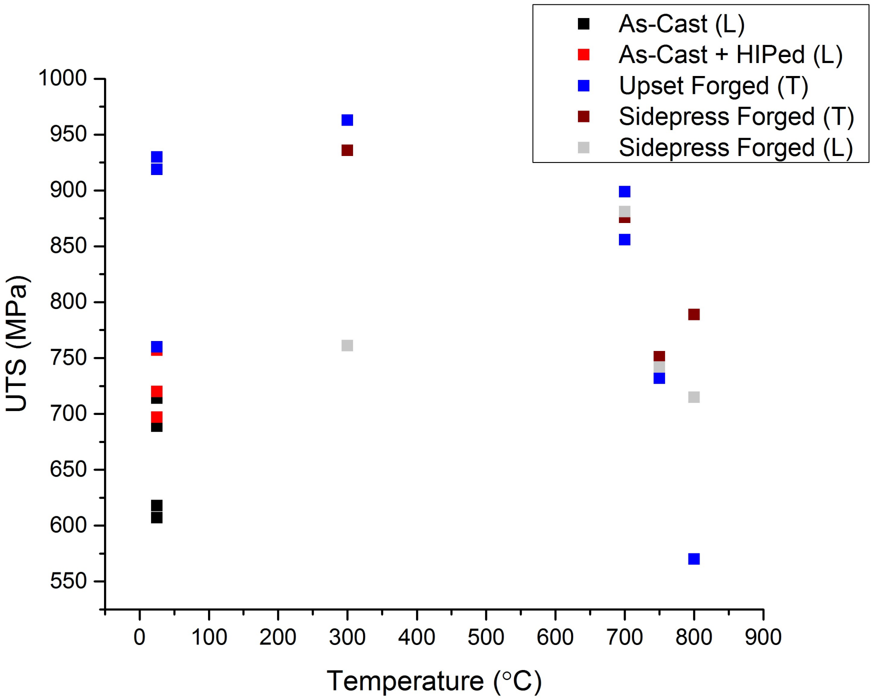

Figure 4.27: Effects of processing conditions, sample orientation, and test temperature on ultimate tensile strength.

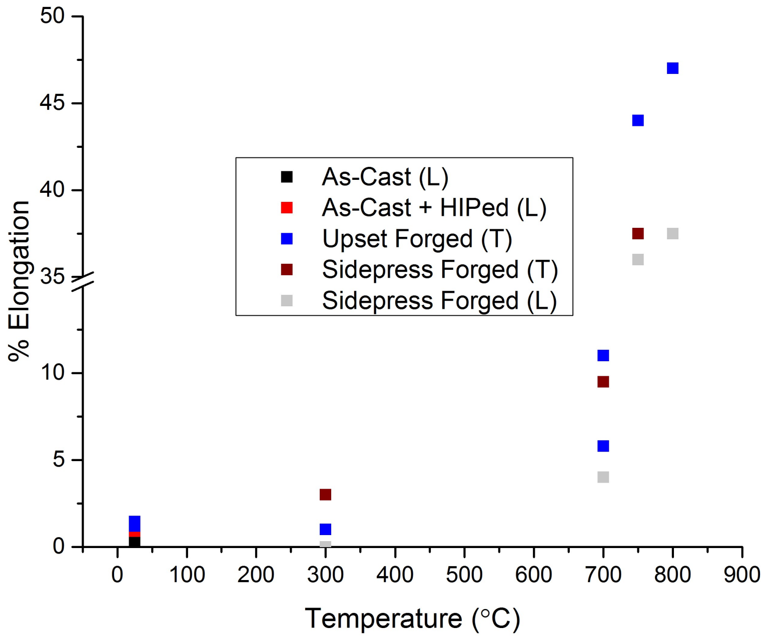

Figure 4.28: Effects of processing conditions, sample orientation, and test temperature on percent elongation.

Figure 4.29 shows the fracture surface of the as-cast sample that exhibits inter- and translamellar fracture with little evidence of ductile fracture. Longitudinal cross-sections taken from the failed tensile specimens, shown in Figures 4.30-4.33, reveal fracture that appears to follow the brittle β_o in the as-cast and cast + HIP samples. Also evident in these samples is interlamellar cracking that occurs in regions where the β_o is not contiguous.

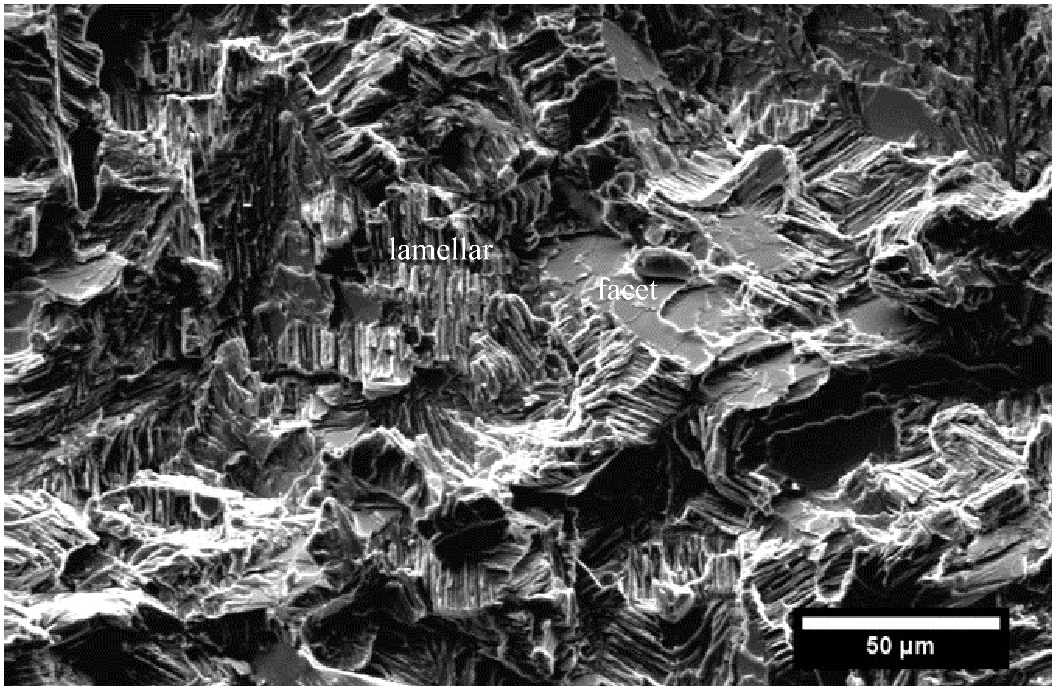

Figure 4.29: SEM-SE image of the tensile room temperature fracture surface taken of the as-cast TNM at a strain rate of $0.001s^{-1}$.

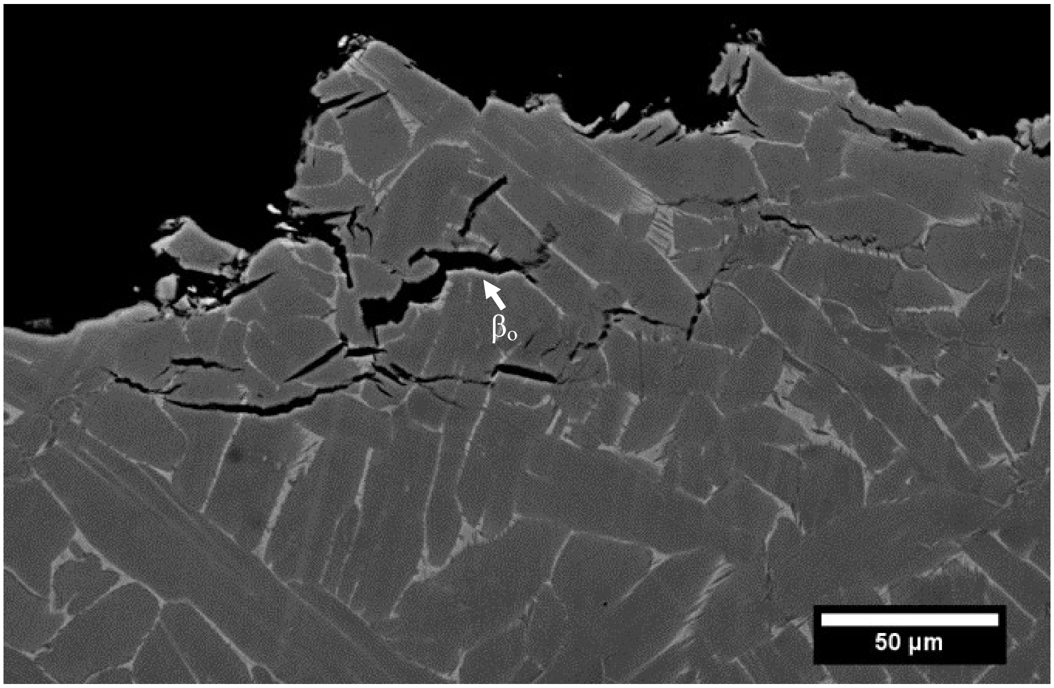

Figure 4.30: SEM-BSE image of the polished midplane of as-cast tensile specimen of TNM tested at room temperature at a strain rate of $0.001s^{-1}$. Subsurface damage was evident in all samples.

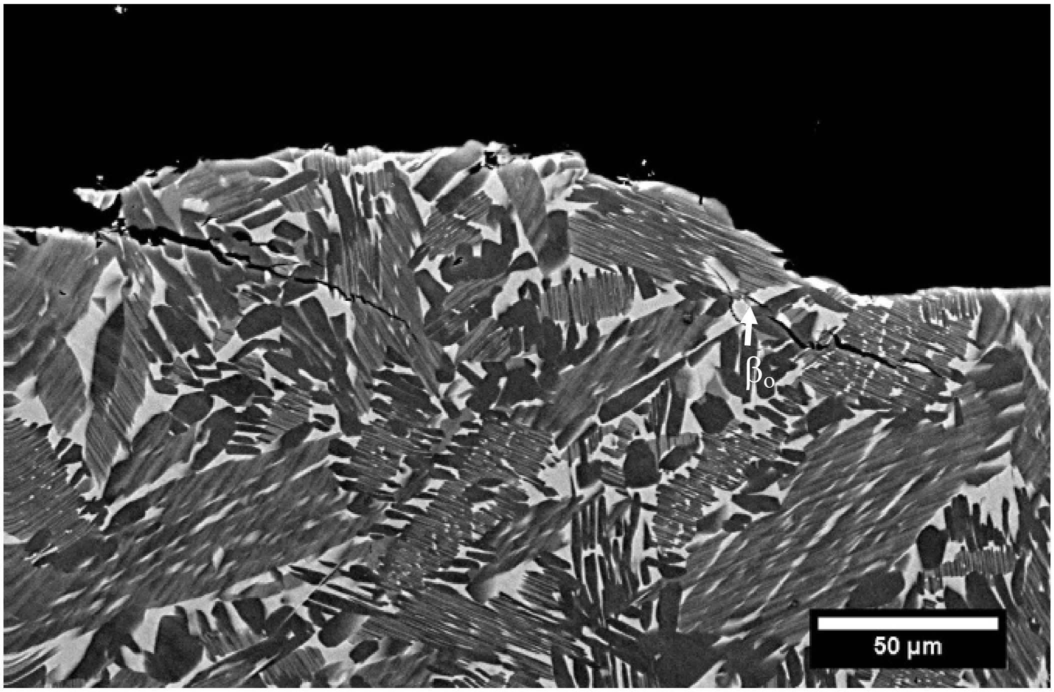

Figure 4.31: SEM-BSE image of the polished midplane of as-cast + HIP TNM tensile specimen tested at room temperature at a strain rate of $0.001s^{-1}$. Subsurface damage was evident in all samples.

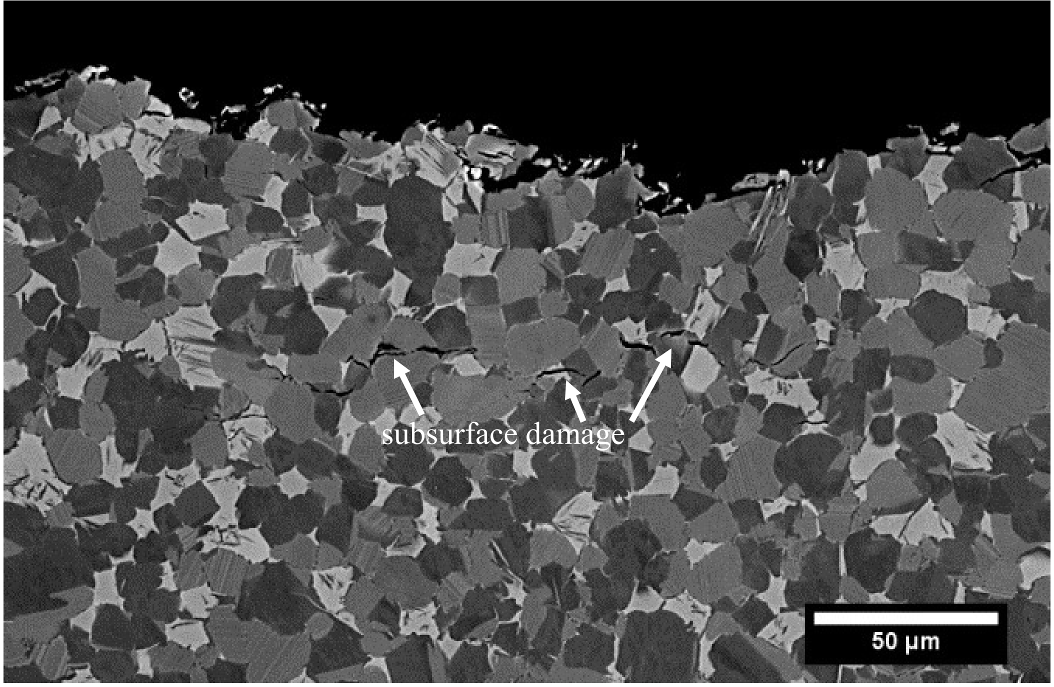

Figure 4.32: SEM-BSE image of the polished midplane of upset-forged TNM tensile specimen tested at room temperature at a strain rate of $0.001s^{-1}$. Subsurface damage was evident in all samples.

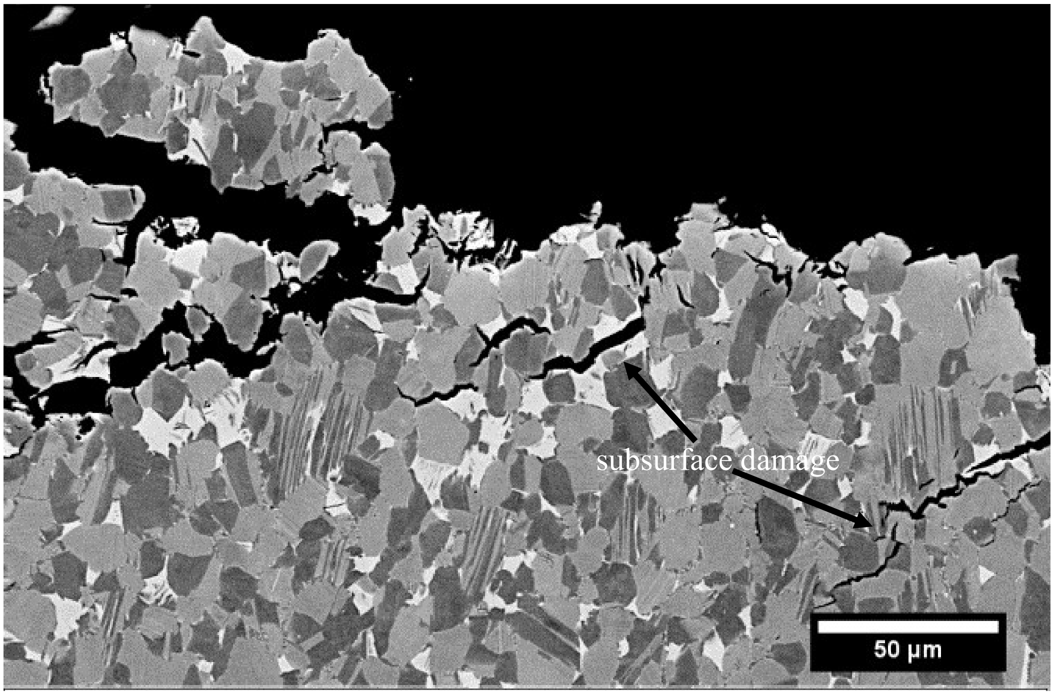

Figure 4.33: SEM-BSE image of the polished midplane of sidepress-forged TNM tensile specimen tested at room temperature at a strain rate of $0.001 s^{-1}$. Subsurface damage was evident in all samples.

The X-ray diffraction conducted on the tensile fracture surfaces is shown in Figure 4.34 while the resulting phase fractions present, using the normalized area under peaks, are summarized in Table 4.3. XRD of the fracture surface of the as-cast and as-cast + HIP samples clearly shows β_0 phase, Figure 4.34 and Table 4.3. This, combined with the SEM-BSE images of the cross-sections reveals preferential cracking along the β_o phase in the as-cast and as-cast+ HIP samples. XRD of fracture surfaces can only be used for qualitative comparisons since the highly non-planar fracture surfaces produce high background noise and can cause pattern distortion.

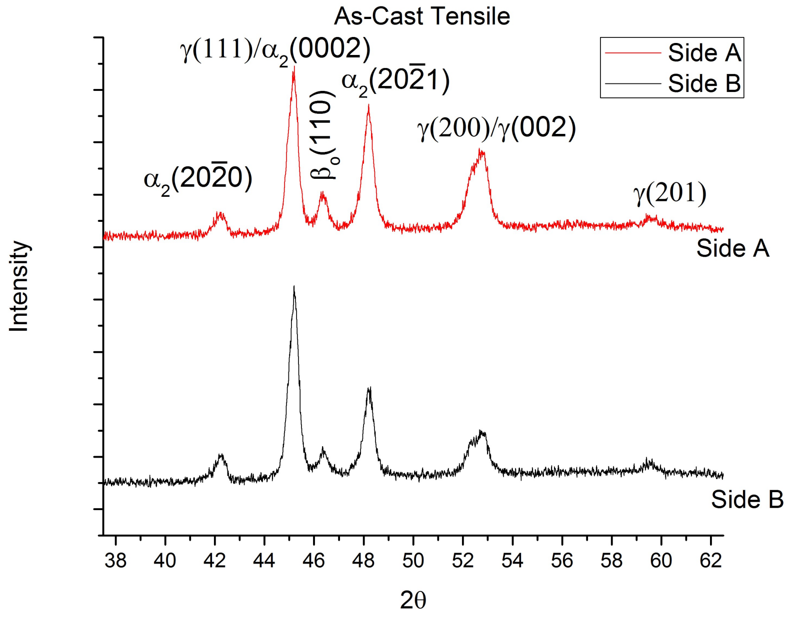

a

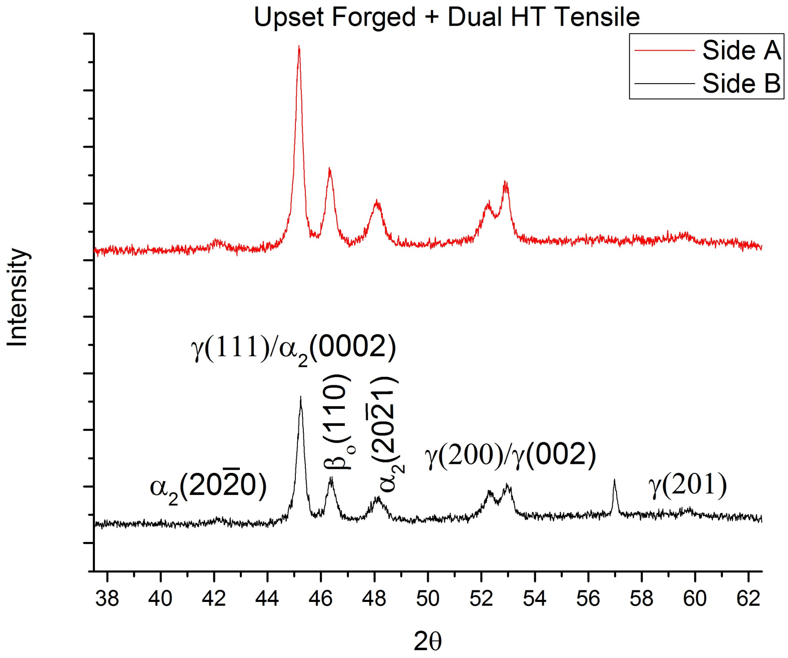

b

Figure 4.34: X-Ray diffraction results of both sides of TNM tensile specimens (a) as-cast (b) upset forged.

Table 4.3: Phase fractions on fracture surface of tensile from XRD scans using the area under the curve method

As-Cast	**Phase fraction (volume %)**
α_2	54,51
β_o	7,5
γ	38,43
HIPed	
α_2	32,41
β_o	12,9
γ	55,49
Upset Forged	
α_2	33,36
β_0	17,17
γ	49,46

In contrast to the as-cast and as-cast + HIP samples, the fracture path revealed by SEM-BSE and XRD in the upset-forged material suggest that the majority of the cracking occurs at the border of the β_o phase and other microstructure features. Phase fractions from XRD of the fracture surface are more similar to that exhibited in the polished cross-sections analyzed via SEM-BSE.

Tensile tests performed at elevated temperatures (Figures 4.26-4.28) exhibited a large drop in strength and increased elongation to failure at temperatures exceeding 700°C for both L and T specimens. The fracture surfaces shown in Figures 4.35-4.38 of the sidepress-forged material tested in the transverse directions at various temperatures reveal changes to the fracture surface morphology with an increasing temperature. The tensile specimens tested at 300 °C and 700 °C show ductile features amongst the more brittle faceted features. The 750 °C and 800°C tensile tests reveal cavitation on the fracture surface without any brittle facets. Figures 4.39-4.42 show the metallographic cross-sections of the fracture surfaces imaged with SEM-BSE. At the lower temperatures, cracking occurs between the phases and appears to be concentrated on the border of the β_o phase, accompanied by some interlamellar cracking. In the high temperature tensile tests, cavitation below the fracture surface is evident and consistent with the high elongation present at these temperatures. The majority of the cavitation occurs in the β_o phase as it is the weakest constituent at these temperatures [32].

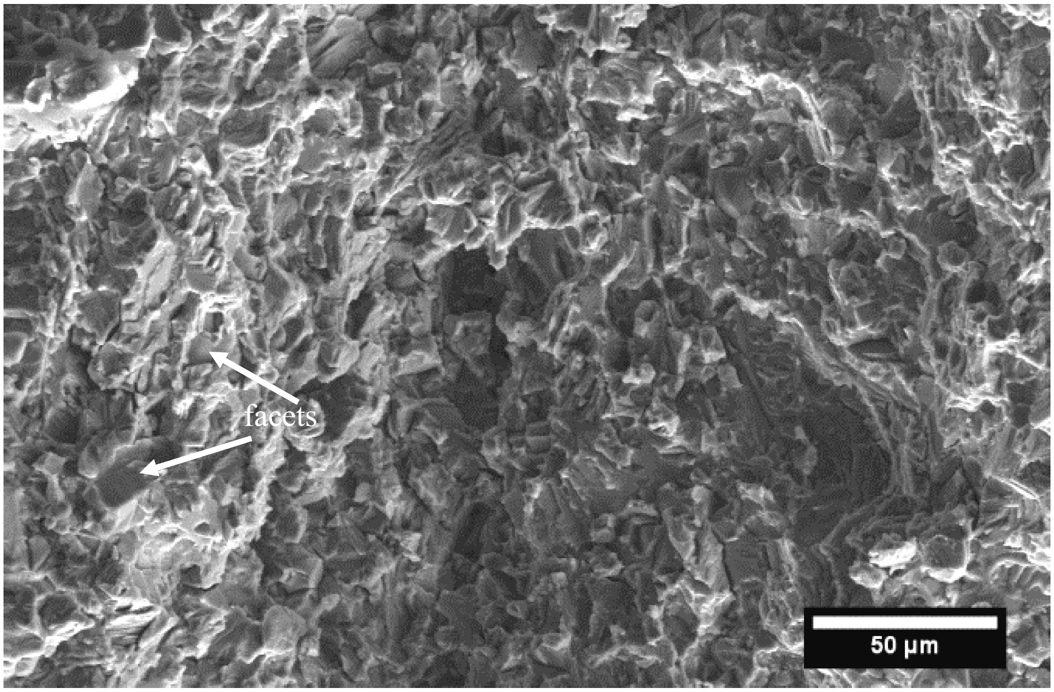

Figure 4.35: SEM-SE images of the tensile fracture surface taken of the sidepress-forged TNM specimen tested in air in the transverse direction at $0.001s^{-1}$ at 300°C.

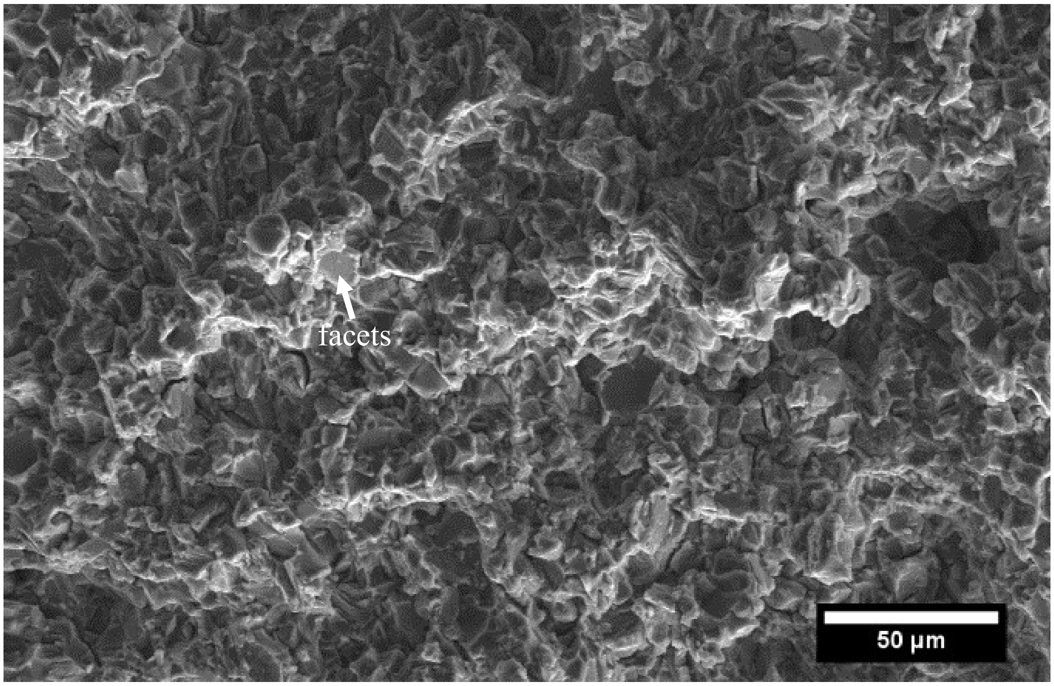

Figure 4.36: SEM-SE images of the tensile fracture surface taken of the sidepress-forged TNM specimen tested in air in the transverse direction at $0.001s^{-1}$ at 700°C.

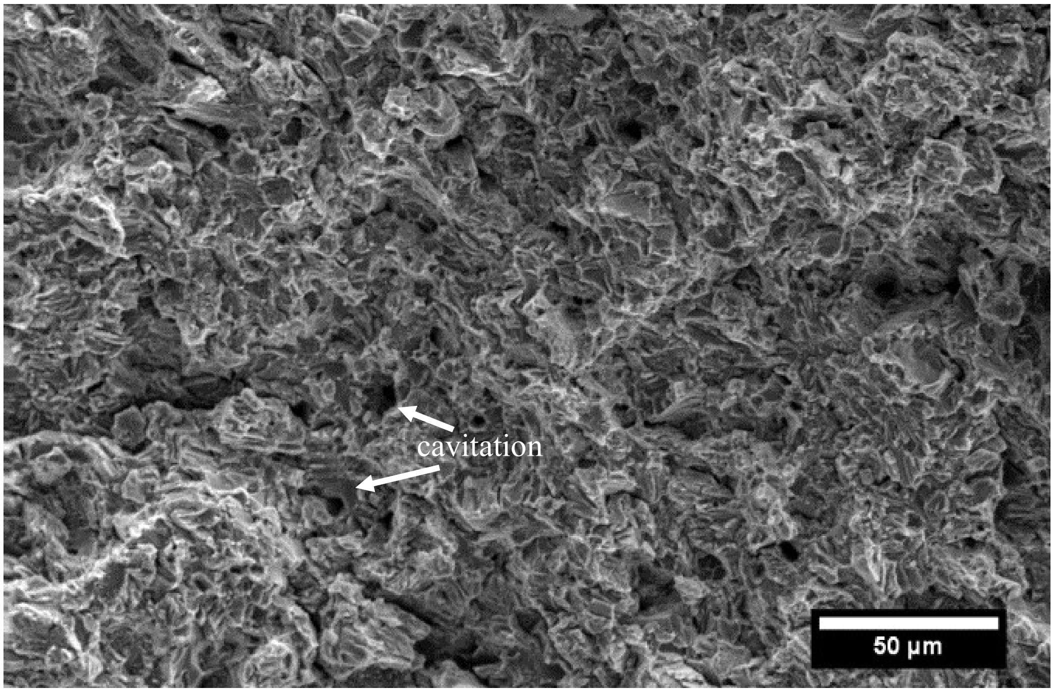

Figure 4.37: SEM-SE images of the tensile fracture surface taken of the sidepress-forged TNM specimen tested in air in the transverse direction at 0.001s^{-1} at 750°C.

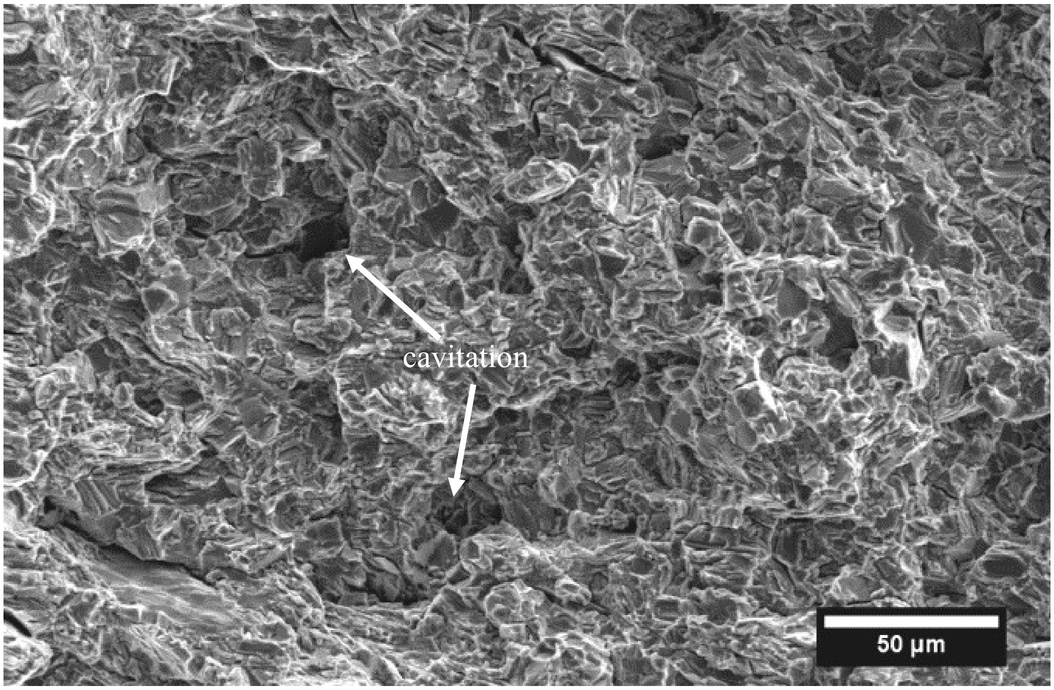

Figure 4.38: SEM-SE images of the tensile fracture surface taken of the sidepress-forged TNM specimen tested in air in the transverse direction at 0.001s^{-1} at 800°C.

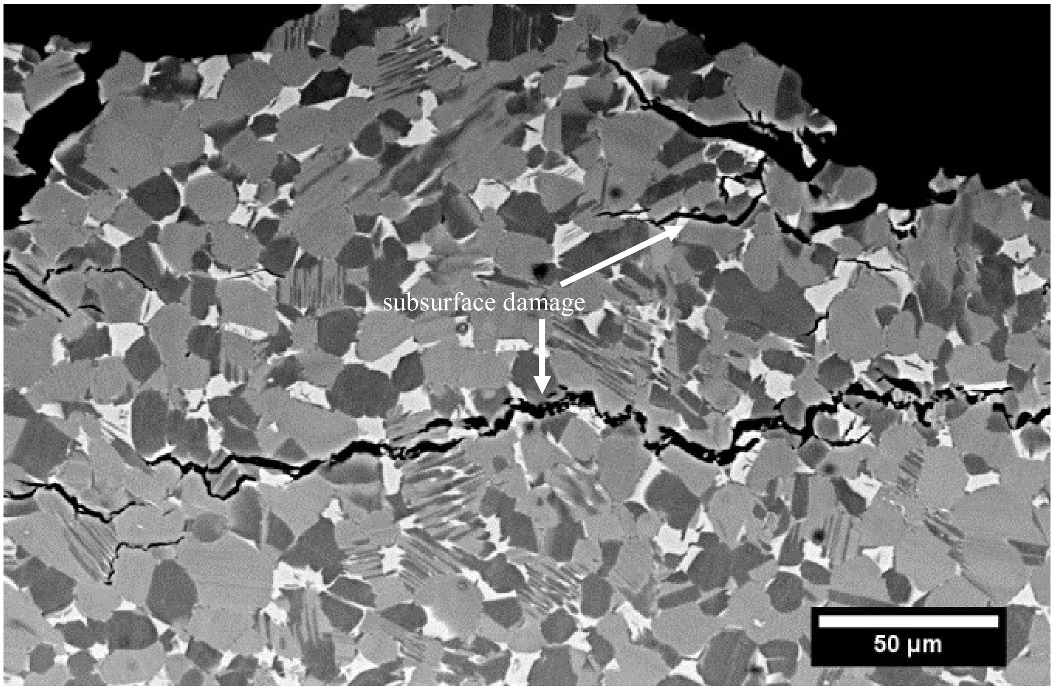

Figure 4.39: SEM-BSE image of the polished midplane of sidepress-forged TNM tensile specimen tested in the transverse direction at 300°C at a strain rate of 0.001s^{-1}. Subsurface damage was evident in all samples.

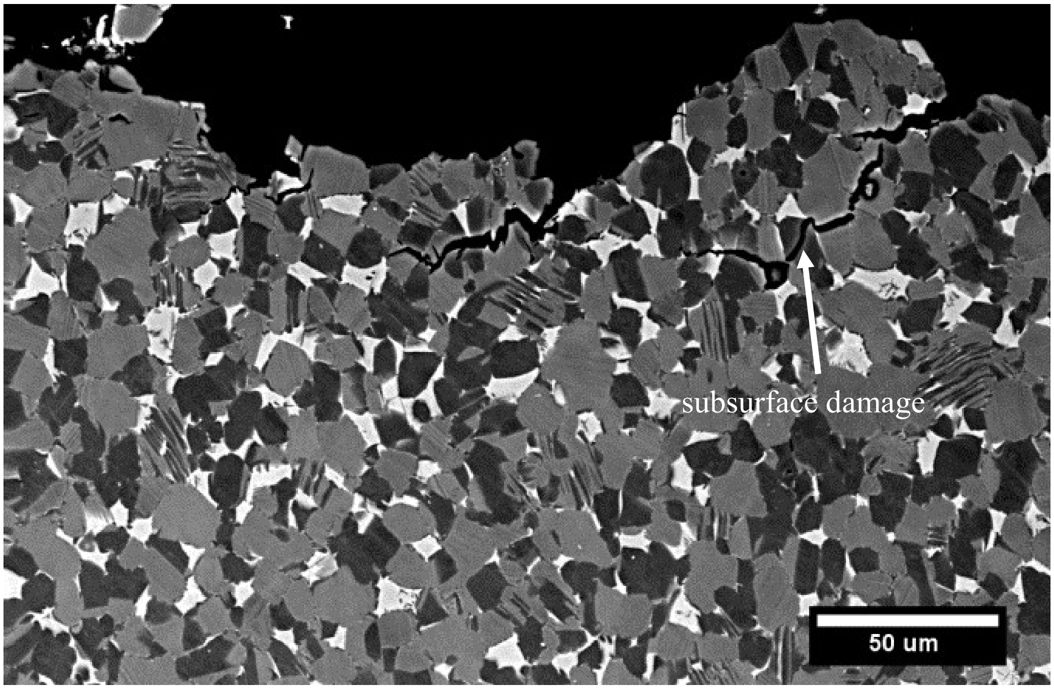

Figure 4.40: SEM-BSE image of the polished midplane of sidepress-forged TNM tensile specimen tested in the transverse direction at 700°C at a strain rate of 0.001s^{-1}. Subsurface damage was evident in all samples.

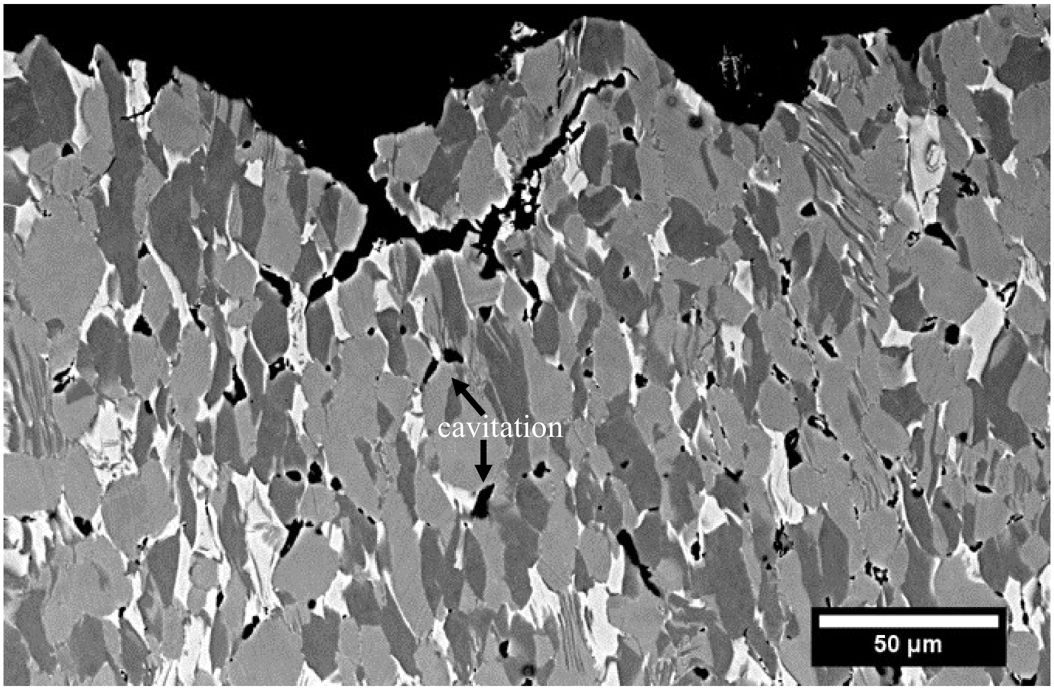

Figure 4.41: SEM-BSE image of the polished midplane of sidepress-forged TNM tensile specimen tested in the transverse direction at 750°C at a strain rate of $0.001s^{-1}$. Subsurface damage was evident in all samples.

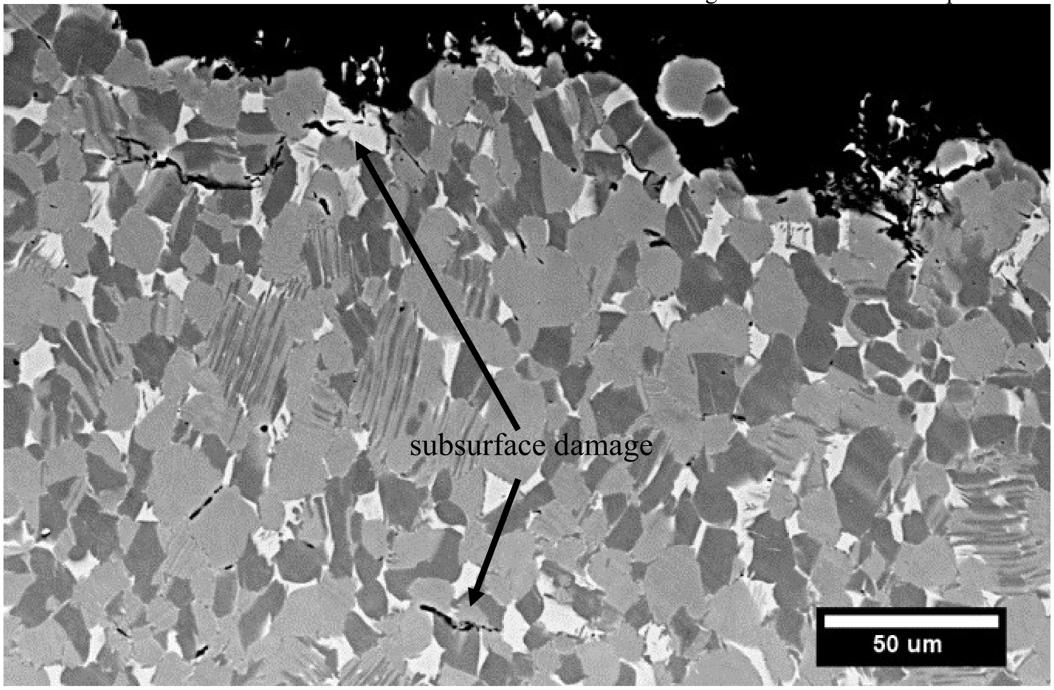

Figure 4.42: SEM-BSE image of the polished midplane of sidepress-forged TNM tensile specimen tested in the transverse direction at 800°C at a strain rate of $0.001s^{-1}$. Subsurface damage was evident in all samples.

The fatigue crack growth data reveals a significant effect of R on the magnitude of the ΔK_{th} for all materials except as-cast + HIPed, decreasing from over 9 MPa√m for R = 0.1 to less than 2 MPa√m at R = 0.9. The fracture surfaces for as-cast and as-cast +

HIP at low ΔK are presented in Figures 4.43-4.46 and show both inter- and translamellar cracking. Facets are also visible on the fracture surface. Figures 4.47-4.50 show the fracture surfaces of upset-forged and sidepress-forged material and reveal facets and small amounts translamellar fracture. Figures 4.51-4.54 show fracture surfaces at catastrophic overload . The forged specimens at catastrophic overload exhibited smaller facets than that exhibited by the as-cast and as-cast + HIP materials. Since the upset-forged specimens did not contain any lamellar structure, cracking occurred between the phases.

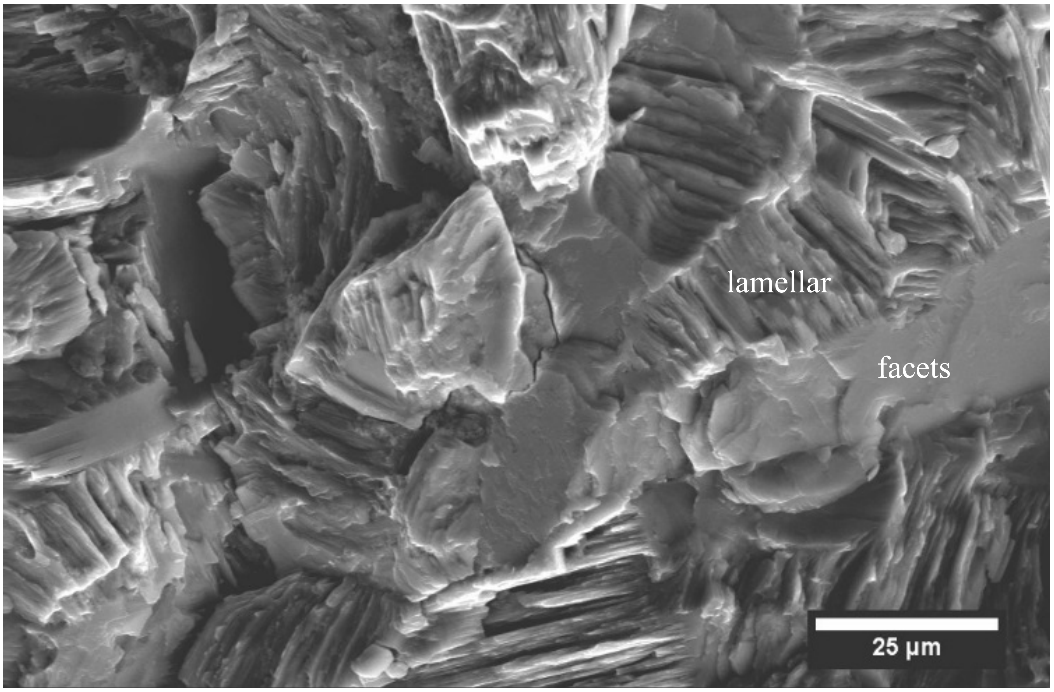

Figure 4.43: Representative fatigue crack SEM-SE fractography of as-cast (L-T) fatigue fracture features in the low ΔK regime at R = 0.3. Crack direction is from top to bottom.

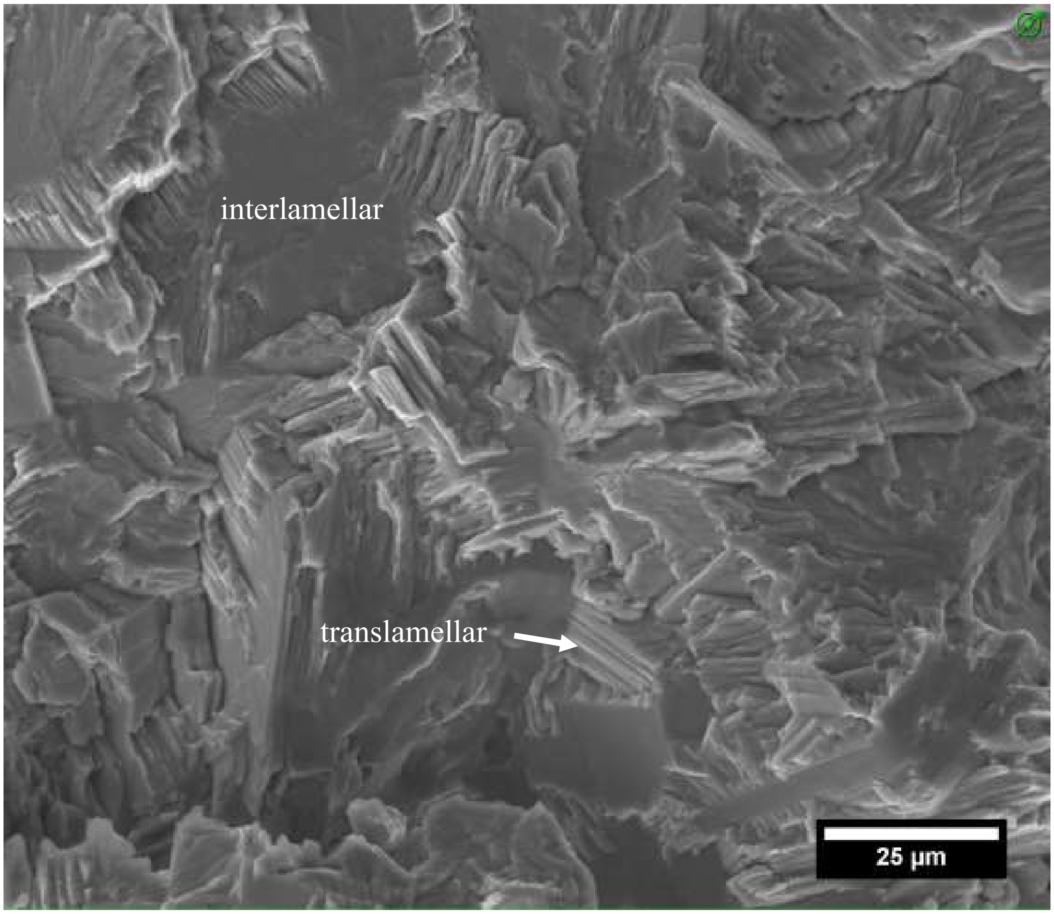

Figure 4.44: Representative fatigue crack SEM-SE fractography of as-cast (T-L) fatigue fracture features in the low ΔK regime at R = 0.3. Crack direction is from top to bottom.

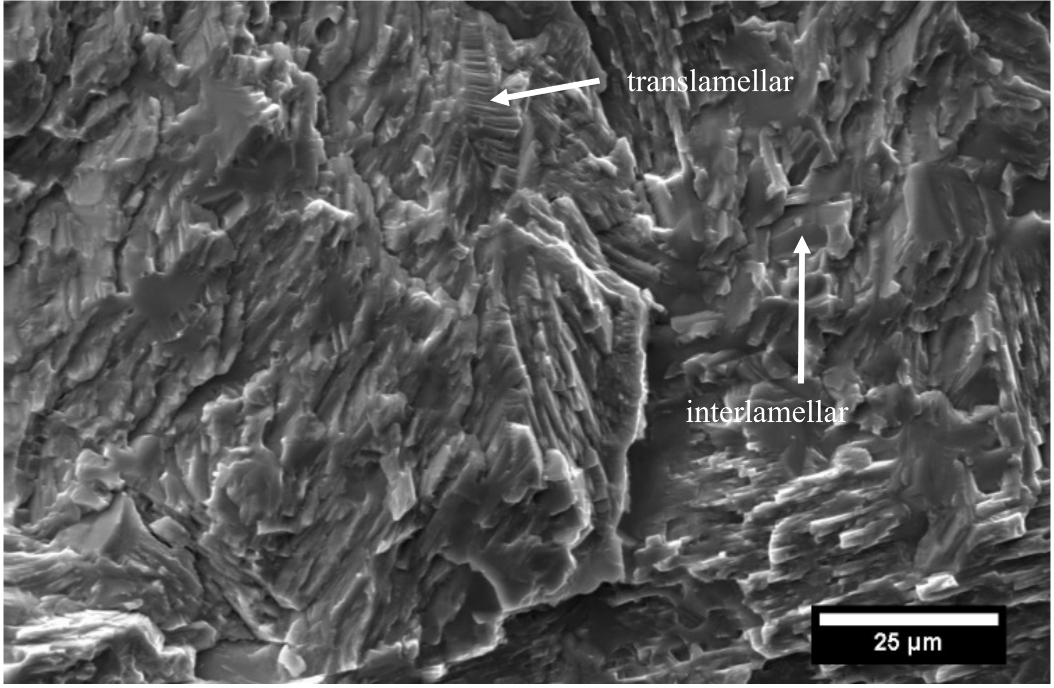

Figure 4.45: Representative fatigue crack SEM-SE fractography of as-cast + HIP (L-T) fatigue fracture features in the low ΔK regime at R = 0.3. Crack direction is from top to bottom.

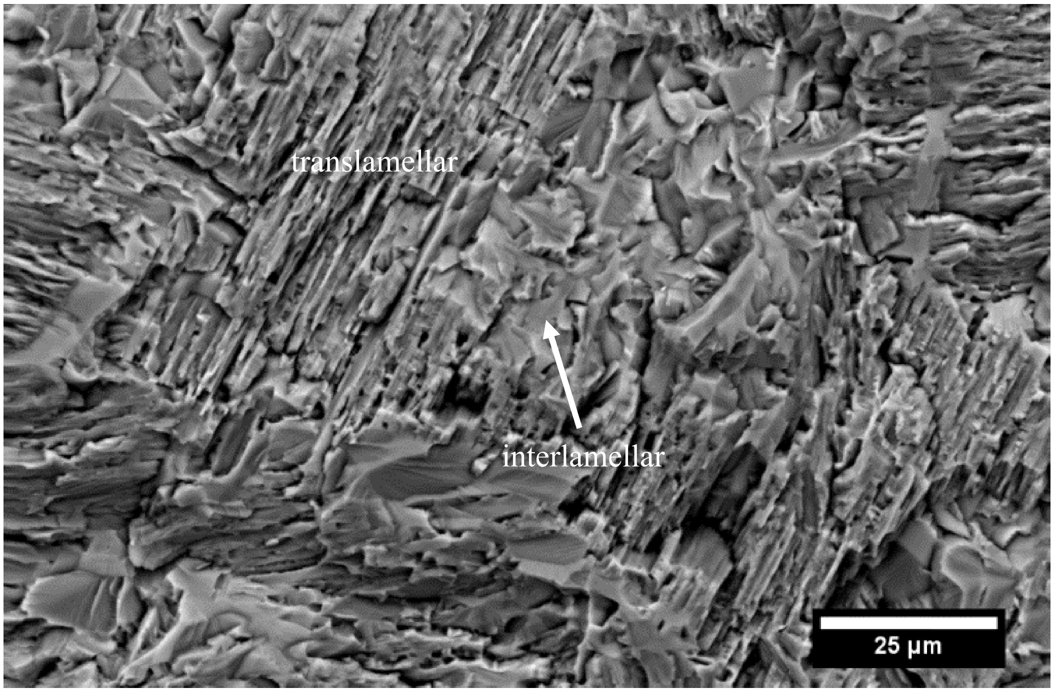

Figure 4.46: Representative fatigue crack SEM-SE fractography of as-cast + HIP (T-L) fatigue fracture features in the low ΔK regime at R = 0.3. Crack direction is from top to bottom.

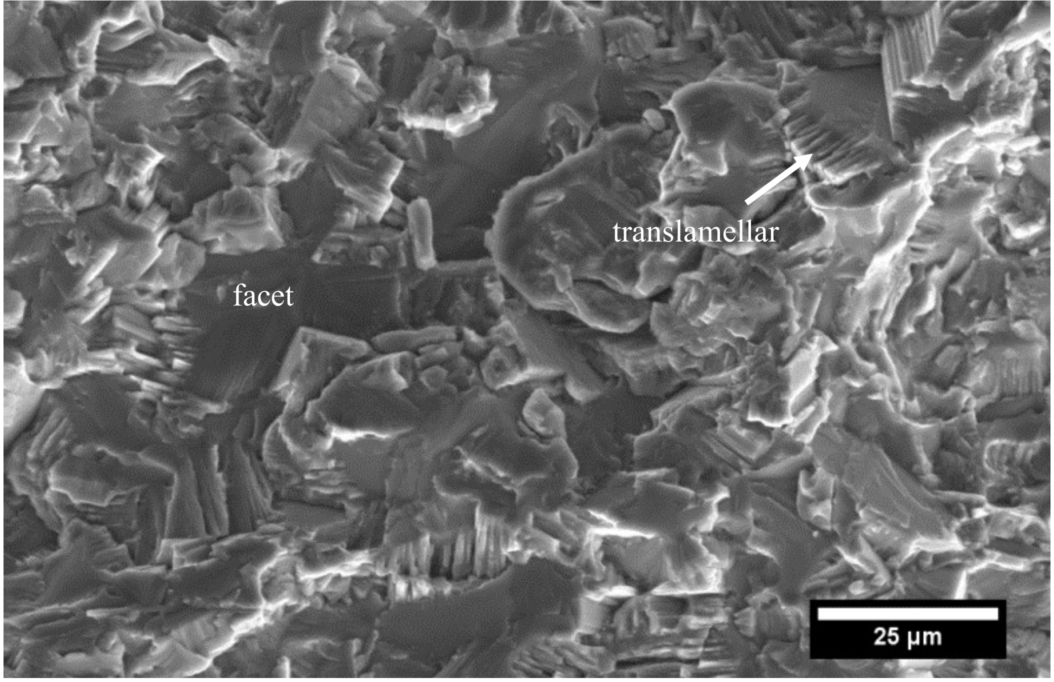

Figure 4.47: Representative fatigue crack SEM-SE fractography of upset-forged fatigue fracture features in the low ΔK regime at R = 0.1. Crack direction is from top to bottom.

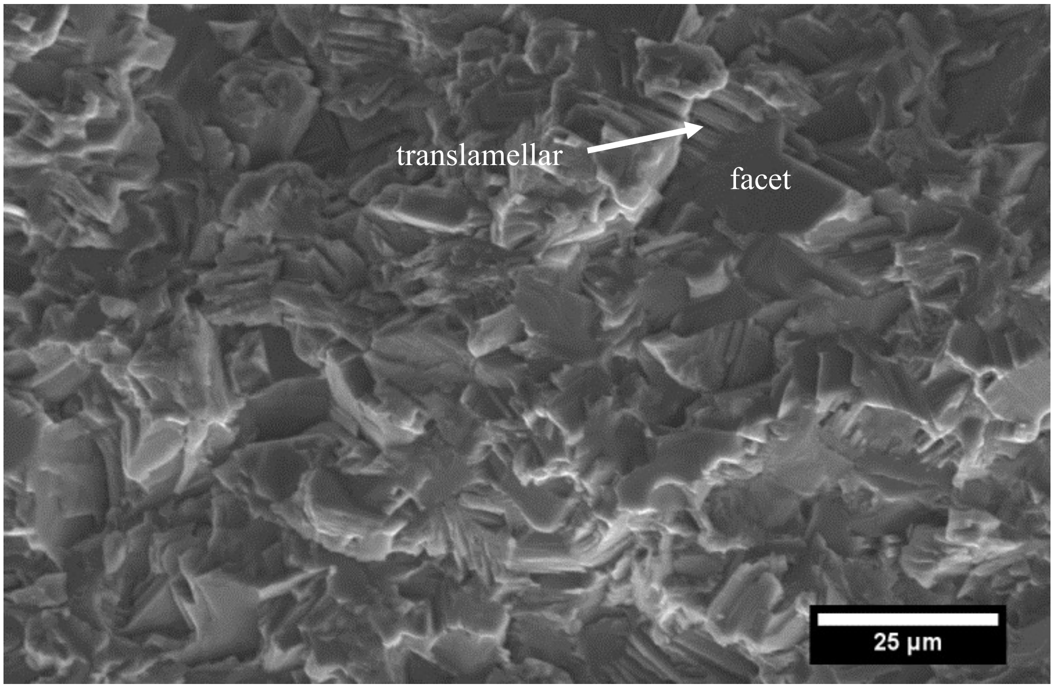

Figure 4.48: Representative fatigue crack SEM-SE fractography of upset-forged fatigue fracture features in the high ΔK regime at R = 0.1. Crack direction is from top to bottom.

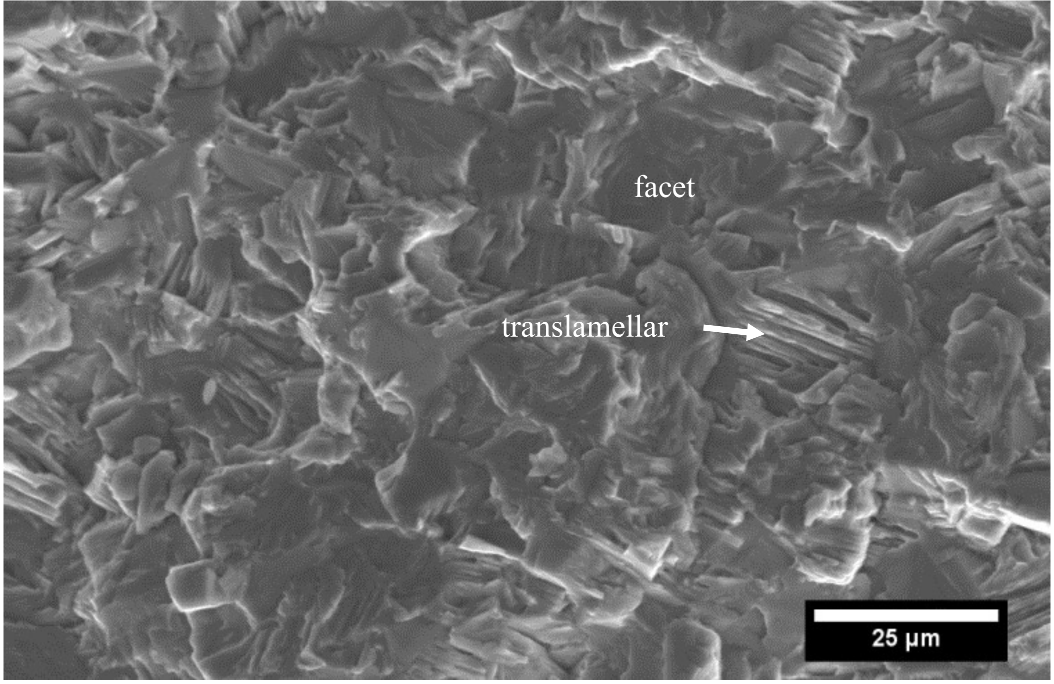

Figure 4.49: Representative fatigue crack SEM-SE fractography of sidepress-forged fatigue fracture features in the low ΔK regime at R = 0.1. Crack direction is from top to bottom.

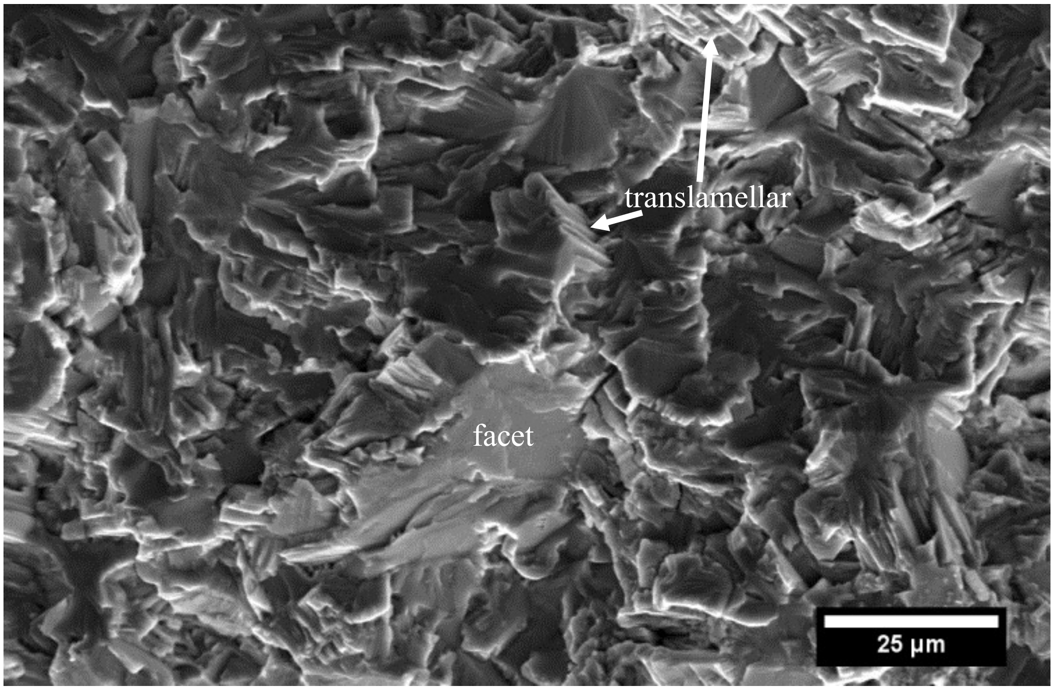

Figure 4.50: Representative fatigue crack SEM-SE fractography of sidepress-forged fatigue fracture features in the high ΔK regime at R = 0.1. Crack direction is from top to bottom.

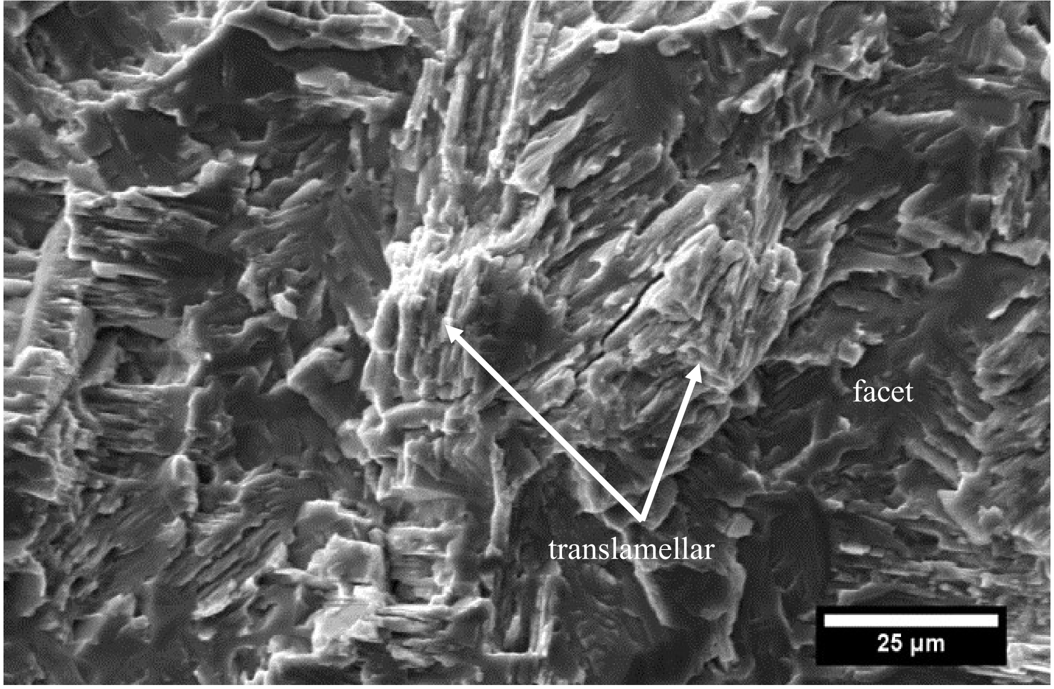

Figure 4.51: Representative fatigue crack SEM-SE fractography of as-cast (T-L) fatigue fracture features in the overload regime at R = 0.1. Crack direction is from top to bottom.

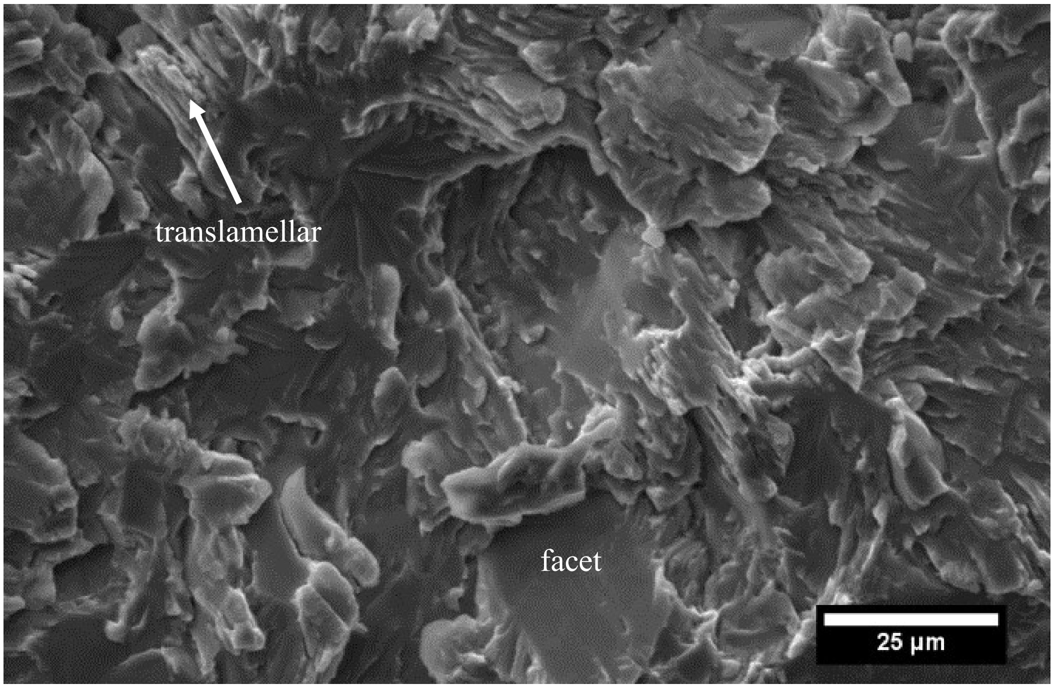

Figure 4.52: Representative fatigue crack SEM-SE fractography of as-cast + HIP (T-L) fatigue fracture features in the overload regime at R = 0.1. Crack direction is from top to bottom.

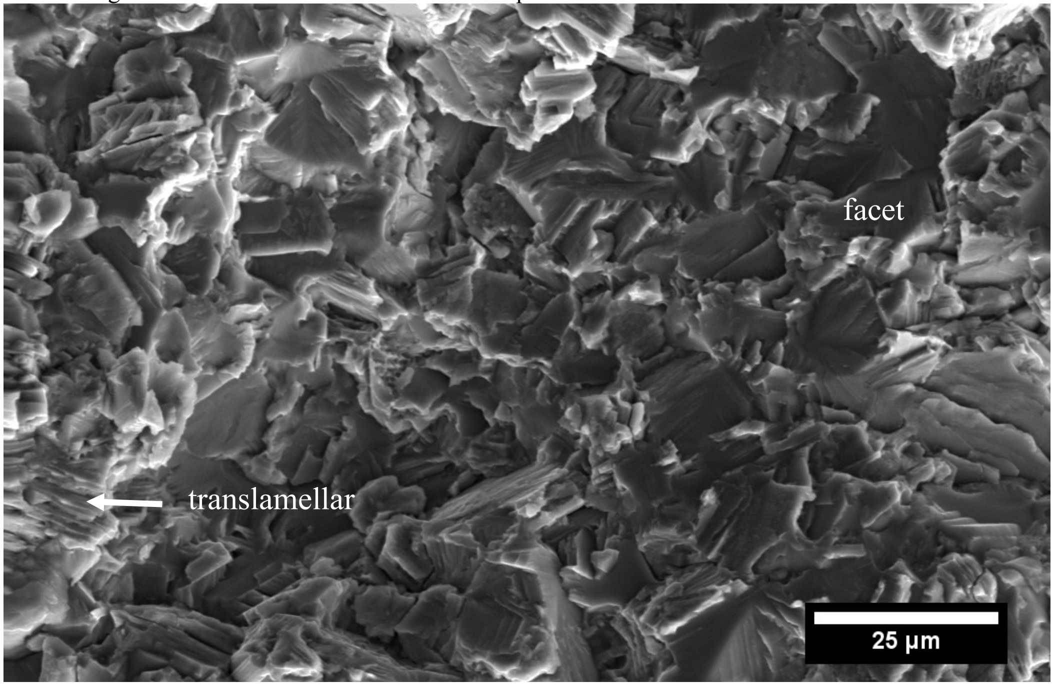

Figure 4.53: Representative fatigue crack SEM-SE fractography of upset-forged fatigue fracture features in the overload regime at R = 0.1. Crack direction is from top to bottom.

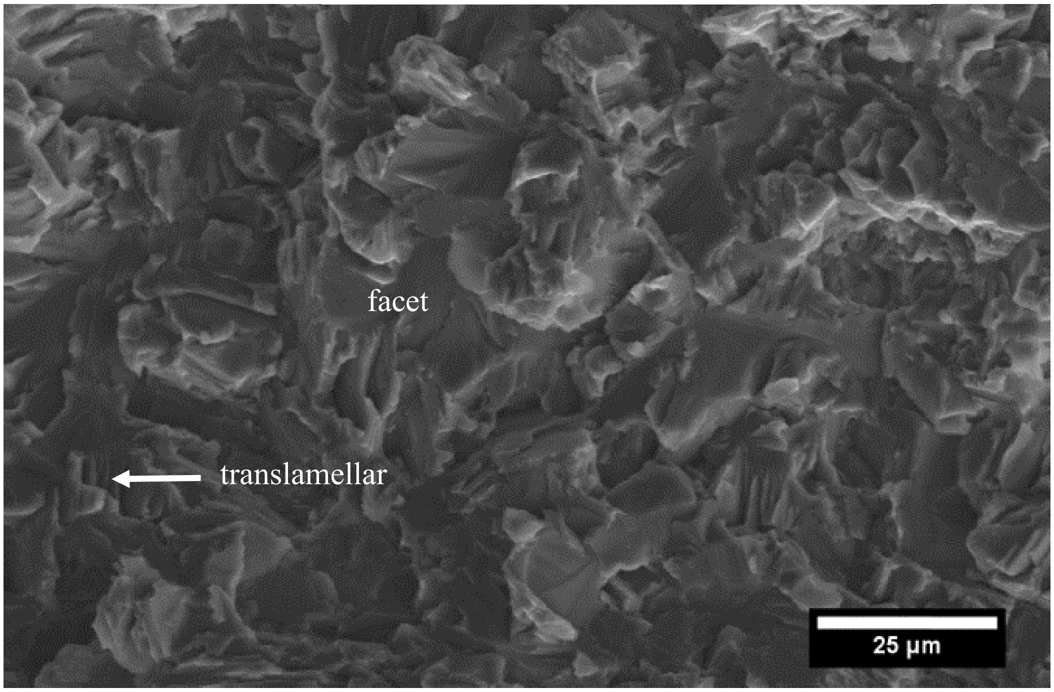

Figure 4.54: Representative fatigue crack SEM-SE fractography of sidepress-forged fatigue fracture features in the overload regime at R = 0.1. Crack direction is from top to bottom.

The X-ray diffraction traces for the different regions of the fatigue fracture surfaces are provided in Figure 4.55, while the resulting phase fractions present, utilizing the normalized area under peaks, are summarized in Table 4.4. XRD of threshold, Paris Regime, and overload regions indicates that the crack path likely changes during different portions of the d*a*/d*N* vs. ΔK plots. As summarized in Table 5, the as-cast specimens exhibited a larger amount of β_o phase on the fatigue fracture surface in the Paris regime and overload region than is present in the bulk. The smaller amount of β_o found at threshold vs Paris regime and overload leads to the suggestion the cracking is starting in the lamellar microstructure and then cracking to a boundary with β_o and following the β_o in the Paris and overload regimes. This type of cracking was also reported in work by Wessel [82]. In that work cracks in the lameller region at α_2/γ boundaries that propagated to the colony boundary then produced cracks in the β_o phase. This further supports the assertion that fatigue cracks preferentially propagate along the β_o phase in the as-cast and as-cast + HIP material. In contrast, both the upset-forged and sidepress-forged fatigue fracture surface exhibits a more random phase fraction present throughout the crack path, suggesting that no preferential crack path is present. This is also consistent with the tensile sample crack path fractography.

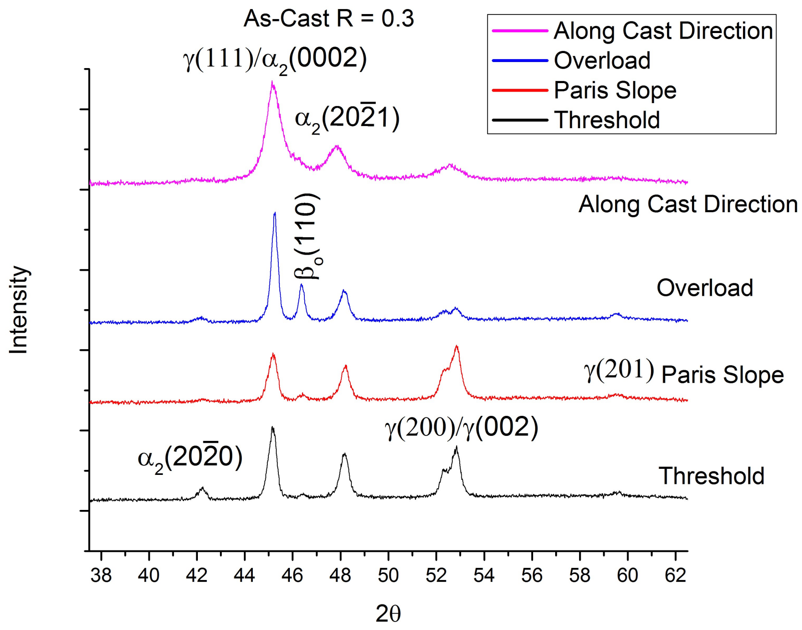

(a)

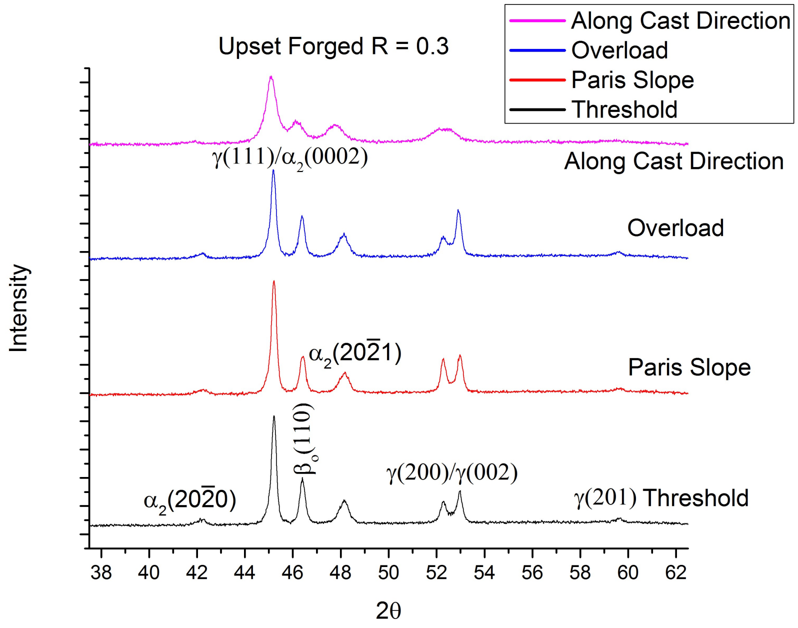

(b)

Figure 4.55: X-Ray diffraction results at different regions of the fatigue fracture surface of TNM sample fatigue in room tmeperature lab air at R = 0.3 (a) as-cast (b) Upset-forged.

Table 4.4: Phase fractions present on different regions of fatigue fracture surfaces from XRD scans using the area under the curve method compared to metallography.

	Phase Fraction (Volume %)			
	Threshold region	**Paris Slope region**	**Overload region**	**Polished cross section along cast direction**
As-Cast				
α_2	45,45	50,37	50,48	57
β_o	0,0.5	0.9,2	6,15	0
γ	54,54	49,56	44,37	43
Upset Forged				
α_2	37,38	40,37	35,37	45
β_o	11,17	15,15	13,16	15
γ	52,45	45,49	51,48	40
Sidepress Forged				
α_2	44,49	42,41	40,40	41
β_0	14,11	9,9	7,9	8
γ	41,40	49,50	52,51	51

To further examine the source(s) of crack path selection and microstructure effects with changes in ΔK and K_{max} during fatigue crack growth, the monotonic and cyclic plastic zone sizes were calculated to determine the microstructural features sampled. The maximum monotonic plane-strain plastic zone radius is given by

$$r_{os} = \frac{1}{6\pi}\left[\frac{K_{max}}{\sigma_o}\right]^2 \tag{4.3}$$

where σ_o is the yield strength of the material (680 MPa for as-cast and as-cast + HIPed and 755 MPa for forged) [54], and K_{max} is the maximum stress intensity in the fatigue cycle at different regions of the d*a*/d*N* vs. ΔK plot (e.g., threshold, Paris Law, overload). The cyclic plastic zone size is smaller than that in static loading and is affected by reverse plasticity [54] that leaves a wake of plasticity behind the crack tip. This induces residual stress in the crack tip region which also may play a role in crack closure. The cyclic plastic zone radius is given by

$$r_{oc} = \frac{1}{6\pi}\left[\frac{\Delta K}{2\sigma_o}\right]^2 \qquad (4.4)$$

The calculated size of the maximum monotonic and cyclic plastic zone sizes at ΔK_{th} and overload for both orientations and microstructures are given in Table 4.5, assuming plain-strain conditions. The maximum plastic zone radius size using K_{max} at threshold for the as-cast L-T material at R = 0.3 is 7-9 μm, comparable to the colony size (20-40 μm), while the As-Cast + HIPed at R = 0.3 is 3.3 μm and 17.7 μm again similar to the colony size. For forged and heat treated specimens tested at R = 0.3, the maximum plastic zone size is 7.8-9.6 μm. Similar maximum plastic zone sizes are calculated at threshold for the other R values and orientations when using $K_{max,}$ Table 4.5.

In contrast, the cyclic plastic zone is considerably smaller than the colony size at the fatigue threshold for all the R values and orientations tested, indicating that only a single colony is sampled in the plane of view, and only about 500 colonies are sampled across the thickness for the as-cast TNM samples. Thus, the orientation of only a few colonies will dominate the cyclic plastic zone size and crack growth if cyclic plasticity controls cracking.

Table 4.5: Cyclic plastic zone of TNM at thresholds calculated with ΔK and K_{max}

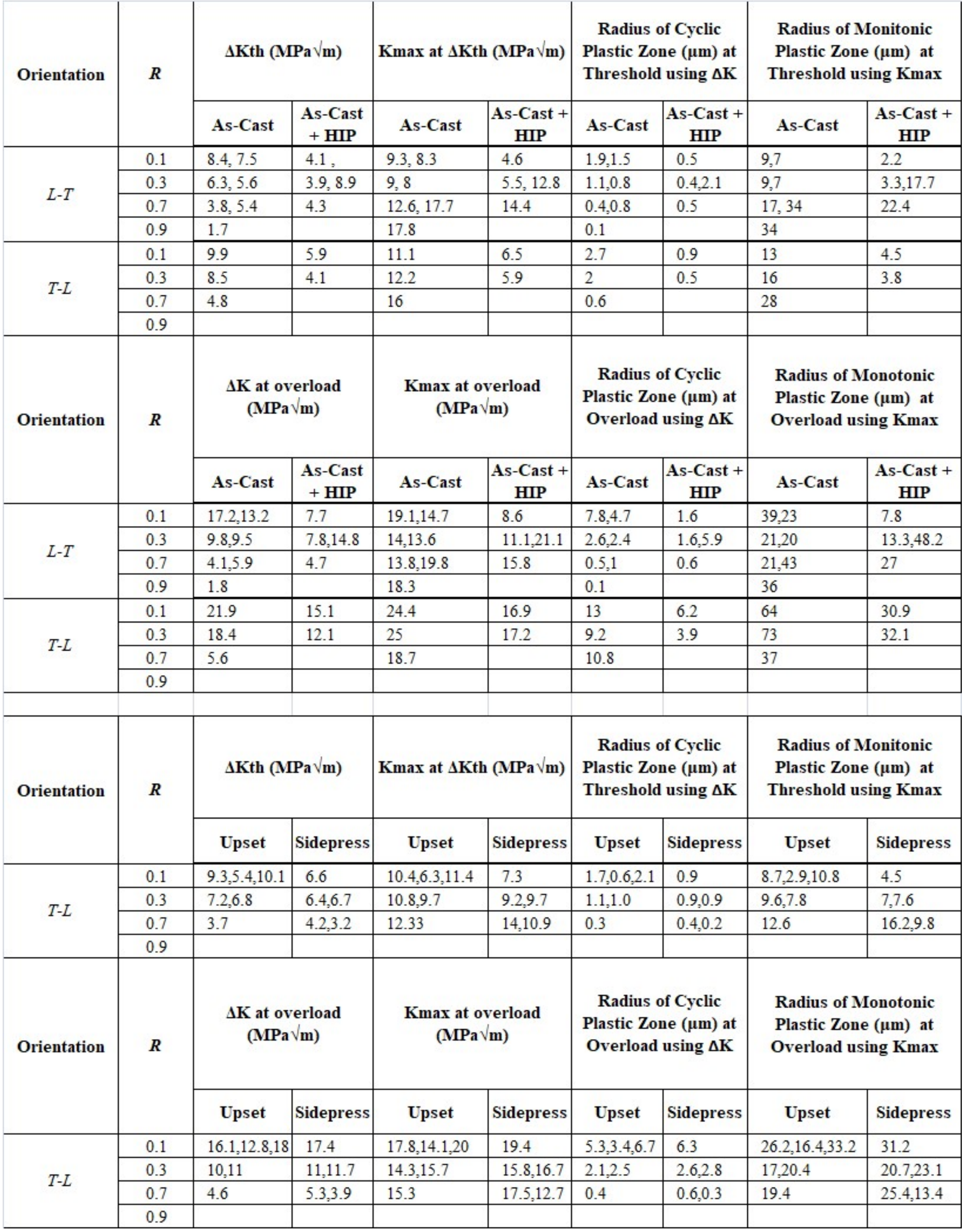

Orientation	R	ΔKth (MPa√m)		Kmax at ΔKth (MPa√m)		Radius of Cyclic Plastic Zone (µm) at Threshold using ΔK		Radius of Monitonic Plastic Zone (µm) at Threshold using Kmax	
		As-Cast	As-Cast + HIP	As-Cast	As-Cast + HIP	As-Cast	As-Cast + HIP	As-Cast	As-Cast + HIP
L-T	0.1	8.4, 7.5	4.1 ,	9.3, 8.3	4.6	1.9,1.5	0.5	9,7	2.2
	0.3	6.3, 5.6	3.9, 8.9	9, 8	5.5, 12.8	1.1,0.8	0.4,2.1	9,7	3.3,17.7
	0.7	3.8, 5.4	4.3	12.6, 17.7	14.4	0.4,0.8	0.5	17, 34	22.4
	0.9	1.7		17.8		0.1		34	
T-L	0.1	9.9	5.9	11.1	6.5	2.7	0.9	13	4.5
	0.3	8.5	4.1	12.2	5.9	2	0.5	16	3.8
	0.7	4.8		16		0.6		28	
	0.9								

Orientation	R	ΔK at overload (MPa√m)		Kmax at overload (MPa√m)		Radius of Cyclic Plastic Zone (µm) at Overload using ΔK		Radius of Monotonic Plastic Zone (µm) at Overload using Kmax	
		As-Cast	As-Cast + HIP	As-Cast	As-Cast + HIP	As-Cast	As-Cast + HIP	As-Cast	As-Cast + HIP
L-T	0.1	17.2,13.2	7.7	19.1,14.7	8.6	7.8,4.7	1.6	39,23	7.8
	0.3	9.8,9.5	7.8,14.8	14,13.6	11.1,21.1	2.6,2.4	1.6,5.9	21,20	13.3,48.2
	0.7	4.1,5.9	4.7	13.8,19.8	15.8	0.5,1	0.6	21,43	27
	0.9	1.8		18.3		0.1		36	
T-L	0.1	21.9	15.1	24.4	16.9	13	6.2	64	30.9
	0.3	18.4	12.1	25	17.2	9.2	3.9	73	32.1
	0.7	5.6		18.7		10.8		37	
	0.9								

Orientation	R	ΔKth (MPa√m)		Kmax at ΔKth (MPa√m)		Radius of Cyclic Plastic Zone (µm) at Threshold using ΔK		Radius of Monitonic Plastic Zone (µm) at Threshold using Kmax	
		Upset	Sidepress	Upset	Sidepress	Upset	Sidepress	Upset	Sidepress
T-L	0.1	9.3,5.4,10.1	6.6	10.4,6.3,11.4	7.3	1.7,0.6,2.1	0.9	8.7,2.9,10.8	4.5
	0.3	7.2,6.8	6.4,6.7	10.8,9.7	9.2,9.7	1.1,1.0	0.9,0.9	9.6,7.8	7,7.6
	0.7	3.7	4.2,3.2	12.33	14,10.9	0.3	0.4,0.2	12.6	16.2,9.8
	0.9								

Orientation	R	ΔK at overload (MPa√m)		Kmax at overload (MPa√m)		Radius of Cyclic Plastic Zone (µm) at Overload using ΔK		Radius of Monotonic Plastic Zone (µm) at Overload using Kmax	
		Upset	Sidepress	Upset	Sidepress	Upset	Sidepress	Upset	Sidepress
T-L	0.1	16.1,12.8,18	17.4	17.8,14.1,20	19.4	5.3,3.4,6.7	6.3	26.2,16.4,33.2	31.2
	0.3	10,11	11,11.7	14.3,15.7	15.8,16.7	2.1,2.5	2.6,2.8	17,20.4	20.7,23.1
	0.7	4.6	5.3,3.9	15.3	17.5,12.7	0.4	0.6,0.3	19.4	25.4,13.4
	0.9								

While the cyclic plastic zone size at threshold is on the order of the interlamellar spacing, the maximum plastic zone size at threshold approaches the colony size for the as-cast material. Thus, at high R values, the maximum plastic zone size will sample a full colony at threshold in the as-cast material as well as the β_o on the colony boundaries. Schematics of the plastic zones are shown in Figures 4.56 and 4.57 for tests conducted at R = 0.1. For the as-cast material, the material sampled by the maximum monotonic plastic zone will enable the crack to follow the brittle β_o phase present on the colony boundaries, producing the large effect of R on the threshold, if dominated by K_{max} [83]. This is consistent with the fatigue fracture surface of the as-cast sample shown in Figures 4.43 and 4.44, that reveals a rough fracture path that arises from following the β_o on the colony boundaries. At catastrophic overload, the maximum plastic zone is on the order of the colony size at all R values, which allows easy sampling of the brittle β_o on the colony boundaries throughout the sample thickness, producing similar values for K_{max} at failure for all R values.

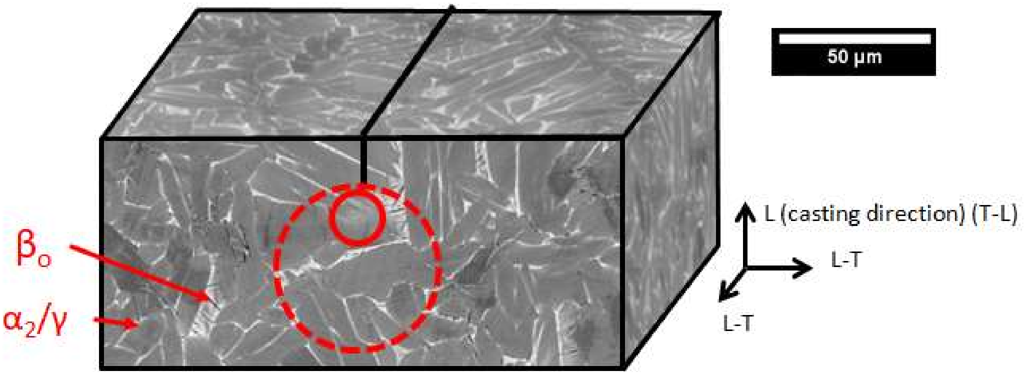

Figure 4.56: Maximum monotonic and cyclic plastic zone sizes calculated for fatigue crack growth experiments conducted at R = 0.1 for as-cast. The solid line represents the calculated plastic zone size at threshold; dashed line for overload.

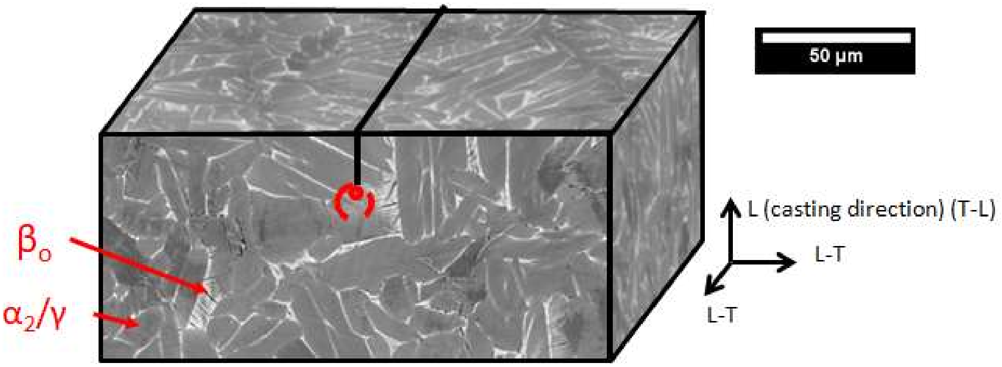

Figure 4.57: Cyclic plastic zone sizes calculated for fatigue crack growth experiments conducted at R = 0.1 for as-cast. The solid line represents the calculated plastic zone size at threshold; dashed line for overload.

The cyclic plastic zone at threshold for the as-cast + HIP material is also on the order of the interlamellar spacing, while the maximum plastic zone at threshold approaches the size of the microstructural features. The plastic zone samples the large amounts of globular β_o in the HIPed specimens. In this case, the propagating fatigue crack samples the brittle β_o, producing a smaller drop in ΔK_{th} than exhibited by the other microstructures. The maximum plastic zone size at overload enables sampling of β_o, producing a similar K_{max} at failure regardless of R, similar to the as-cast material.

The forged plus heat treated specimens produce a cyclic plastic zone size at threshold that is on the order of the interlamellar spacing, while the maximum plastic zone size at threshold is on the order of the larger microstructural features. Based on this, the maximum plastic zone size can sample one phase in the field of view, enabling cracking in that single phase or phase boundary. Schematics of the plastic zones are shown with the microstructures in Figures 4.58-4.61 Since there is no continuous β_o for cracking to follow, the crack to must select the other phases. This also suggests that small changes to the microstructure and phase contiguity could have a large effect on fatigue crack growth.

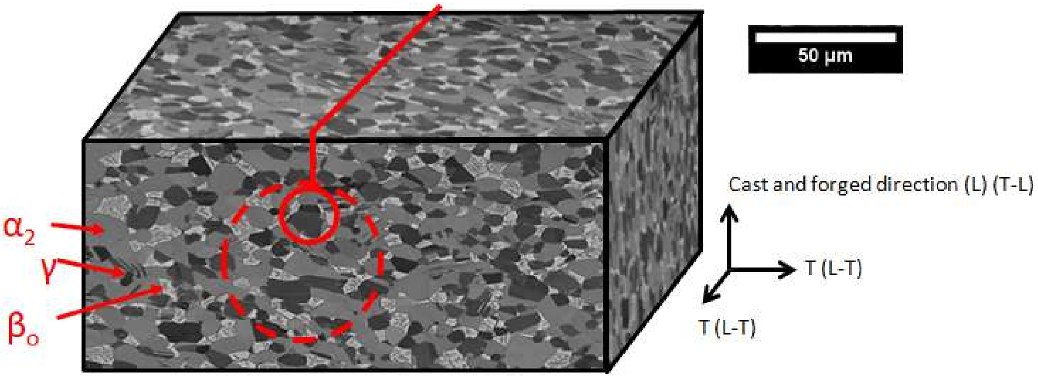

Figure 4.58: Maximum monotonic plastic zone sizes calculated for fatigue crack growth experiments conducted at R = 0.1 for upset-forged. The solid line represents the calculated plastic zone size at threshold; dashed line for overload.

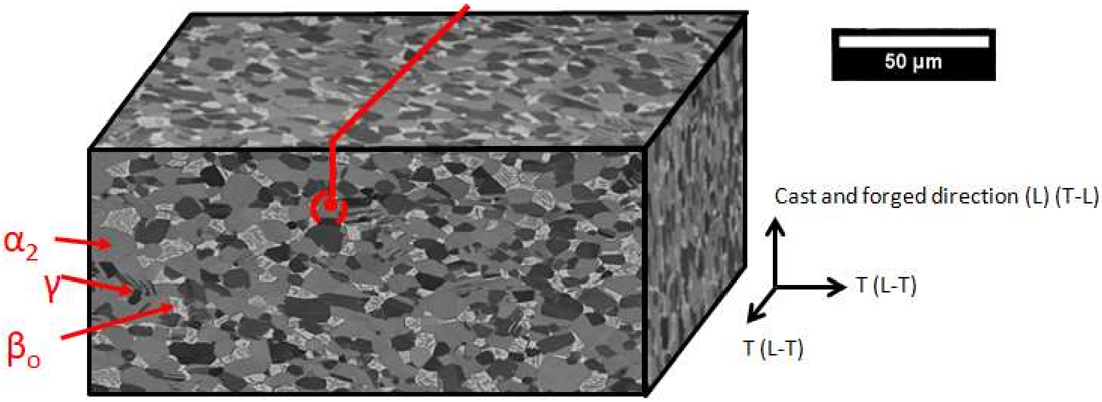

Figure 4.59: Cyclic plastic zone sizes calculated for fatigue crack growth experiments conducted at R = 0.1 for upset-forged. The solid line represents the calculated plastic zone size at threshold; dashed line for overload.

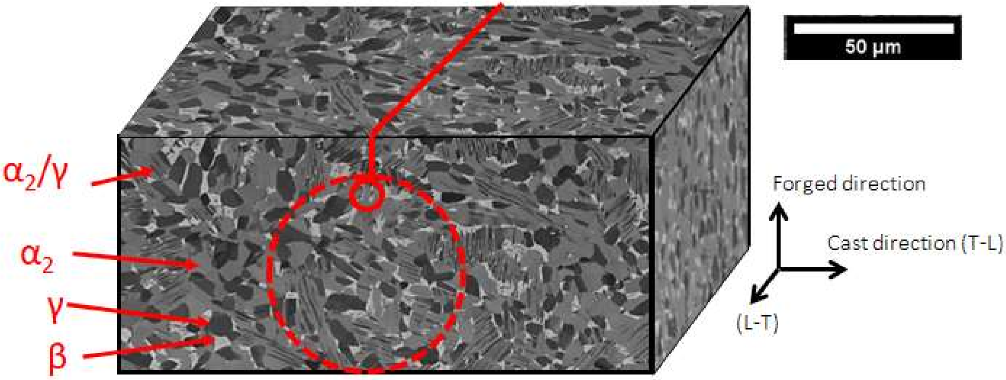

Figure 4.60: Maximum plastic zone sizes calculated for fatigue crack growth experiments conducted at R = 0.1 for sidepress-forged. The solid line represents the calculated plastic zone size at threshold; dashed line for overload.

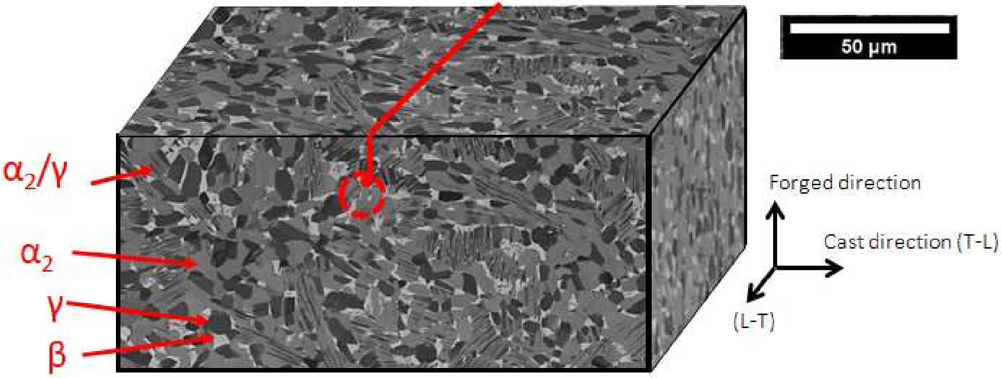

Figure 4.61: Cyclic plastic zone sizes calculated for fatigue crack growth experiments conducted at R = 0.1 for sidepress-forged. The solid line represents the calculated plastic zone size at threshold; dashed line for overload.

To examine the specific dependence of K_{max} on fatigue, the fracture crack growth rate data d*a*/d*N*, can be replotted vs. K_{max}. This was done in the past by Dauskardt with data on Al_2O_3-28% vol SiC as shown in Figure 4.62 [84]. The cyclic fatigue crack growth is clearly sensitive to the load ratio and the entire growth rate curve is shifted to lower values with increasing values of R . The fatigue data replotted vs K_{max} collapses onto a single line, indicating that K_{max} has dominant affect on the fatigue crack growth properties.

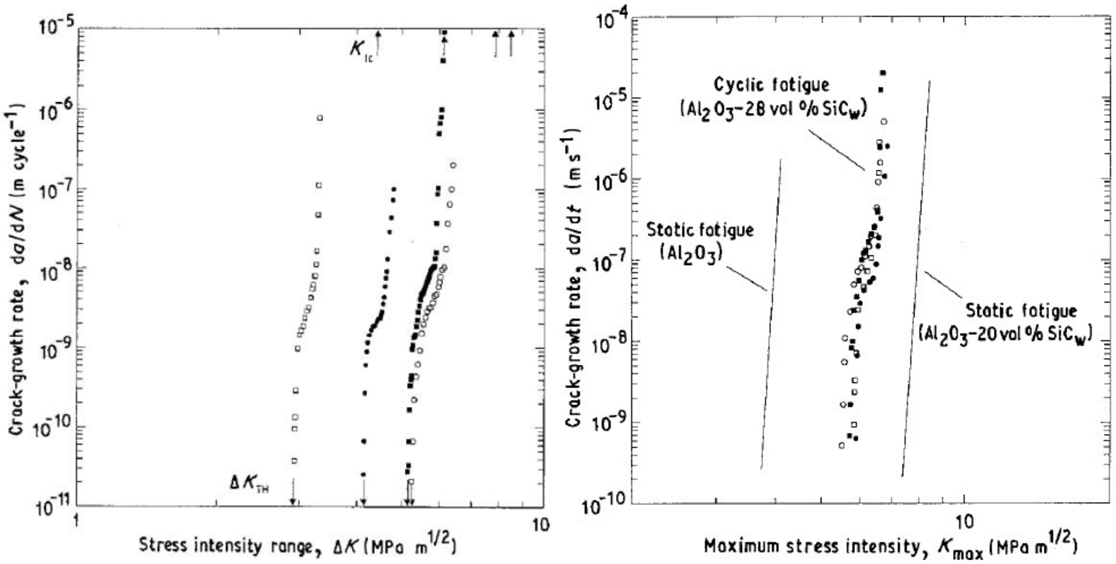

Figure 4.62: (left) Variation in cyclic fatigue-crack growth rates d*a*/d*N* , in Al2)3-28 vol % SiC ceramic composite with applied stress-intensity range, for load ratios of (○) 0.05, (■) 0.1, (●) 0.3 and (□) 0.5. Tests are performed at 25 Hz frequency in ambient temperatures air. (right) Comparison of cyclic fatigue-crack velocities, as functions of time, d*a*/d*t*, with correspoinding crack-velocity data for both unreinforced Al2O3 and Al_2O_3-SiC obtained under monotonic loading [84].

In order to acess the effects of microstructural features on the crack path as well as the R-dependence of both ΔK_{th} and *m*, the fatigue crack growth data were first plotted as d*a*/d*N* v K_{max} as shown in Figure 4.63. The data does not completely collapse onto a single curve, suggesting an important, but not completely dominating effect K_{max} on the fatigue crack growth rate. *m* is ~ 9 at low R and is above 90 at high R, again suggesting a large effect of K_{max} on the crack growth rate. The brittle mode of failure and absence of striations on the fatigue fracture surfaces supports an important role of K_{max} on the fatigue crack growth rate. The brittle fracture features are on the order of the calculated plastic zone and d*a*/d*N* in certain regions, consistent with incremental crack growth of that size in certain regions of the fracture surface.

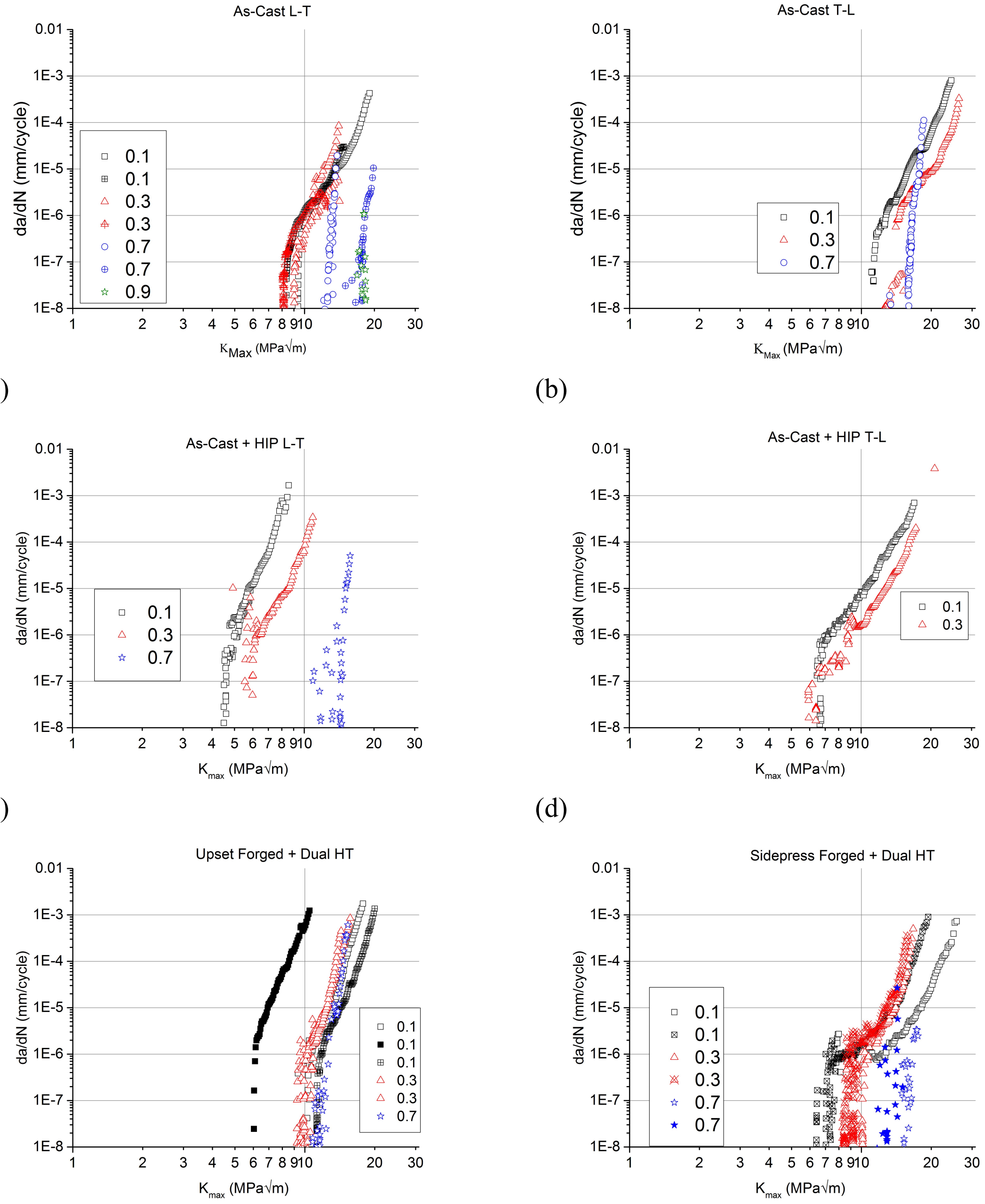

(a) (b)

(c) (d)

(e) (f)

Figure 4.63: $K_{\max}$ vs. da/dN curves of (a) as-cast L-T (b) as-cast T-L (c) as-cast + HIPed L-T (d) as-cast + HIPed T-L (e) upset forged + Dual HT (f) sidepress forged + Dual HT at various R values.

In the current study, the similarity of fracture surfaces resulting from cyclic and monotonic loading suggests that fracture modes similar to those obtained under monotonic loading (e.g., static modes) may be triggered by $K_{\max}$ in the fatigue cycle. In this case, the crack-growth rates obtained during cyclic loading should display a marked sensitivity to the maximum stress intensity factor, K_{max}, or the load ratio, R. The lack of K_{max} convergence of the data indicates that a dual K_{max}-ΔK approach may be needed for these materials.

A number of other models have been reported to describe load ratio effects in a variety of metallic alloys [67] that rely on contributions from both K_{max} and ΔK. The relative effects of K_{max} and ΔK can be captured using:

$$da/_{dN} = C'(K_{max})^n(\Delta K)^p \qquad (4.5)$$

where C', n, and p are constants. This equation can be solved by noting that $K_{max} = \Delta K/(1-R)$ and equation 4.5 can be rewritten as

$$da/_{dN} = C'/(1-R)^n(\Delta K)^{(n+p)} \qquad (4.6)$$

For a constant R, the values of C and *m* are:

$$C = C'/(1-R)^n \qquad (4.7a)$$

$$m = n + p \qquad (4.7b)$$

The calculated values for C and m obtained from the fatigue crack growth tests conducted with a constant R are insufficient to solve for the three unknowns in equation (4.7). One approach that has been suggested and used by others [85] is to conduct constant K_{max} tests during fatigue as shown in the schematic in Figure 4.64. This enables the generation of a d*a*/d*N* vs. ΔK plot with varying R values. In the present work, the effect of ΔK on d*a*/d*N* was experimentally determined by conducting a series of K_{max}/decreasing-ΔK tests. The power law dependence of growth rate on the applied ΔK expected from equation 3, where $(C'(K_{max})^n$ is a constant, is apparent in Figure 4.65, where the value of the slope p, from Equation 4.5 is 2.2 for as-cast L-T at R = 0.1. Using Equation (4.7), the crack growth relationship may be written as for as-cast L-T for R = 0.1:

$$da/dN = 3.93 \times 10^{-16}(K_{max})^{7.1}(\Delta K)^{2.2} \tag{4.8}$$

in which the sensitivity of crack growth rates to K_{max} is immediately apparent. Table 4.6 gives the values of C', n, and p for the various R values and specimens, i.e., as-cast, upset-forged, sidepress-forged. The data suggests that K_{max} plays a significant contribution to the fatigue crack growth of the as-cast material at all R values. However, the lack of complete K_{max} convergence of the data does reveal on important role of ΔK, although the value for p = 2.2 in equation 4.8 indicates a much more reduced role. In contrast, Table 6 indicates that the upset-forged and sidepress-forged materials exhibit a greater dependence on ΔK (i.e., higher p) and less dependence on K_{max} (i.e., lower n).

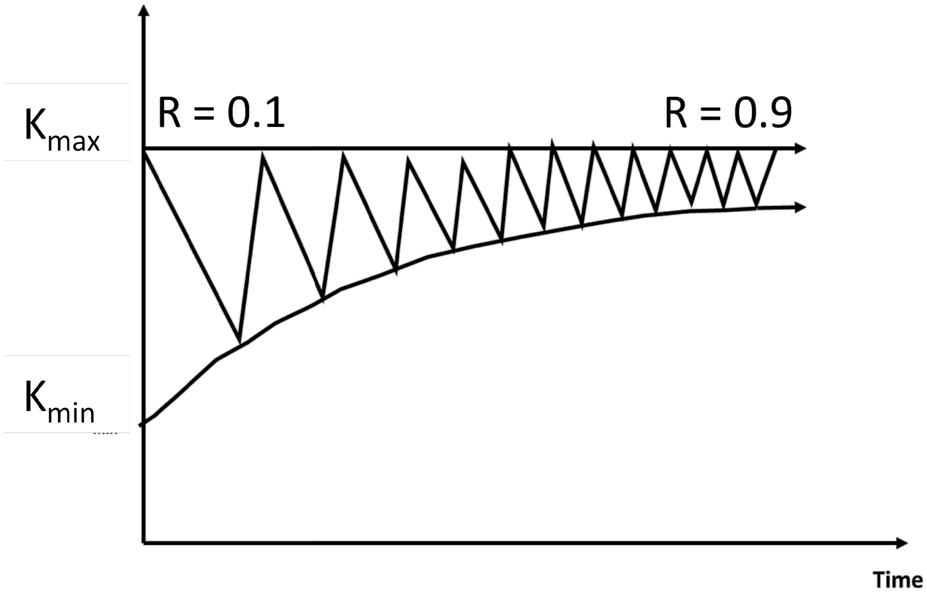

Figure 4.64: Schematic of constant K_{max} test.

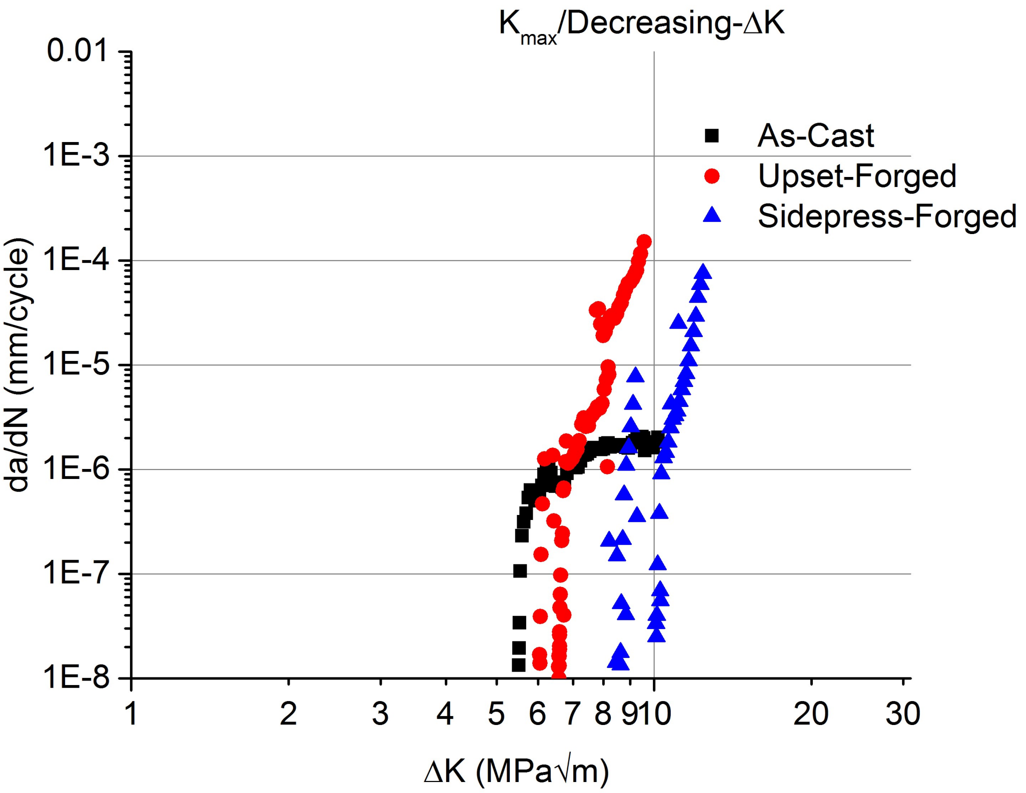

Figure 4.65: Fatigue-crack propagation rates, d*a*/d*N*, plotted as function of the applied stress-intensity range, ΔK, for the constant-K_{max} portion of the test.

Table 4.6: Values of C', n, and P for as-cast, Upset-forged, and Sidepress-forged

	R	Orientation	n	p
As-Cast	0.1	L-T	7.1	2.2
	0.1	L-T	7.2	2.2
	0.1	T-L	7	2.2
	0.3	L-T	7.3	2.2
	0.3	L-T	7.3	2.2
	0.3	T-L	7.3	2.2
	0.7	L-T	23	12
	0.7	L-T	25	12
	0.7	T-L	36	12
Upset-Forged	0.1	T-L	2.1	11.3
	0.1	T-L	5.5	11.3
	0.1	T-L	1.5	11.3
	0.3	T-L	7	11.3
	0.3	T-L	6	11
	0.7	T-L	24	16
Sidepress-Forged	0.1	L-T	1.1	12
	0.3	L-T	4.5	12
	0.3	L-T	0.5	12
	0.7	L-T	6	12
	0.7	L-T	5	12

The two parameter fatigue crack growth approach using equation 4.7 has been reported for many material systems. A summary of the *n* and *p* values reported in their works is given in Table 4.7. From these other works, it is clear that intermetallics typically exhibit similar *p* and *n* exponents compared to metals where $p >> n$ and ceramics where $n>>p$ [57]. Fatigue crack growth in metallic systems are thus typically dominated by ΔK (i.e., high p) while brittle ceramics systems are dominated by K_{max} (i.e., high n). Intermetallics appear to exhibit dual behavior. The observation that *n* is much greater than *p* for the as-cast TNM reveals K_{max} dominance with behavior more ceramic-like than metallic. This results from the preferential brittle crack path that is following the

β_o on colony boundaries. The greater ceramic-like behavior the as-cast TNM must be considered if this material is used as K_{max} has a larger effect on the fatigue crack growth properties than that of other intermetallics. However, the deformation processed TNM (i.e., upset forged, sidepressed-forged) show a greater dependence on ΔK (i.e., higher p) than K_{max} (i.e., lower p). The beneficial microstructure changes and lack of grain boundary β_0 forces a completely different fracture path and one that appears to be more dominated by ΔK than K_{max}.

Table 4.7: n and p values for various materials for two parameter fatigue crack growth in order from most K_{max} dominated to ΔK dominated.

Material	**n (K_{max})**	**p (ΔK)**	**Reference**
SiC	36	1.9	[86]
WC-Co	29	5	[87]
$MoSi_2$/Nb	13.2	7.5	[88]
Al_2O_3-SiC	10.2	4.8	[85]
$Zr_{41.2}$ $Ti_{13.8}Cu_{12.5}$ $Ni_{10}Be_{22.5}$	2.3	1.2	[89]
Ni_{50}-Ti_{50}	1.7	1.7	[90]
Ni-superalloy	0.4	3	[91]
XD gamma-based titanium aluminide	5.6	10.3	[92]

4.4 Conclusions of TNM Behavior After Various Processing Steps

The evolution of tensile and fatigue crack growth behavior of Ti-43.5Al-4Nb-1Mo-0.B (TNM) with processing is studied by evaluating as-cast, cast+HIP, and forged (upset and sidepress) conditions. The fatigue crack growth experiments were conducted by testing over a range of load ratios, R, and stress intensity levels, in the *L-T* and *T-L* directions. Based on the observations of this investigation and analyses, the following conclusions were drawn:

i. Microstructures of the as-cast, cast+HIP, and forged conditions were characterized with a combination of SEM and XRD analysis. Significant changes to the phases present and their morphology were obtained via the forging and final heat treatment.

ii. The tension and fatigue experiments conducted at room temperature revealed translamellar, interlamellar, and brittle fracture features for all of the conditions tested. No fatigue striations were observed on the fatigue crack growth specimens tested under any condition (i.e., as-cast vs. forged, different load ratios).

iii. Metallographic cross sections of failed tension samples tested at room temperature revealed preferential fracture along the brittle grain boundary β_0 present in the as-cast and cast+HIP samples. This was confirmed by XRD analyses of the fracture surface that showed the presence of β_0 on the tensile fracture surfaces that exceeded the amount of β_0 present in metallographic cross sections.

iv. Forged samples tested in tension at room temperature revealed a different fracture path from those of the as-cast or cast+HIP samples, due to the significant microstructure changes resulting from the forging and dual heat treatments employed. Increased ductility was obtained in high temperature tests while metallographic cross sections of failed high temperature samples revealed a distinct change in fracture micromechanisms and non-propagating sub-surface cracks.

v. The fatigue crack growth behavior was very dependent on the material condition (i.e. as-cast, cast+HIP, forged) as well as load ratio, R. In particular, increasing the load ratio, R, for all of the materials tested, had a larger effect on reducing the fatigue threshold than reported for other TiAl materials.

vi. The fatigue threshold and Paris exponent for the as-cast and cast+HIP material exhibited a strong dependence on load ratio, R. Metallographic cross-sections of the broken samples revealed preferential cracking along the β_0 , while XRD of the fracture surfaces showed the presence of β_0 on the fatigue fracture surfaces that exceeded the amount of β_0 present in metallographic cross sections.

vii. While the as-cast and cast+HIP material exhibited fatigue crack growth behavior that appeared to be strongly affected by Kmax in the fatigue cycle, the crack growth rates did not completely converge when plotted vs. Kmax, suggesting an additional effect of ΔK in the fatigue cycle. This was examined and confirmed using a two parameter fatigue crack approach that captured the dominant role of Kmax with contributions from ΔK in the fatigue cycle.

viii. The fatigue threshold and Paris exponent for the forged and dual heat treated materials (i.e. upset, sidepress) similarly exhibited a strong dependence on load ratio, R, for portions of the fatigue crack growth curve. However, the dependence of the cracking using the two parameter fatigue crack growth approach revealed a greater effect of ΔK in the fatigue cycle, and a more minor effect of Kmax, in contrast to the behavior of the as-cast and cast+HIP material. This change in behavior was rationalized by examining the changes in microstructure and fracture path of the forged material in comparison to the as-cast and cast+HIP material.

ix. The changes in fracture path between materials and at different portions of the fatigue crack growth curve were rationalized by examining both the maximum monotonic plastic zone size and the cyclic plastic zone size present in these regimes, and their relation to the dominant microstructure features present.

x. The K_{max} at catastrophic failure in the fatigue crack growth experiments was not affected by load ratio, R. The values were similar to those obtained on fatigue pre-cracked samples tested for toughness and somewhat lower than notched samples tested.

5. Future Work

The research in this thesis has a number of different areas the could become the focus of other work that could be explored in order to further understand the factors controlling fatigue crack growth of TNM and use in jet engines.

1. Duplication of tests to confirm the results reported in this work. Most conditions had only one or two tests conducted and more are needed to validate the data for use in design and certification.
2. Fatigue tests at elevated temperatures to validate the fatigue properties at elevated temperatures. This work only examined room temperature fatigue, which is important, but the engines operate at high temperatures and fatigue in the 700 °C range is needed to allow understand the important factors controlling fatigue at elevated temperatures.
3. Extended aging at service temperatures is needed to insure that the microstructure is stable at. Once extended aging is performed fatigue and tensile tests are needed to determine the effects of such aging on mechanical properties.
4. Surface science with the use of TOF-SIMS and Auger SEM to quantify the elements present fracture surfaces. If higher amounts of molybdenum are found on the surface than in the bulk that would further support the contention that the preferential cracking occurs through β_o in as-cast TNM.

5. Corrosion testing in severe environments is needed to confirm that, like other TiAl alloys, that corrosion is not an issue and engine gases do not have a negative effect on the mechanical properties.
6. TEM foils taken from the crack tips of samples removed at the fatigue threshold. These TNM foils would allow investigation of the local crack path. It would also reveal what phase(s) are involved with crack reinitiation and how phase boundaries might affect crack growth.
7. Creep testing is needed to insure that the TNM does not creep at service temperature and will be able to be used in the loading and environmental conditions that jet engines operate at.

6. Appendices

6.1 Lifetime Calculations

Time of life or number of cycle to failure can be calculated using a closed form solution assuming that the crack growth rate is given by equation 6.1 and 6.2 and can be approximated as constant over the range of crack length a_i to a_f:

$$\frac{\mathrm{d}a}{\mathrm{d}N} = f(\Delta K, R) = C\ (\Delta K)^m \qquad (6.1)$$

$$\Delta K = F\ \Delta S\sqrt{\pi a} \qquad (6.2)$$

If this is true, then the cycles to failure can be calculated using equation 6.3:

$$N_{if} = \frac{a_f^{1-m/2} - a_i^{1-m/2}}{C\left(F\Delta S\sqrt{\pi a}\right)^m (1-\frac{m}{2})} \qquad (6.3)$$

where F is given by equation 6.4 from ASTM E399 [56] and ΔS for stress is given by equation 6.5 for three point bending from Dowling [54]:

$$f\left(\frac{a}{w}\right) = 3\sqrt{\frac{a}{w}} * \frac{1.99-\left(\frac{a}{w}\right)\left(1-\frac{a}{W}\right)[2.15-3.93\frac{a}{W}+2.7\left(\frac{a}{W}\right)^2]}{2\left(1+2\frac{a}{W}\right)(1-\frac{a}{w})^{3/2}} \qquad (6.4)$$

$$S = \frac{6\frac{P(\frac{S}{2})}{2}}{W^2 t} \qquad (6.5)$$

s is the span of the tests, a is the crack length, W is the width of the specimen, t is the thickness of the specimen, m is the Paris exponent. Using these equations the number of cycles for crack growth from 1 mm to 10 mm was calculated for different stress ratios and different R ratios, using different Paris exponents. The number of cycles required for this amount of crack growth is given in Table 6.1. The calculation show that such high Paris exponents produce a much smaller number of cycles. Thus, design of structure using such a material should focus on design using ΔK_{th}. Although lower Paris exponents produce more cycles for crack growth, conservative design should still use ΔK_{th}.

Table 6.1: Number of cycles to grow crack from 1 mm to 10 mm. R = 0.1 vs R = 0.7 and different *m* used.

R	Paris Slope	ΔS (Mpa)	ai	af	Cycles
0.1	9.1	60	1 mm	10 mm	5.45E+09
0.1	9.1	80	1 mm	10 mm	3.98E+08
0.1	9.1	100	1 mm	10 mm	52000000
0.1	9.1	120	1 mm	10 mm	9937000
0.7	35	60	1 mm	10 mm	2118000
0.7	35	80	1 mm	10 mm	90
0.7	35	100	1 mm	10 mm	<1
0.7	35	120	1 mm	10 mm	<1

6.2. Appendices (Publications)

Fatigue Crack Growth and Fracture Behavior of As-Cast Ti-43.5Al-4Nb-1Mo-0.1B (TNM) Compared to Ti-48Al-2Nb-2Cr (4822)

Matthew S. Dahar[a], **Sesh A. Tamirisakandala**[b], **John J. Lewandowski**[a]

[a]*Case Western Reserve University, Department of Materials Science and Engineering, Cleveland, OH 44106*

[b]*Arconic Titanium & Engineered Products, Niles, OH 44446*

ABSTRACT

The effects of sample orientation and load ratio on the room-temperature fatigue crack growth and fracture behavior of a third-generation gamma titanium aluminide Ti-43.5Al-4Nb-1Mo-0.1B (TNM) were determined and compared with that of a second-generation alloy Ti-48Al-2Nb-2Cr (4822). Both materials are currently used as low pressure turbine blades in fuel-efficient gas turbine engines. Bend bar specimens, excised from the as-cast articles in the longitudinal and transverse directions to the casting direction, were tested at room temperature in lab air. Load ratios in the range 0.1–0.9 were used in fatigue testing to determine their effects on the fatigue threshold, Paris law slope, and stress intensity at overload in fatigue. Microscopy and fractography were used to document the effects of sample orientation on the fatigue crack path and morphology. Significant effects of changes in load ratio were observed on the fatigue threshold and Paris law slope, while effects of sample orientation were minimal for both alloys. The effects of microstructure length scale and differences in micro-constituents are discussed in relation to the properties measured.

1. INTRODUCTION

Gamma titanium aluminides consisting of γ-TiAl (ordered face-centered tetragonal $L1_o$ structure) plus α_2-Ti_3Al (ordered hexagonal DO_{19} structure) phases have emerged as promising candidates with attractive mechanical properties (e.g., tensile and creep strength) as a replacement for heavy nickel-based superalloys for intermediate-temperature applications such as low pressure turbine (LPT) blades of fuel-efficient jet engines [1], [2]. The second generation alloy compositions can be generalized as: Ti-(45-48)Al – (1-3)X1 – (2-5)Y1 – (<1)Z1, where X1 = Cr, Mn, V; Y1 = Nb, Ta, W, Mo; Z1 = Si, B, C (all compositions expressed in atomic percent). Ti-48Al-2Cr-2Nb (4822) is a second generation alloy that has been in service since 2011 on GEnx™ engine LPT cast blades. Third generation alloy compositions can be represented as: Ti-(42-45)Al – (0-10)X2 – (0-3)Y2 – (0-1)Z2 – (0-0.5)RE, where X2 = Cr, Mn, Nb, Ta; Y2 = Mo, W, Hf, Zr; Z2 = C, B, Si; and RE = rare earth elements. Ti-43.5Al-4Nb-1Mo-0.1B (TNM), which entered service in 2016 through the Pratt & Whitney PurePower™ geared turbo fan engine LPT forged blade, is a third generation alloy with enhanced performance compared to the second generation 4822. A refined as-cast grain size due to trace B additions and a higher volume fraction of high-temperature β-TiAl (disordered body centered cubic structure) phase due to balanced amounts of Nb and Mo impart enhanced hot workability [3], [4]. The ability to minimize volume fraction of β_o-TiAl (ordered B2 structure) phase via post-forging heat treatment provides balanced properties for TNM at room and service temperatures.

Coarse-grained lamellar microstructures exhibit relatively high fracture toughness and creep resistance, but poor tensile ductility, especially at room temperature. Fine-grained duplex microstructures exhibit low fracture toughness and creep resistance, but moderate tensile ductility at ambient temperatures. This inverse correlation between tensile properties and resistance to fracture requires a careful selection of the microstructure for achieving balanced engineering properties [1], [2], [5], [6]. Previous studies on γ-TiAl have shown that the fatigue crack growth rate d*a*/d*N* and threshold level ΔK_{th} are dependent on the fabrication method and resulting microstructure [7]–[11]. Studies have also suggested that crack closure can play a role in the variation of fatigue threshold behavior and load ratio, *R*. Decreasing the lamellar spacing decreases the creep rate while increasing the fatigue crack growth resistance and ductility. It is empirically known that an increase of grain size or colony size increases the fracture toughness at the expense of fracture strain in tension [12]. The β_o phase surrounding α_2/γ lamellae significantly impacts the fracture properties [7] by providing a preferential fracture initiation and growth path due to its brittle nature.

While a two phase ($\gamma+\alpha_2$) alloy with a fully lamellar microstructure is used only in cast product form of 4822, a three phase ($\gamma+\alpha_2+\beta/\beta_o$) TNM alloy is used in forged product form with greater microstructural flexibility. In both alloys, the as-cast microstructure is the foundation for final product microstructure that significantly influences the performance. Prior work by the present co-authors on as-cast 4822 demonstrated that *R* and orientation significantly influence d*a*/d*N* and fracture behavior [13]. A strong dependence of d*a*/d*N* upon the applied stress-intensity range Δ*K* was reported and Paris law slope *m* values greater than 10 were observed [13]. High *m* values significantly reduce the predicted component life and require the applied Δ*K* levels to remain below the fatigue threshold ΔK_{th} in order to prevent significant fatigue crack growth and/or failure. The objective of the present study is to address the following questions:

i) Does a refined microstructure in as-cast TNM change the fatigue crack growth and fracture behavior compared to as-cast 4822?

ii) Does R and/or orientation influence fatigue crack growth parameters in as-cast TNM?

iii) Does the β_o phase in as-cast TNM affect the fatigue crack growth and fracture behavior?

Micro-mechanistic understanding of fatigue crack growth and fracture behavior was obtained based on test data generated on production-quality materials at various R values and orientations with respect to the casting direction, corroborated with extensive metallography and fractography, and plastic zone size analysis.

2. PROGRAM MATERIALS AND EXPERIMENTAL PROCEDURES

2.1 Materials

Second and third generation gamma TiAl alloys with nominal chemical compositions (in atomic percent) of Ti-48Al-2Cr-2Nb (4822) and Ti-43.5Al-4Nb-1Mo-0.1B (TNM) were investigated in this study. Complete chemical compositions are given in Table 1. The 4822 was cast at GE Global Research Center, Schenectady, NY, to a geometry shown in Figure 1. The rib and gate were removed to obtain a 100-mm long rectangular plate of 50-mm width x 9.5-mm thickness. These plates were bisected along the length via electric discharge machining (EDM) to obtain two 25-mm width bend bars. Notches were placed to enable cracks to propagate in the *L-T* and *T-L* orientations. The

TNM alloy was cast into a 50.8 mm diameter x 3353 mm long ingot at Arconic Titanium and Engineered Products, Niles, OH. Bend bars in the *L-T* and *T-L* directions were excised from this ingot as shown in Figure 1.

The microstructures (optical and SEM) of as-cast 4822 and TNM program materials at different length scales are compared in Figure 2. The average ($\gamma+\alpha_2$) colony size (determined by linear intercept method) of 4822 was 1000 μm ± 144 μm and γ lath width was 1.77 ± 0.5 μm. TNM microstructure consisted of: lamellar ($\gamma+\alpha_2$) colonies in the 20–40 μm size range, γ lath widths of ~0.2 μm, and β_o of ~9 vol. % at grain/colony boundaries (determined using image analysis software MIPAR [14]).

2.2 Mechanical Testing and Characterization

Fracture toughness and fatigue crack growth rate tests were conducted on single-edge-notched and fatigue pre-cracked bend bar specimens prepared in accordance with ASTM standard E399 [15] and E647 [16]. Notches were placed using a slow speed diamond wire saw with a radius of 100 μm. Within the constraints of available cast article sizes, duplicate bend bars with the following dimensions satisfying ASTM E399 were prepared to probe representative microstructure volumes: 4822 *L-T* samples of 100 mm x 9.5 mm x 25 mm, 4822 *T-L* samples of 25 mm x 9.5 mm x 12 mm, TNM *L-T* samples of 50 mm x 20 mm x 12.5 mm, and TNM *T-L* samples of 35 mm x 20 mm x 12.5 mm.

Fatigue crack growth rate tests were performed at room temperature in laboratory air using a closed-loop servo-hydraulic testing machine under cyclic stress-intensity (ΔK) control at a frequency of 20 Hz and at the load ratios, $R = K_{\min}/K_{\max}$, of 0.1, 0.3, 0.7, and 0.9. Crack growth rate was measured using direct current potential drop technique per

ASTM E647 [16]. Fatigue threshold, ΔK_{th}, operationally defined as the applied ΔK below which da/dN < 10^{-7} mm/cycle, was obtained by using a variable ΔK/constant-R load shedding scheme. Cyclic crack growth results are presented in terms of crack growth rate per cycle (da/dN) as a function of the applied stress intensity, $\Delta K = (K_{\text{max}} - K_{\text{min}})$. The test was started at a mid-range ΔK and used load-shedding to reach the threshold. The test was then stopped and restarted at a mid-range ΔK and the crack was grown to failure. After failure, the Paris slope m and K_{max} at failure were determined. Plane-strain fracture toughness tests were conducted on bend bars with notch length a in the range $0.45W$ to $0.55W$ (W = specimen width) in accordance with ASTM E399 [15] on a span of 30-mm and at a displacement rate of 0.5 mm/min. Fracture surfaces were examined using a FEI Quanta 200 SEM at 20 kV. In addition, crack paths were analyzed using both optical and backscattered electron imaging.

Tensile tests were performed on TNM using subscale tensile specimens with a double button head design and a gauge length of 20.3 mm conforming to ASTM E8 [17]. Tensile tests were performed at a strain rate of 10^{-3} s^{-1} and strain was measured using a non-contact video extensometer (from UVID™, LLC). Tensile tests were not preformed on Ti-4822 and lack of material prevented testing.

3. RESULTS

Fatigue crack growth rate curves (da/dN vs ΔK) of both alloys in both *L-T* and *T-L* directions at R = 0.1, 0.3, 0.7, and 0.9 are presented in Figure 3. Fatigue threshold ΔK_{th}, Paris slope m, and $K_{\text{c}} = K_{\text{max}}$ at overload at various R as well as static notch fracture toughness for both alloys in both orientations are summarized in Figure 4. Both alloys exhibited decreasing ΔK_{th} with increasing R, Figure 4 and Table 2. The influence of orientation on ΔK_{th} was more pronounced in TNM (compared to 4822), as evidenced by the rapid drop in ΔK_{th} with increasing R, and the absolute ΔK_{th} values at equivalent R were lower (Figure 4 and Table 2). The ΔK_{th} at $R = 0.9$ for 4822 is significantly lower than that obtained at lower R, while increasing R shifted all of the da/dN-ΔK curves to the left. Paris slopes for both alloys in both orientations increased dramatically, from 9 at $R = 0.1$ to nearly 100 at $R = 0.9$. The K_c at failure in fatigue was not significantly affected by R, as seen in Figure 4(c). Tensile tests on TNM revealed a 0.2% yield strength of 680 MPa and ultimate tensile strength of 700 MPa with less than 0.5% plastic elongation.

Typical fatigue fractographs taken at different magnifications for 4822 and TNM tested in the *L-T* and T-L orientation are compared in Figures 5 and 6. Both alloys exhibited brittle faceted failure features while the 4822 exhibited larger scale features compared to the TNM. Closer examination of the flat facets on the fracture surface in the Paris law regime revealed an absence of fatigue striations. High magnification fractographs at catastrophic overload in the fatigue tests and at various R and ΔK are shown in Figure 7. Fracture surface features in both alloys were predominantly brittle with small amounts of local plastic deformation. The influence of ΔK or R on fractographic features is insignificant. Figure 8 shows a comparison of 3D surface roughness profiles of fracture surfaces taken at intermediate ΔK over an area of 7 x 7 mm^2 (taken with Keyence VHX-2000 microscope) for 4822 and TNM, both fatigue tested at $R = 0.3$ in *T-L* orientation. These show a surface roughness in the range of 800-1750 µm for 4822 and only 50–280 µm for TNM. Figure 9 shows a typical fractograph of TNM tensile tested specimens. Brittle fracture and surface roughness with singular features similar to those exhibited by the fatigue specimens are evident.

Crack path analysis was performed on polished and etched cross-sections of failed fatigue specimens. An example for a 4822 *T-L* sample fatigue tested to threshold at R = 0.7 is presented in Figure 10. The crack path shows interlamellar and translamellar cracking that results from the propagation of the crack seeking the path of least resistance. The crack follows the colony boundaries and lamellae, causing the interlamellar and translamellar cracking along with some secondary cracking. Crack path for a TNM *L-T* sample tested to threshold at R = 0.1 presented in Figure 11 shows microcrack propagation along β_o at colony boundaries, both along the crack path and subsurface. Cross-sections of the failed fatigue specimens in the L-T direction at R = 0.7 were mounted and polished to show the crack path on one side of the specimens as shown in Figure 12. The cross-sections confirm what was seen in previous crack path analysis.

4. DISCUSSION

The fatigue crack growth data reveals a significant effect of R on the magnitude of the ΔK_{th} for 4822, decreasing from over 9 MPa√m for R = 0.1 to less than 2 MPa√m at R = 0.9. At a given R, the TNM shows a lower ΔK_{th} in both orientations compared to 4822. Crack closure can significantly impact the fatigue threshold and one key difference between the 4822 and TNM relates to the large differences in fracture surface roughness.

As discussed elsewhere [18], the roughness-induced crack closure arises due to the linkage of mismatched planes of deflected microcracks via a process involving shear deformation and the fracture of thin ligaments. This has been postulated as the origin of roughness-induced closure observed in other Ti alloys and reported for TiAl alloys with large colony size similar to the 4822 in this study [19]. The higher fracture resistance exhibited by the lamellar microstructure is attributed to the deflected crack path which results in shear ligaments of large length and larger plastic dissipation contributed by the fracturing of the lamellar ligaments [5], [18], [20], [21].

The irregular or rough fracture surfaces can induce high closure loads at low *R* when in-plane shear wedges open the crack at contact points along the crack face. The reduction in the effectiveness of this closure mechanism increases as the crack tip open displacement (CTOD) increases [22] and the crack faces are held apart.

The effect of changes in ΔK and K_{max} in the fatigue cycle on the surface roughness can be estimated by determining the plastic zone size and examining how this compares to the microstructural features sampled. The monotonic plastic zone radius in plane-strain is given by

$$r_{os} = \frac{1}{6\pi}\left[\frac{K}{\sigma_o}\right]^2 \tag{1}$$

where σ_o is the yield strength of the material (342 MPa for 4822 and 680 MPa for TNM) [23]. The plastic zone size under cyclic loading will be smaller than that in static loading and is affected by reverse plasticity [23]. As the crack tip cycles during fatigue, the plastic zone leaves a wake of plasticity behind the crack tip. This induces residual stress in the crack tip region and may also play a role in crack closure. The cyclic plastic zone radius is given by

$$r_{oc} = \frac{1}{6\pi}\left[\frac{\Delta K}{2\sigma_o}\right]^2 \tag{2}$$

The calculated size of the monotonic and cyclic plastic zone at ΔK_{th} and overload for both 4822 and TNM ΔK and K_{max} are given in Table 2, assuming plain-strain conditions. The plastic zone size using K_{max} at threshold for the *T-L* test direction at $R = 0.3$ is 125 µm for

4822 which is considerably smaller than the colony size (~1000 μm). For TNM tested at R = 0.3, the plastic zone size at threshold using K_{max} is 16 μm, which is comparable to the colony size (~20–40 μm). Similar sizes are computed for other *R* values and orientations tested when using K_{max}. However, the cyclic plastic zone is considerably smaller than the colony size at the fatigue threshold for all of the *R* values and orientations tested, indicating that only a single colony is sampled in the plane of view, out of ~ 13 colonies of 4822 and 500 colonies of TNM sampled through the thickness. Thus, the orientation of only a few colonies dominates fatigue crack growth.

The cyclic plastic zone size at ΔK_{th} for 4822 is only on the order of the interlamellar spacing for all R values while the maximum plastic zone size is still only 1/5 to 1/10 of the colony size. The maximum plastic zone size still does not sample a full colony, suggesting that the drop in threshold with increasing *R* is from roughness-induced crack closure, consistent with the high surface roughness shown in Figure 8. At overload, the plastic zone sizes at K_{max} are still at most only 1/5 of the colony size at all *R* values, thus sampling only a few colonies throughout the sample and producing similar values for K_{max} at failure.

For TNM, the cyclic plastic zone at threshold is on the order of the interlamellar spacing, while the maximum plastic zone size approaches the colony size. Thus, at high *R* values, the maximum plastic zone size will sample a full colony in the field of view and many through the sample thickness. However, this will enable the crack to follow the brittle beta phase present on the colony boundaries and likely give rise to the large effects of R on the threshold. Since the surface roughness of the TNM samples, as seen in Figure 8, is low, this limits any contribution from roughness-induced closure. At overload, the plastic zone sizes at K_{max} are of the order of the colony size at all R values, easily sampling the brittle beta regions on the colony boundaries throughout the sample thickness and producing similar values for K_{max} at failure for all R values.

In order to begin to address the effects of microstructural features on the crack path as well as the R dependence of both ΔK_{th} and m, the fatigue crack growth data was first plotted as da/dN vs. K_{max} as shown in Figure 13. The data for both 4822 and TNM do not completely collapse onto a single curve, suggesting an important, but not completely dominating effect of K_{max} on the fatigue crack growth rate. In addition, m is ~ 9 at low R and approaches 100 at high R, again suggesting an important effect of K_{max} on the crack growth rate. Furthermore, brittle modes of failure and absence of striations on the fatigue fracture surfaces support an important role of K_{max} on the fatigue crack growth rate. For example, brittle fracture surface facets roughly 100 μm in size were exhibited by 4822. While these features are less than the colony size, they are in the range of the calculated plastic zone sizes and da/dN in certain regions, consistent with incremental crack growth of that size in certain regions of the fracture surface.

The data obtained on the 4822 and TNM exhibit characteristics that are similar to those exhibited by some metallic alloys [24]–[26] and intermetallics [13], with metallic-like Paris slopes in the range 3-5 at low R significantly increasing to >10 with an increase in R. In these systems, it has been shown that the increase in m with increasing R corresponds with an increase in static modes of brittle fracture that produce elevated crack growth rates that continue to increase with increasing R. In previous works [13, 23-25], such static modes of fracture included intergranular and cleavage failure. In the present work, the brittle fracture features in 4822 are likely to contribute to large increments in crack growth at a given ΔK, and are likely driven by K_{max} as no fatigue striations were evident. In TNM, the crack path appears to be dominated by brittle β_o along colony boundaries, also providing a brittle crack path that should be dominated by K_{max} and not ΔK. The continuous brittle β_o present around the lamellar colonies allow the crack, once initiated, to propagate unhindered. Once the crack reaches an end of a lamellar colony, the crack seeks a more favorable path, producing interlamellar and translamellar cracking. These fatigue crack growth mechanisms are similar to those reported by Leitner in TNM [74].

It must be noted that the present work was conducted on as-cast TNM material. Deformation processing is known to produce significant effects on the mechanical behavior of intermetallics due to various beneficial microstructure modification [27]. Studies are underway to understand the influence of deformation processing on fatigue and fracture behavior of TNM and the present work was conducted in order to provide a baseline understanding of the features affecting fatigue crack growth in the starting as-cast material.

5. CONCLUSIONS

The fatigue crack growth behavior of Ti-48Al-2Cr-2Nb (4822) and Ti-43.5Al-4Nb-1Mo-0.1B (TNM) in the as-cast condition were determined by testing over a range of *R* and stress intensity levels, in the *L-T* and *T-L* directions. Based on the observations of this investigation, the following conclusions were drawn:

i) The as-cast 4822 had a large ($\gamma+\alpha_2$) colony size (~1000 μm) and lath width of ~ 1.77 μm while the TNM had small colonies (20-40 μm) and fine lamellar spacing of ~ 0.2 μm.

ii) The fatigue fracture surfaces in both alloys in both orientations showed translamellar, interlamellar, and brittle fracture features. No fatigue striations were observed on the specimens tested in either orientation.

iii) The fatigue crack threshold was very dependent on load ratio. In particular, increasing the load ratio had a larger effect on reducing the fatigue threshold than reported for other TiAl materials.

iv) The fracture surface roughness quantified using confocal microscopy was large in 4822 (e.g., on the order of the colony size ~ 1000 μm). In contrast, the surface roughness of TNM was considerably less but similarly on the order of the colony size (20-40 μm). The roughness of the surface in 4822 is produced by the cracks traversing the lamellar colonies causing interlamellar and translamellar cracking. These crack patterns were also found in previous studies on TiAl containing a lamellar structure, but the scale of roughness on the fracture was much greater in the 4822 than in other versions including TNM.

v) The Paris slope m for as-cast 4822 and TNM shows a large dependence on R, increasing from around 9 at $R = 0.1$ to over 90 at $R = 0.9$. Microstructural effects on the crack path were used to rationalize this observation.

vi) The fatigue threshold, Paris slope, fracture toughness, and notch toughness are not measurably affected by sample orientation and are similar for 4822 and TNM.

Acknowledgements

This work was supported by Arconic Titanium & Engineered Products with partial support provided by the CWRU Arthur P. Armington Professorship. MD acknowledges Student Co-op support at Arconic Titanium & Engineered Products.

REFERENCES

[1] Y.-W. Kim, “Ordered intermetallic alloys, part III: gamma titanium aluminides,” *Jom*, vol. 46, no. 7, pp. 30–39, 1994.

[2] Y.-W. Kim and D. M. Dimiduk, “Progress in the understanding of gamma titanium aluminides,” *JOM*, vol. 43, no. 8, pp. 40–47, Aug. 1991.

[3] H. Clemens and S. Mayer, “Design, Processing, Microstructure, Properties, and Applications of Advanced Intermetallic TiAl Alloys,” *Adv. Eng. Mater.*, vol. 15, no. 4, pp. 191–215, Apr. 2013.

[4] H. Clemens, S. Wilfried, V. Güther, and S. Mayer, “ADVANCED INTERMETALLIC TITANIUM ALUMINIDES.” Ti-2015 Conference.

[5] K. S. Chan and Y.-W. Kim, “Influence of microstructure on crack-tip micromechanics and fracture behaviors of a two-phase TiAl alloy,” *Metall. Trans. A*, vol. 23, no. 6, pp. 1663–1677, 1992.

[6] K. S. Chan, “Toughening mechanisms in titanium aluminides,” *Metall. Trans. A*, vol. 24, no. 3, pp. 569–583, 1993.

[7] T. Leitner, M. Schloffer, S. Mayer, J. Eßlinger, H. Clemens, and R. Pippan, “Fracture and R-curve behavior of an intermetallic β-stabilized TiAl alloy with different nearly lamellar microstructures,” *Intermetallics*, vol. 53, pp. 1–9, Oct. 2014.

[8] W. O. Soboyejo, P. B. Aswath, and C. Mercer, “Mechanisms of fatigue crack growth in Ti-48Al at ambient and elevated temperature,” *Scr. Metall. Mater.*, vol. 33, no. 7, pp. 1169–1176, 1995.

[9] J. J. Kruzic, J. P. Campbell, and R. O. Ritchie, “On the fatigue behavior of γ-based titanium aluminides: role of small cracks,” *Acta Mater.*, vol. 47, no. 3, pp. 801–816, Feb. 1999.

[10] C. Mercer, J. Lou, and W. O. Soboyejo, “An investigation of fatigue crack growth in a cast lamellar Ti-48Al-2Cr-2Nb alloy,” *Mater. Sci. Eng. A*, vol. 284, no. 1, pp. 235–245, 2000.

[11] C. Choi, H. J. Kim, Y.-T. Lee, Y.-W. Kim, and C. S. Lee, “Effects of microstructural parameters on the fatigue crack growth of fully lamellar γ-TiAl alloys,” *Mater. Sci. Eng. A*, vol. 329–331, pp. 545–556, Jun. 2002.

[12] K. S. Chan and Y.-W. Kim, “Effects of lamellae spacing and colony size on the fracture resistance of a fully-lamellar TiAl alloy,” *Acta Metall. Mater.*, vol. 43, no. 2, pp. 439–451, Feb. 1995.

[13] M. S. Dahar, S. M. Seifi, B. P. Bewlay, and J. J. Lewandowski, “Effects of test orientation on fracture and fatigue crack growth behavior of third generation as-cast Ti–48Al–2Nb–2Cr,” *Intermetallics*, vol. 57, pp. 73–82, Feb. 2015.

[14] “Powerful Image Analysis,” *MIPAR*. [Online]. Available: http://www.mipar.us/. [Accessed: 14-Feb-2017].

[15] ASTM Standard E399, “Test Method for Linear-Elastic Plane-Strain Fracture Toughness K1c of Metallic Materials,” ASTM International, 2009.

[16] ASTM Standard E647, “Standard Test Method for Measurement of Fatigue Crack Growth Rates,” ASTM International, 2011.

[17] ASTM Standard E8, “ASTM E8/E8M-16a Standard Test Methods for Tension Testing of Metallic Materials,” ASTM International, West Conshohocken, PA, 2016.

[18] K. S. Chan, “Micromechanics of shear ligament toughening,” *Metall. Trans. A*, vol. 22, no. 9, pp. 2021–2029, 1991.

[19] K. S. Chan, “Understanding fracture toughness in gamma TiAl,” *JOM*, vol. 44, no. 5, pp. 30–38, 1992.

[20] K. S. Chan and Y.-W. Kim, “Fracture Processes in a Two-Phase Gamma Titanium Aluminide Alloy,” in *Microstructure/property relationships in titanium aluminides and alloys*, Y.-W. Kim and R. R. Boyer, Eds. Warrendale, Pa: TMS, 1991, pp. 179–196.

[21] S. . Kampe, “Microstructure Morphology Effects on Fracture Toughness of a Cast Near-Gamma Titanium Aluminide Alloy,” in *Microstructure/property relationships in titanium aluminides and alloys*, Y.-W. Kim and R. R. Boyer, Eds. Warrendale, Pa: TMS, 1991, pp. 313–322.

[22] R. O. Ritchie and S. Suresh, “Some considerations on fatigue crack closure at near-threshold stress intensities due to fracture surface morphology,” *Metall. Trans. A*, vol. 13, no. 5, pp. 937–940, May 1982.

[23] N. E. Dowling, *Mechanical Behavior of Materials*, 3rd edition. Upper Saddle River, NJ: Oearson Pretice Hall, 2007.

[24] R. O. Ritchie and J. F. Knott, “Mechanisms of fatigue crack growth in low alloy steel,” *Acta Metall.*, vol. 21, no. 5, pp. 639–648, May 1973.

[25] A. B. El-Shabasy and J. J. Lewandowski, “Effects of load ratio, R, and test temperature on fatigue crack growth of fully pearlitic eutectoid steel (fatigue crack growth of pearlitic steel),” *Int. J. Fatigue*, vol. 26, no. 3, pp. 305–309, Mar. 2004.

[26] R. O. Ritchie, “Mechanisms of fatigue crack propagation in metals, ceramics and composites: Role of crack tip shielding,” *Mater. Sci. Eng. A*, vol. 103, no. 1, pp. 15–28, Aug. 1988.

[27] M. G. Mendiratta, J. J. Lewandowski, and D. M. Dimiduk, “Strength and ductile-phase toughening in the two-phase Nb/Nb5Si3 alloys,” *Metall. Trans. A*, vol. 22, no. 7, pp. 1573–1583, 1991.

Table 1. Chemical compositions (in at. %) of program materials.

Alloy	**Al**	**Cr**	**Nb**	**Mo**	**B**	**C**	**O**	**Ti**
4822	48	2	2			0.030	0.190	bal
TNM	43.56		4.05	0.97	0.1	0.008	0.061	bal

Table 2. Cyclic plastic zone size of 4822 and TNM at threshold calculated with ΔK_{th} and K_{max}.

Orientation	***R***	**ΔKth (MPa√m)**		**Kmax at ΔKth (MPa√m)**		**Radius of Cyclic Plastic Zone (μm) at Threshold using ΔK**		**Radius of Monitonic Plastic Zone (μm) at Threshold using Kmax**	
		4822	**TNM**	**4822**	**TNM**	**4822**	**TNM**	**4822**	**TNM**
L-T	0.1	9.2	8.4, 7.5	10.2	9.3, 8.3	10.6	1.9,19.5	52	9, 7
	0.3	8.0	6.3, 5.6	11.4	9, 8	8	1.1,0.8	65	9, 7
	0.7	5.8	3.8, 5.4	19.5	12.6, 17.7	4.3	0.4,0.8	174	17, 34
	0.9	2.2	1.7	21.5	17.8	0.6	0.1	212	34
T-L	0.1		9.9		11.1		2.7		13
	0.3	9.4	8.5	15.8	12.2	6.3	2	125	16
	0.7	6.0, 6.2	4.8	19, 20.9	16	4.5,4.8	0.6	182, 216	28
	0.9	1.6,1.8		16.1,18.4		0.3,0.4		131,171	
Orientation	***R***	**ΔK at overload (MPa√m)**		**Kmax at overload (MPa√m)**		**Radius of Cyclic Plastic Zone (μm) at Overload using ΔK**		**Radius of Monotonic Plastic Zone (μm) at Overload using Kmax**	
		4822	**TNM**	**4822**	**TNM**	**4822**	**TNM**	**4822**	**TNM**
L-T	0.1	17.5	17.2,13.2	19.4	19.1,14.7	38.6	7.8,4.7	190	39,23
	0.3	8.9	9.8,9.5	12.6	14,13.6	9.9	2.6,2.4	80	21,20
	0.7	6.1	4.1,5.9	20.2	13.8,19.8	4.7	0.5,1	208	21,43
	0.9	2.2	1.8	22.4	18.3	0.6	0.1	253	36
T-L	0.1		21.9		24.4		13		64
	0.3	16.6	18.4	18.8	25	240	9.2	286	73
	0.7	6.2,6.9	5.6	20.5,23	18.7	213,270	10.8	213,270	37
	0.9	1.7,2.2		16.8,21.8		0.4,0.6		143,242	

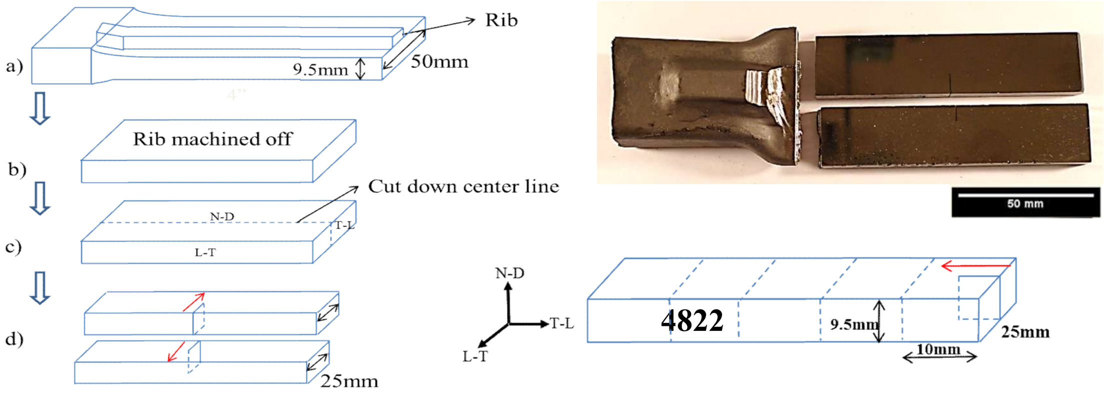

TNM

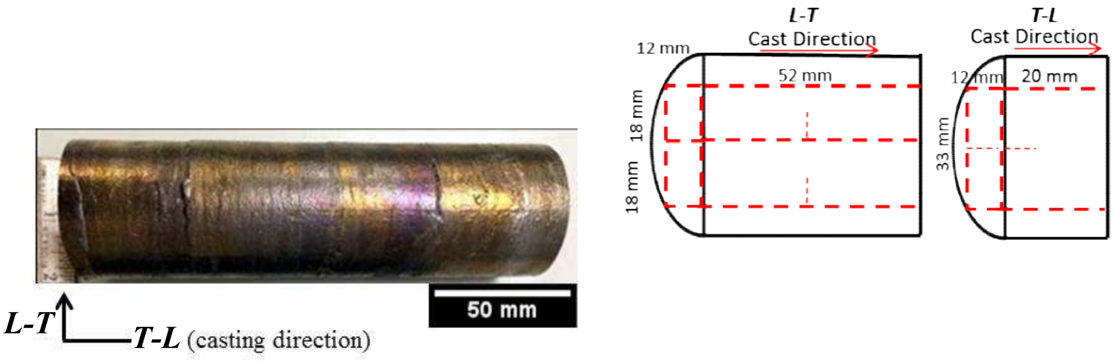

Fig. 1: As-cast 4822 (top) and TNM (bottom) test specimens extraction plans in *L-T* and *T-L* orientations.

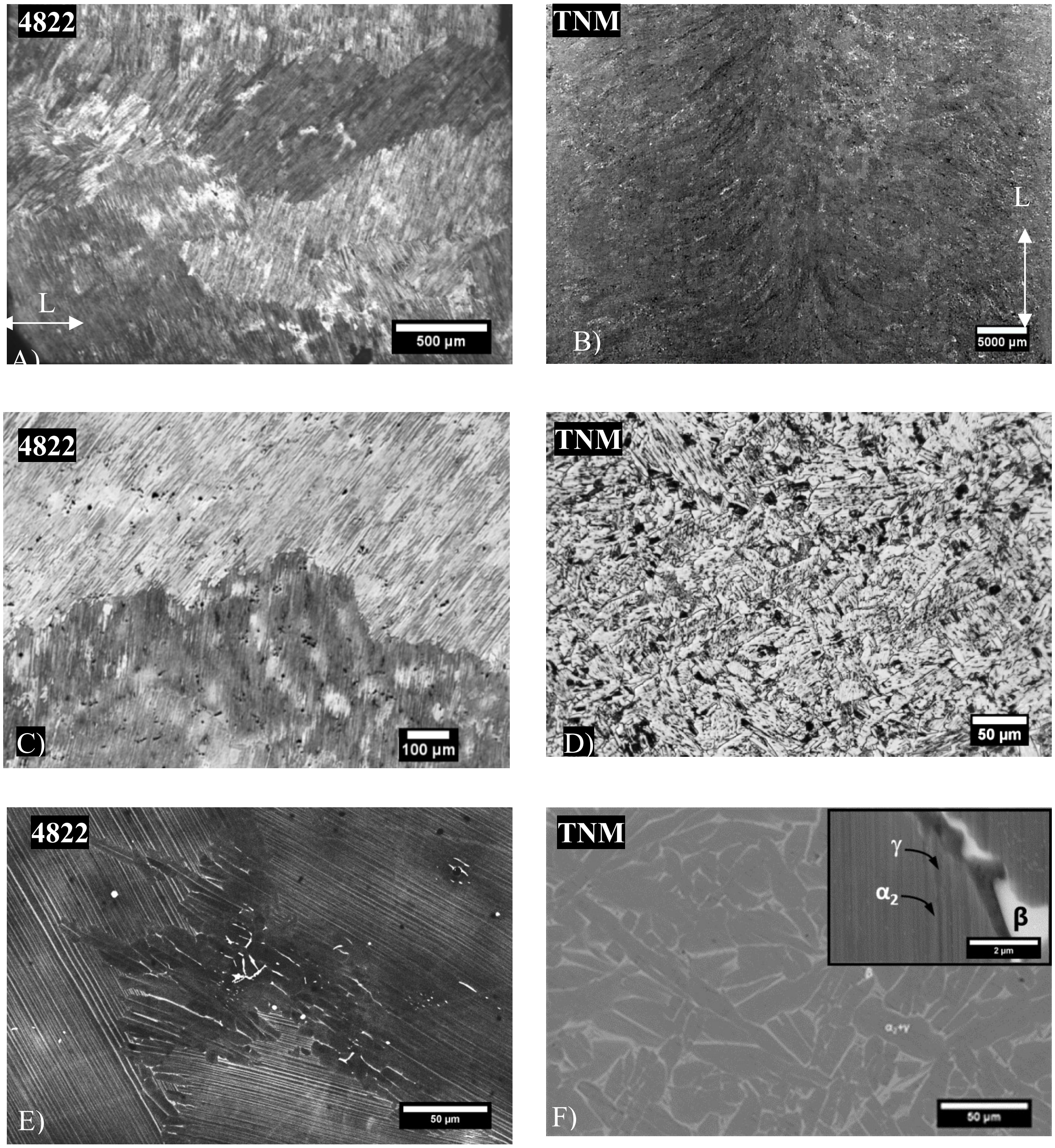
4822
L
500 µm
A)
TNM
L
5000 µm
B)
4822
100 µm
C)
TNM
50 µm
D)
4822
50 µm
E)
TNM
γ
α_2
β
2 µm
β
$\alpha_2+\gamma$
50 µm
F)

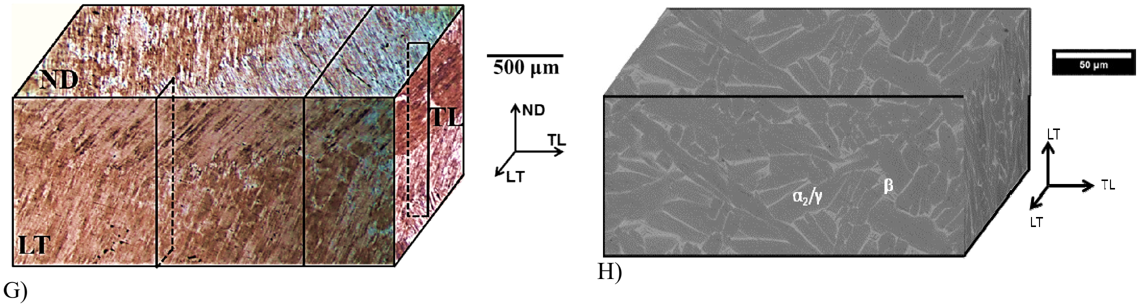

Fig. 2: Microstructures of as-cast 4822 (left) and TNM (right) program materials: A) 4822 optical macrograph, B) TNM optical macrograph, C) 4822 optical micrograph, D) TNM optical micrograph, E) 4822 backscattered electron image, F) TNM backscattered electron image. G) 3D 4822 optical micrographs, and H) TNM 3D backscatter electron image. Optical micrographs were obtained on samples etched with Krolls reagent. Phase contrast in backscattered electron images is: γ-grey, α_2- dark, and β_o - bright.

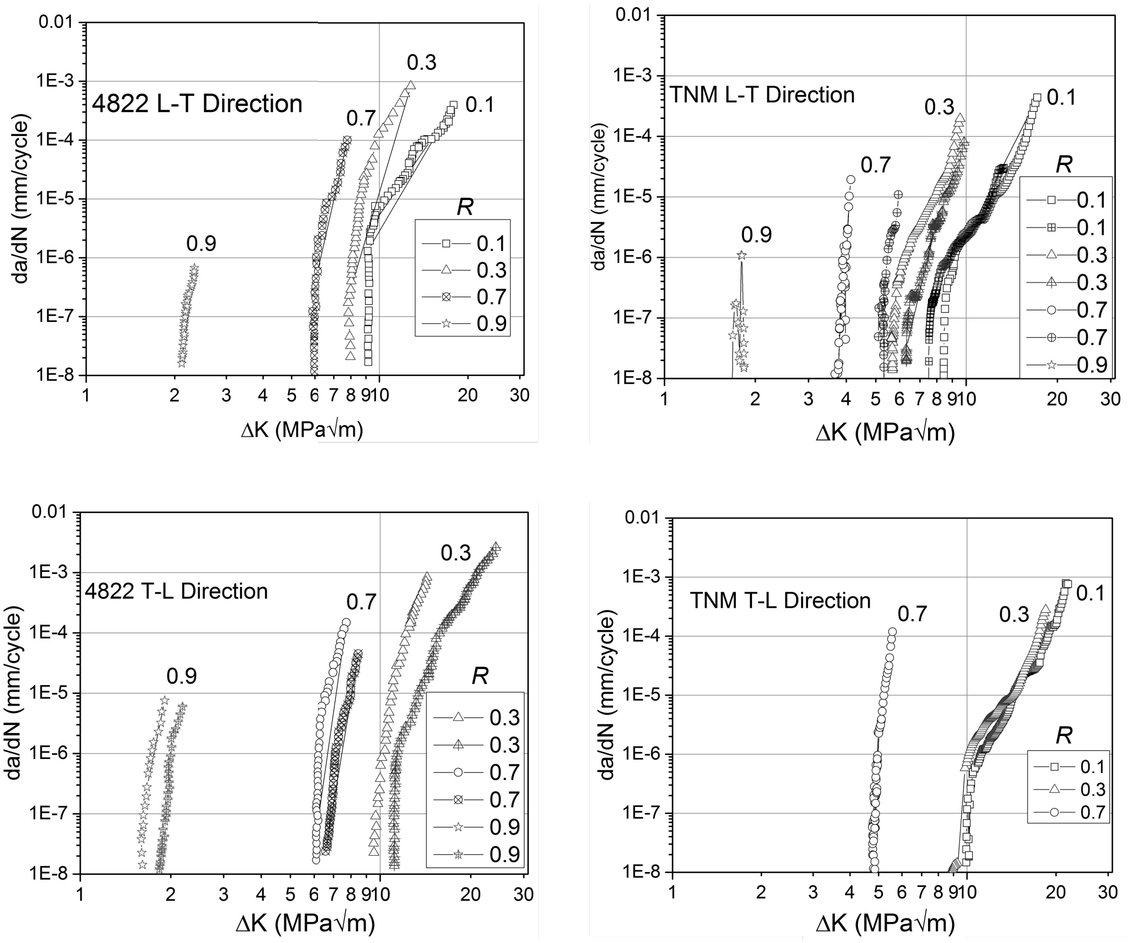

Fig. 3: Effect of load ratio *R* on fatigue crack growth rate curves of specimens tested in *L-T* direction (top) and *T-L* direction (bottom) of as-cast 4822 (left) and TNM (right).

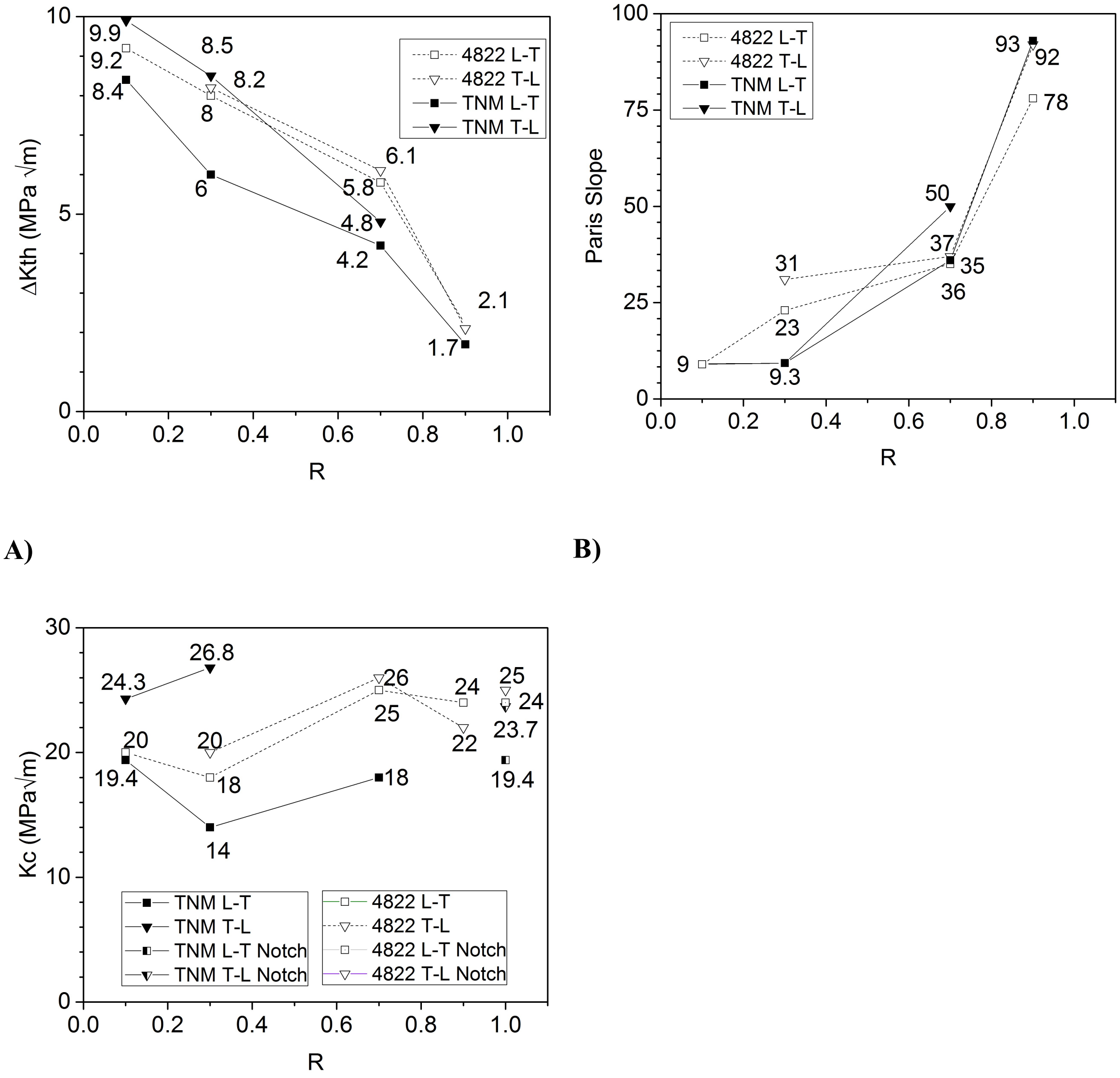

A)

B)

C)

Fig. 4: Effect of load ratio *R* on A) fatigue threshold Δ*K*th, B) Paris slope *m*, and C) *K* at overload failure K_c and notch toughness for 4822 and TNM in both *L-T* and *T-L* orientations.

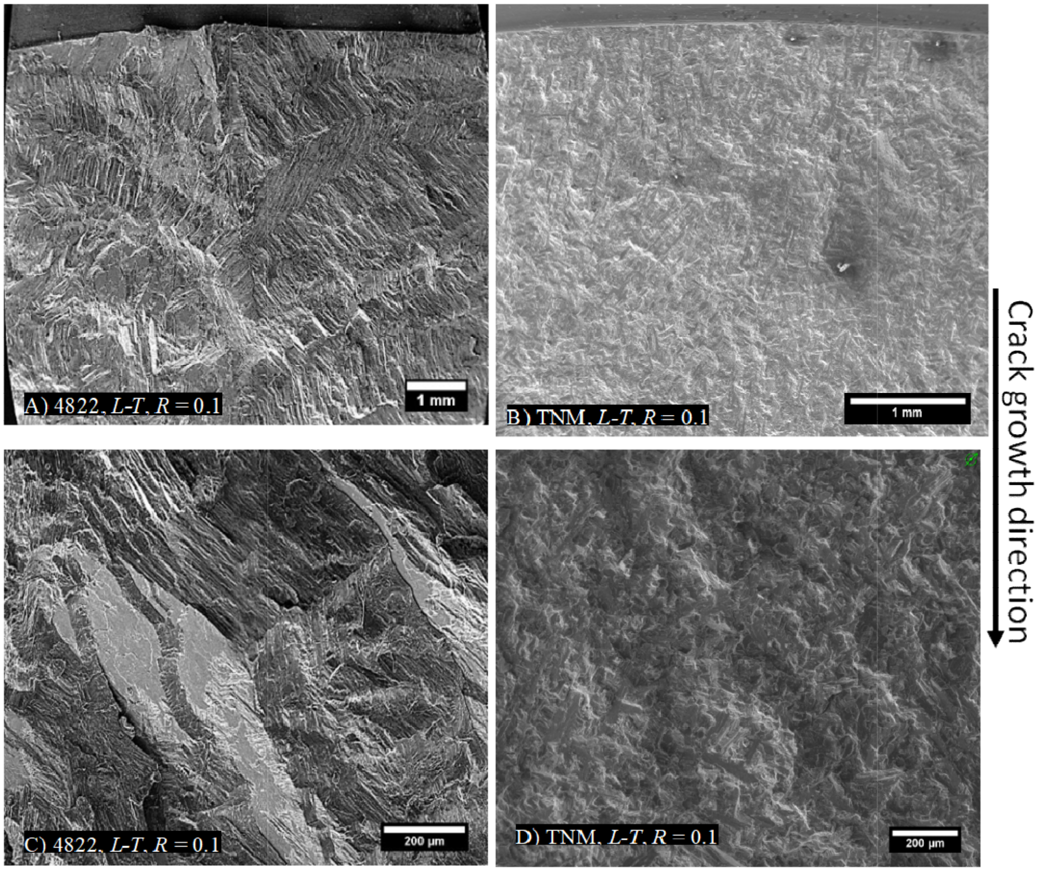

Fig. 5: SEM fractographs of fatigue specimen surfaces tested at R = 0.1 in the *L-T* direction: A) 4822 overview, B) TNM overview, C) 4822 overload region,and D) TNM overload region. Crack growth direction is from top to bottom.

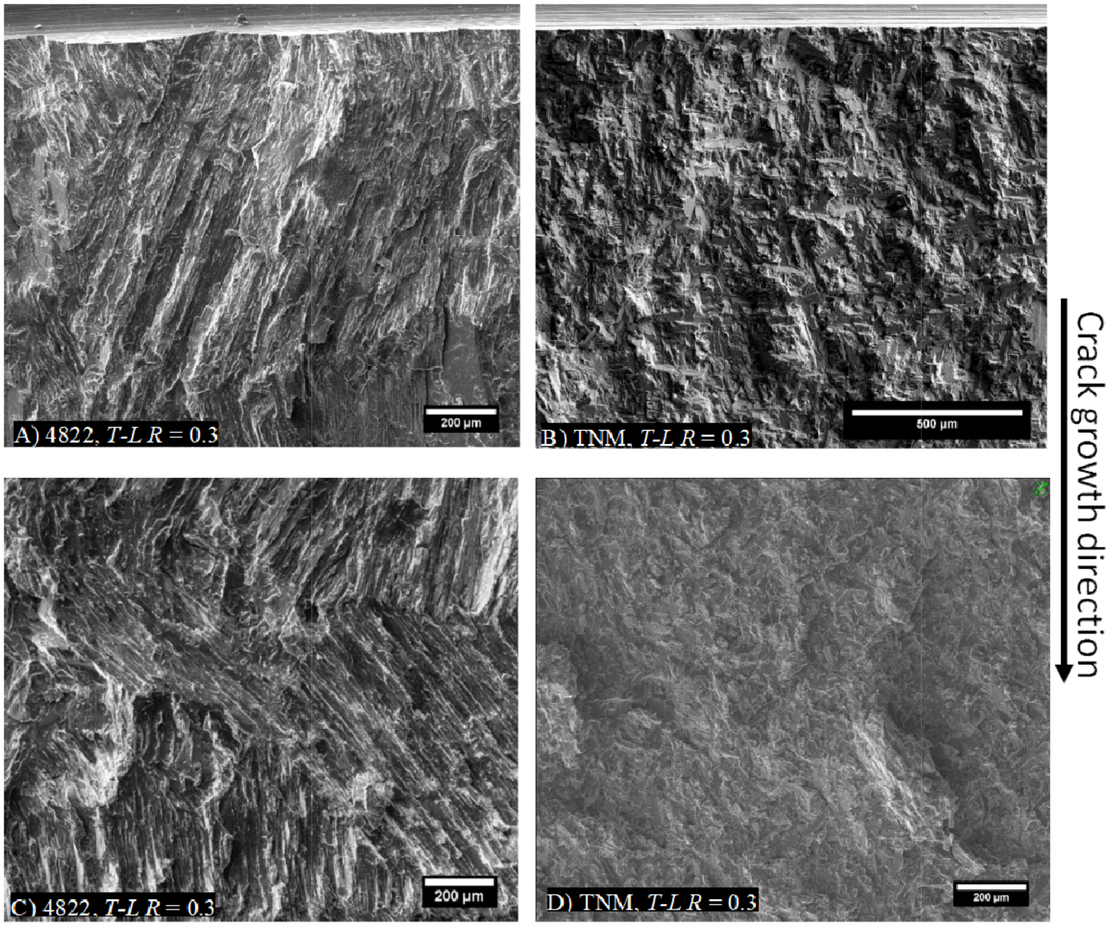

Fig: 6. SEM fractographs of fatigue specimen surfaces tested at R=0.3 in the *T-L* direction: A) 4822 overview, B) TNM overview, C) 4822 overload region, D) TNM overload region. Crack growth direction is from top to bottom.

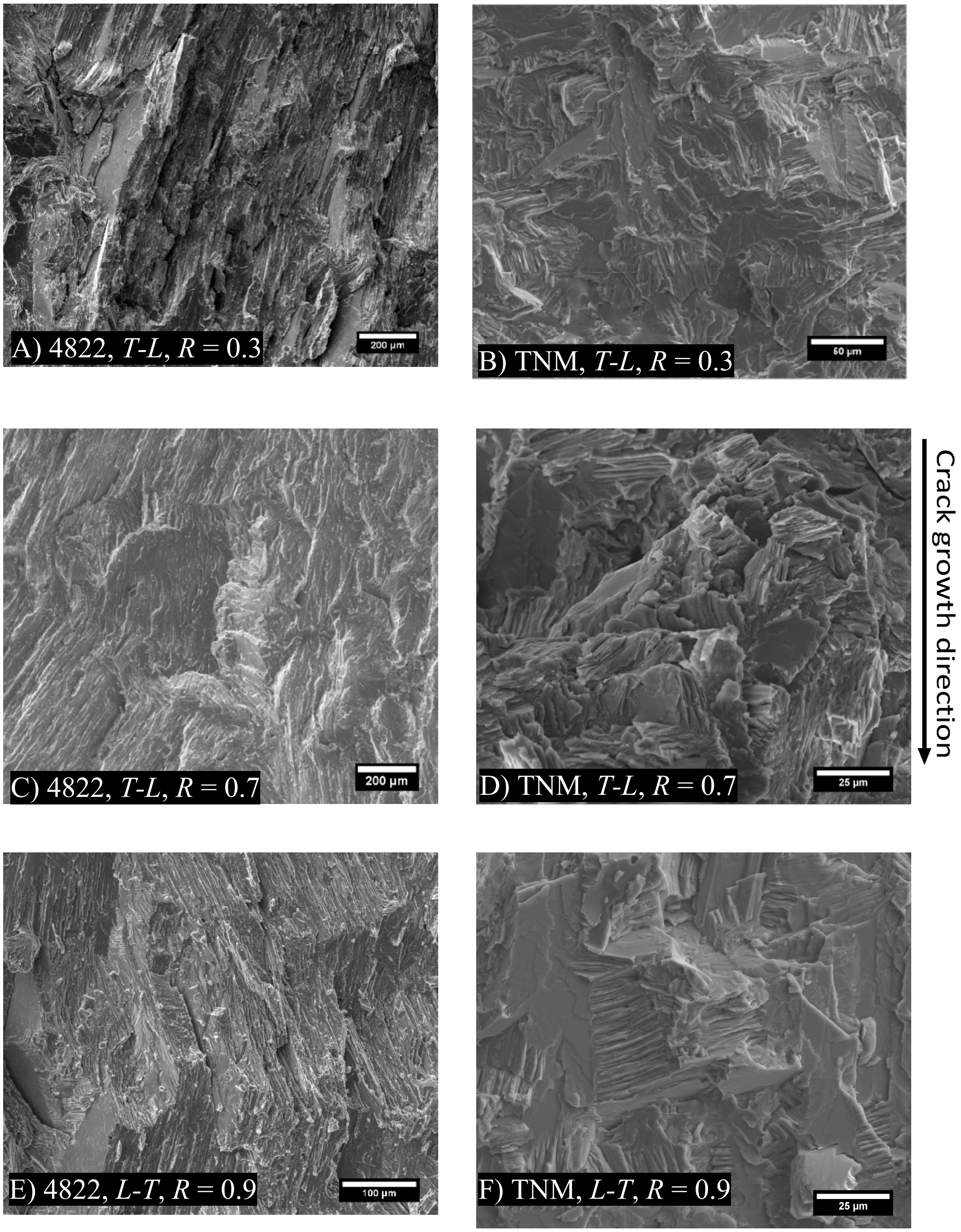

Fig. 7: SEM fractographs of specimens of specimens tested at different load ratios and at various ΔK: A) 4822, *T-L*, $R = 0.3$, rising ΔK, B) TNM, *T-L*, $R = 0.3$, rising ΔK, C) 4822, *T-L*, $R = 0.7$, at threshold, D) TNM, *T-L*, $R = 0.7$, at threshold, E) 4822, *L-T*, $R = 0.9$, rising ΔK, and F) TNM, *L-T*, $R = 0.9$, rising ΔK. Crack growth direction is from top to bottom.

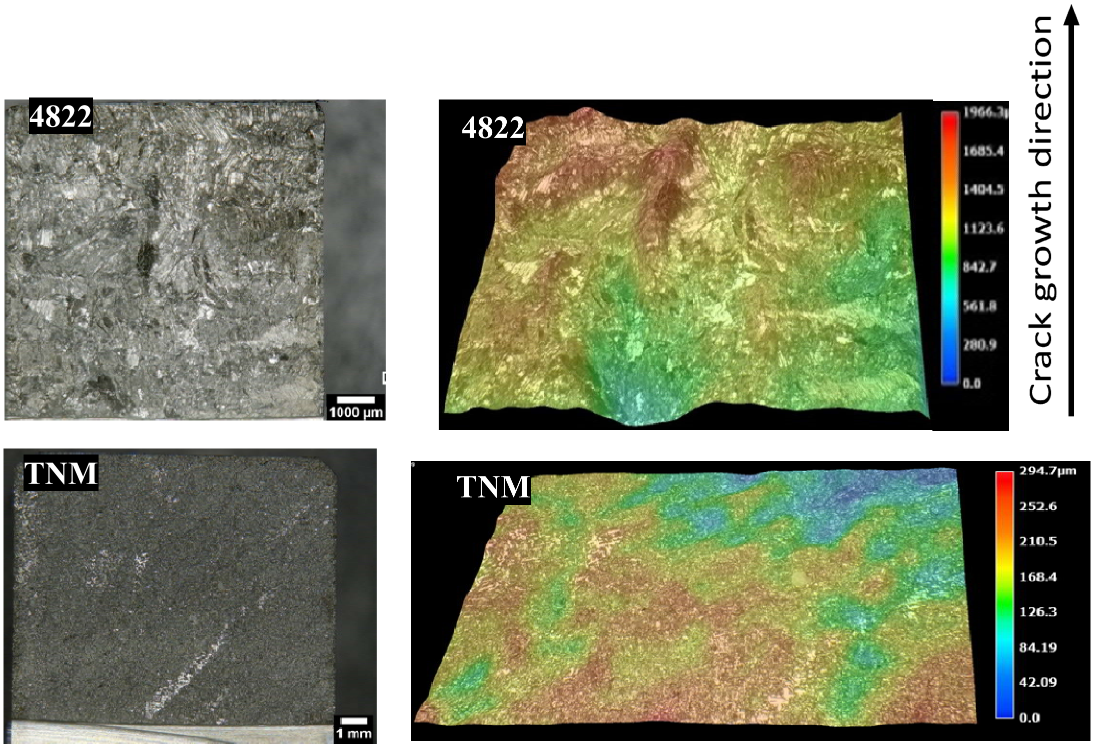

Fig. 8: 3D surface roughness plot of 4822 (top) and TNM (bottom) 7 mm x 7 mm area taken at intermediate ΔK, both specimens fatigue tested in the *T-L* direction at *R* = 0.3. For 4822, a peak of 1750 µm exists at the top left corner with troughs of 800 µm. The peak represents large roughness resulting from fatigue crack growth across a grain oriented in a different direction to adjacent grains. TNM sample exhibits a peak height of approximately 280 µm and troughs of 50 µm.

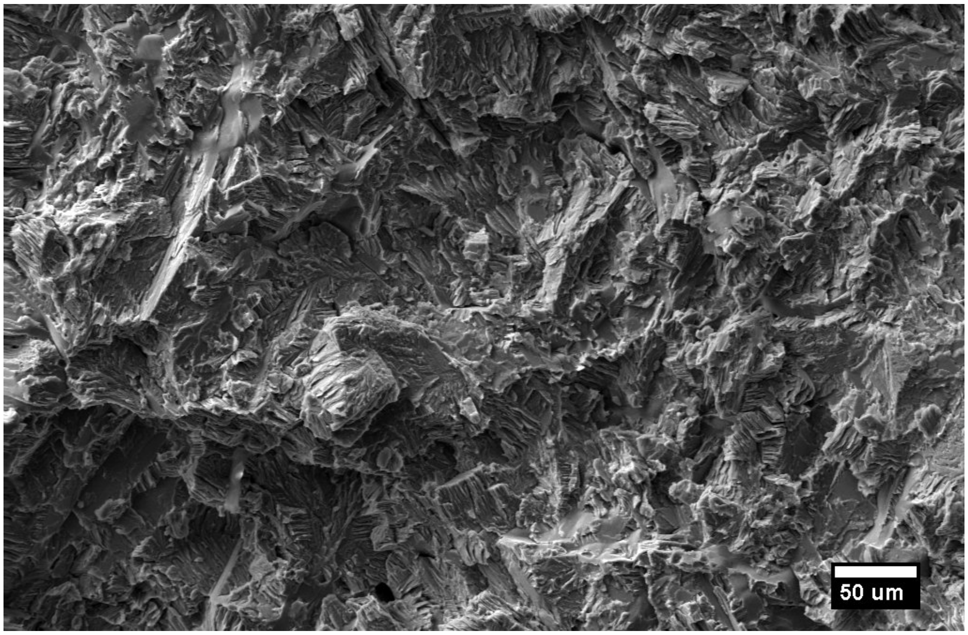

Fig 9: SEM fractograph (backscattered electron imaging mode) of TNM tensile specimen (yield strength = 680 MPa, plastic elongation < 0.5%) showing mostly brittle faceted fracture.

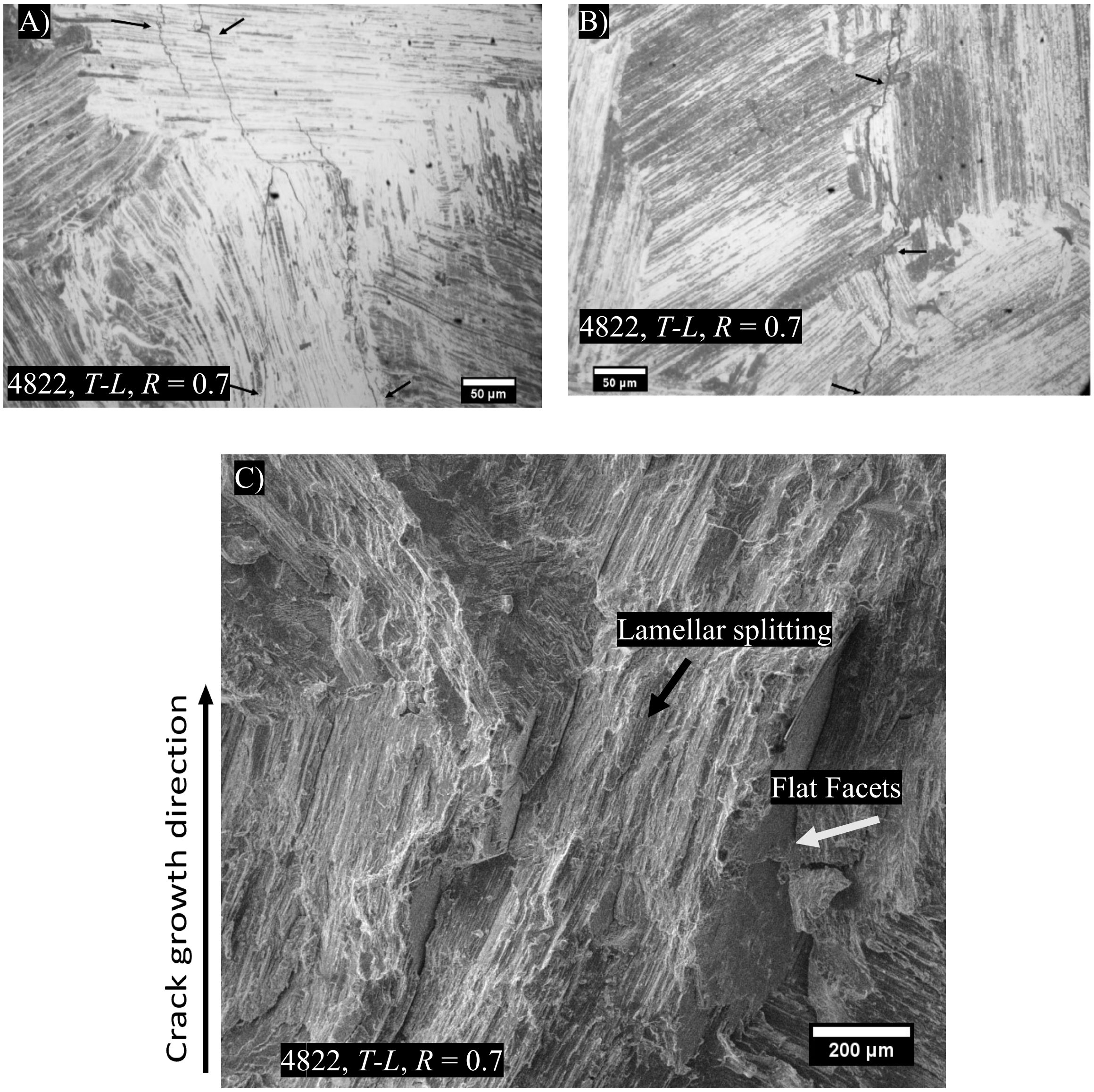

Fig. 10: Crack path in 4822 specimen fatigue tested in the *T-L* direction to threshold at *R* = 0.7. Crack growth direction is from bottom to top with arrows in A) and B) pointing to the crack path. Optical micrograph (etched with Krolls reagent) showing A) translamellar and interlamellar cracks as well as secondary cracking, B) crack following a colony boundary, and C) secondary electron SEM fractograph in the overload region showing lamellar splitting (black arrow) and flat brittle facets (white arrow).

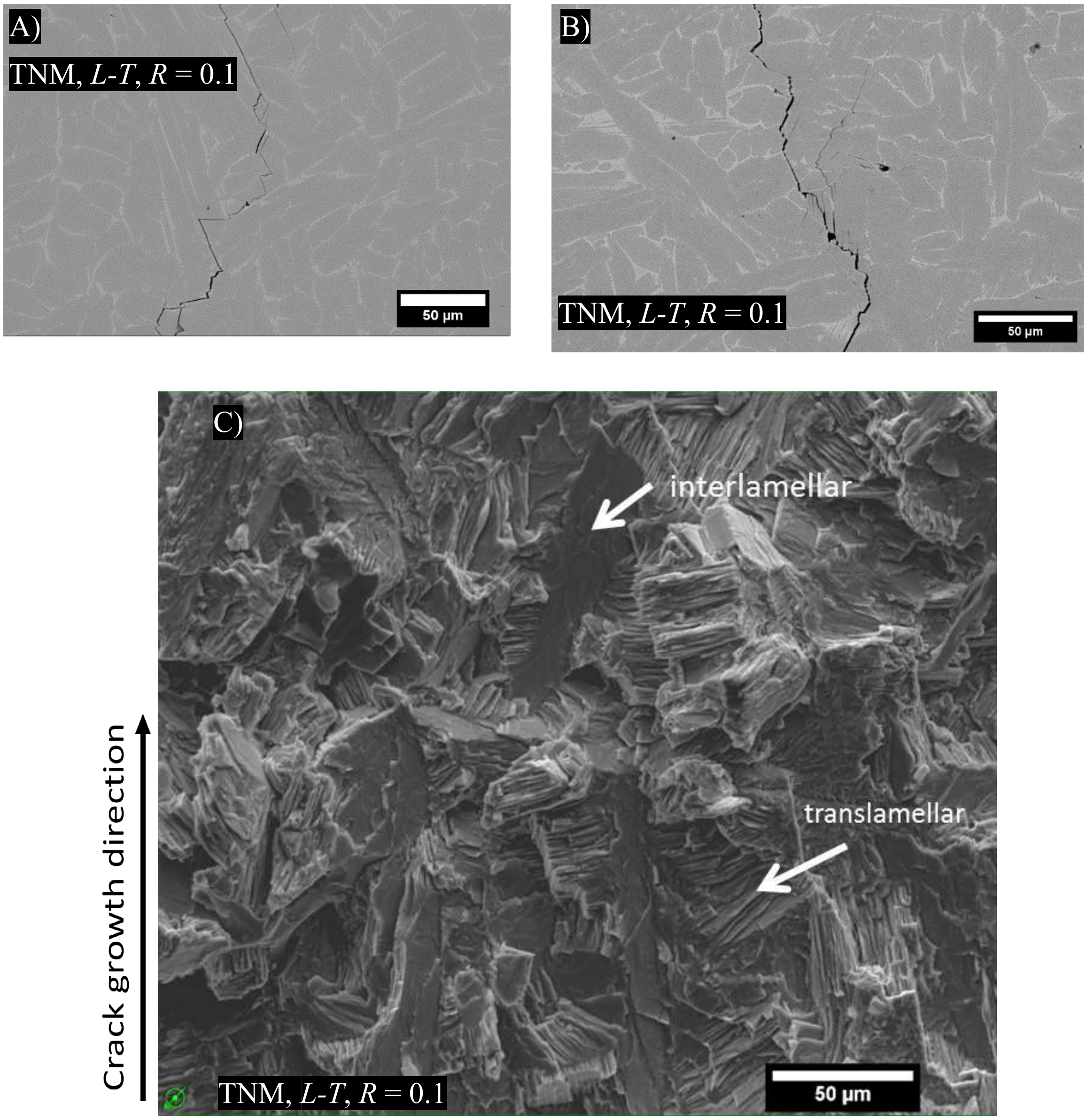

Fig. 11: Crack path of TNM specimen fatigue tested in the *L-T* direction to threshold at *R* = 0.1. Crack growth direction is from bottom to top. Backscattered electron images showing A) translamellar and interlamellar cracking with the crack following β_o at colony boundaries, B) secondary cracking and microcracking away from the crack path, and C) SEM fractograph in the medium ΔK region showing translamellar cracking with lamellar splitting and interlamellar fracture.

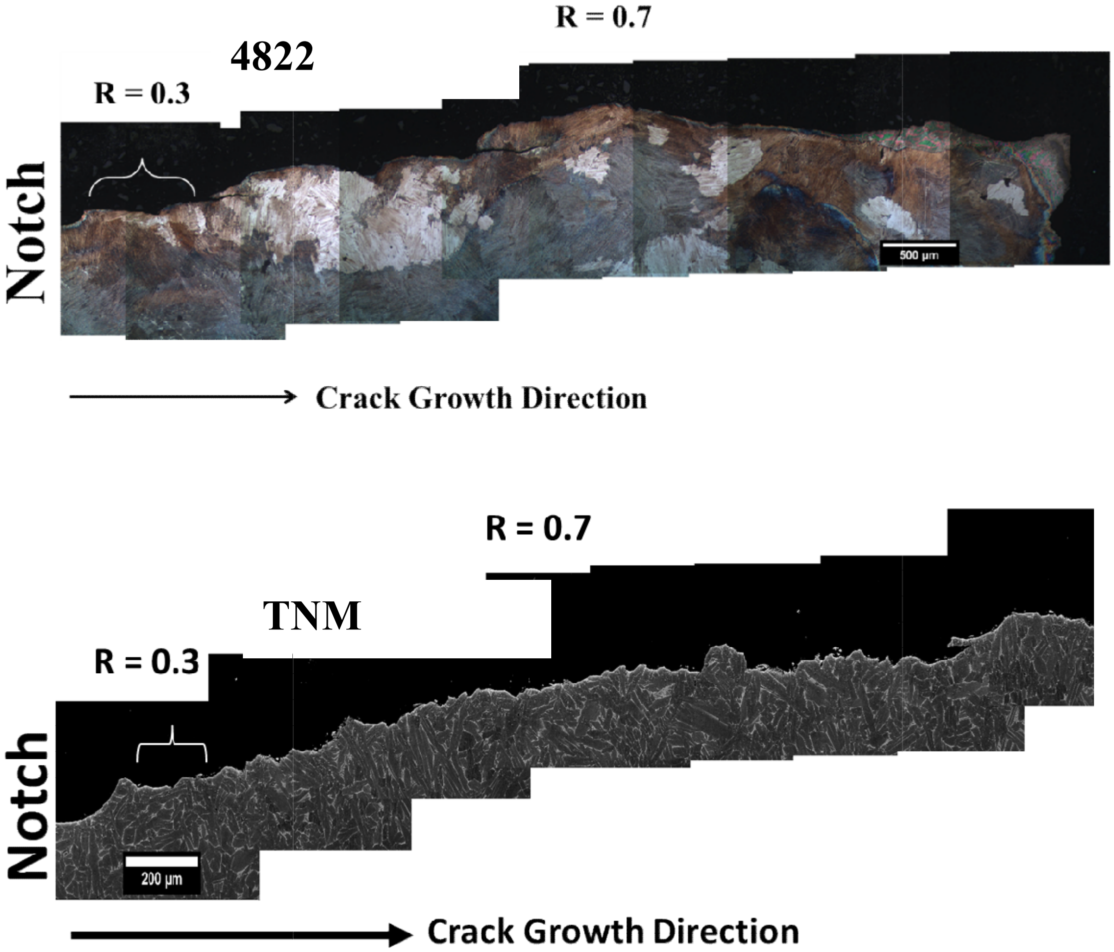

Fig. 12: (Top) Crack path of (optical) 4822 L-T broken sample fatigued at R = 0.3 and then R = 0.7. Secondary cracking is seen and the crack path follows the microstructure and produces significant roughness. (Bottom) Crack path of TNM (BSE) L-T broken sample fatigued at R = 0.3 and then R = 0.7

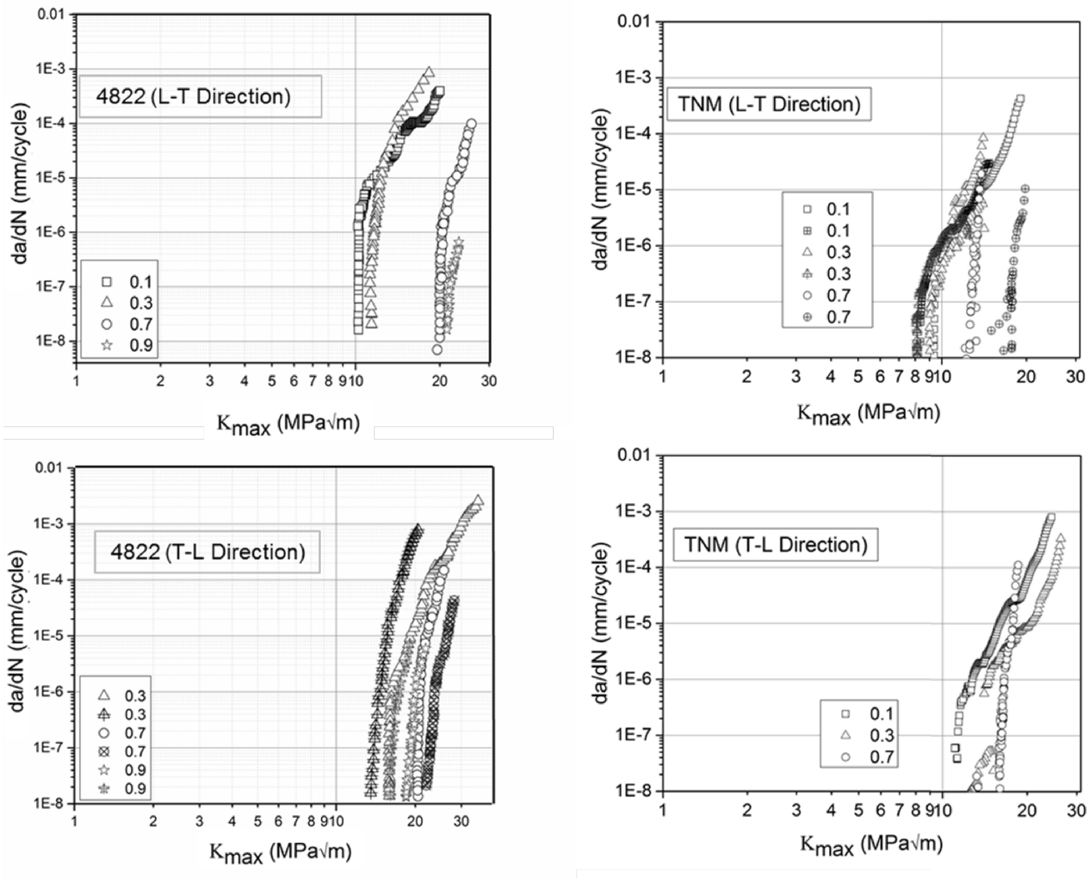

Fig. 13: $K_{\max}$ vs. d*a*/d*N* curves of 4822 (left) and TNM (right) tested in *L-T* (top) and *T-L* (bottom) directions at various *R* values.

6. References

[1] G. Sauthoff, *Intermetallics*, 1st ed. Weinheim, NY: Wiley-VCH, 1995.

[2] S. Djanarthany, J.-C. Viala, and J. Bouix, “An overview of monolithic titanium aluminides based on Ti3Al and TiAl,” *Mater. Chem. Phys.*, vol. 72, no. 3, pp. 301–319, Dec. 2001.

[3] Y.-W. Kim, “Intermetallic alloys based on gamma titanium aluminide,” *JOM*, vol. 41, no. 7, pp. 24–30, Jul. 1989.

[4] W. Voice, “The future use of gamma titanium aluminides by Rolls-Royce,” *Aircr. Eng. Aerosp. Technol.*, vol. 71, no. 4, pp. 337–340, Aug. 1999.

[5] F. H. Froes, C. Suryanarayana, and D. Eliezer, “Review Synthesis, Properties and Applications of Titanium Aluminides,” *J. Mater. Sci.*, vol. 27, pp. 5113–5140, 1992.

[6] W. E. Voice, M. Henderson, E. F. J. Shelton, and X. Wu, “Gamma titanium aluminide, TNB,” *Intermetallics*, vol. 13, no. 9, pp. 959–964, Sep. 2005.

[7] D. M. Dimiduk, “Gamma titanium aluminide alloys—an assessment within the competition of aerospace structural materials,” *Mater. Sci. Eng. A*, vol. 263, no. 2, pp. 281–288, May 1999.

[8] W. O. Soboyejo, W. Shen, J. Lou, C. Mercer, V. Sinha, and A. B. O. Soboyejo, “A probabilistic framework for the modeling of fatigue in cast lamellar gamma-based titanium aluminides,” *Mech. Mater.*, vol. 36, no. 1–2, pp. 177–197, Jan. 2004.

[9] A. W. Sommer and G. . Keijzers, *Gamma Titanium Aluminides 2003*. PA: TMS, 2003.

[10] R. Schulte, “TITANIUM Europe 2013 Summary,” in *TITANIUM Europe 2013 Summary*, Hamburg, Germany, 2013.

[11] H. Wang, R. C. Reed, J.-C. Gebelin, and N. Warnken, “On the modelling of the point defects in the ordered B2 phase of the Ti–Al system: Combining CALPHAD with first-principles calculations,” *Calphad*, vol. 39, pp. 21–26, Dec. 2012.

[12] K. B. Kothari, “Manufacturing techniques for titanium aluminide based alloys and metal matrix composites,” 2010.

[13] Y.-W. Kim, “Ordered intermetallic alloys, part III: gamma titanium aluminides,” *Jom*, vol. 46, no. 7, pp. 30–39, 1994.

[14] Y.-W. Kim, “Effects of microstructure on the deformation and fracture of γ-TiAl alloys,” *Mater. Sci. Eng. A*, vol. 192–193, Part 2, pp. 519–533, Feb. 1995.

[15] Y.-W. (Y-W.) Kim, “Microstructural evolution and mechanical properties of a forged gamma titanium aluminide alloy,” *Acta Metall. Mater.*, vol. 40, no. 6, pp. 1121–1134, Jun. 1992.

[16] G. Das, H. Kestler, H. Clemens, and P. A. Bartolotta, “Sheet gamma TiAl: Status and opportunities,” *JOM*, vol. 56, no. 11, pp. 42–45, Nov. 2004.

[17] Y.-W. Kim and D. M. Dimiduk, “Progress in the understanding of gamma titanium aluminides,” *JOM*, vol. 43, no. 8, pp. 40–47, Aug. 1991.

[18] S. Zghal, S. Naka, and A. Couret, “A QUANTITATIVE TEM ANALYSIS OF THE LAMELLAR MICROSTRUCTURE IN TiAl BASED ALLOYS,” *Acta Mater.*, vol. 45, no. 7, pp. 3005–3015, Jul. 1997.

[19] C. L. Fu and M. H. Yoo, “Interfacial energies in two-phase TiAl-Ti3Al alloy,” *Scr. Mater.*, vol. 37, no. 10, pp. 1453–1459, Nov. 1997.

[20] Y. Yamamoto, M. Takeyama, and T. Matsuo, “Stability of lamellar microstructure consisting of γ/γ interfaces in Ti–48Al–8Nb single crystal at elevated temperatures,” *Mater. Sci. Eng. A*, vol. 329, no. Supplement C, pp. 631–636, Jun. 2002.

[21] J. N. Wang and T. G. Nieh, “The role of ledges in creep of TiAl alloys with fine lamellar structures,” *Acta Mater.*, vol. 46, no. 6, pp. 1887–1901, Mar. 1998.

[22] W. J. Zhang, L. Francesconi, E. Evangelista, and G. L. Chen, “Characterization of widmanstätten laths and interlocking boundaries in fully-lamellar TiAl-base alloy,” *Scr. Mater.*, vol. 37, no. 5, pp. 627–633, Sep. 1997.

[23] F. Herrouin, D. Hu, P. Bowen, and I. P. Jones, “Microstructural changes during creep of a fully lamellar TiAl alloy,” *Acta Mater.*, vol. 46, no. 14, pp. 4963–4972, Sep. 1998.

[24] T. Noda, M. Okabe, S. Isobe, and M. Sayashi, “Silicide precipitation strengthened TiAl,” *Mater. Sci. Eng. A*, vol. 192, pp. 774–779, 1995.

[25] L. M. Hsiung and T. G. Nieh, “Substructure in a creep deformed lamellar TiAl alloy,” *Scr. Mater.*, vol. 36, no. 3, pp. 323–330, 1997.

[26] M. H. Loretto, A. B. Godfrey, D. Hu, P. A. Blenkinsop, I. P. Jones, and T. T. Cheng, “The influence of composition and processing on the structure and properties of TiAl-based alloys,” *Intermetallics*, vol. 6, no. 7, pp. 663–666, Jan. 1998.

[27] J. Beddoes, D. Y. Seo, W. R. Chen, and L. Zhao, “Relationship between tensile and primary creep properties of near γ-TiAl intermetallics,” *Intermetallics*, vol. 9, no. 10–11, pp. 915–922, Oct. 2001.

[28] F.-Y. Hsu, H.-J. Klaar, G.-X. Wang, and M. Dahms, “Influence of Si content on microstructure of TiAl alloys,” *Mater. Charact.*, vol. 36, no. 4, pp. 371–378, Apr. 1996.

[29] T. T. Cheng and M. R. Willis, “Effects of aging on the microstructure and creep properties of γ-TiAl containing heavy alloying,” *Scr. Mater.*, vol. 39, no. 9, pp. 1255–1265, Oct. 1998.

[30] W. Wunderlich, T. Kremser, and G. Frommeyer, “Mobile dislocations at the α2/γ phase boundaries in intermetallic TiAl/Ti3Al-alloys,” *Acta Metall. Mater.*, vol. 41, no. 6, pp. 1791–1799, Jun. 1993.

[31] B. J. Inkson, H. Clemens, and J. Marien, “γ α2 B2 Lamellar Domains in Rolled TiAl,” *Scr. Mater.*, vol. 38, no. 9, pp. 1377–1382, Apr. 1998.

[32] H. Clemens and S. Mayer, “Design, Processing, Microstructure, Properties, and Applications of Advanced Intermetallic TiAl Alloys,” *Adv. Eng. Mater.*, vol. 15, no. 4, pp. 191–215, Apr. 2013.

[33] A. B. Godfrey and M. H. Loretto, “The nature of complex precipitates associated with the addition of boron to a γ-based titanium aluminide,” *Intermetallics*, vol. 4, no. 1, pp. 47–53, Jan. 1996.

[34] H. Clemens *et al.*, “In and ex situ investigations of the β-phase in a Nb and Mo containing γ-TiAl based alloy,” *Intermetallics*, vol. 16, no. 6, pp. 827–833, Jun. 2008.

[35] H. Clemens, W. Wallgram, S. Kremmer, V. Güther, A. Otto, and A. Bartels, “Design of Novel β-Solidifying TiAl Alloys with Adjustable β/B2-Phase Fraction and Excellent Hot-Workability,” *Adv. Eng. Mater.*, vol. 10, no. 8, pp. 707–713, Aug. 2008.

[36] F. Appel, M. Oehring, and R. Wagner, “Novel design concepts for gamma-base titanium aluminide alloys,” *Intermetallics*, vol. 8, no. 9–11, pp. 1283–1312, Sep. 2000.

[37] W. Wallgram, T. Schmölzer, L. Cha, G. Das, V. Güther, and H. Clemens, “Technology and mechanical properties of advanced γ-TiAl based alloys,” *Int. J. Mater. Res.*, vol. 100, no. 8, pp. 1021–1030, 2009.

[38] N. Saunders, “Gamma Titanium Aluminides 1999,” Warrendale, Pa: TNM, 1999, p. 183.

[39] H. F. Chladil *et al.*, “Experimental studies and thermodynamic simulation of phase transformations in high Nb containing γ-TiAl based alloys,” *Int. J. Mater. Res.*, vol. 98, no. 11, pp. 1131–1137, Nov. 2007.

[40] H. F. Chladil *et al.*, “Phase transformations in high niobium and carbon containing γ-TiAl based alloys,” *Intermetallics*, vol. 14, no. 10–11, pp. 1194–1198, Oct. 2006.

[41] I. J. Watson *et al.*, “In Situ Characterization of a Nb and Mo Containing γ-TiAl Based Alloy Using Neutron Diffraction and High-Temperature Microscopy,” *Adv. Eng. Mater.*, vol. 11, no. 11, pp. 932–937, Nov. 2009.

[42] T. Schmoelzer *et al.*, “Phase fractions, transition and ordering temperatures in TiAl–Nb–Mo alloys: An in- and ex-situ study,” *Intermetallics*, vol. 18, no. 8, pp. 1544–1552, Aug. 2010.

[43] E. Schwaighofer *et al.*, “Microstructural design and mechanical properties of a cast and heat-treated intermetallic multi-phase γ-TiAl based alloy,” *Intermetallics*, vol. 44, pp. 128–140, Jan. 2014.

[44] M. Schloffer *et al.*, “Microstructure development and hardness of a powder metallurgical multi phase γ-TiAl based alloy,” *Intermetallics*, vol. 22, pp. 231–240, Mar. 2012.

[45] L. Cha, H. Clemens, and G. Dehm, “Microstructure evolution and mechanical properties of an intermetallic Ti-43.5Al-4Nb-1Mo-0.1B alloy after ageing below the eutectoid temperature,” *Int. J. Mater. Res.*, vol. 102, no. 6, pp. 703–708, 2011.

[46] Z. Jin and T. R. Bieler, “An in-situ observation of mechanical twin nucleation and propagation in TiAl,” *Philos. Mag. A*, vol. 71, no. 5, pp. 925–947, May 1995.

[47] B. Skrotzki, M. Ünal, and G. Eggeler, “On the role of mechanical twinning in creep of a near-γ TiAl-alloy with duplex microstructure,” *Scr. Mater.*, vol. 39, no. 8, pp. 1023–1029, Sep. 1998.

[48] T. Matsuo, T. Nozaki, T. Asai, S. Y. Chang, and M. Takeyama, “Effect of lamellar plates on creep resistance in near gamma TiAl alloys,” *Intermetallics*, vol. 6, no. 7, pp. 695–698, Jan. 1998.

[49] V. K. Vasudevan, S. A. Court, P. Kurath, and H. L. Fraser, “Effect of grain size and temperature on the yield stress of the intermetallic compound TiAl,” *Scr. Metall.*, vol. 23, no. 4, pp. 467–469, Apr. 1989.

[50] T. Kawabata, T. Kanai, and O. Izumi, “Positive temperature dependence of the yield stress in TiAl L10 type superlattice intermetallic compound single crystals at 293–1273 K,” *Acta Metall.*, vol. 33, no. 7, pp. 1355–1366, Jul. 1985.

[51] V. K. Vasudevan, M. A. Stucke, S. A. Court, and H. L. Fraser, “The influence of second phase Ti3Al on the deformation mechanisms in TiAl,” *Philos. Mag. Lett.*, vol. 59, no. 6, pp. 299–307, Jun. 1989.

[52] M. Werwer, R. Kabir, A. Cornec, and K.-H. Schwalbe, "Fracture in lamellar TiAl simulated with the cohesive model," *Eng. Fract. Mech.*, vol. 74, no. 16, pp. 2615–2638, Nov. 2007.

[53] F. Appel and R. Wagner, "Microstructure and deformation of two-phase γ-titanium aluminides," *Mater. Sci. Eng. R Rep.*, vol. 22, no. 5, pp. 187–268, May 1998.

[54] N. E. Dowling, *Mechanical Behavior of Materials*, 3rd edition. Upper Saddle River, NJ: Oearson Pretice Hall, 2007.

[55] "Fracture Toughness." [Online]. Available: https://www.nde-ed.org/EducationResources/CommunityCollege/Materials/Mechanical/FractureToughness.htm. [Accessed: 22-Nov-2017].

[56] ASTM Standard E399, "Test Method for Linear-Elastic Plane-Strain Fracture Toughness K1c of Metallic Materials," ASTM International, 2009.

[57] R. O. Ritchie, "Mechanisms of fatigue-crack propagation in ductile and brittle solids," *Int. J. Fract.*, vol. 100, no. 1, pp. 55–83, 1999.

[58] P. . Paris, M. P. Gomez, and W. . Anderson, "A rational analytic theory of fatigue," *Trend Eng.*, no. 13, pp. 9–14, 1961.

[59] R. O. Ritchie, "Near-threshold fatigue crack propagation in ultra-high strength steel: influence of load ratio and cyclic strength," *J. Eng. Mater. Technol.*, vol. 99, no. 3, pp. 195–204, 1977.

[60] R. O. Ritchie, "Mechanisms of fatigue crack propagation in metals, ceramics and composites: Role of crack tip shielding," *Mater. Sci. Eng. A*, vol. 103, no. 1, pp. 15–28, Aug. 1988.

[61] R. O. Ritchie, C. J. Gilbert, and J. M. McNaney, "Mechanics and mechanisms of fatigue damage and crack growth in advanced materials," *Int. J. Solids Struct.*, vol. 37, no. 1–2, pp. 311–329, Jan. 2000.

[62] "Advanced Manufacturing and Mechanical Reliability Characterization Center." [Online]. Available: http://ammrc.case.edu/. [Accessed: 30-Mar-2014].

[63] ASTM Standard E647, "Standard Test Method for Measurement of Fatigue Crack Growth Rates," ASTM International, 2011.

[64] P. Donehoo, W. Yu, and R. O. Ritchie, "On the growth of cracks at the fatigue threshold following compression overloads: Role of load ratio," *Mater. Sci. Eng.*, vol. 74, no. 1, pp. 11–17, Sep. 1985.

[65] J. C. Newman Jr. and Y. Yamada, "Compression precracking methods to generate near-threshold fatigue-crack-growth-rate data," *Int. J. Fatigue*, vol. 32, no. 6, pp. 879–885, Jun. 2010.

[66] J. Newman Jr., J. Schneider, A. Daniel, and D. McKnight, "Compression pre-cracking to generate near threshold fatigue-crack-growth rates in two aluminum alloys," *Int. J. Fatigue*, vol. 27, no. 10–12, pp. 1432–1440, Oct. 2005.

[67] S. Suresh, L. Ewart, M. Maden, W. S. Slaughter, and M. Nguyen, "Fracture toughness measurements in ceramics: Pre-cracking in cyclic compression," *J. Mater. Sci.*, vol. 22, no. 4, pp. 1271–1276, 1987.

[68] ASTM Standard E1820, "Test Method for Measurement of Fracture Toughness," ASTM International, West Conshohocken, PA, 2011.

[69] ASTM Standard E8, "ASTM E8/E8M-16a Standard Test Methods for Tension Testing of Metallic Materials," ASTM International, West Conshohocken, PA, 2016.

[70] R. Jenkins and R. Snyder, *Introduction to X-Ray Powder Diffractometry*, 1st ed. Wiley-Interscience, 1996.

[71] K. S. Chan, "Micromechanics of shear ligament toughening," *Metall. Trans. A*, vol. 22, no. 9, pp. 2021–2029, 1991.

[72] K. S. Chan, "Understanding fracture toughness in gamma TiAl," *JOM*, vol. 44, no. 5, pp. 30–38, 1992.

[73] K. S. Chan and Y.-W. Kim, "Fracture Processes in a Two-Phase Gamma Titanium Aluminide Alloy," in *Microstructure/property relationships in titanium aluminides and alloys*, Y.-W. Kim and R. R. Boyer, Eds. Warrendale, Pa: TMS, 1991, pp. 179–196.

[74] K. S. Chan and Y.-W. Kim, "Influence of microstructure on crack-tip micromechanics and fracture behaviors of a two-phase TiAl alloy," *Metall. Trans. A*, vol. 23, no. 6, pp. 1663–1677, 1992.

[75] S. . Kampe, "Microstructure Morphology Effects on Fracture Toughness of a Cast Near-Gamma Titanium Aluminide Alloy," in *Microstructure/property relationships in titanium aluminides and alloys*, Y.-W. Kim and R. R. Boyer, Eds. Warrendale, Pa: TMS, 1991, pp. 313–322.

[76] R. O. Ritchie and S. Suresh, "Some considerations on fatigue crack closure at near-threshold stress intensities due to fracture surface morphology," *Metall. Trans. A*, vol. 13, no. 5, pp. 937–940, May 1982.

[77] R. O. Ritchie and J. F. Knott, "Mechanisms of fatigue crack growth in low alloy steel," *Acta Metall.*, vol. 21, no. 5, pp. 639–648, May 1973.

[78] A. B. El-Shabasy and J. J. Lewandowski, "Effects of load ratio, R, and test temperature on fatigue crack growth of fully pearlitic eutectoid steel (fatigue crack growth of pearlitic steel)," *Int. J. Fatigue*, vol. 26, no. 3, pp. 305–309, Mar. 2004.

[79] M. S. Dahar, S. M. Seifi, B. P. Bewlay, and J. J. Lewandowski, "Effects of test orientation on fracture and fatigue crack growth behavior of third generation as-cast Ti–48Al–2Nb–2Cr," *Intermetallics*, vol. 57, pp. 73–82, Feb. 2015.

[80] T. Leitner, M. Schloffer, S. Mayer, J. Eßlinger, H. Clemens, and R. Pippan, "Fracture and R-curve behavior of an intermetallic β-stabilized TiAl alloy with different nearly lamellar microstructures," *Intermetallics*, vol. 53, pp. 1–9, Oct. 2014.

[81] M. G. Mendiratta, J. J. Lewandowski, and D. M. Dimiduk, "Strength and ductile-phase toughening in the two-phase Nb/Nb5Si3 alloys," *Metall. Trans. A*, vol. 22, no. 7, pp. 1573–1583, 1991.

[82] W. Wessel, F. Zeismann, and A. Brueckner-Foit, "Short fatigue cracks in intermetallic γ-TiAl-alloys: SHORT CRACKS IN INTERMETALLIC TIAL," *Fatigue Fract. Eng. Mater. Struct.*, vol. 38, no. 12, pp. 1507–1518, Dec. 2015.

[83] M. S. Dahar, S. A. Tamirisakandala, and J. J. Lewandowski, "Fatigue crack growth and fracture behavior of as-cast Ti-43.5Al-4Nb-1Mo-0.1B (TNM) compared to Ti-48Al-2Nb-2Cr (4822)," *Intermetallics*, vol. 91, no. Supplement C, pp. 158–168, Dec. 2017.

[84] R. H. Dauskardt, B. J. Dalgleish, D. Yao, R. O. Ritchie, and P. F. Becher, "Cyclic fatigue-crack propagation in a silicon carbide whisker-reinforced alumina composite: role of load ratio," *J. Mater. Sci.*, vol. 28, no. 12, pp. 3258–3266, 1993.

[85] R. H. Dauskardt, M. R. James, J. R. Porter, and R. O. Ritchie, “Cyclic Fatigue-Crack Growth in a SiC-Whisker-Reinforced Alumina Ceramic Composite: Long- and Small-Crack Behavior,” *J. Am. Ceram. Soc.*, vol. 75, no. 4, pp. 759–771, 1992.

[86] C. J. Gilbert, J. . Cao, W. . Moberlychan, L. . Dejonghe, and R. O. Ritchie, “Cyclic fatigue and resistance-curve behavior of an in situ toughened silicon carbide with Al-B-C additions,” *Acta Mater.*, vol. 44, no. 8, pp. 3199–3214, 1996.

[87] Y. Torres, M. Anglada, and L. Llanes, “Fatigue mechanics of WC–Co cemented carbides,” *Int. J. Refract. Met. Hard Mater.*, vol. 19, no. 4, pp. 341–348, 2001.

[88] K. Badrinarayanan, A. L. McKelvey, R. O. Ritchie, and K. V. Rao, “Fracture and fatigue-crack growth behavior in ductile-phase toughened molybdenum disilicide: Effects of niobium wirevs particulate reinforcements,” *Metall. Mater. Trans. A*, vol. 27, no. 12, pp. 3781–3792, 1996.

[89] C. J. Gilbert, V. Schroeder, and R. O. Ritchie, “Mechanisms for fracture and fatigue-crack propagation in a bulk metallic glass,” *Metall. Mater. Trans. A*, vol. 30, no. 7, pp. 1739–1753, 1999.

[90] A. L. McKelvey and R. O. Ritchie, “Fatigue-crack growth behavior in the superelastic and shape-memory alloy Nitinol,” *Metall. Mater. Trans. A*, vol. 32, no. 3, pp. 731–743, 2001.

[91] R. H. Van Stone, “Residual life prediction methods for gas turbine components,” *Mater. Sci. Eng. A*, vol. 103, no. 1, pp. 49–61, 1988.

[92] J. P. Campbell, R. O. Ritchie, and K. V. Rao, “The effect of microstructure on fracture toughness and fatigue crack growth behavior in γ-titanium aluminide based intermetallics,” *Metall. Mater. Trans. A*, vol. 30, no. 3, pp. 563–577, 1999.